BURNING VELOCITY AND LOWER FLAMMABILITY LIMITS OF HYBRID MIXTURES CONTAINING COMBUSTIBLE DUST AND FLAMMABLE GAS

by

Chris T. Cloney

Submitted in partial fulfillment of the requirements
for the degree of Doctor of Philosophy

at

Dalhousie University
Halifax, Nova Scotia
April 2018

Dedicated To: The families and communities suffering loss from combustible dust fires and explosions.

Table of Contents

List of Tables . . . . . **viii**

List of Figures . . . . . **xiii**

Abstract . . . . . **xiv**

List of Symbols and Abbreviations Used . . . . . **xv**

Acknowledgements . . . . . **xxi**

Chapter 1 Introduction **1**

1.1 Motivation 2
1.1.1 Hybrid Mixtures 2
1.1.2 Prevention and Protection 3
1.1.3 Current Limitations 4
1.1.4 Role of Fundamental Knowledge 4
1.2 Scope of Work 5
1.2.1 Explosion Process 6
1.2.2 Scales Involved 7
1.2.3 Current Model 9
1.3 Objectives and Contribution 9
1.4 Thesis Outline 10
1.4.1 Previous Work of the Current Author 11

Chapter 2 Literature Review **13**

2.1 Burning Velocity 13
2.1.1 Closed-Chamber Explosion Testing 15
2.1.2 Explosion Regime Diagrams 17
2.1.3 Literature Coverage 18
2.1.4 Proposed Additional Regimes 20
2.2 Lower Flammability Limits 24
2.2.1 Methane Gas 25
2.2.2 Coal Dust 25
2.2.3 Hybrid Mixing Rules 27
2.2.4 Comparison to the Literature 29

2.3 CFD Modeling of Laminar Dust Flames 31
2.3.1 Previous Literature Models 31
2.3.2 Role of Radiation 32

Chapter 3 Model Description 34

3.1 Gas-Phase Transport 34
3.1.1 Governing Equations 34
3.1.2 Viscous Transport 36
3.1.3 Heat Flux 37
3.1.4 Species Diffusion 38
3.1.5 Gas-Phase Chemistry 41
3.1.6 Thermophysical Properties 43
3.1.7 Simplified Equations 44
3.1.8 Comparison between Gas-Flame Models 45
3.2 Particle-Phase Transport 45
3.2.1 Governing Equations 46
3.2.2 Exchange Terms 46
3.2.3 Particle Drag 48
3.2.4 Particle Heating 49
3.2.5 Particle Devolatilization 49
3.2.6 Particle Surface Reactions 50
3.3 Comparison to Previous Literature Models 52

Chapter 4 Numerical Approach 55

4.1 Numerical Domain 55
4.1.1 Boundary Conditions 56
4.2 Multiphase Discretization 57
4.2.1 Gas Phase Exchange 57
4.2.2 Discrete and Continuum Particle Representations 58
4.2.3 Comparison of the Two Representations 58
4.3 Numerical Solution 59
4.3.1 Pressure-Velocity Coupling 59
4.3.2 Lagrange Solution 60
4.3.3 Gas-Phase Chemistry 60
4.3.4 Equation Coupling 61
4.4 Simulation Approach 61
4.4.1 Example Dust Flame Simulation 62

4.5 Solver Modifications 63

Chapter 5 Methane Flames 64

5.1 Model Verification 64
5.1.1 Ignition Delay 65
5.1.2 Thermophysical Parameters 67
5.1.3 Transport Parameters 68
5.1.4 Flame Structure 71
5.1.5 Burning Velocity 72
5.1.6 Flame Temperature 78
5.1.7 Effect of Modeling Parameters 78
5.2 Flame Thickness 80
5.2.1 Measurement Approach 80
5.2.2 Simulation Results 81
5.3 Flame Reaction Timescale 83
5.3.1 Calculation Approach 83
5.3.2 Simulation Results 84
5.4 Discussion of Results 85
5.4.1 Implications for Hybrid Mixtures 86
5.4.2 Accuracy of the CFD Model 86

Chapter 6 Coal Dust Flames 88

6.1 Model Verification 88
6.1.1 Momentum and Heat Exchange 88
6.1.2 Flame Structure 91
6.1.3 Burning Velocity 93
6.1.4 Effect of Initial Temperature 96
6.1.5 Effect of Modeling Parameters 98
6.2 Role of Reaction Mechanism 100
6.2.1 Flame Propagation 101
6.2.2 Flame Temperature 106
6.2.3 Burning Velocity 107
6.3 Role of Discrete Combustion 109
6.3.1 Flame Propagation 109
6.3.2 Burning Velocity 112
6.4 Flame Structure 113
6.4.1 Simulation Results 113

6.4.2 Combustion Regimes . . . 115
6.5 Discussion of Results . . . 117
6.5.1 Implications for Hybrid Mixtures . . . 117
6.5.2 Practical Implications . . . 117
6.5.3 Accuracy of the CFD Model . . . 118

Chapter 7 Hybrid Flames . . . 120

7.1 Model Verification . . . 120
7.1.1 Coupling Interaction . . . 120
7.1.2 Effect of Initial Temperature . . . 122
7.1.3 Burning Velocity . . . 124
7.2 Timescale Analysis . . . 125
7.2.1 Calculated Timescales . . . 126
7.2.2 Simulation Results . . . 127
7.3 Role of Equivalence Ratio . . . 128
7.3.1 Volatile Component Alone . . . 129
7.3.2 Volatile and Surface Reaction . . . 130
7.3.3 Effect of Particle Diameter . . . 131
7.4 Role of Discrete Combustion . . . 132
7.4.1 Burning Velocity . . . 132
7.4.2 Length-to-Diameter Ratio . . . 133
7.5 Combustion Regimes . . . 135
7.5.1 10 µm Particles . . . 135
7.5.2 33 µm Particles . . . 137
7.6 Discussion of Results . . . 139
7.6.1 Comparison to Explosion Regime Diagrams . . . 140
7.6.2 Practical Implications . . . 140
7.6.3 Discrete Particle Combustion . . . 143
7.6.4 Accuracy of the CFD Model . . . 144

Chapter 8 Lower Flammability Limits . . . 145

8.1 Methane Gas . . . 145
8.1.1 Flame Structure . . . 145
8.1.2 Role of Reaction Mechanism . . . 147
8.1.3 Flammability Criteria . . . 149
8.2 Coal Dust . . . 150
8.2.1 Flame Structure . . . 150

8.2.2 Role of Reaction Mechanism 151
8.2.3 Role of Particle Diameter and Discrete Combustion 153
8.3 Hybrid Mixtures 155
8.3.1 10 µm Particles 156
8.3.2 33 µm Particles 160
8.4 Discussion of Results 161
8.4.1 Evaluation of Mixing Rules 162
8.4.2 Implications for Experimental Testing 163
8.4.3 Accuracy of the CFD Model 164

Chapter 9 Conclusion 166

9.1 Summary of Results 167
9.1.1 Combustion Regimes 167
9.1.2 Lower Flammability Limits 168
9.1.3 Discrete Particle Combustion 169
9.1.4 Accuracy of the CFD Model 169
9.1.5 Practical Implications 171
9.2 Recommendations 172
9.2.1 Future Work 173

References 174

Appendix A Equivalence Ratio Calculation 189

List of Tables

2.1 Summary of closed-chamber explosion data for hybrid systems in the literature 15

2.2 Summary of literature data for lower explosion limits of hybrid mixtures 30

3.1 Gas-phase chemistry reaction mechanisms used in the current work 42

3.2 Single-step and two-step global reaction model parameters . . . 42

3.3 Comparison between gas phase flame simulation models explored in this work 45

3.4 Comparison of modeling parameters used in this work and previous studies from the literature [65] 53

4.1 Boundary conditions for one-dimensional flame simulation. . . . 57

5.1 Summary of methane flame characteristics with four reaction mechanisms 84

6.1 Summary of coal dust combustion regimes and flame characteristics with increasing dust concentration 118

7.1 Comparison between explosion regimes proposed from the literature and combustion regimes presented in the current work . . 142

8.1 Flame characteristics near the methane gas LFL using the DRM19 reaction mechanism 150

8.2 Coal dust flame characteristics for 10 µm particles near the LFL using different reaction mechanisms 152

A.1 Balanced stoichiometry for methane gas in air used to calculate specie mass fractions for the stoichiometric fuel-to-air ratio . . 190

A.2 Balanced stoichiometry for coal dust in air including volatile methane and carbon components 193

List of Figures

1.1 Five requirements for a dust or hybrid explosion 5

1.2 Unwrapping the dust explosion pentagon to illustrate the process involved [43] 6

1.3 Scales associated with dust explosions with corresponding modeling methodologies [43] 8

2.1 Hybrid explosion regimes originally proposed in the literature by Garcia-Agreda [97] and Garcia-Agreda et al. [29] 17

2.2 Approximate literature coverage for experimental studies investigating burning velocity of hybrid mixtures 19

2.3 Ratio of K_{m} for the hybrid explosion to that from the dust-only explosion from four literature studies 21

2.4 Hybrid explosion regime diagram for low-reactivity dust reproduced from the experiments of Denkevits [18] 23

2.5 Hybrid explosion regime diagram for high-reactivity dust reproduced from the experiments of Denkevits and Hoess [88] . . . 24

4.1 Schematic of one-dimensional computational domain 56

4.2 Example transient temperature profile for 4 µm coal particles at 144.3 $\mathrm{g/m^3}$ concentration 62

5.1 Comparison of ignition delay times in a CPFMR with four reaction mechanisms 66

5.2 Temperature as a function of time in a CPFMR using the DRM19 reaction mechanism 66

5.3 Species mass fraction as a function of time in a CPFMR using the DRM19 reaction mechanism 67

5.4 Gas density and specific heat as a function of time in a CPFMR using the DRM19 reaction mechanism 68

5.5 Gas viscosity, thermal conductivity, and species mass diffusivity in a CPFMR using the DRM19 reaction mechanism 69

5.6 Methane flame structure with different computational models using the DRM19 reaction mechanism 71

5.7 Distribution of minor species in a methane flame with different computational models using the DRM19 reaction mechanism . 72

5.8 Methane burning velocity using Cantera$^{\text{multi}}$ with different reaction mechanisms compared to experimental data 73

5.9 Comparison of methane burning velocity using Cantera$^{\text{multi}}$, Cantera$^{\text{mix}}$, Cantera$^{\text{unity}}$, and the current simulation model . . 75

5.10 Methane burning velocity using the current model with different reaction mechanisms compared to experimental data 77

5.11 Methane flame temperature compared to adiabatic temperature calculated with Cantera using the GRI53 mechanism 78

5.12 Methane burning velocity for varying cell resolutions and equivalence ratios 79

5.13 Example methane flame thickness calculation using the DRM19 reaction mechanism ($\Phi_g = 0.8$) 81

5.14 Methane flame thickness from experimental measurements and simulation models 82

5.15 Methane flame thickness from the current model using the direct measurement approach 83

5.16 Methane flame reaction timescale calculated with four reaction mechanisms with the current model 85

6.1 Velocity of a 10 µm particle placed in air flowing at a constant velocity of 1 m/s 89

6.2 Temperature of a 10 µm particle placed in a stationary gas at a temperature of 2000 K 90

6.3 Coal dust flame structure with 4 µm particles and 144.3 g/m^3 concentration at ambient temperature and pressure 92

6.4 Heat release rate for a coal dust flame with 4 µm particles and 144.3 g/m^3 concentration at ambient temperature and pressure 93

6.5 Coal dust burning velocity at ambient temperature and pressure compared to simulation results of Smoot and Horton [78] . . . 94

6.6 Coal dust burning velocity at ambient temperature and pressure compared to experimental data of Horton et al. [77] 95

6.7 Coal dust burning velocity at elevated initial temperatures compared to results from the literature 97

6.8 Flame profile using MP1 chemistry model with surface reactions and different diffusivity constants 98

6.9 Burning velocity and normalized burning velocity as a function of coal dust concentration at different cell resolutions 100

6.10 Coal dust flame propagation for 10 and 33 µm particles at various concentrations using different reaction mechanisms 102

6.11 Flame ignition process in 10 µm particles at a concentration of 180 g/m^3 using the DRM19 mechanism 104

6.12 Flame quenching process in 33 µm particles at a concentration of 650 g/m^3 using the BFER2 mechanism 105

6.13 Flame structure for 33 µm particles at a concentration of 400 g/m^3 using the DRM19 mechanism 106

6.14 Coal dust flame temperature for 10 and 33 µm particles with different reaction mechanisms 107

6.15 Coal dust burning velocity at ambient temperature with different reaction mechanisms 108

6.16 Flame position versus time using MP1 and DRM19 mechanisms and continuum and discrete particle representations 110

6.17 Flame profile using DRM19 chemistry model and a discrete particle representation 111

6.18 Coal dust burning velocity using the continuum and discrete particle representations at different initial temperatures 112

6.19 Coal dust flame structure at different dust concentrations using the MP1 mechanism at ambient initial temperature 114

6.20 Coal dust combustion regimes predicted from flame structure analysis 115

7.1 Comparison of hybrid flame normalized burning velocity for coal dust and methane gas to the data of Xie et al. [80] 121

7.2 Comparison of hybrid flame normalized burning velocity to the experimental data of Lee et al. [82] 123

7.3 Comparison of hybrid burning velocity of coal dust and methane gas to the experimental data of Horton et al. [77] 125

7.4 Particle heating, devolatilization, and surface reaction timescales compared to the flame residence time 126

7.5 Effect of particle size on the burning velocity for hybrid mixtures of reacting and nonreacting particles 127

7.6 Hybrid burning velocity as a function of volatile component equivalence ratio (methane gas and dust volatiles) 129

7.7 Hybrid burning velocity as a function of the total equivalence ratio (methane gas with coal dust volatiles and surface reaction) 130

7.8 Hybrid burning velocity for 33 µm particles as a function of the volatile component and total equivalence ratios 131

7.9 Hybrid burning velocity using the continuum and discrete particle representations and the MP1 reaction mechanism 133

7.10 Hybrid burning velocity as a function of length-to-diameter ratio for 10 and 33 µm coal dust particles 134

7.11 Hybrid mixture burning velocity for 10 µm coal particles at different initial methane gas equivalence ratios 136

7.12 Burning velocity and combustion regime diagram for hybrid mixtures of 10 µm coal dust particles and methane gas 137

7.13 Hybrid mixture burning velocity for 33 µm coal particles at different initial methane gas equivalence ratios 138

7.14 Burning velocity and combustion regime diagram for hybrid mixtures of 33 µm coal dust particles and methane gas 139

7.15 Combustion regime diagram from the literature compared to those developed in the current work 141

8.1 Methane flame structure at equivalence ratios of 0.5, 0.45, and 0.40 using the DRM19 reaction mechanism 146

8.2 Methane burning velocity near the LFL using different reaction mechanisms 147

8.3 Methane flame temperature at 100 ms into the simulation near the LFL using different reaction mechanisms 148

8.4 Coal dust flame structure at concentrations of 40, 45, and 50 g/m^3 using the DRM19 reaction mechanism for 10 µm particles . . . 151

8.5 Coal dust burning velocity near the LFL for 10 µm particles using four reaction mechanisms 152

8.6 Coal dust flame propagation for 10 and 33 µm particles near the dust LFL 154

8.7 Coal dust burning velocity near the LFL for different particle sizes using the DRM19 reaction mechanism 155

8.8 Flame position as a function of time and flame structure near the LFL for 10 µm particles using the continuum representation 156

8.9 LFLs for hybrid mixtures of 10 µm coal dust using the continuum particle representation 158

8.10 LFLs for hybrid mixtures of 10 µm coal dust using the discrete particle representation 159

8.11 LFLs for hybrid mixtures of 33 µm coal dust using the continuum and discrete particle representations 160

Abstract

Hybrid mixtures of combustible dust and flammable gas may demonstrate increased burning velocities and reduced lower flammability limits (LFL) over the fuels individually. This can increase explosion likelihood and severity in industrial operations and makes it difficult to develop and implement explosion prevention and protection strategies. The objective of this work is to extend the current knowledge of laminar burning velocity and LFLs of hybrid mixtures. This is achieved using computational fluid dynamics (CFD) modeling to analyze flame structure, burning velocity, and propagation limits. The computational model includes global approximations to molecular transport, and the accuracy of four reaction mechanisms with increasing complexity are explored.

Simulations investigating the structure of coal dust flames, the effect of equivalence ratio on hybrid mixtures, and coupling interaction between gas flame propagation and particle combustion, are explored in this work. These simulations allow combustion regime diagrams to be created for hybrid mixtures. In these diagrams, six regimes are identified: fuel-lean, fuel-rich, volatile-rich, transition flames, kinetic-limited flames, and impeded-gas flames.

Mixing rules for lower flammability limits of methane gas and coal dust mixtures are evaluated based on results from the CFD model. Linear mixing based on Le Chatelier's law is found to agree with the simulation results for 10 µm coal dust particles. Larger particles with 33 µm diameters demonstrated strong flame propagation at concentrations slightly wider than Le Chatelier's Law, but not as wide as Bartknetch's curve.

The results from this work provide novel classifications of burning velocity enhancement for hybrid mixtures, illustrate that linear mixing rules approximately delineate LFLs for coal dust and methane gas, and verify the accuracy of the CFD model. These results can be used to guide experimental testing for research programs or hazard assessments, and the CFD model provides an open platform to explore and extend the fundamental knowledge of flame propagation in dust and hybrid mixtures.

List of Abbreviations and Symbols Used

Abbreviations

Acronym	Description
BC	Bartknecht's Curve
BFER2	Two-Step Global Reaction Mechanism
BV	Burning Velocity
CFD	Computational Fluid Dynamics
CFL	Courant-Friedrichs-Lewy Condition
CPFMR	Constant-Pressure, Fixed-Mass Reactor
CPU	Central Processing Unit
CX	Calculated Approach
DRM19	19-Specie Reduced Reaction Mechanism
GRI53	53-Specie Detailed Reaction Mechanism
JANAF	Joint Army Navy Air Force
JC	Jiang's Curve
LFL	Lower Flammability Limit
LCL	Le Chatelier's Law
MCC	Micro Crystalline Cellulose
MEC	Minimum Explosible Concentration
MP1	Single-Step Global Reaction Mechanism
MX	Direct Measurement Approach
NBV	Normalized Burning Velocity
NFPA	National Fire Protection Association
PISO	Pressure Implicit with Split Operator
SIMPLE	Semi-Implicit Method for Pressure Linked Equations

Roman Symbols

Symbol	Description	Units
a_i	specific heat fit parameters	various

A	Arrhenius pre-exponential factor	-
A_s	surface area	m^2
A_μ	Sutherland's coefficient	$\mathrm{Pa\,s\,K}^{-1}$
c	molar mass	mole
C	constant in Jiang's curve	-
C_D	drag coefficient	-
C_p	specific heat at constant pressure	$\mathrm{J\,kg}^{-1}\mathrm{K}^{-1}$
C_s	specific heat of a particle	$\mathrm{J\,kg}^{-1}\mathrm{K}^{-1}$
C_v	specific heat at constant volume	$\mathrm{J\,kg}^{-1}\mathrm{K}^{-1}$
d	diameter	m
D	mass diffusivity coefficient	$\mathrm{m}^2\mathrm{s}^{-1}$
D_{kj}	binary diffusivity coefficient	$\mathrm{m}^2\mathrm{s}^{-1}$
$D_{\mathrm{T},k}$	thermal diffusivity coefficient	$\mathrm{m}^2\mathrm{s}^{-1}$
D_s	surface mass diffusivity coefficient	$\mathrm{m}^2\mathrm{s}^{-1}$
D_s^*	scaled surface mass diffusivity coefficient	$\mathrm{m}^2\mathrm{s}^{-1}$
e	specific energy	$\mathrm{J\,kg}^{-1}$
e_s	sensible specific energy	$\mathrm{J\,kg}^{-1}$
e_t	total specific energy	$\mathrm{J\,kg}^{-1}$
E_a	Arrhenius activation energy	$\mathrm{J\,kg}^{-1}$
F	force	N
F/A	fuel-to-air ratio	-
$\mathbf{g}$	gravity vector	$\mathrm{m\,s}^{-2}$
h	specific enthalpy	$\mathrm{J\,kg}^{-1}$
h_s	sensible specific enthalpy	$\mathrm{J\,kg}^{-1}$
h_sc	sensible and chemical specific enthalpy	$\mathrm{J\,kg}^{-1}$
h_t	total specific enthalpy	$\mathrm{J\,kg}^{-1}$
h_tnc	total nonchemical specific enthalpy	$\mathrm{J\,kg}^{-1}$
$\dot{H}$	heat exchange rate	$\mathrm{J\,s}^{-1}$
k_r	reaction rate coefficient	s^{-1}
K_D	surface reaction rate coefficient	$\mathrm{kg\,m}^{-2}\,\mathrm{s}^{-1}\,\mathrm{Pa}^{-1}$
K_G	maximum K_m in gas concentration range	$\mathrm{bar\,m\,s}^{-1}$

K_{m}	sized-normalized maximum $\mathrm{d}P/\mathrm{d}t$	$\mathrm{bar\,m\,s^{-1}}$
K_{St}	maximum K_{m} in dust concentration range	$\mathrm{bar\,m\,s^{-1}}$
l_{f}	flame thickness	m
l_{ph}	preheat zone thickness	m
L_s	centre-to-centre particle spacing	m
L_{v}	latent heat of devolatilization	$\mathrm{J\,kg^{-1}}$
m	mass	kg
$\dot{m}$	mass transfer rate	$\mathrm{kg\,s^{-1}}$
M	molecular weight	$\mathrm{kg\,mol^{-1}}$
M_{kj}	reduced molecular weight	$\mathrm{kg\,mol^{-1}}$
n_r	Arrhenius temperature exponent	-
N_k	number of species	-
N_{p}	number of particles	-
N_r	number of reactions	-
P	pressure, partial pressure	Pa
P_{m}	maximum change in pressure	bar
P_{max}	maximum P_{m} in dust concentration range	bar
q	reaction heat release	$\mathrm{J\,mol^{-1}}$
$\mathbf{q}$	heat transfer vector	$\mathrm{J\,m^{-2}\,s^{-1}}$
$\dot{Q}$	energy transfer rate	$\mathrm{J\,s^{-1}}$
$\dot{S}_i$	transport equation source term	various
S_{L}	laminar burning velocity	$\mathrm{m\,s^{-1}}$
t	time dimension	s
T	temperature	K
T_μ	Sutherland's temperature	K
u	velocity	$\mathrm{m\,s^{-1}}$
$\mathbf{U}$	velocity vector	$\mathrm{m\,s^{-1}}$
V	diffusion velocity	$\mathrm{m\,s^{-1}}$
V^*	estimated diffusion velocity	$\mathrm{m\,s^{-1}}$
$\mathcal{V}$	volume	$\mathrm{m^3}$
$\mathbf{V}$	diffusion velocity vector	$\mathrm{m\,s^{-1}}$

x	space dimension, position	m
X	mole fraction	-
Y	mass fraction	-

Greek Symbols

Symbol	Description	Units
α	thermal diffusivity	$\mathrm{m^2\,s^{-1}}$
δ_{mn}	Kronecker delta	-
$\Delta h_\mathrm{f}^\circ$	specific enthalpy of formation	$\mathrm{J\,kg^{-1}}$
Δt	simulation timestep	s
Δx	simulation cell size	m
ϵ	heat retention coefficient	-
η	molar concentration	$\mathrm{mol\,m^{-1}}$
λ	thermal conductivity	$\mathrm{W\,m^{-1}\,K^{-1}}$
μ	dynamic viscosity	$\mathrm{Pa\,s}$
μ'	bulk dynamic viscosity	$\mathrm{Pa\,s}$
ν'	stoichiometric coefficients (reactants)	-
ν''	stoichiometric coefficients (products)	-
ρ	density	$\mathrm{kg\,m^{-3}}$
σ	mass concentration	$\mathrm{kg\,m^{-3}}$
$\bar{\sigma}$	collision diameter	m
$\bar{\sigma}_{kj}$	reduced collision diameter	m
$\boldsymbol{\sigma}$	stress tensor	$\mathrm{N\,m^{-2}}$
τ_f	flame reaction timescale/flame residence time	s
τ_h	particle heating timescale	s
τ_{mn}	viscous stress tensor	$\mathrm{N\,m^{-2}}$
τ_p	particle combustion timescale	s
τ_s	particle surface reaction timescale	s
τ_u	particle drag timescale	s
τ_v	particle devolatilization timescale	s
τ_vol	time for gas flame to reach vessel walls	s

ϕ	mass flux	$\mathrm{kg\,m^{-2}\,s^{-1}}$
Φ	equivalence ratio	-
Φ_{kj}	Wilke coefficient	-
ψ	particle mass fraction	-
$\dot{\omega}$	reaction rate	$\mathrm{mol\,m^{-3}\,s^{-1}}$
Ω	collision integral	$\mathrm{m^3\,s^{-1}}$

Constants and Non-Dimensional Numbers

Symbol	**Description**	**Units**
$\mathcal{A}$	Avogadro's Number	$\mathrm{mol^{-1}}$
k_{B}	Boltzmann's constant	$\mathrm{J\,K^{-1}}$
Le	Lewis Number	-
Nu	Nusselt Number	-
Pr	Prandlt Number	-
π	pi	-
Re	Reynolds Number	-
$\mathcal{R}$	universal gas constant	$\mathrm{J\,mol^{-1}\,K^{-1}}$
$\mathcal{R}_{\mathrm{Sp}}$	specific gas constant	$\mathrm{J\,kg^{-1}\,K^{-1}}$
Sc	Schmidt Number	-

Subscripts and Superscripts

Symbol	**Description**
$\circ$	initial
b	backward
c	correction
k, j	specie indices
f	forward, formation
g	gas
h	hybrid
global	global model
l, m, n	dimension indices

mix	mixed parameters, mixed species model
mol	mol based parameter
multi	multispecie model
p	particle
r	reaction
s	surface
t	total
St	stoichiometric
v	volatiles, devolatilization
unity	unity Lewis number model

Acknowledgements

I am indebted to Dr. Paul Amyotte and Dr. Robert Ripley for their co-supervision of this thesis. Dr. Amyotte introduced me to the world of process safety and dust explosion, and Dr. Ripley introduced me to computational fluid dynamics and the scientific study of particle physics. Without these introductions, I would not have started down the path to my PhD and without their excitement, knowledge, and guidance, completion of this body of work would not have been possible.

I would also like to thank Dr. Michael Pegg and Dr. Faisal Khan for their ongoing efforts, technical discussion, and helpful suggestions during my comprehensive exams and project research. Thank you to Dr. Jan Haelssig for supervising my directed study course and helping to introduce me to the OpenFOAM platform.

It is a pleasure to thank my colleagues at Martec for their support and encouragement during several years of my thesis. In particular, I wish to thank Laura Donahue for her mentorship and guidance. I also appreciate the countless hours solving technical challenges and forming friendships with those on the Chinook team.

To my family, I am forever thankful for your love and support. From Mom, Dad, Kevin, Trevor, Renea and Lynda, I learned the power of drive, inspiration, connection, and kindness. To my friends back home, the Duenchs, and my other extended family, I appreciate your positive thoughts and patience through these busy years. To Tom and Perry, thank you for your ongoing friendship and showing me the way by achieving your doctorates first.

Last, and most importantly, I wish to thank my wife Kellie. You are my balance, my joy, and my reason why. From the halls of residence to match day and beyond, you have been the one constant and the only reason for my success.

I gratefully acknowledge the financial support provided for this research by the Natural Sciences and Engineering Research Council of Canada (NSERC), the Government of Nova Scotia through the Nova Scotia Research and Innovation Graduate Scholarship, and Dalhousie University.

Chapter 1

Introduction

On the morning of May 9, 1992, 26 underground coal miners were finishing their shift at the Westray mine in the community of Plymouth in Pictou County, Nova Scotia. The mine had opened just seven months earlier and promised the creation of 300 needed jobs in the area. Secured by more than $100 million in provincial and federal loans, the mine was expected to deliver 700,000 tons of coal per year to Nova Scotia Power Corporation in its first 15 years of operation [1].

All of that changed at 5:18 am when a spark from the drilling equipment at the mine face ignited a methane gas explosion followed by a coal dust explosion, which propagated throughout the mine [2]. Mine equipment and the entrance were destroyed, and the blast shook houses kilometres away. All 26 men working in the mine were killed in what would be the largest workplace catastrophe in Nova Scotia since the 1917 explosion in the Halifax Harbour [3].

The aftermath of the Westray explosion included a five-year inquiry by the province, resulting in the publishing of "The Westray Story – A Predictable Path to Disaster" [1] and a criminal trial for mine managers. Several deficiencies in the mine safety program were revealed including inadequate ventilation, human tampering with methane level monitors, inadequate removal and cleanup of latent coal dust deposits, and an ineffective rock dust inerting program [4].

Although there were technical questions about the ignition event, flame transmission throughout the mine gallery, and human factors leading up to the blast, one thing is certain — the personal loss to the families of the victims and community is unquantifiable. What can be measured includes the death of 26 human beings; the total destruction of the mining operations; bankruptcy of the mine parent company, Curragh resources; millions of dollars in severance and unemployment costs; over $100 million in defaulted government loans; and the cost of a five-year criminal investigation of the mine managers [2].

1.1 Motivation

One of the most concerning issues around the Westray explosion is how well-known the hazard of combustible dust explosions was at the time and how frequently they occur. Between 1900 and 1956, 1123 dust explosions were reported in the United States by the National Fire Protection Association (see NFPA report [5] as referenced by Eckhoff [6]). A further 281 "major" dust explosions were reported by the US Chemical Safety Board (CSB) between 1980 and 2005 [7], resulting in 119 fatalities and 718 injures. Internationally, Nifuku et al. [8] report 269 dust explosions in Japan from 1952 to 1995, Eckhoff [6] reports 357 in Germany from 1965 to 1980, Mannan and Waldram [9] report 984 dust fires and explosions in the United Kingdom between 1958 and 1988, and Yan and Yu [10] report 72 dust explosions in industries not including coal mining in China from 1981 to 2011.

In total, these more than 2000 incidents account for over 1000 fatalities and 4000 injuries across various industries in the 20th century. These numbers do not include the often limited reporting in less developed nations [11] or the particularly devastating coal mine explosions reported in China [12], which increase the fatalities by more than a factor of four [13]. They also do not take into account the fact that dust explosions are very often underreported or misreported [9]. Yuan et al. [12] provide an extensive summary of the literature data including a review of the dusts, equipment, and industries involved. The overarching motivation for any dust explosion research program is to eliminate or reduce loss from these types of incidents, and understanding the phenomena involved is a lead driver for the current thesis effort.

1.1.1 Hybrid Mixtures

Hybrid explosions involve situations where both combustible dust (e.g., coal, sawdust, grain, sugar, or plastics) and flammable gas (e.g., methane, hydrogen, volatiles from dust off-gassing, or flammable vapors from liquid evaporation) are mixed together before or during flame propagation [14]. These mixtures have been reported in several industries including mining [15], agricultural [16], pharmaceutical [17], nuclear [18], and general processing [19]. These so-called "nontraditional" fuel systems [20, 21] demonstrate increased flame propagation rates (i.e., burning velocity) and reduced

lower flammability limits compared to the dust alone [6, 14].

1.1.2 Prevention and Protection

Dastidar et al. [22] present a five-step procedure for evaluating dust and hybrid mixture explosion hazards in processing plants. The first step of this process involves characterizing reactivity and flammability of the materials used in the facility. This data includes the minimum explosible concentration (MEC) of the dust, the lower flammability limit (LFL) of the gas, maximum pressure caused by an explosion in a closed vessel (P_{m}), and the size-normalized maximum rate of pressure rise caused by an explosion in a closed vessel (K_{m}). The final step of the process is to devise and implement a hazard mitigation plan that includes strategies to prevent an explosion from occurring and to protect the facility and workers in the case where one does occur.

Prevention of an explosion can be achieved by keeping the materials involved below their respective flammability criteria (collectively referred to as LFL in this work) [22]. The engineering design guidance for hybrid mixtures in NFPA 69 and NFPA 654 specifies that the combined concentration of the combustible dust and flammable gas stay below 25 % of the combined LFL [23, 24]. Under the ASTM International standards, the combined LFL is determined experimentally using closed-chamber explosion testing following ATSM E 1515 [25].

Protection from an explosion can be achieved by mitigating the pressure rise in process equipment or arresting the flame during propagation [6]. Two approaches to this include venting through blow-out panels [26] or suppressing the explosion using thermal or chemical agents [24]. Both of these strategies require experimental testing to determine P_{max} and K_{St} (maximum P_{m} and K_{m} in the dust concentration range under specific test conditions [27]). These parameters are used to predict the flame propagation rate, size deflagration vent panels, or trigger suppression equipment [24, 26].

A leading difficulty in hybrid explosion prevention and protection is the number of experimental tests required to fully characterize the fuel. While a single dust may require 10 tests to determine K_{St} when the concentration at which it occurs is near $750\,\mathrm{g/m^3}$ [27] and six tests to determine MEC when it is near $50\,\mathrm{g/m^3}$ [25], a

hybrid mixture requires this to be repeated at each gas concentration of interest [26]. This time consuming and potentially expensive testing may push companies to avoid getting their materials characterized or to use $P_{\max}$ and K_{St} for the dust alone, which could lead to underprotection. Alternately, NFPA 68 allows a K_{St} of 500 bar-m/s to be used for hybrid mixtures where the dust has a $K_{\mathrm{St}} < 300$ bar-m/s and the gas has a burning velocity within 30 % of the value for propane [26]. However, this may be overly conservative as Pellmont [28] found hybrid mixtures of propane and five industrial dusts to have K_{St} values of 150 bar-m/s or less. Overall, more knowledge is required to efficiently characterize the reactivity and flammability of hybrid mixtures and this lack of knowledge demonstrates a need for systematic research in this field [14].

1.1.3 Current Limitations

Flame propagation and the coupling interaction between dust and gas combustion has been explored for hybrid mixtures by Garcia-Agreda et al. [29] and Sanchirico et al. [30]. These authors visually represented K_{m} as an Explosion Regime Diagram on a plane with dust concentration on the ordinate and gas concentration on the abscissa. They then divided the diagram into five regimes based on the dust MEC and gas LFL: dust-driven explosion, gas-driven explosion, dual-fuel explosion, synergistic explosion, and no explosion. Although this regime diagram provides an insightful way to view experimental data, the divisions give no indication of the fundamental combustion processes occurring and require development to guide experimental testing programs.

Several authors have attempted to provide mixing rules for the combined LFL of hybrid mixtures with regard to the dust MEC and gas LFL alone [14, 31, 32, 33]. This is desirable to reduce the number of experimental tests required and to provide insight into the nature of flammability limits in hybrid mixtures. To date, no one mixing rule has been able to capture experimental observations from many different tests, and little fundamental knowledge is available on hybrid LFLs.

1.1.4 Role of Fundamental Knowledge

In his review of the current status and future trends in dust explosion research, Eckhoff [34] emphasizes the future role of fundamental knowledge in assessing and controlling dust explosion hazards. Specifically, he highlights a limited understanding

of the generation of explosible dust clouds and combustion phenomena during flame propagation as key areas requiring more research. Eckhoff [34] and Ogle [35] suggest comprehensive mathematical models such as Computational Fluid Dynamics (CFD) as valuable research tools in this area

A lack of tools to explore and extend the knowledge of fundamental processes in dust flames is hampering the integration of fundamental knowledge into prevention and protection practices [36]. CFD models capable of simulating the microscale features of dust flames (e.g., [37, 38]) may be too computationally expensive to apply to industrially relevant scenarios and large-scale operations. On the other hand, macroscale modeling approaches (e.g., [39, 40]) may include many empirical input parameters and simplified models, making it difficult to explore fundamental flame propagation processes [41].

A main driver of the current work is to develop a CFD model capable of capturing the microscale properties of burning velocity and flammability limits of hybrid mixtures, which can also be extended to industrially relevant scenarios in future investigations. Developing the model on an open platform that is available to all researchers in the community is also an important criterion for this work.

1.2 Scope of Work

To determine the scope of the CFD simulations, the different processes involved in dust and hybrid explosions need to be explored. The five elements involved in dust or hybrid explosion prevention are typically depicted as the explosion pentagon [6] as shown in Figure 1.1. Each side of the pentagon indicates a requirement necessary for an explosion to occur.

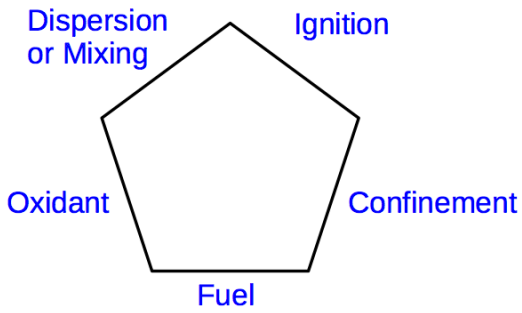

Figure 1.1: Five requirements for a dust or hybrid explosion.

In the explosion pentagon, the fuel is the dust or hybrid mixture, and the oxidizer in industrial scenarios is typically oxygen in air [42]. Under the conditions in which dust is not involved but the gas is above the LFL, a gas explosion hazard is present. In both cases, the fuel must be dispersed in the oxidizing gas at flammable concentrations for an explosion hazard to exist. An ignition source capable of igniting the fuel-oxidiser mixture must also be present to initiate the explosion. Lastly, confinement of the resulting flame propagation is required for pressure to rise to produce destructive forces.

Explosion prevention often focuses on removing one or more components of the pentagon in Figure 1.1 to stop the explosion from occurring [22]. Although the explosion pentagon is useful from a prevention perspective, it does not provide insight into the interaction between different requirements or how to protect from flame propagation once it occurs [43].

1.2.1 Explosion Process

The process involved during a dust explosion may be illustrated by "unwrapping" the explosion pentagon [43]. The resulting process diagram is presented in Figure 1.2 and shows interconnections between different elements of the pentagon. For a flame to propagate, the concentration of the dust and gas in the hybrid mixture must be above the LFL. Explosion severity is then governed by the interaction between flame propagation, confinement, and flame acceleration. These are termed "system interactions" in the figure.

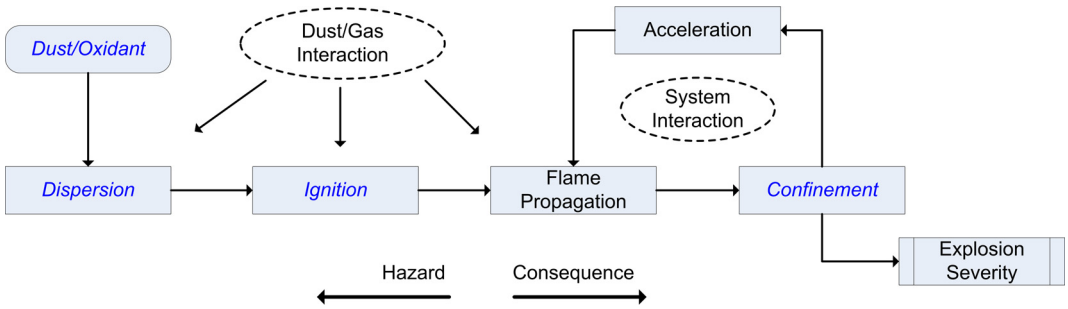

Figure 1.2: Unwrapping the dust explosion pentagon to illustrate the process involved [43].

The current work focuses on flame propagation in hybrid mixtures. This is the

first block on the "consequences" side of Figure 1.2. Specifically, LFLs (i.e., the combined concentrations under which a flame cannot propagate in the mixture) and burning velocities (i.e., the propagation rate under laminar flow and unstretched flame conditions) are explored. These fundamental parameters are a starting point for understanding explosion likelihood and severity in industrial systems and are not well characterized for hybrid mixtures to date.

The fuel system analyzed in this thesis is influenced by the fuel involved in mine explosions such as Westray and includes methane gas, coal dust, and hybrid mixtures of the two. In a typical coal mine explosion, a primary gas flame propagates along the mine gallery and lifts the coal dust into suspension [44]. A secondary explosion of this suspended coal dust cloud can then self-propagate throughout the mine as fuel is available [45]. The fuel for the secondary explosion may be dust alone or a hybrid mixture, depending on the particular scenario [46].

The system geometry explored in this work is also representative of coal mine explosions. The mine gallery is represented as a horizontal tube with a square cross-section and is broken into two main sections down its length. The first main section contains methane gas, which is initiated as a propagating flame. This flame propagates into the second "test" section, which contains either methane gas, coal dust, or a hybrid mixture of the two. The burning velocity is measured in the test section by comparing the flame position at different times during the simulation. To explore the LFLs, the concentration in the test section is reduced until a flame is no longer able to propagate. Modeling assumptions include homogeneous dispersion of the dust and gas cloud, monodisperse and spherical coal dust particles, and the effects of gravity including dust settling and flame buoyancy are neglected.

1.2.2 Scales Involved

One difficulty in CFD research is determining the level of simplification to include in the computational model [47]. If too much detail is included, computational resources may become prohibitively expensive [48]. If too little detail is included, the fundamental processes may not be resolved [49].

The different scales involved in hybrid explosions are summarized schematically in Figure 1.3 along with the investigation and modeling methodologies suggested by

Cloney et al. [43]. The geometric scales span at least 12 orders of magnitude from molecular heat and mass transfer on the order of nanometres, up to full processing plants and mines with scales on the order of kilometres.

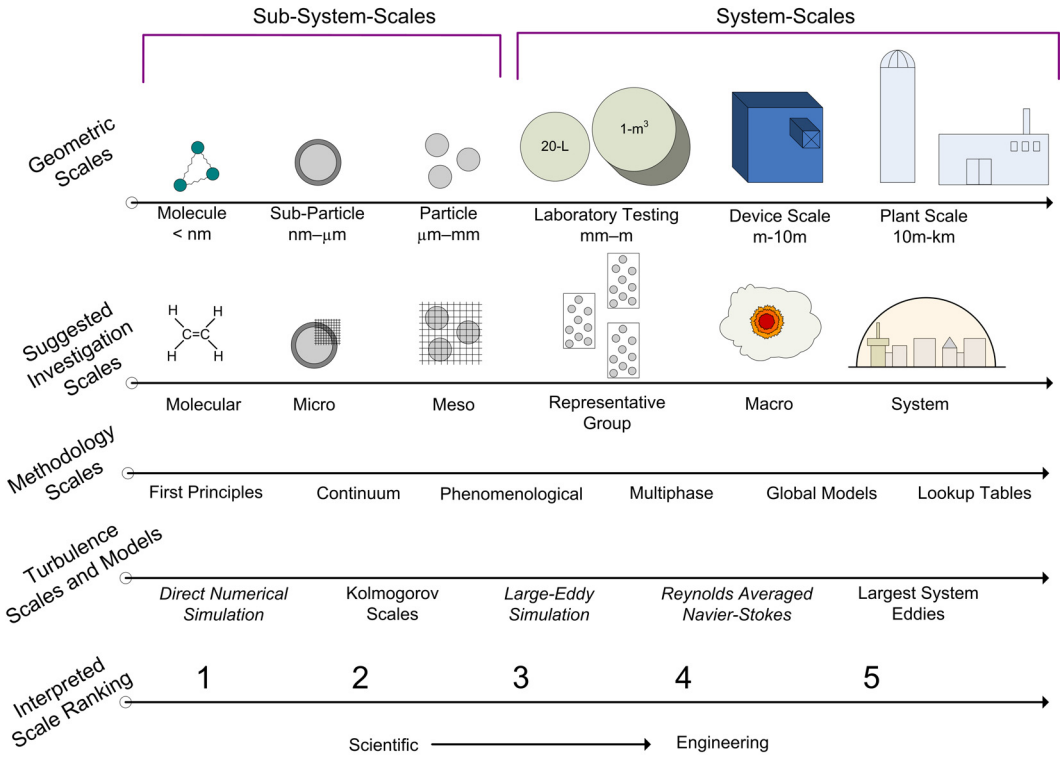

Figure 1.3: Scales associated with dust explosions with corresponding modeling methodologies [43].

Generally, two approaches to CFD modeling of dust and hybrid flames have been applied in the literature. In the first approach, macroscale modeling at full system scale (e.g., Skjold [50]), and device scale (e.g., Castellanos et al. [51]) have been used to analyze system interaction [52], confinement [53, 54], and flame acceleration [55]. These CFD models rely on empirical descriptions of flame propagation [39] and sub-grid modeling approaches [56], and may need experimental input such as $P_{\max}$ and K_{St} to calibrate the computational models [40]. Although some macroscale simulations have been applied to hybrid mixtures [16, 57], the empirical inputs required and model assumptions stop them from being able to analyze the burning velocity and flammability limits.

The second approach to modeling dust and hybrid flames involves microscale simulations based on first-principles gas theory to capture sub-particle and molecular

transport effects on flame propagation [37, 38, 58]. Simplified versions of these models have been applied to hybrid mixtures of methane and carbon [59, 60]. However, the full detail models may be too computational expensive to apply to laboratory, device, or system scales [48].

An example of the cost of large system-scale simulations is demonstrated in the work of Houim et al. [61, 62]. In these investigations, the authors completed large-scale simulations of coal mine explosions that included small-scale features such as dust lifting and particle-particle interaction. These simulations required 70,000 CPU hours and a large network of computer clusters [62]. Although very detailed information can be gained from these types of simulations, their use is generally unavailable to many individuals in the research community.

1.2.3 Current Model

The current CFD model is developed based on the openly available OpenFOAM CFD toolkit [63]. Although some modifications were necessary, the solver was left unchanged from the core distribution where possible, so that other researchers will be able to reproduce and extend the work presented in this thesis. The focus of the current work is on burning velocity and LFLs of hybrid mixtures, but care is taken to employ computational models that may allow larger system scales to be explored in the future.

In this work, molecular processes such as gas viscosity, thermal conductivity, and gas diffusion were approximated using global approaches. First-principle derivations are available [64] but may be too computationally expensive to extend in future work. Furthermore, many input parameters from these detailed models must be estimated [37], and improvement in accuracy from their use remains to be demonstrated [36]. Specifically, a unity Lewis number approximation for gas diffusion was employed, with the goal of verifying the accuracy of this approach in simulating dust and hybrid flames.

1.3 Objectives and Contribution

The objective of this thesis is to extend the current knowledge of laminar burning velocity and LFLs of hybrid mixtures of combustible dust and flammable gas. This

is achieved using a CFD model to simulate flame propagation in gas, dust, and hybrid mixtures, and analyzing the resulting flame structure, burning velocity, coupling interaction, combustion timescales, and propagation limits. Analysis of these parameters allows novel combustion regimes to be identified and mixing rules for LFLs of hybrid mixtures to be explored. Special attention is also given to the role of gas-phase reaction mechanisms and discrete particle combustion on flame propagation for dust and hybrid mixtures.

The main contributions of this work are as follows:

- A CFD model based on a unity Lewis number assumption is verified to explore the laminar burning velocity of dust and hybrid flames.
- Hybrid mixture regime diagrams are redefined in terms of flame structure and illustrate the effect of particle diameter.
- Guidance on LFL mixing rules is provided for hybrid mixtures of coal dust and methane gas.
- The impact of discrete particle combustion on hybrid burning velocity at low dust concentrations and on the hybrid LFLs is explored.

1.4 Thesis Outline

The first four chapters of this thesis outline background information on burning velocity and flammability limits, and describe the CFD model. The following three chapters analyze simulation results for methane flames, coal dust flames and hybrid flames. The final results chapter compares simulation results for hybrid LFLs with mixing rules from the literature. This is followed by the summary, conclusions, and recommendations from the thesis.

This thesis is structured as follows:

Chapter 1 provides background information on motivation, scope of work, objectives and contribution, and previous work.

Chapter 2 presents a review of the literature on laminar burning velocity, LFLs, and CFD modeling of laminar dust and hybrid flames.

Chapter 3 describes the mathematical model used in this work and compares it to those from the literature.

Chapter 4 discusses the solution methods used in the current model.

Chapter 5 analyzes methane flame simulations to determine flame thickness and reaction timescales.

Chapter 6 analyzes coal dust flame simulations to determine flame structure and the role of discrete combustion.

Chapter 7 analyzes hybrid flame simulations to explore coupling interaction between dust and gas and presents combustion regime diagrams.

Chapter 8 explores the LFLs of hybrid mixtures and compares the results to available mixing rules in the literature.

Chapter 9 presents the summary, conclusions, and recommendations of the thesis.

1.4.1 Previous Work of the Current Author

During completion of this thesis, the author co-authored several scientific articles in the area of dust and hybrid flame propagation [36, 43, 65, 66, 67, 68]. Although each of these investigations provided part of the framework for this research, three publications are referenced extensively in this thesis:

- [36] C.T. Cloney, R.C. Ripley, M.J. Pegg, and P.R. Amyotte. Laminar burning velocity and structure of coal dust flames using a unity Lewis number CFD model. *Combustion and Flame*, 190:87–102, 2018.
- [43] C.T. Cloney, P.R. Amyotte, F.I. Khan, and R.C. Ripley. Development of an organizational framework for studying dust explosion phenomena. *Journal of Loss Prevention in the Process Industries*, 30:228–235, 2014.
- [65] C.T. Cloney, R.C. Ripley, M.J. Pegg, and P.R. Amyotte. Evaluating regime diagrams for closed volume hybrid explosions. *Journal of Loss Prevention in the Process Industries*, 49:912–918, 2017.

Based on these publications, the organizational model developed by Cloney et al. [43] is used to determine the scope of the CFD simulations and is referred to extensively in Chapter 1. The evaluation of explosion regime diagrams from experimental data by Cloney et al. [65] is used to lay the groundwork for the development of combustion

regime diagrams, and is referred to extensively in Chapter 2. Lastly, the literature review, CFD model development, simulation results, and model verification of methane and coal dust flames completed by Cloney et al. [36] are referred to extensively in Chapters 2–6. In these chapters, some passages have been quoted verbatim from the referenced works and modified figures have been included. In all cases, the current thesis author was the lead contributor in terms of problem formulation, completion of the underlying research, and manuscript preparation. As such, this work comprises the body of novel contributions made by the current author.

Chapter 2

Literature Review

The majority of research literature on burning velocity and LFLs of hybrid mixtures is completed using experimental techniques. The major findings of these studies are summarized in the following sections with special attention given to characterising regime diagrams and LFL mixing rules. This is followed by a discussion of the previous CFD modeling of laminar coal dust flames in the literature. Results from these models are compared extensively to the current CFD model in Chapter 6 of the thesis.

2.1 Burning Velocity

Various approaches are used to explore burning velocity and flame speed in hybrid mixtures, including open or closed tubes, open burners, and closed chambers. Small-scale flame tubes with lengths less than 1 m have been used by several authors and allow optical access to explore particle velocity [69], phases of flame propagation and wall interaction [70], visual indicators of turbulence [71], and flame stretch effects [72]. Large-scale flame tubes ranging from 2 to 30 m in length allow investigation into the effect of obstacles and coal dust deposits on flame velocity [73], deflagration-to-detonation transition and the impact of suppression agents [74], and pressure piling from zones containing fuel to those without [75].

The main difficulty in both open and closed tubes is estimating the burning velocity from the measured flame speed. Turbulence in the flow field [71], turbulence intensity induced by the flame [70], flame acceleration and wall interaction [74], and flame stretch [72] all need to be accounted for in the calculation. In larger tubes, pressure fluctuations due to acoustic interactions [73] and difficulties obtaining a homogeneous fuel cloud [69] make the results specific to the apparatus used, and conclusions may not be applicable to other systems containing hybrid mixtures.

Small-scale open burners were used for some of the first measurements of coal dust burning velocities (e.g., see Howard and Essenhigh [76] and Horton and Smoot [77]).

A thorough discussion of this work was provided by the reviews of Smoot and Horton [78] and Krazinski et al. [79]. The main advantages of these systems is that they can be investigated under laminar conditions [77] and that the standing flame allows diagnostic techniques such as temperature measurements [77] and particle sampling [76]. Bradley et al. [37] discuss the drawbacks of open burners and indicate that experimental approaches to achieve ignition, such as using preheated surfaces, having the fuel come in contact with gas flames, and adding small amounts of gaseous fuel to the dust, influence burning velocity results and account for scatter in the literature data.

Two groups of studies have been completed to explore the burning velocity of hybrid mixtures using open burners. Xie et al. [80] used a 1.02 cm-diameter burner and a shadowgraph technique to measure the burning velocity of mixtures of coal dust and methane gas under laminar flow conditions. Rockwell et al. [81] explored turbulent burning velocities for these mixtures using a modified version of the same burner design and by overlapping the shadowgraph images at multiple instances of time. More recently, Lee et al. [82] extended this analysis to measure the impact of the initial temperature on the burning velocity of coal dust and methane gas mixtures.

In the second group of open burner studies involving hybrid mixtures, Soo et al. [83] used the "flame knife" and particle burner concepts developed by Goroshin et al. [84, 85] to explore the burning velocity, flame temperature, and flame structure of aluminum dust and methane gas mixtures. Julien et al. [86] also used this burner design to explore particle combustion regimes in iron dust and methane gas mixtures. Both studies indicated coupled and uncoupled flame structures at different fuel concentrations.

Although the aforementioned flame tube and burner studies provide valuable insight into the combustion processes involved in hybrid flames, the overall coverage of different fuel types is low. With many studies involving methane gas and coal dust or select metal dusts, the data are insufficient to characterize the overall burning velocity behaviour of hybrid mixtures. Investigations involving closed explosion chambers provide an alternative body of experimental data, where many more combinations of combustible dust and flammable gas have been characterized.

2.1.1 Closed-Chamber Explosion Testing

Although closed-chamber explosion testing does not measure burning velocity directly, it is the ASTM-recommended standard approach for determining prevention and protection parameters [27]. Venting and suppression systems are typically designed based on the conversion of K_{St} determined from these tests to a flame propagation velocity [23, 24]. Furthermore, macroscale simulation codes may require these tests for empirical burning velocity fits [39, 40, 41]. Lastly, most of the experimental data for hybrid mixtures has been generated from closed-chamber explosion testing.

The literature for hybrid explosion in closed chambers was evaluated by Cloney et al. [65] who suggested extensions to existing regime diagrams. A summary of the experimental data reviewed in this work is given in Table 2.1. In each entry in the table the combustible dust, flammable gas, ignition energy, and ignition delay explored are presented.

Table 2.1: Summary of closed-chamber explosion data for hybrid systems in the literature.

Reference	**Dust**	**Gas**	**Ignition Energy**	**Ignition Delay**
Ajrash et al. [87]	Coal	Methane	Multiple	60 ms
Hossain et al. [17]	Multiple	Multiple	10 kJ	60 ms
Denkevits and Hoess [88]	Aluminum	Hydrogen	Spark	60 ms
Kosinski et al. [89]	Carbon Black	Propane	1 kJ	Multiple
Khalil [90]	Activated Carbon	Hydrogen	10 kJ	60 ms
Li et al. [91]	Coal	Methane	10 kJ	60 ms
Di Benedetto et al. [92]	Niacin	Methane	Multiple	Multiple
Garica-Agreda et al. [29]	Niacin	Methane	Spark	0 ms
Sanchirico et al. [30]	Niacin	Acetone	Spark	Multiple
Amyotte et al. [93]	Polyethylene	Multiple	10 kJ	60 ms
Denkevits [94]	Tungsten	Hydrogen	Spark	60 ms
Dufaud et al. [95]	Multiple	Multiple	10 kJ	Unknown
Dufaud et al. [96]	Niacin	Diisopropyl Ether	10 kJ	Unknown
Denkevits [18]	Graphite	Hydrogen	Spark	60 ms
Pilão et al. [19]	Cork	Methane	2.5 kJ	400 ms

The closed-chamber investigations summarized in Table 2.1 can be broken into two categories: those that use high-strength chemical ignitors to initiate the hybrid explosion and those that use low-energy spark ignition. The studies with high-strength chemical ignitors generally explore a small fraction of the explosible concentration

range for the hybrid mixture. For example, Amyotte et al. [93], Khalil [90], and Hossain et al. [17] explore hybrid mixtures with the flammable gas below the LFL concentration. Furthermore, Li et al. [91] and Ajrash et al. [87] explore relatively fixed dust concentrations with additions of various amounts of flammable gas, while Khalil [90] explores both low gas concentrations and stoichiometric conditions with different amounts of combustible dust.

From the studies with high-strength chemical ignitors that include multiple fuel combinations, Dufaud et al. [95, 96] demonstrated non-linear additive effects on the burning velocity of hybrid mixtures for combinations of magnesium stearate/ethanol, niacin/diisopropyl ether, and antibiotic dust/toluene. Alternatively, Amyotte et al. [93] found that K_{St} scaled linearly for polyethylene mixed with ethylene, hexane, and propane for low gas concentrations. Hossain et al. [17] investigated explosions in mixtures of micro crystalline cellulose (MCC) with methanol, ethanol, and isopropanol and found that enhancement effects were different depending on whether the dust was pre-wetted with the solvent or vaporized in the atmosphere prior to the explosion. The difference in these reported outcomes illustrates the complexity of hybrid explosion dynamics and demonstrates a need for further research in this area [65].

The two studies using medium-strength chemical ignitors further illustrate this point. Contrary to previous investigations showing enhancing effects, Pilão et al. [19] found that the addition of methane gas below its LFL had little effect on P_{max} and K_{St} until the gas concentration reached 3.5 % by volume. Kosinski et al. [89] demonstrated that the addition of carbon black dust, which would not explode on its own with a 1-kJ ignition energy, could enhance the explosion severity of propane only when the propane concentration was above 3 %. In contrast to the other investigations, these authors found that hybrid mixtures would not explode when either fuel was below its individual flammability criteria.

The investigations using low-energy spark ignition covered a broader range of hybrid mixtures, allowing the burning velocity and flame coupling effects to be explored more generally. Gracia-Agreda et al. [29] explored a wide range of mixtures of niacin dust and methane gas and developed different explosion regimes based on the individual concentrations. Sanchirico et al. [30] extended this analysis with mixtures of niacin dust and acetone gas and explored the effect of ignition delay time and

turbulence level on the results. Lastly, Denkevits [94] and Denkevits and Hoess [88] explored mixtures of tungsten and hydrogen, and aluminum and hydrogen, respectively, and reviewed flame coupling for a range of flammable concentrations. These results are explored in more detail in the following sections.

2.1.2 Explosion Regime Diagrams

Gracia-Agreda et al. [29] were the first to plot hybrid explosion data as a so-called "explosion regime diagram". The regime diagram originally presented in their work has been reconstructed in Figure 2.1 for reference. The data were taken from the appendices of Garcia-Agreda [97] but differ slightly from Garcia-Agreda et al. [29].

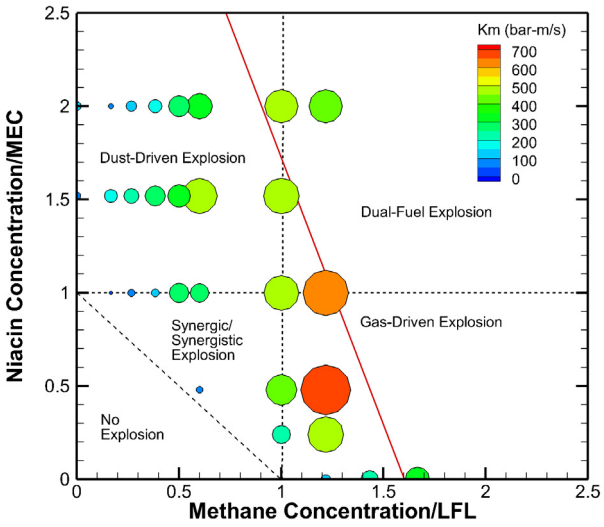

Figure 2.1: Hybrid explosion regimes originally proposed by Garcia-Agreda [97] and Garcia-Agreda et al. [29] in their work with niacin/methane mixtures and spark ignition.

In their explosion regime diagram, Garcia-Agreda [97] and Garcia-Agreda et al. [29] plotted K_{m} for explosion of individual hybrid mixtures on a plane with dust concentration on the ordinate and gas concentration on the abscissa. They also normalized the dust concentration axis by the dust MEC and the gas concentration axis by the gas LFL. They then divided the diagram into five regimes depending on which fuel was above its respective flammability criteria: gas-driven explosion, dust-driven explosion, dual-fuel explosion, synergic/synergistic explosion, and no explosion.

The work of Garcia-Agreda et al. [29] was extended by Sanchirico et al. [30], who investigated the impact of the turbulence level on K_{m} and plotted the literature data of Pilão et al. [19] and Denkevits [18] in terms of explosion regime diagrams. Russo et al. [98] also developed a theoretical model to predict K_{m} of hybrid mixtures and found that it matched experimental results in the gas-driven and dual-fuel regimes. No attempt was made to compare this model for dust-driven or synergistic explosions.

Other authors have also used the concept of combustion regimes to explain the burning velocity and flame structure of hybrid mixtures. Soo et al. [83] and Julien et al. [86] explored particle-combustion regimes for mixtures of methane gas with aluminum particles and iron particles, respectively, and found different degrees of coupling depending on the dust and gas concentrations. These coupling regimes had a pronounced effect on flame structure and the resulting burning velocity. Julien et al. [99] also illustrated flame propagation regimes for aluminum dust clouds at different concentrations including cellular flames, stable flames, and pulsating flames. These flame structures had an important effect on propagation velocities and likely apply to hybrid flames as well.

2.1.3 Literature Coverage

To visually illustrate the literature available to understand hybrid mixture flame propagation regimes, the data in Table 2.1 is summarized graphically in Figure 2.2 for high-energy chemical ignitors and spark ignition, respectively. The axes in each plot have not been normalized, so that the data available can be compared relative to the "optimum" dust concentration (where the K_{St} is measured) and the stoichiometric gas concentration.

As discussed in the previous section, experimental studies using high-strength chemical ignitors cover a very limited portion of hybrid mixture concentrations, typically focusing on the dust-driven explosion regime of Garcia-Agreda et al. [29]. This is shown in Figure 2.2 (a) by the narrow bands of coverage obtained by the individual studies evaluated. A possible exception is the work of Dufaud et al. [95, 96], which appears to capture the broader flammable regime from the lower limits to the optimum and stoichiometric concentrations. However, the experimental data is difficult to extract in these investigations, and could not be analyzed extensively.

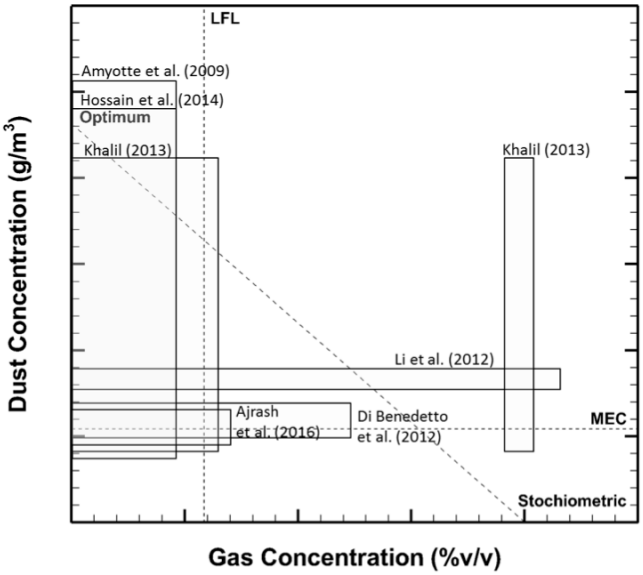

(a) 10-kJ Ignition Energy

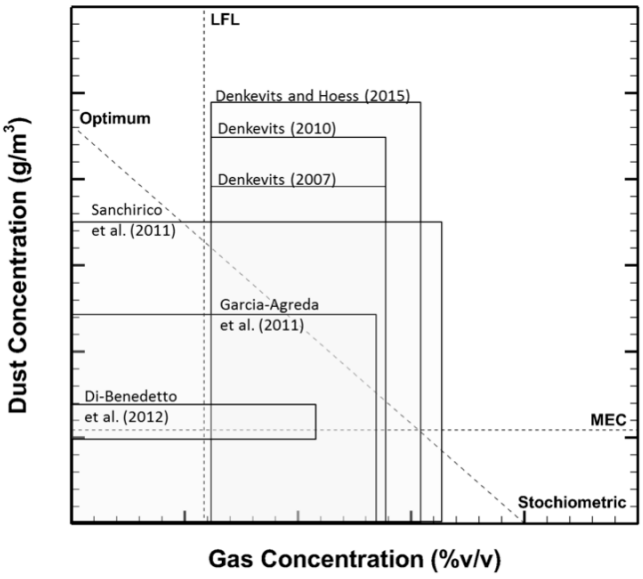

(b) Spark Ignition

Figure 2.2: Approximate literature coverage for experimental studies investigating burning velocity of hybrid mixtures.

The investigations that use low-strength spark ignition cover a broader range of hybrid mixtures, as shown in Figure 2.2 (b). Combined with the explosion regime

diagrams developed and used by Garcia-Agreda et al. [29] and Sanchirico et al. [30], the studies of Denkevits [18], Denkevits [94], and Denkevits and Hoess [88] can be used to explore the coupling interaction between gas and dust flames in hybrid mixtures and propose additional regimes for combustion diagrams. In general, the low coverage of the flammable concentration range for any particular investigation in Figure 2.2 further illustrates the difficulties in experimentation of hybrid mixtures and demonstrates a need to better understand the coupling regimes that are present.

2.1.4 Proposed Additional Regimes

In a previous work, Cloney et al. [65] reviewed the available experimental data to extend the explosion regimes identified by Gracia-Agreda et al. [29]. Four investigations using high-strength chemical ignitors were analyzed to explore the dust-driven regime, and two investigations using spark ignition were analyzed to explore the gas-driven and dual-fuel regimes.

In the dust-driven regime, the experimental results of Khalil [90] for activated carbon/hydrogen mixtures using a 10-kJ ignition energy showed a size-normalized maximum rate of pressure rise enhancement of 20 % when the gas was below its LFL. This is in contrast to the studies of Amyotte et al. [93] and Ajrash et al. [87] that showed maximum increases ranging from a factor of 2.0 to 5.2 for coal/methane mixtures, respectively. Hossain et al. [17] further found a maximum increase of a factor of 2.4 for pharmaceutical mixtures.

The main difference in the work of Khalil [90] is that activated carbon reacted heterogeneously with air, while dusts in the other investigations reacted homogeneously. This comparison suggests that burning velocity enhancement in the dust-driven regime is higher for homogeneously reacting dusts such as coal, than those that react only heterogeneously.

To further explore the dust-driven regime, Figure 2.3 shows the size-normalized maximum rate of pressure rise for the homogeneously reacting dusts. The figure axes are normalized by the dust MEC and gas LFL, and K_{m} for each test is normalized by K_{m} for the dust-only experiment at that concentration. This plot shows the rate of pressure rise enhancement of the hybrid mixtures in the dust-driven explosion regime.

Although there is a fair degree of scatter in the experimental results, a general

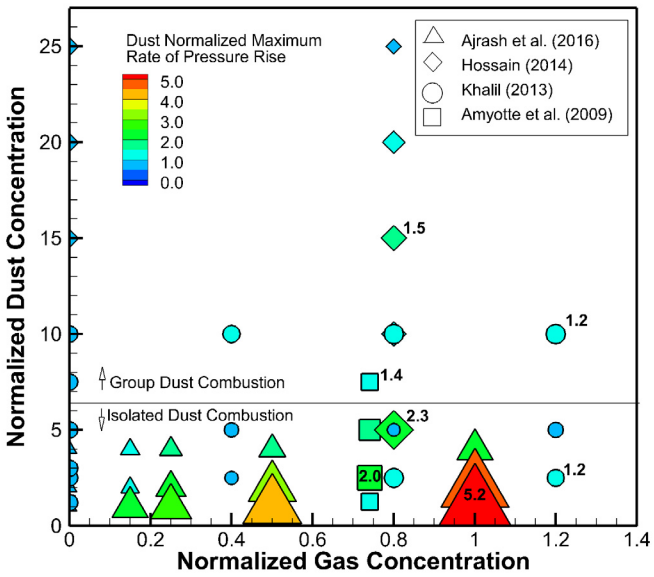

Figure 2.3: Ratio of K_{m} for the hybrid explosion to that from the dust-only explosion at the same concentration with 10-kJ ignition energy. The maximum ratio for each study and in each of the two proposed regimes is also indicated as text inside or beside the corresponding symbol.

conclusion is that enhancement of the explosion is more pronounced when the dust is close to the MEC. Cloney et al. [65] proposed that two combustion regimes were present in the dust-driven explosion regime:

- Isolated Dust Combustion – Addition of flammable gas has a large impact on K_{m} due to flame bridging.
- Group Dust Combustion – Addition of flammable gas has a moderate or small impact on K_{m}.

These results are highlighted by the maximum normalized K_{m} in each regime, which are indicated with text beside their respective symbol in Figure 2.3. In the isolated combustion regime, the enhancement is larger than a factor of 2.0, while it is less than 1.5 in the group combustion regime. These combustion regimes have been suggested previously in the dust explosion literature [100, 101] and studied in the droplet combustion literature [102, 103] but have not been studied in relation to hybrid mixtures, to the author's knowledge. As such, the current computation model

has been designed so that discrete particle combustion can be explored explicitly in the simulation results.

In terms of dual-fuel and gas-driven regimes, Denkevits [18] explored pressure-time traces and product gas composition for hybrid mixtures of carbon dust (mean particle size of 4 µm) and hydrogen gas using spark ignition. From this analysis, he was able to explore coupling between the dust and gas flames.

The results of Denkevits [18] in the 20-L chamber are summarized as a regime diagram in Figure 2.4. As in the previous diagrams, the size and colour of the circles represents K_{m} for each mixture. The solid red line in the figure represents nominally stoichiometric mixtures, where the stoichiometric concentration of graphite is calculated as 110 g/m^3 and the stoichiometric percentage volume fraction of hydrogen is taken as 29 %. The dashed red line is the effective stoichiometric mixture, where all of the oxygen in the vessel is consumed [18]. The maximum P_{m} and K_{m} are indicated as text beside the corresponding symbol in Figure 2.4. In all cases, the maximum P_{m} has a magnitude less than 10 bar and the maximum K_{m} has a magnitude greater than 50 bar-m/s.

The hybrid explosion results for carbon/hydrogen mixtures demonstrate four explosion regimes that are indicated by comparing the P_{m} and K_{m} of the gas-only explosion to those of the hybrid mixtures. These four regimes can be summarized as follows:

- No Explosion – Ignition energy not sufficient to ignite mixture;
- Gas-Only Explosion – Addition of dust decreases P_{m} and K_{m};
- Two-Stage Explosion – Addition of dust increases P_{m} and decreases K_{m}; and,
- Single-Stage Explosion – Addition of dust increases P_{m} and K_{m}.

In a later investigation, Denkevits and Hoess [88] performed the same experiments with hydrogen gas and highly reactive aluminum dust (mean particle size from 1–2 µm). The results from this investigation are summarized in terms of an explosion regime diagram in Figure 2.5. No experiments were performed below the gas LFLs so the no-explosion regime was not present in these results.

The experimental results for aluminum/hydrogen mixtures demonstrated the same three explosion regimes as the less reactive carbon dust: gas-only explosion, two-stage

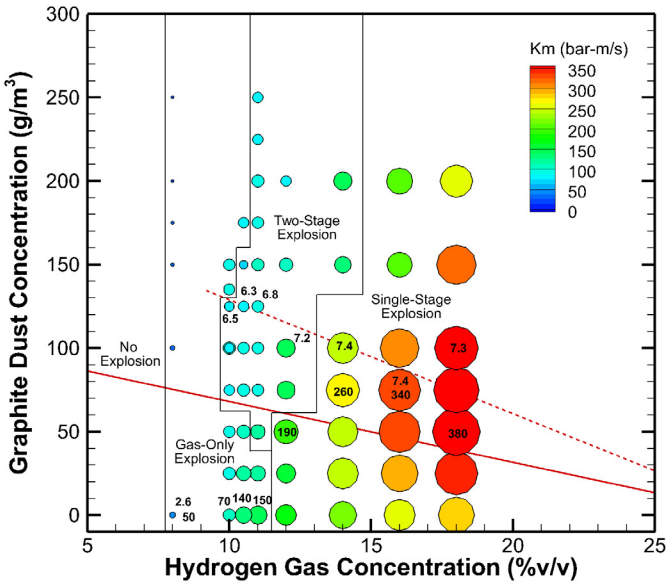

Figure 2.4: Hybrid explosion regime diagram for low-reactivity dust reproduced from the experimental data of Denkevits [18] for spark ignition and 60-ms delay. The largest values of P_{m} (bar) and K_{m} (bar-m/s) are indicated for each recorded gas concentration as text.

explosion, and single-stage explosion. However, an additional regime was also present. Above a dust concentration of 600 g/m^3, the addition of hydrogen gas either decreased K_{m} or had little effect on the explosion parameters. Denkevits and Hoess [88] found that very little hydrogen was consumed in these mixtures and concluded that the gas only acted to ignite the dust flame which consumed all of the oxygen in the system. This leads to an additional proposed explosion regime:

- Dust-Only Explosion – Addition of gas decreases P_{m} and K_{m} or has little effect on the explosion parameters.

The physical interpretation of the gas-only, two-stage, single-stage, and dust-only explosion regimes can be envisioned based on competing reaction fronts. For low-reactivity dust, the particles may react inside the gas flame (single-stage explosion), behind the gas flame (two-stage explosion), or not at all (gas-only explosion). Alternatively, highly-reactive dust may react faster than the gas, causing the dust-only explosion regime. Comparison of the different timescales involved in hybrid flame coupling is completed using CFD simulation in the current thesis (see Section 7.2).

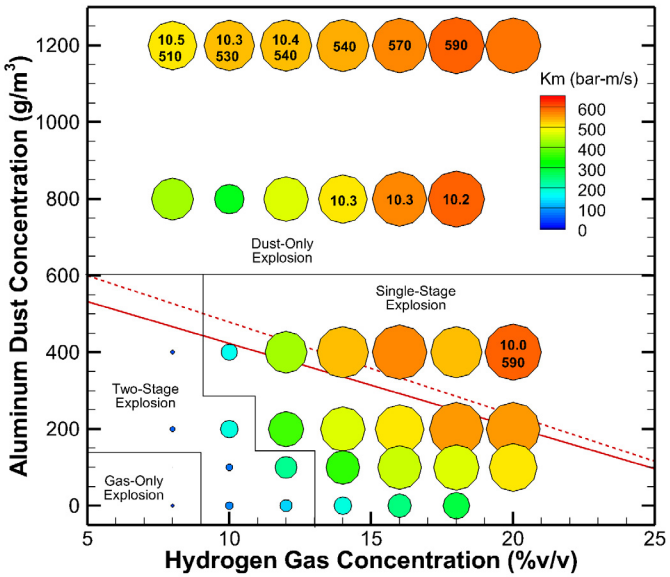

Figure 2.5: Hybrid explosion regime diagram for high-reactivity dust reproduced from the experimental data of Denkevits and Hoess [88] for spark ignition and 60-ms delay. The largest values of P_{m} (bar) and K_{m} (bar-m/s) are indicated as text for each recorded gas concentration.

2.2 Lower Flammability Limits

Historically, LFLs for gas flames have been determined by visual observation in vertical tubes [104]. Care had to be taken that the tube was wide enough to avoid substantial heat loss and long enough that effects of the ignition source on flame propagation were minimized [105]. Furthermore, the limits measured in upward propagating flames were wider than in downward propagating flames due to convective buoyancy effects [106]. In 1952, Coward and Jones [107] recorded limits for over 150 individual gases and mixtures in this type of apparatus. They proposed a standard test vessel with at least a 5-cm diameter and a length of 1.5 m.

Alternative experimental equipment has also been used to determine the LFL of gas flames including flat-flame burners [104] and small tubes with fixed spark-gap widths (see DIN 51649 and prEN1839 standards as described by Britton [106]). Closed explosion chambers using a pressure-based criterion have also been used by several authors [106, 108, 109, 110] to determine LFLs for gases and MECs for dusts.

Most of the LFL data available for hybrid mixtures are generated using closed explosion chambers (e.g., see [14, 15, 32, 33, 111]). Mixing rules for calculating hybrid mixture LFL based on the gas LFL and dust MEC have been proposed based on Le Chatelier's law (LCL; see Mashuga and Crowl [112]), Bartknecht's curve (BC; see Bartknecht [14]), and Jiang's curve. (JC; see Jiang et al. [32]). These relations are presented and explored in terms of the available literature at the end of this section, after a review of the LFL of methane and coal dust alone.

2.2.1 Methane Gas

Due to a dependence on the experimental apparatus [105] and defined propagation criteria [106], a wide array of methane LFL values have been reported in the literature. Experimental data is summarized in the works of Coward and Jones [113] and Britton [106]. Coward and Jones recommended a value of 5.3 % methane by volume but noted values as low as 5.01 %, experimentally. Britton summarized values between 5.0 and 6.7 % reported between the years 1816 and 1915, and values generally between 4.5 and 5.0 % between the years 1916 and 2000. In other investigations using closed explosion chambers, values of 5.0 % and 4.85 % have been reported by Cashdollar et al. [109] and Mashuga and Crowl [114], respectively.

2.2.2 Coal Dust

Most of the MEC data for coal dust has been generated using closed explosion chambers. Hertzberg et al. [108] demonstrated that the apparent lean limit of coal dust decreases with increasing ignition energy in the 20-L chamber. Using 2.5 and 5-kJ ignition energies, they found a lean limit of 90 g/m^3 for Pittsburgh coal having a broad size distribution with a surface mean diameter of 30 µm and a mass mean diameter of 50 µm. Several years later, using a 5-kJ ignition energy, Going et al. [110] measured an MEC of 60 g/m^3 in a 20-L chamber for Pittsburgh coal with the same surface and mass mean diameters, 1 % moisture content, and 37 % volatiles. These authors also found a higher MEC ranging from 80 to 90 g/m^3 in a 1-m^3 vessel for Pittsburgh coal. For a higher volatile Gilsonite dust with a lower particle diameter, Going et al. [110] found a lower MEC between 30 and 41 g/m^3 in both experimental vessels.

Chawla et al. [115] performed a systematic study of the role of volatile content

on coal dust MEC in a 20-L chamber using 2.5, 5, and 10-kJ ignition energies. Using the ASTM standard criteria [25] and 5-kJ ignition energy, these authors found an MEC of 20 g/m^3 for Gilsonite with 83 % volatile matter, of 50 g/m^3 for Pittsburgh coal with 34 % volatile matter, and of 300 g/m^3 for oil shale with 28 % volatile matter. These results demonstrate that the MEC of coal dust decreases with increasing volatile content. Chawla et al. [115] also found a relatively low MEC of 50 g/m^3 for Pocahontas coal with a recorded volatile content of 16 %. These authors suggested that the low ash content of the Pocahontas coal (5 %) acted to lower the MEC value.

Amyotte et al. [15] explored the ignitability of two coal dusts each with two particle size distributions in a 26-L explosion chamber. They found that a 5-kJ ignition energy was required to achieve asymptotic values representative of the true lean flammability limit of the dusts. For Phalen (mine) coal with approximately 30 % volatile content, 14 % ash, and 1.5 % moisture, the MEC decreased from 90 to 70 g/m^3 when the mean diameter was reduced from 30 to 19 µm. For Prince (mine) coal with approximately 37 % volatile content, 7 % ash, and 4.4 % moisture, the MEC decreased from 70 to 60 g/m^3 when the mean diameter was reduced from 29 to 22 µm.

Yuan et al. [116] and Cashdollar [117] also systematically studied the effect of particle diameter on coal dust MEC in a 20-L chamber. Using 5-kJ ignition energy, Yuan et al. [116] explored the MEC of a bituminous coal dust with three size distributions: 43–75 µm, 75–125 µm, and 125–550 µm. For dust samples with 2.4 % moisture content, MEC was found to increase linearly from 40 to 60 g/m^3 as the mean diameter increased from approximately 60 to 330 µm.

Using 2.5-kJ ignition energy, Cashdollar [117] demonstrated somewhat different results, showing that several broad and narrow size distributions of Pittsburgh coal (37 % volatiles, 6 % ash, 1 % moisture) had an MEC decreasing from 100 to 60 g/m^3 as the particle diameter was increased from 2 to 50 µm. After 50 µm, the MEC increased to an asymptotically large value as the particle diameter approached 300 µm. Cashdollar [117] also investigated the change in particle size distribution during dispersion, showing insignificant decreases in particle diameter (less than 10 %). This suggests that fragmentation of the coal dust did not impact their conclusions on the change in MEC with particle diameter. As suggested by Cashdollar [117] and demonstrated by Kalejaiye et al. [118] some dust may undergo fragmentation up to 50 % of

the original particle size during dispersion, so this parameter is important to consider during closed-chamber experiments.

In addition to particle diameter, Yuan et al. [116] explored the effect of moisture content on the MEC of bituminous coal. These authors found that the MEC of the two smaller size distributions decreased almost linearly with moisture content. For the 43–75 µm diameter range, MEC decreased from 65 to 60 g/m^3 as the moisture content was decreased from 10 to 2.4 %. Extrapolating their results to 0 % moisture content gives an MEC of 35 g/m^3 for bituminous coal dust with 20 % volatile and 42 % ash content.

2.2.3 Hybrid Mixing Rules

Early investigation into the flammability limits of hybrid mixtures was completed more than a century ago by Engler [119]. As described by Echkoff [6], Engler indicated that a non-explosible concentration of charcoal dust could be made explosible by adding 2.5 % methane gas. This demonstrated early on that hybrid mixture explosion can occur when both fuels are below their independent flammability limits.

In his textbook, Field [31] reviewed the early work on hybrid mixtures and stated that Le Chatelier's Law (LCL), which is based on the mixed flammability limits of flammable gases, provides a reasonable estimate for hybrid mixtures. The assumptions involved in deriving LCL are given by Mashuga and Crowl [112]. The final result for a two component mixture can be written as:

$$\sigma_{\mathrm{h}}^{\mathrm{MEC}} = \sigma_{\mathrm{p}}^{\mathrm{MEC}} \left(1 - \frac{X}{X_{\mathrm{LFL}}} \right) \tag{2.1}$$

where $\sigma_{\mathrm{p}}^{\mathrm{MEC}}$ and X_{LFL} are the measured MEC of the dust and LFL of the gas, respectively. From Equation 2.1, the flammability limit of the dust in a hybrid mixture, $\sigma_{\mathrm{h}}^{\mathrm{MEC}}$, can be estimated at a specified gas concentration, X. Note that the gas concentration is typically specified in percent by volume and the dust concentration by mass per unit volume.

In his work, Field [31] also stated that that "synergies may exist" and explosion limits may be wider than specified by LCL. Under these conditions, less dust is required at a specified gas concentration than predicted by Equation 2.1.

Explosion limits wider than LCL were also demonstrated by Pellmont [28] and

Bartknecht [14] for PVC dust with propane and methane gas, respectively. Experiments were completed in a 1-m^3 chamber using a 10-kJ ignition energy. This led to "Bartknecht's curve (BC)" relation for hybrid mixtures [14]:

$$\sigma_{\mathrm{h}}^{\mathrm{MEC}} = \sigma_{\mathrm{p}}^{\mathrm{MEC}} \left(1 - \frac{X}{X_{\mathrm{LFL}}}\right)^2 \tag{2.2}$$

Several investigations were published after Barknecht showing various levels of agreement and disagreement with both relations. Amyotte [15] presented explosion results in a 26-L chamber with ignition energies ranging from 0.138 to 10 kJ. At 5 and 10-kJ ignition energies, hybrid mixtures with 2 % methane and two different ranks of coal dust showed agreement with LCL. Conversely, Landman [120] presented experimental results for hybrid mixtures of two coal dust samples with methane that systematically showed limits wider than Equation 2.1 as suggested by BC.

Chatrathi et al. [111] explored explosion characteristics of several hybrid mixtures in a 1-m^3 chamber. With a 550 ms delay time and 10-kJ ignition energy, the explosion limits of cornstarch and propane mixtures were systematically narrower than LCL; that is, more fuel was needed than measured from a liner combination of the limits. Khalili et al. [121] explored explosion limits of three hybrid mixtures and found that mixtures of magnesium stearate and ethanol, and starch and methane, had limits delineated by BC, but mixtures of oilcake dust and hexane had limits narrower than both BC and LCL. Addai [122] investigated eight different hybrid mixtures and found four had narrower limits than LCL, two had wider limits, and two were in moderate agreement with the linear condition.

In 2007, Prugh [123] summarized hybrid explosion data from multiple sources and suggested that the limit behaviour depended on the ratio of the maximum rate of pressure rise of the dust at worst-case conditions, to the maximum rate of pressure rise of the gas at worst-case conditions ($K_{\mathrm{St}}/K_{\mathrm{G}}$). Prugh suggested that when this ratio was less than unity, the limits would be wider than LCL as suggested by BC, and when the ratio was larger than unity, the limits would be narrower. This relation seemed to hold for the six hybrid mixtures reviewed, but K_{G} was taken at laminar conditions.

Jiang et al. [32] proposed a novel mixing relation ("Jiang's Curve", JC) based on a concept similar to Prugh's [123], except both K_{St} and K_{G} were determined at the

same turbulence level using the same ignition energy:

$$\sigma_{\mathrm{h}}^{\mathrm{MEC}} = \sigma_{\mathrm{p}}^{\mathrm{MEC}} \left(1 - \frac{X}{X_{\mathrm{LFL}}}\right)^{C\frac{K_{\mathrm{St}}}{K_{\mathrm{G}}}} \tag{2.3}$$

where the constant C is fit to experimental data. In their work using a 36-L explosion chamber, a 75-ms delay time, and 2.5-kJ ignition energy, a fit value of $C = 1.12 \mp 0.03$ agreed very well for mixtures of cornstarch/methane, niacin/methane, niacin/ethane, and niacin/ethylene [32]. Jiang et al. [33] extended this work and found that the correlation and empirical constant were independent of the turbulence level and ignition energy with chemical ignitors. They also explored the data of Sanchirico et al. [30], demonstrating that the correlation fit very well with spark ignition in a 20-L chamber.

2.2.4 Comparison to the Literature

To explore the validity of the relation proposed by Jiang et al. [32], a summary of the available literature data for hybrid LFLs is given in Table 2.2. Where possible, Table 2.2 includes the reported MEC, K_{St}, LFL, and K_{G}. A blank space in the table indicates that the data is not available in the study and some values were estimated by the current author from plots available in the individual studies. The final column shows whether the results indicated explosion limits that were narrower or wider than LCL (linear indicates agreement with LCL).

The results from Jiang et al. [32, 33] agree very well with JC, and demonstrate explosibility limits narrower than LCL. The results from Prugh [123] also seem to agree with this relation, with the explosion limits being predicted by the ratio of $K_{\mathrm{St}}/K_{\mathrm{G}}$. However, the value used for K_{G} (55 bar-m/s) appears to be based on laminar conditions. In reality, this should be much higher (e.g., 250–300 bar-m/s as reported by others for turbulent conditions), and the ratio would be less than unity.

Several other studies, such as Chatrathi [111], Pellmont [28], Khalili et al. [121], and Bartknecht [14], either report $K_{\mathrm{St}}/K_{\mathrm{G}}$ ratios less than unity or can be assumed to have values less than unity from looking at the measurements of others, but also report flammability limits wider or equal to LCL.

Although the relation provided by Jiang et al. [32] provides a good starting point for characterizing explosion limits of hybrid mixtures and matches their experimental

Table 2.2: Summary of literature data for lower explosion limits of hybrid mixtures. The results column indicates whether the experimental data agrees with Le Chaterlier's Law (linear), or is narrower or wider than the linear condition. Units are as follows: MEC (g/m^3), K_{St} (bar-m/s), LFL (% volume), and K_G (bar-m/s).

Reference	**Dust**	**MEC**	$\boldsymbol{K_{St}}$	**Gas**	**LFL**	$\boldsymbol{K_G}$	$\boldsymbol{K_{St}/K_G}$	**Result**
Jiang et al. [33]	Niacin	75	160	Methane	5	290	0.55	Narrower
	Niacin	75	164	Methane	5	294	0.56	Narrower
	Niacin	75	165	Methane	5	300	0.55	Narrower
	Niacin	75	130	Methane	5	250	0.52	Narrower
	Cornstarch	100	175	Methane	5	290	0.60	Narrower
	Cornstarch	100	140	Methane	5	250	0.56	Narrower
	Niacin	75	160	Propane	2.1	410	0.39	Narrower
	Cornstarch	100	140	Propane	2.1	410	0.43	Narrower
Jiang et al. [32]	Cornstarch	100	175	Methane	5	290	0.60	Narrower
	Niacin	75	160	Methane	5	290	0.55	Narrower
	Niacin	75	160	Ethane	3	360	0.44	Narrower
	Niacin	75	160	Ethane	2.7	400	0.40	Narrower
Sanchirico et al. [30]	Niacin	125	160	Acetone	2.5	600	0.27	Narrower
	Niacin	125	140	Acetone	2.5	500	0.28	Narrower
	Niacin	125	60	Acetone	2.5	300	0.20	Narrower
	Niacin	125	60	Acetone	2.5	300	0.20	Narrower
Prugh [123]	PVC	200	168	Methane	5	55	3.64	Wider
	Pea Flour	60	110	Propane	2.1	100	1.1	Linear
	Cellulose	30	110	Propane	2.1	100	2.2	Linear
	Cornstarch	70	128	Hydrogen	4	550	0.23	Narrower
Chatrathi [111]	Cornstarch	90	242	Propane	1.8	485	0.50	Linear
Pellmont [28]	PVC	200	70	Propane	1.9	350	0.20	Wider
Khalili et al. [121]	Wheat Starch	150		Methane	5			Wider
Amyotte et al. [15]	Coal	90		Methane	5			Linear
	Coal	70		Methane	5			Linear
Bartknecht [14]	PVC	250	75	Methane	4.5			Wider
Addai et al. [122]	Toner	60		Hydrogen	6			Narrower
	Lycopodium	250		Hydrogen	6			Narrower
	Polyethylene	250		Hydrogen	6			Narrower
	Starch	250		Hydrogen	6			Linear
	Toner	60		Methane	5			Wider
	Lycopodium	250		Methane	5			Linear
	Polyethylene	250		Methane	5			Narrower
	Starch	250		Methane	5			Wider
Landman [120]	Coal	75		Methane	4			Wider
	Coal	150		Methane	4			Wider
Nifuku et al. [124]	Polyurethane			Cyclopentane				

data exceptionally well, the discrepancies with other data in the literature suggest that more research is required in this area. The current thesis looks to address this problem from a fundamental starting point by investigating LFLs under laminar flow conditions. The impact of particle diameter and discrete combustion on the LFL is also explored with the current CFD model.

2.3 CFD Modeling of Laminar Dust Flames

Although the first CFD simulations of laminar coal dust flames were completed over 40 years ago, very few studies have been completed to date. Both the experimental and modeling work prior to the 1980s is summarized by the papers of Smoot and Horton [78] and Krazinski et al. [79]. The work summarized by these authors can generally be divided into two categories: those where radiation played a moderate role in flame propagation and those where it was the dominant mechanism. At atmospheric pressure and temperature, the former tends to predict flame speed between 5 and 35 cm/s and flame thickness between 5 and 10 mm, whereas the latter tends to predict flame speed in excess of 50 cm/s and flame thickness on the order of 1 m or larger [79].

Krazinski et al. [79] summarized the two groups of studies into Class I and Class II scenarios. Class I refers to investigations involving open tubes and small burners with lower flame propagation velocity and smaller flame thickness. Class II refers to investigations involving enclosed furnaces where flame velocities were recorded up to 100 cm/s. These authors state that the lower flame speed in the smaller systems is due to radiative heat loss to the surroundings, while radiative preheating in the flame front causes the higher flame speeds in the larger systems.

2.3.1 Previous Literature Models

The mathematical model presented by Smoot and Horton [78] is representative of the Class I scenario, as is the CFD model employed in the current work. In their simulations, Smoot and Horton [78] predicted burning velocities between 15 and 30 cm/s for 10 µm particles and between 13 and 17 cm/s for 33 µm particles. Although these calculations did not include heat loss, they had similar burning velocities when compared to experimental data [77], suggesting that the assertion of Krazinski et al. [79] that radiative heat loss dominates the flame speed, is at least partially incorrect for these systems. Including radiative heating in these simulations had a moderate effect with a 17% increase in burning velocity for 33 µm particles at 300 g/m^3.

In 1989, Bradley et al. [59] began development of a comprehensive CFD model for flame propagation in methane-graphite-air mixtures and “fine” coal dust in air.

In the coal dust simulations, methane was assumed to be the only devolatilization component, a simplified treatment of heterogeneous reaction was used, and radiative heating was neglected. Radiative heat loss to the surroundings was assumed to be dependent on particle diameter and showed an approximate 8 and 40 % reduction in burning velocity at 150 g/m^3 for 10 µm and 1 µm particles, respectively.

In a more recent investigation, Bradley et al. [60] extended the CFD model to include multispecies heterogeneous reaction at the particle surface and the effects of radiative preheating in the particle cloud. This model was validated against experimental data in a low pressure burner at 0.16 atm so that a thicker flame could be observed. Flame structure and burning velocity for a single simulation result (4 µm, 144.3 g/m^3) at atmospheric conditions were also reported. The effect of radiative preheating was moderate, causing a slight increase in intermediate species and a 2 % increase in burning velocity.

Although the comprehensive model was further extended to include multipath "speciated" devolatilization and more detailed physical modeling [37, 58], it was not until recently that predictions were given for dust flames at ambient pressure [38]. These simulations presented varying burning velocities depending on the devolatilization model and devolatilization parameters, and flame propagation could not be achieved without increasing the initial mixture temperature. Results from simulation models of Smoot and Horton [78], Bradley et al. [60], and Park and Park [38] are compared extensively to the current simulation model in Chapter 6 of this thesis.

2.3.2 Role of Radiation

The findings of Krazinski et al. [79], and more generally the two classes of coal dust flame propagation, can be alternatively interpreted based on recent investigation into multiphase flame radiation. Although this is an open research area [125, 126], recent investigation by Droujko et al. [127] suggests that the role of radiation depends on the size of the dust cloud.

Julien et al. [125] calculated the radiative heating length of a 12 µm aluminum powder to be approximately 25 cm and suggested that radiation would not preheat the dust ahead of the flame in systems shorter than this distance. Droujko et al. [127] suggest that this is the main difference between Class I and Class II scenarios

explored by Krazinski et al. [79]. In other words, the open tubes and burners were too small for radiation to impact the flame speed, while the enclosed vessels were large enough for preheating in front of the flame to occur.

Droujko et al. [127] also suggest that due to the difference in physical scales, the molecular processes in the flame front and radiative preheating can be decoupled. As such, radiation may not impact molecular heat transfer that occurs at the scale of the flame reaction zone, and the molecular processes may not influence radiation. This led these authors to suggest that an effective method to investigate radiation is to predict preheating in front of the flame based on the size of the dust cloud and then use this value as an initial condition to calculate molecular flame propagation.

In the current investigation, radiative preheating is not included in the computational model. This allows for a scale-independent burning velocity to be determined, which is representative of what would be seen using laboratory scale experiments. However, simulations were also completed at increased initial temperature. As suggested by Droujko et al. [127], these results may be used in future studies to illustrate the effect of radiation at larger system scales once the amount of radiative preheating can be determined.

Chapter 3

Model Description

The CFD model employed in this work builds on the coalChemistryFoam solver from the OpenFoam toolkit version 3.0.1 [63]. The equations governing transport processes, thermophysical parameters, and reaction chemistry are given for the gas and particle phases in the following sections. This chapter concludes with a comparison between the current model and those employed previously in the literature.

3.1 Gas-Phase Transport

The current model includes an Eulerian discretization of the gas-phase transport equations, global approximations of gas viscosity and thermal conductivity, and a unity Lewis number approach for gas diffusivity. To evaluate the impact of the mass, momentum, and energy transfer assumptions, gas flame simulations are compared to the Cantera package [128] using three sets of modeling assumptions: multispecies models based on molecular gas theory, mixture-averaged models, and a unity Lewis number approach. In the following sections, the governing equations for each model are given. Parameters for the multispecies, mixture-averaged, and global models are indicated with the superscripts "multi," "mix," and "global," respectively.

3.1.1 Governing Equations

The transient, multispecies, reactive equations for mass, momentum, and energy transport are solved for the gas-phase in this work [129]. The multidimensional, general form version of these equations can be given in vector form as follows:

$$\frac{\partial \rho}{\partial t} = -\nabla \cdot (\rho \mathbf{U}) + \dot{S}_{\rho} \tag{3.1}$$

$$\frac{\partial \rho \mathbf{U}}{\partial t} = -\nabla \cdot (\rho \mathbf{U}\mathbf{U}) + \nabla \cdot (\boldsymbol{\sigma}) + \rho \mathbf{g} + \dot{S}_{\rho \mathbf{U}} \tag{3.2}$$

$$\frac{\partial \rho Y_k}{\partial t} = -\nabla \cdot (\rho Y_k \left[\mathbf{U} + \mathbf{V}_k\right]) + \dot{S}_{\rho Y_k} \tag{3.3}$$

$$\frac{\partial \rho e_\mathrm{t}}{\partial t} = -\nabla \cdot (\rho e_\mathrm{t} \mathbf{U}) - \nabla \cdot (\mathbf{q}) + \rho \left(\mathbf{U} \cdot \mathbf{g}\right) - \nabla \cdot (P\mathbf{U}) + \dot{S}_{\rho e_\mathrm{t}} \tag{3.4}$$

where ρ is density, $\mathbf{U}$ is velocity, $\boldsymbol{\sigma}$ is the stress tensor, $\mathbf{g}$ is the gravity vector, Y_k is mass fraction of species k, $\mathbf{V}_k$ is diffusion velocity of species k, e_t is total specific energy, and $\mathbf{q}$ is the heat flux vector. The source terms on the right-hand side of each transport equation are denoted as $\dot{S}_i$ and have units of the transported quantity (ρ, $\rho\mathbf{U}$, ρY_k, and ρe_t) per second.

The total specific energy includes the specific sensible, kinetic, and chemical energy of the gas.

$$e_\mathrm{t} = e_\mathrm{s} + \frac{\mathbf{U}\mathbf{U}}{2} + \sum_{k=1}^{N_k} Y_k \Delta h^\circ_{\mathrm{f},k} \tag{3.5}$$

where e_s is specific sensible energy, $\Delta h^\circ_\mathrm{f}$ is the enthalpy of formation of species k, and N_k is the total number of species.

Lastly, the system of equations is closed using the ideal gas law relating pressure, density, and temperature:

$$\rho = \frac{1}{\mathcal{R}_\mathrm{Sp} T} P \tag{3.6}$$

$$\mathcal{R}_\mathrm{Sp} = \frac{\mathcal{R}}{M_\mathrm{mix}} \tag{3.7}$$

where $\mathcal{R}_\mathrm{Sp}$ is the specific gas constant, $\mathcal{R}$ is the universal gas constant, T is the temperature, P is the pressure, and M_mix is the molecular weight of the gas mixture. The mixture molecular weight is calculated from the individual species:

$$M_\mathrm{mix} = \sum_{k=1}^{N_k} X_k M_k = \frac{1}{\sum\limits_{k=1}^{N_k} Y_k / M_k} \tag{3.8}$$

where M_k is the individual species molecular weight and X_k is the mole fraction of species k.

3.1.2 Viscous Transport

For Newtonian fluids, the stress tensor can be divided into pressure and viscous stress components [130]:

$$\boldsymbol{\sigma} = -P\delta_{mn} + \tau_{mn} = -P\delta_{mn} + \left[\left(\mu' - \frac{2}{3}\mu\right)\frac{\partial u_l}{\partial x_l} + \mu\left(\frac{\partial u_m}{\partial x_n} + \frac{\partial u_n}{\partial x_m}\right)\right] \tag{3.9}$$

where τ_{mn} is the viscous stress tensor, μ is the dynamic viscosity, and μ' is the bulk viscosity. The subscript notation is such that u_m is the component of velocity in the direction m, denoted by x_m. The operator δ_{mn} is the Kronecker delta function, which takes a value of one when $m = n$ and zero otherwise.

Stokes' hypothesis [131] is typically used for combustion processes as described by Kuo [130] and states that $\mu' = 0$. Reducing the stress tensor for application to one dimension and dropping the subscripts gives:

$$\boldsymbol{\sigma} = -P + \mu\frac{\partial u}{\partial x} \tag{3.10}$$

For gasses containing a mixture of species, several methods to estimate the overall viscosity from that of the individual species exist. The method of Wilke [132], as outlined by Poling et al. [133], ignores second-order effects from kinetic gas theory and proposes the following relation:

$$\mu^{\text{multi}} = \sum_{k=1}^{N_k} \frac{X_k \mu_k}{\sum_{j=1}^{N_k} X_j \Phi_{\text{kj}}} \tag{3.11}$$

$$\Phi_{\text{kj}} = \frac{\left[1 + \left(\mu_k/\mu_j\right)^{1/2}\left(M_j/M_k\right)^{1/4}\right]^2}{\left[8\left(1 + M_k/M_j\right)\right]^{1/2}} \tag{3.12}$$

where μ_k is the viscosity of species k. Individual component viscosities can be calculated using the Chapman-Enskog treatment as described by Hirschfelder et al. [134]:

$$\mu_k = \frac{5}{16}\frac{\sqrt{\pi M_k k_{\text{B}} T}}{\pi \bar{\sigma}_k^2 \Omega_{kk}^{(2,2)\star}} \tag{3.13}$$

where k_{B} is the Boltzmann constant, $\bar{\sigma}_k$ is the collision diameter, and $\Omega_{kk}^{(2,2)\star}$ is the collision integral determined from the Lennard-Jones (6-12) potential [64].

Determination of multispecies transport parameters is an expensive computational process. For example, computing μ^{multi} requires $\mathcal{O}\left(N_k^2\right)$ operations, which can become large when many chemical species are being used. Alternative approximations to the bulk gas transport properties exist, such as Sutherland's law [135], which specifies viscosity as a function of gas temperature and requires $\mathcal{O}\left(1\right)$ operations:

$$\mu^{\text{global}} = \frac{A_\mu T}{1 + T_\mu / T} \tag{3.14}$$

These approximate relations are attractive when designing a computational model that will be extended to multidimensional simulations and the degree of error may be of similar magnitude as the experimental techniques available to study these systems.

3.1.3 Heat Flux

The heat flux vector can be divided into components from conduction, interspecies diffusion, and Dufour effects [130]. In one dimension this equation can be shown as:

$$\mathbf{q} = -\lambda \frac{\partial T}{\partial x} + \rho \sum_{k=1}^{N_k} h_{\text{sc},k} Y_k V_k + \mathcal{R} T \sum_{k=1}^{N_k} \sum_{j=1}^{N_k} \frac{X_j D_{\text{T},k}}{M_k D_{kj}} \left(V_k - V_j\right) \tag{3.15}$$

where λ is thermal conductivity, $h_{\text{sc},k}$ includes the sensible and chemical enthalpy of species k ($h_{\text{sc},k} = h_{\text{s},k} + \Delta h^\circ_{\text{f},k}$), D_{kj} is the binary diffusivity coefficient between any two pairs of species in the mixture, and $D_{\text{T},k}$ is thermal diffusivity.

No closed form solution exists in molecular theory for computing the multispecies thermal conductivity, diffusivity coefficients, and thermal diffusion coefficients under a rigorous treatment. Instead, λ^{multi}, D_{kj}^{multi}, and $D_{\text{T},k}$ must be calculated from a system of equations [64, 136]. This process involves inverting a $N_k \times N_k$ matrix for the binary diffusion coefficients and solving a $3N_k \times 3N_k$ system of algebraic equations for thermal conductivity and thermal diffusion [64].

An alternative approach requiring less computational effort is to compute mixture-averaged transport properties. In the mixture-averaged approach, the Cantera software package uses the relation proposed by Mathur et al. [137] as described by Kee et al. [64]:

$$\lambda^{\text{mix}} = \frac{1}{2}\left(\sum_{k=1}^{N_k} X_k\lambda_k + \frac{1}{\sum\limits_{k=1}^{N_k} X_k/\lambda_k}\right) \tag{3.16}$$

where λ_k is the thermal conductivity of an individual species derived from molecular theory:

$$\lambda_k = \frac{25}{32\pi^{1/2}}\left(\frac{k_{\text{B}}T}{M_k}\right)^{1/2}\frac{C_{\text{v}}}{\bar{\sigma}_k^2\mathcal{A}\Omega_{kk}^{(2,2)\star}} \tag{3.17}$$

where $\mathcal{A}$ is Avogadro's constant. Kee et al. [64] state that there is no reliable mixture-averaged approach available to compute $D_{\text{T},k}$, and as such, rigorous multispecies theory is necessary when thermal diffusion is required.

An approximate value for thermal conductivity can be achieved using the modified Eucken model as summarized by Poling et al. [133]. This model approximates translation and internal degrees of freedom within polyatomic gasses and allows the thermal conductivity to be specified in relation to viscosity:

$$\lambda^{\text{global}} = \mu\left(1.32C_{\text{v}} + 1.77\mathcal{R}\right) \tag{3.18}$$

where C_{v} is specific heat of the gas mixture at a constant volume and μ is calculated using the global model.

3.1.4 Species Diffusion

Multispecies diffusion velocity can be expressed as the following, using a first-order approximation to molecular theory [129]:

$$X_k\mathbf{V}_k = -\sum_{k=1}^{N_k} D_{kj}^{\text{multi}}\mathbf{d_k} - D_{\text{T},k}\frac{\nabla T}{T} \tag{3.19}$$

$$\mathbf{d_k} = \nabla X_k + \left(X_k - Y_k\right)\frac{\nabla P}{P} \tag{3.20}$$

where the last term in Equation 3.19 is the Soret effect responsible for species diffusion due to temperature gradients, and the last term in Equation 3.20 is species diffusion due to pressure gradients.

As noted above, determining the multicomponent diffusion velocities is a computationally expensive procedure. A mixture-averaged approach to species diffusion is given by the Hirschfelder-Curtis approximation as described by Kuo [129]. In one dimension, the following relation is developed:

$$X_k V_k^* = -D_k^{\text{mix}} \frac{\partial X_k}{\partial x} \tag{3.21}$$

$$D_k^{\text{mix}} = \frac{1 - X_k}{\sum_{j \neq k}^{N_k} X_j / D_{kj}} \tag{3.22}$$

where V_k^* is the estimated diffusion velocity and D_k^{mix} represents the diffusion of species k into the mixture of other gasses. The binary diffusion coefficients are determined from molecular theory as follows [64]:

$$D_{kj} = \frac{3}{16} \frac{\sqrt{2\pi k_{\text{B}}^3 T^3 / M_{kj}}}{P \pi \bar{\sigma}_{kj}^2 \Omega_{kk}^{(1,1)\star}} \tag{3.23}$$

where $\Omega_{kk}^{(1,1)\star}$ is an additional collision integral from the Lennard-Jones (6-12) potential [64], M_{kj} is the reduced molecular weight of the species pair, and $\bar{\sigma}_{kj}$ is the reduced collision diameter. Kee et al. [64] specify the reduced parameters using the following combining rules:

$$M_{kj} = \frac{2}{\frac{1}{M_k} + \frac{1}{M_j}} \tag{3.24}$$

$$\bar{\sigma}_{kj} = \frac{\bar{\sigma}_k + \bar{\sigma}_j}{2} \tag{3.25}$$

When a mixture-averaged approached is used for species diffusion, special care must be taken to ensure conservation of mass. This is typically achieved by enforcing the following condition [129]:

$$\sum_{k=1}^{N_k} Y_k V_k = 0 \tag{3.26}$$

This leads to the definition of a correction velocity which is applied to the estimated diffusion velocities of all species:

$$V_k = V_k^* + V_\mathrm{c} \tag{3.27}$$

$$V_\mathrm{c} = -\sum_{k=1}^{N_k} Y_k V_k \tag{3.28}$$

where V_c is the correction velocity and V_k is the diffusion velocity used in the species mass transport equations.

As expressed by Kuo and Acharya [129], many combustion codes use a simplified approach for diffusion velocity based on Fick's law approximation:

$$Y_k V_k^* = -D_k^{\mathrm{global}} \frac{\partial Y_k}{\partial x} \tag{3.29}$$

The main difficulty in this approach is determining an appropriate diffusion coefficient. One solution is to calculate the diffusion coefficient assuming a unity Lewis number [129]:

$$\mathrm{Le}_k = \frac{\alpha}{D_k} = \frac{\lambda}{\rho C_\mathrm{p} D_k} = 1 \tag{3.30}$$

Under this assumption, all of the species diffusivities are equal and can be specified in terms of thermal diffusivity:

$$D_k^{\mathrm{global}} = D = \frac{\lambda}{\rho C_\mathrm{p}} = \alpha \tag{3.31}$$

The main advantage of the unity Lewis number assumption is computational effort. Using this approach, computing species diffusion becomes a minimal part of the code solution time. The governing equations are also simplified as the correction velocity term is reduced to zero:

$$V_\mathrm{c} = -\sum_{k=1}^{N_k} D \frac{\partial Y_k}{\partial x} = -D \sum_{k=1}^{N_k} \frac{\partial Y_k}{\partial x} = 0 \tag{3.32}$$

The main disadvantage to a unity Lewis number assumption is that the flame structure may be incorrectly represented. All species are assumed to have the same diffusivity, and lighter components will not propagate upstream into the flame front. Thermal and mass diffusion are also assumed to be equal, which may alter the preheating zone in the flame front. The impact of the unity Lewis number assumption

is evaluated by comparing the global, mixed, and multispecies models for methane flames in this work (see Section 5.1).

3.1.5 Gas-Phase Chemistry

Gas-phase reaction chemistry is described by a set of coupled kinetic equations that can be represented as the following summation [65]:

$$\sum_{k=1}^{N_k} \nu'_{k,r}\eta_k \rightleftharpoons \sum_{k=1}^{N_k} \nu''_{k,r}\eta_k, r = 1, N_\mathrm{r} \tag{3.33}$$

where N_r is the overall number of reactions, $\nu'_{k,r}$ is the stochiometric coefficient of a given reactant species in a given reaction, $\nu''_{k,r}$ is the stochiometric coefficient of a given product species in a given reaction, and η_k is the species molar concentration (mol/m^3).

The overall rate of any specific reaction ($\dot{\omega}_r$, mol/m^3-s) is determined based on a general Arrhenius expression for the forward and backward reaction coefficients:

$$\dot{\omega}_r = k_r^\mathrm{f} \prod_{k=1}^{N_k} \eta_k^{\nu'_{k,r}} - k_r^\mathrm{b} \prod_{k=1}^{N_k} \eta_k^{\nu''_{k,r}} \tag{3.34}$$

$$k_r = A_r T^{n_r} e^{\left(-\frac{E_{\mathrm{a},r}}{\mathcal{R}T}\right)} \tag{3.35}$$

where A_r is the Arrhenius pre-exponential factor, n_r is the temperature coefficient, and $E_{\mathrm{a},r}$ is the activation energy (J/kg). The units of A_r depend on the order of the reaction.

The contribution of gas-phase chemistry reactions to the species mass and enthalpy transport equations is specified as:

$$\dot{S}^\mathrm{G}_{\rho Y_k} = M_k \sum_{r=1}^{N_r} \left(\nu''_{k,r} - \nu'_{k,r}\right) \dot{\omega}_r \tag{3.36}$$

$$\dot{S}^\mathrm{G}_{\rho h_\mathrm{tnc}} = \sum_{r=1}^{N_r} q_r \dot{\omega}_r \tag{3.37}$$

where q_r is the overall heat release from the reaction and h_tnc is the total nonchemical specific enthalpy (defined in Equation 3.48). The heat release is calculated from the

stoichiometric coefficients and the heat of the formation of species involved in each reaction:

$$q_r = \sum_{k=1}^{N_k} M_k \left(\nu''_{k,r} - \nu'_{k,r}\right) \Delta h^\circ_{\mathrm{f},k} \tag{3.38}$$

Four gas-phase reaction mechanisms with increasing complexity were used in the current work and are summarized in Table 3.1. The literature references, total number of species and total reaction steps for each mechanism are given in the table.

Table 3.1: Gas-phase chemistry reaction mechanisms used in the current work.

Mechanism	**Species**	**Reactions**	**Reference**
MP1	5	1	CERFACS [138]
BFER2	6	2	Franzelli et al. [139]
DRM19	19	84	Kazakov and Frenklach [140]
GRI53	53	325	Smith et al. [141]

In Table 3.1, MP1 and BFER2 are global reaction mechanisms with a single-step and a two-step reaction model, respectively. The DRM19 mechanism was determined using a chemistry reduction technique starting with GRI-Mech 1.2 [142, 143]. GRI53 is the most recent update to the detailed methane mechanism from the Global Research Institute (version number GRI-Mech 3.0 [141]).

The reaction parameters for the MP1 and BFER2 mechanisms were provided from Cantera [138] and are summarized in Table 3.2. MP1 involves a single irreversible Arrhenius reaction, while BFER2 involves irreversible and reversible reaction steps. The model parameters for BFER2 are based on the model of Franzelli et al. [139], except that a constant pre-exponential factor is used and the temperature exponent has been modified from 0.8 to 0.7 [138].

Table 3.2: Single-step and two-step global reaction model parameters.

Name	**Reaction**	$\boldsymbol{A_r}$	$\boldsymbol{n_r}$	$\boldsymbol{E_{\mathrm{a},r}/\mathcal{R}}$ (K)	**Reaction Orders**
MP1	$CH_4 + 2\,O_2 \longrightarrow CO_2 + 2\,H_2O$	3.47851×10^{8}	0.0	10063.8	$[CH_4]^1[O_2]^{0.5}$
BFER2 (1)	$CH_4 + 1.5\,O_2 \longrightarrow CO + 2\,H_2O$	1.73859×10^{9}	0.0	17863.3	$[CH_4]^{0.5}[O_2]^{0.65}$
BFER2 (2)	$CO + 0.5\,O_2 \longleftrightarrow CO_2$	6.32456×10^{6}	0.7	6038.29	$[CO]^1[O_2]^{0.5}$

In addition to the three Arrhenius parameters, some reactants in the global mechanisms have specific orders as indicated in Table 3.2. The rate parameters for the

DRM19 and GRI53 mechanisms can be found as reported by the original authors provided in Table 3.1.

3.1.6 Thermophysical Properties

Due to the large temperature gradients in combustion problems, the change in thermophysical properties must be included in the computational model. Specific heat can be specified as a temperature-based polynomial function fit to tabulated data such as the JANAF tables (see Stull and Prophet [144] as described by Kuo and Acharya [129]):

$$\frac{C_{\mathrm{p},k}^{\mathrm{mol}}(T)}{\mathcal{R}^{\mathrm{mol}}} = a_{0,k} + a_{1,k}T + a_{2,k}T^2 + a_{3,k}T^3 + a_{4,k}T^4 \tag{3.39}$$

where $C_{\mathrm{p},k}^{\mathrm{mol}}$ is the specific heat of species k on a molar basis and the constants $a_{0,k}$ to $a_{4,k}$ are fit to the tabulated data.

Specific enthalpy (sensible + chemical, h_{sc}) can be determined from specific heat based on the definition:

$$h_{\mathrm{sc},k} = \int_{T_{\mathrm{Ref}}}^{T} C_{\mathrm{p},k} dT + \Delta h_{\mathrm{f},k}^{\circ} \tag{3.40}$$

Integrating Equation 3.39 gives the following polynomial for the specific heat of species k:

$$\frac{h_{\mathrm{sc},k}^{\mathrm{mol}}(T)}{T\mathcal{R}^{\mathrm{mol}}} = a_{0,k} + \frac{a_{1,k}}{2}T + \frac{a_{2,k}}{3}T^2 + \frac{a_{3,k}}{4}T^3 + \frac{a_{4,k}}{5}T^4 + \frac{a_{5,k}}{T} \tag{3.41}$$

where another value, $a_{5,k}$, is required from the tabulated data for the integration constant. In the current work, all chemistry models use the polynomial fits for $a_{0,k}$ to $a_{5,k}$ given with the GRI-Mech 3.0 chemistry mechanism provided with the Cantera package [138, 141]. This mechanism includes two-region, five parameter fits for all of the species used in this work.

The specific heat and specific enthalpy of the gas mixture can be specified from the component values based on the following mixing rules [129]:

$$C_{\mathrm{p}} = \sum_{k=1}^{N_k} C_{\mathrm{p},k}^{\mathrm{mol}} \frac{Y_k}{M_k} \tag{3.42}$$

$$h_{\mathrm{sc}} = \sum_{k=1}^{N_k} h_{\mathrm{sc},k}^{\mathrm{mol}} \frac{Y_k}{M_k} \tag{3.43}$$

3.1.7 Simplified Equations

The complexity of the gas phase governing equations can be reduced by substituting the simplifications outlined in the previous sections. Reducing the equations to one dimension, defining a mass flux variable ($\phi = \rho u$), and neglecting gravity gives the following simplified transport equations:

$$\frac{\partial \rho}{\partial t} = -\frac{\partial \phi}{\partial x} + \dot{S}_{\rho}^{\mathrm{P}} \tag{3.44}$$

$$\frac{\partial \rho u}{\partial t} = -\frac{\partial \phi u}{\partial x} + \frac{\partial}{\partial x}\left(\mu \frac{\partial u}{\partial x}\right) - \frac{\partial P}{\partial x} + \dot{S}_{\rho u}^{\mathrm{P}} \tag{3.45}$$

$$\frac{\partial \rho Y_k}{\partial t} = -\frac{\partial \phi Y_k}{\partial x} + \frac{\partial}{\partial x}\left(\rho D \frac{\partial Y_k}{\partial x}\right) + \dot{S}_{\rho Y_k}^{\mathrm{P}} + \dot{S}_{\rho Y_k}^{\mathrm{G}} \tag{3.46}$$

$$\frac{\partial \rho h_{\mathrm{tnc}}}{\partial t} - \frac{\partial P}{\partial t} = -\frac{\partial \phi h_{\mathrm{tnc}}}{\partial x} + \frac{\partial}{\partial x}\left(\rho \alpha \frac{\partial h_{\mathrm{s}}}{\partial x}\right) + \dot{S}_{\rho h_{\mathrm{tnc}}}^{\mathrm{P}} + \dot{S}_{\rho h_{\mathrm{tnc}}}^{\mathrm{G}} \tag{3.47}$$

where the source terms have been expanded to include contributions from the particle and gas phases, denoted with the superscripts P and G, respectively. The stress tensor definition in Equation 3.10 has been combined with Equation 3.14 and substituted into Equation 3.2 to formulate the transport of momentum. Fick's law as outlined in Equation 3.29 has been combined with the unity Lewis number assumption (Equation 3.30 and substituted into Equation 3.31, $D = \alpha$) and Equation 3.3 to formulate the transport of species mass.

The energy equation has been modified to include the total specific enthalpy without the chemical component and sensible specific enthalpy. These are related to the total specific enthalpy through the following closure equations [129]:

$$h_{\mathrm{tnc}} = h_{\mathrm{s}} + \frac{\mathbf{UU}}{2} \tag{3.48}$$

$$h_{\mathrm{t}} = h_{\mathrm{tnc}} + \sum_{k=1}^{N_k} Y_k \Delta h_{\mathrm{f},k}^{\circ} \tag{3.49}$$

Derivation of the enthalpy transport equation (Equation 3.47) from the total specific energy (Equation 3.4) can be found in combustion modeling textbooks such as Kuo and Acharya [129]. The derivation assumes Fick's law for species diffusion, a unity Lewis number, and that viscous energy dissipation is negligible ($\frac{\partial}{\partial x}\left(u\mu\frac{\partial u}{\partial x}\right) \approx 0$). This is a common assumption in low-Mach number flows with combustion [47].

3.1.8 Comparison between Gas-Flame Models

The impact of the gas-phase modeling assumptions is explored by comparing gas-flame simulations from the current model with Cantera Version 2.3.0 [128]. The different transport modeling assumptions used in each simulation model are listed in Table 3.3. The governing equations for viscous transport, heat flux, and species diffusion are listed and were outlined in the previous sections.

Table 3.3: Comparison between gas phase flame simulation models explored in this work.

Simulation Model	**Dynamic Viscosity**	**Thermal Conductivity**	**Species Diffusivity**	**Thermal Diffusivity**
Cantera$^{\text{multi}}$	μ^{multi}	λ^{multi}	D_{kj}^{multi}	$D_{\text{T},k}$
Cantera$^{\text{mix}}$	μ^{multi}	λ^{mix}	D_{kj}^{mix}	-
Cantera$^{\text{unity}}$	μ^{multi}	λ^{mix}	D_{k}^{global}	-
Current Model	μ^{global}	λ^{global}	D_{k}^{global}	-

The multispecies and mixed approaches to viscous transport, heat flux, and species diffusion are included in the standard Cantera release. A modified version of Cantera, which includes the unity Lewis number assumption, was also created to isolate the impact of the species diffusion assumption on gas flame propagation. Comparison between the current model and the various Cantera versions allows the impact of the modeling assumptions to be explored individually, which demonstrates the potential impact on dust and hybrid flames.

3.2 Particle-Phase Transport

The particle phase is discretized using a group Lagrange approach where individual particles or particle groups are tracked through time and space [65]. The governing

equations and physical models used in the current work are described in the following sections.

3.2.1 Governing Equations

Particle motion is governed by Newton's second law as a balance between particle acceleration and the forces acting on the particle mass. Particle velocity and position are defined as:

$$m_{\mathrm{p}} \frac{\mathrm{d}u_{\mathrm{p}}}{\mathrm{d}t} = F_{\mathrm{p}} \tag{3.50}$$

$$\frac{\mathrm{d}x_{\mathrm{p}}}{\mathrm{d}t} = u_{\mathrm{p}} \tag{3.51}$$

where m_{p} is the mass of an individual particle, u_{p} is the particle velocity, x_{p} is the particle position, and F_{p} is the sum of the forces acting on the particle.

Conservation of energy gives the following equation for change in enthalpy:

$$m_{\mathrm{p}} \frac{\mathrm{d}h_{\mathrm{p}}}{\mathrm{d}t} = \dot{H}_{\mathrm{p}} + \dot{Q}_{\mathrm{v,p}} + \epsilon_{\mathrm{p}} \dot{Q}_{\mathrm{s,p}} \tag{3.52}$$

where h_{p} is the particle specific enthalpy and $\dot{H}_{\mathrm{p}}$, $\dot{Q}_{\mathrm{v,p}}$, and $\dot{Q}_{\mathrm{s,p}}$ represent energy exchange with the gas, energy exchange due to devolatilization, and energy exchange due to surface reactions, respectively. ϵ_{p} is the heat retention coefficient that governs division of energy from surface reactions to heating the particle or the gas surrounding the particle.

In the current model, the particle diameter is held constant and density is reduced by devolatilization and surface reaction [65]. This is in contrast to Smoot and Horton [78], who assumed the particle swelled during combustion, and Bradley et al. [60] and Park and Park [38], who used a shrinking particle model. Assuming a constant particle diameter increases particle momentum and heat transfer timescales, and tends to underpredict surface reactions relative to the shrinking particle models.

3.2.2 Exchange Terms

The particle source terms in Equation 3.44 to Equation 3.47 are calculated by summing the force, energy, and mass transfer contributions from each individual particle

in the computational cell. Dividing this summation by the cell volume gives the following relations for particle momentum, enthalpy, and species mass transfer source terms [65]:

$$\dot{S}^{\mathrm{P}}_{\rho u} = -\frac{1}{\mathcal{V}} \sum_{\mathcal{V}} N_{\mathrm{p}} F_{\mathrm{p}} \tag{3.53}$$

$$\dot{S}^{\mathrm{P}}_{\rho h_{\mathrm{tnc}}} = -\frac{1}{\mathcal{V}} \sum_{\mathcal{V}} N_{\mathrm{p}} \left(\dot{H}_{\mathrm{p}} + (1 - \epsilon_{\mathrm{p}}) \, \dot{Q}_{\mathrm{s,p}} \right) \tag{3.54}$$

$$\dot{S}^{\mathrm{P}}_{\rho Y_k} = -\frac{1}{\mathcal{V}} \sum_{\mathcal{V}} N_{\mathrm{p}} \dot{m}^{\mathrm{P}}_k \tag{3.55}$$

where $\dot{m}^{\mathrm{P}}_k$ is the summation of species mass transfer from the particle due to devolatilization and surface reactions, $\dot{Q}_{\mathrm{s,p}}$ is the rate of energy release from the surface reactions, and $\mathcal{V}$ is cell volume. The variable N_{p} is the number of physical particles represented by a single Lagrange group. These groups have the collective mass, momentum, and energy of the particles they represent.

Lastly, the particle source term in the overall gas phase mass transport equation is the summation of the particle source terms in the individual species mass transport equations:

$$\dot{S}^{\mathrm{P}}_{\rho} = \sum_{k=1}^{N_k} \dot{S}^{\mathrm{P}}_{\rho Y_k} \tag{3.56}$$

For real-world-scale applications, the number of particles in a Lagrange group is typically much larger than unity. However, the scale in the current work is on the order of centimetres and each group can be used to represent a single particle ($N_{\mathrm{p}} = 1.0$). Furthermore, simulations are completed where the groups are "over-discretized" ($N_{\mathrm{p}} < 1.0$) to represent a continuum. This allows comparison to previous results in the literature that employed an Eulerian discretization, while comparison of the two representations allows the impact of discrete particle combustion to be explored. The discrete and continuum particle representations are described further in Section 4.2.2.

3.2.3 Particle Drag

Momentum exchange is governed by drag force assuming a spherical particle. Following the work of Faeth [145], the Basset and virtual mass forces are neglected due to the low pressure and high density ratios studied here. Gravity is neglected and pressure gradient terms are small, as the flow is nearly isobaric [65]. The resulting equations for particle drag force and drag coefficient are given as follows:

$$F_{\mathrm{p}} = -\frac{\pi d_{\mathrm{p}}^2}{8}\rho C_{\mathrm{D}}|u_{\mathrm{p}} - u|\left(u_{\mathrm{p}} - u\right) \tag{3.57}$$

$$C_{\mathrm{D}} = \begin{cases} 0.424, & \text{if } \mathrm{Re_p} \geq 1000 \\ \frac{24}{\mathrm{Re_p}}\left(1 + \frac{1}{6}\mathrm{Re_p^{2/3}}\right) & \text{otherwise} \end{cases} \tag{3.58}$$

where C_{D} is the drag coefficient proposed by Putnam [146], as described by Kuo and Acharya [129], and d_{p} is the particle diameter. The particle Reynolds number is defined as:

$$\mathrm{Re_p} = \frac{\rho|u_{\mathrm{p}} - u|d_{\mathrm{p}}}{\mu_{\mathrm{s}}} \tag{3.59}$$

where the subscript "s" denotes properties at the surface of the particle which are calculated using the 1/3 weighting of the gas and particle temperature [147].

Equations 3.57–3.59 can be combined with Equation 3.50 to give the overall momentum balance for a particle:

$$m_{\mathrm{p}}\frac{\mathrm{d}u_{\mathrm{p}}}{\mathrm{d}t} = \frac{3}{4}\frac{C_{\mathrm{D}}\mathrm{Re_p}\mu_{\mathrm{s}}\left(u_{\mathrm{p}} - u\right)}{d_{\mathrm{p}}^2\rho_{\mathrm{p}}} \tag{3.60}$$

This equation can be integrated analytically using the initial conditions $u_{\mathrm{p}} = u_{\mathrm{p}}^{\circ}$ when t= 0.

$$u_{\mathrm{p}}\left(t\right) = u + \left(u_{\mathrm{p}}^{\circ} - u\right)e^{-t/\tau_u} \tag{3.61}$$

where $u_{\mathrm{p}}\left(t\right)$ is the particle velocity at a given instance in time, u is the gas velocity, and u_{p}° is the initial particle velocity. The coefficients on the right hand side of Equation 3.60 have been collected into the particle drag relaxation timescale (τ_u) as follows:

$$\tau_u = \frac{4}{3}\frac{d_\mathrm{p}^2 \rho_\mathrm{p}}{C_\mathrm{D}\mathrm{Re}_\mathrm{p}\mu_\mathrm{s}} \tag{3.62}$$

To solve for particle velocity, Equation 3.60 is integrated analytically using the relaxation timescale given in Equation 3.62.

3.2.4 Particle Heating

The energy exchange is calculated by heating at the particle surface and heterogeneous surface reactions. A small Biot number is assumed, and the temperature distribution throughout the particle is uniform. The resulting relations for particle heat transfer and Nusselt number [148] are given as follows:

$$\dot{H}_\mathrm{p} = \pi d_\mathrm{p} \lambda_\mathrm{s} \mathrm{Nu} \left(T - T_\mathrm{p}\right) \tag{3.63}$$

$$\mathrm{Nu} = 2 + 0.6\mathrm{Re}_\mathrm{p}^{1/2}\mathrm{Pr}^{1/3} \tag{3.64}$$

where Nu and Pr are the nondimensional Nusselt and Prandlt numbers.

Similarly to the momentum exchange, Equation 3.52 and Equation 3.63 can be rearranged and integrated to solve for particle temperature. After rearranging, the thermal relaxation timescale is determined as:

$$\tau_\mathrm{h} = \frac{m_\mathrm{p} C_\mathrm{s} \left(T + T^\star - T_\mathrm{p}\right)}{\epsilon_\mathrm{p}\dot{Q}_\mathrm{s,p} + \pi d_\mathrm{p}\lambda_\mathrm{s}\mathrm{Nu}\left(T - T_\mathrm{p}\right)} \tag{3.65}$$

$$T^\star = \frac{\epsilon_\mathrm{p}\dot{Q}_\mathrm{s,p}}{\pi d_\mathrm{p}\mathrm{Nu}\lambda_\mathrm{s}} \tag{3.66}$$

Letting the heat retention coefficient go to zero ($\epsilon_\mathrm{p} = 0$) gives the familiar timescale for heating of a spherical particle without surface reaction [149]:

$$\tau_\mathrm{h} = \frac{m_\mathrm{p} C_\mathrm{s}}{\pi d_\mathrm{p}\lambda_\mathrm{s}\mathrm{Nu}} \tag{3.67}$$

3.2.5 Particle Devolatilization

Following the work of Bradley et al. [60], the particle composition is assumed to be 40 % methane and 60 % carbon in this work, and ash and moisture contents are

assumed to be negligible. Particle devolatilization is described by a single-step Arrhenius expression:

$$\dot{m}^{\mathrm{P}}_{\mathrm{CH_4}} = -m^{\mathrm{P}}_{\mathrm{CH_4}} A_{\mathrm{v}} e^{\left(-\frac{E_{\mathrm{a,v}}}{\mathcal{R}T_{\mathrm{p}}}\right)} \tag{3.68}$$

where A_{v} and $E_{\mathrm{a,v}}$ are the devolatilization pre-exponential factor and activation energy, respectively, and are taken as $1.0{\times}10^{13}$ 1/s and $1.8{\times}10^{8}$ J/kg, respectively [60]. Dixon-Lewis et al. [150] demonstrated that the burning velocity is insensitive to reducing the devolatilization rate by up to three orders of magnitude using this model.

Heat is removed from the particle due to devolatilization based on the following relation:

$$\dot{Q}_{\mathrm{v,p}} = \dot{m}^{\mathrm{P}}_{\mathrm{CH_4}} L_{\mathrm{v}} \tag{3.69}$$

where L_{v} is a user specified latent heat of devolatilization taken as 1.72 MJ/kg.

Equation 3.68 can be integrated analytically using the initial condition $m^{\mathrm{P}}_{\mathrm{CH_4}} = \left(m^{\mathrm{P}}_{\mathrm{CH_4}}\right)^{\circ}$ when $t = 0$.

$$m^{\mathrm{P}}_{\mathrm{CH_4}}(t) = m^{\mathrm{P}}_{\mathrm{CH_4}} e^{-t/\tau_{\mathrm{v}}} \tag{3.70}$$

$$\tau_{\mathrm{v}} = \frac{1}{A_{\mathrm{v}} e^{\left(-\frac{E_{\mathrm{a,v}}}{\mathcal{R}T_{\mathrm{p}}}\right)}} \tag{3.71}$$

where τ_{v} is the characteristic timescale associated with devolitilization.

3.2.6 Particle Surface Reactions

In the current work, heterogeneous combustion is specified based on a single surface reaction between oxygen molecules and carbon in the coal particle:

$$\mathrm{C_{(s)}} + \mathrm{O_2} \longrightarrow \mathrm{CO_2} \tag{3.72}$$

From this reaction, carbon is consumed from the particle mass, oxygen is consumed from the gas phase, and carbon dioxide is produced. The rate of the surface reaction is specified assuming a diffusion limited process [151]:

$$\dot{m}_{\mathrm{C}}^{\mathrm{P}} = -A_{\mathrm{s}} K_{\mathrm{D}} \left(P_{\mathrm{O_2,g}} - P_{\mathrm{O_2,s}} \right) \tag{3.73}$$

where A_{s} is the particle surface area, K_{D} is a reaction rate coefficient, $P_{\mathrm{O_2,g}}$ is the partial pressure of oxygen in the gas surrounding the particle, and $P_{\mathrm{O_2,s}}$ is the partial pressure of oxygen at the surface of the particle.

Under the diffusion limited assumption, oxygen is consumed as soon as it reaches the surface of the particle ($P_{\mathrm{O_2,s}} = 0$). The partial pressure of oxygen gas can be defined based on the ideal gas law:

$$P_{\mathrm{O_2,g}} = \rho \mathcal{R} T \frac{Y_{\mathrm{O_2}}}{M_{\mathrm{O_2}}} \tag{3.74}$$

Following the work of Field [152] the reaction rate coefficient is specified based on diffusion toward a spherical surface in a stationary fluid:

$$K_{\mathrm{D}} = \frac{2 M_C D_{\mathrm{s}}^*}{d_{\mathrm{p}} \mathcal{R} T_{\mathrm{s}}} \tag{3.75}$$

where D_{s}^* represents the gas diffusivity at the surface of the particle and T_{s} is the film temperature in the particle boundary layer calculated as an average between the gas and particle temperature. Combining Equations 3.73–3.75 gives the final relation for diffusion limited consumption of carbon at the surface of the particle:

$$\dot{m}_{\mathrm{C}}^{\mathrm{P}} = -\frac{4\pi d_{\mathrm{p}} D_{\mathrm{s}}^* Y_{\mathrm{O_2}} T \rho}{T_{\mathrm{p}} + T} \frac{M_{\mathrm{C}}}{M_{\mathrm{O_2}}} \tag{3.76}$$

In the current model the ratio of molecular weights is combined into the diffusivity coefficient such that an input parameter, D_{s}, is defined where $D_{\mathrm{s}}^* = D_{\mathrm{s}} \frac{M_{\mathrm{O_2}}}{M_{\mathrm{C}}}$. The rate of energy produced by surface reactions is specified as:

$$\dot{Q}_{\mathrm{s,p}} = \dot{m}_{\mathrm{C}}^{\mathrm{P}} h_{\mathrm{s,C}} - \dot{m}_{\mathrm{CO_2}}^{\mathrm{P}} M_{\mathrm{CO_2}} \Delta h_{\mathrm{f,CO_2}}^{\circ} \tag{3.77}$$

where $h_{\mathrm{s,C}}$ is the sensible enthalpy of carbon at the given particle temperature and $\Delta h_{\mathrm{f,CO_2}}^{\circ}$ is the heat of formation of CO_2. In the current simulation, a surface reaction heat retention coefficient (ϵ_{p}) of zero was used such that the energy release from the heterogeneous reaction occurs in the gas adjacent to the particle surface. A constant value of $100\,\mathrm{mm^2/s}$ was used for the surface reaction diffusion coefficient (D_{s}), unless specified otherwise.

Lastly, Equation 3.76 can be integrated using the initial condition $m_{\mathrm{C}}^{\mathrm{P}} = \mathcal{V}_{\mathrm{p}}\psi_{\mathrm{s}}^{\circ}\rho_{\mathrm{p}}^{\circ}$ when $t = 0$, where $\mathcal{V}_{\mathrm{p}}$ is the particle volume, $\psi_{\mathrm{s}}^{\circ}$ is the initial mass fraction of carbon and $\rho_{\mathrm{p}}^{\circ}$ is the initial particle density. Performing this integration gives the linear relation:

$$m_{\mathrm{C}}^{\mathrm{P}}(t) = \mathcal{V}_{\mathrm{p}}\psi_{\mathrm{s}}^{\circ}\rho_{\mathrm{p}}^{\circ} - \frac{4\pi d_{\mathrm{p}} D_{\mathrm{s}} Y_{\mathrm{O}_2} T \rho}{T_{\mathrm{p}} + T} t \tag{3.78}$$

A timescale for complete consumption of carbon by surface reaction can be specified by setting $m_{\mathrm{C}}^{\mathrm{P}}(\tau_{\mathrm{s}}) = 0$ and rearranging Equation 3.78:

$$\tau_{\mathrm{s}} = \frac{\psi_{\mathrm{s}}^{\circ}\rho_{\mathrm{p}}^{\circ} d_{\mathrm{p}}^{2}}{24 D_{\mathrm{s}} Y_{\mathrm{O}_2} \rho} \frac{T_{\mathrm{p}} + T}{T} \tag{3.79}$$

3.3 Comparison to Previous Literature Models

A comparison between the models and parameters used in the current work and those used previously in the literature is given in Table 3.4. Results from the current model are compared to Bradley et al. [60] with 4 µm particles to explore flame structure in Section 6.1.2. Results from the current model are also compared to Smoot and Horton [78] to explore the effect of particle size on burning velocity (see Section 6.1.3), and to Park and Park [38] to explore the effect of initial system temperature on the burning velocity (see Section 6.1.4).

Overall, the model employed here has been simplified with respect to thermal conductivity, viscosity, mass diffusivity, devolatilization products, and surface reaction kinetics compared to the other models presented in Table 3.4. This is done intentionally for a number of reasons.

Firstly, increased accuracy from the detailed models remains to be proven for laminar burning velocity in coal dust clouds. Although the simulations of Smoot and Horton [78] and Bradley et al. [60] demonstrate similar burning velocities at a concentration of 144.3 g/m^3, neither agree with the more comprehensive model of Park and Park [38], who predict that flame propagation is not possible at an initial temperature of 300 K. Furthermore, the models of Smoot and Horton [78] and Park and Park [38] disagree with each other, and with the experimental data at high dust concentrations.

Table 3.4: Comparison of modeling parameters used in this work and previous studies from the literature [65].

Parameter	Current	Smoot and Horton [78]	Bradley et al. [60]	Park and Park [38]
Analysis				
Particle Size (µm)	4, 10, 33	10, 33	4	10, 33
Concentration (g/m^3)	100–1000	100–1200	144.3	200–900
Initial Temperature (K)	300, 373, 473	298	298	373, 473, 573
Particles				
Total Density (kg/m^3)	1300	1300	1300	1300
Carbon Density (kg/m^3)	1600	Not Specified	1600	1600
% Volatiles	40	50	40	Detailed
Specific Heat (J/kg-K)	Mixed	1250	Mixed	Mixed
Conductivity (W/m-K)	Mixed	Unknown	Unknown	Unknown
Diameter Model	Constant	10% Swelling	Shrinking	Shrinking
Discretization				
Approach	Lagrangian	Eulerian	Eulerian	Eulerian
Thermal Equilibrium	No	No	Yes	No
Mechanical Equilibrium	No	Yes	Yes	No
Devolatilization				
Model	Arrhenius	Arrhenius	Arrhenius	Arrhenius
Pre-Exponential (1/s)	1.0×10^{13}	5.0×10^{5}	1.0×10^{13}	Global/Detailed
Activation Temperature (K)	21,650	8,907	21,650	Global/Detailed
Latent Heat (MJ/kg)	1.72	1.73	1.72	1.72
Volatile Products	CH_4	C_nH_m, CO, H_2, N_2, OH	CH_4	CH_4, CO, CO_2, H_2O, H_2, HCN, tar
Surface Reaction				
Model	Diffusion	Kinetic/Diffusion	Molecular	Molecular
Attacking Species	O_2	O_2	O_2, H, O, OH	O_2, H, O, OH, CO
Surface Area Factor	1.0	1.0	1.0	< 4.0
Other Models				
Gas Diffusivity	Le = 1	Le = 1	Detailed	Detailed
Gas Viscosity	Sutherland	Chapman-Enskog	Detailed	Detailed
Gas Conductivity	Eucken	Eucken/Wilke	Detailed	Detailed
Gas Specific Heat	JANAF	JANAF	JANAF	JANAF
Pressure	Variable	Constant	Unknown	Unknown
Radiation	No	No	Yes	Yes

Secondly, the coupling of multispecies diffusion and devolatilization, surface reaction, and radiation makes it difficult to explore the impact of any one model alone. It is envisioned that the model employed in the current work can provide a baseline from which the effect of more detailed models can be studied individually. Furthermore, the reduced number of input parameters will allow different combustible dusts to more easily be investigated within the current framework.

Lastly, it seems likely that the models of Bradley et al. [60] and Park and Park [38]

are too computationally expensive to use for laboratory scale, industrial scale, or multidimensional simulations. Moving forward, a simpler model is required to investigate these systems. This model is not previously available and validated for laminar burning velocity within the literature, but is provided in the current work.

Chapter 4

Numerical Approach

This chapter outlines the numerical approach used to solve the governing equations. The computational domain, multiphase discretization, and numerical solution methods are described followed by the simulation process and a description of the modifications to the core coalChemistryFoam solver.

4.1 Numerical Domain

The simulation domain for the current model is shown schematically in Figure 4.1. The one-dimensional domain represents a long flame tube with a square cross-section that is open at both ends. At the start of the simulation, an initial flame profile including temperature, velocity, and species distribution is specified at the downstream end of the tube in a section of pure gas. Upstream from the gas section is a test section that contains either gas, dust, or a hybrid mixture. The case with coal dust is illustrated in Figure 4.1. After the test section, the domain is extended several meters to reduce interaction between pressure waves from the flame and domain boundaries.

A particle cloud length of 1.5 cm is required for the flame to reach a steady propagation velocity in the test section, and a 0.1-cm overlap between the gas section and particle cloud allows a more rapid transition past transient propagation effects. Note that heat losses to the side walls of the domain are neglected, and a slip-velocity boundary is employed, such that the simulation represents an infinitely tall, one-dimensional flame.

Although the computational domain represents an infinitely tall flame, the off-propagation dimensions still have to be set specifically for each particle size so that the proper concentration is represented in the coal cloud. For each simulation, the domain width in the off-axis directions is set to the nominal centre-to-centre separation distance between the particles. This can be determined by rearranging the volume taken by an individual particle in the cloud:

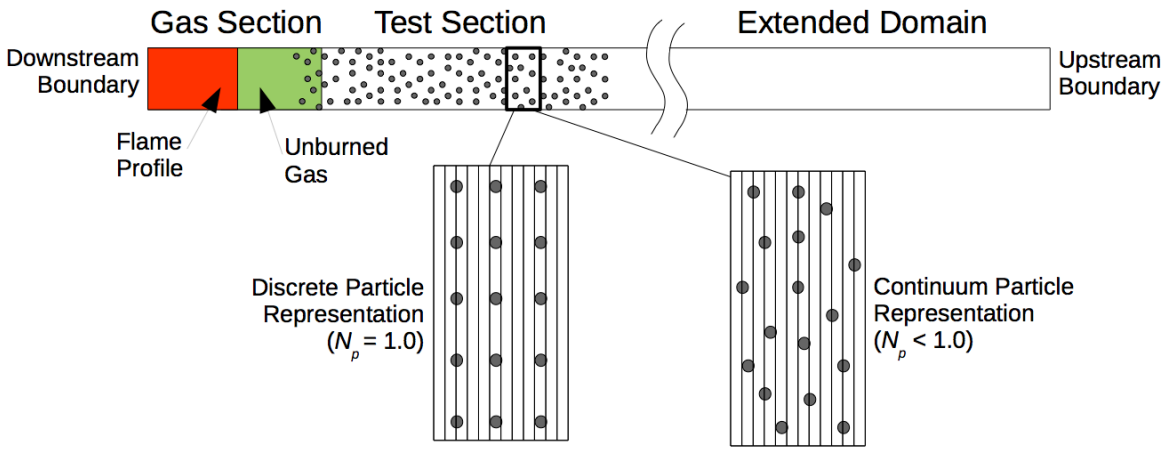

Figure 4.1: Schematic of one-dimensional computational domain showing mesh sections, boundaries, and initial flame location. The cell width in the off-axis directions is the same as the particle separation distance. Insets demonstrate discrete and continuum particle representation and cell discretization.

$$L_s^3 = \frac{\frac{\pi d_\mathrm{p}^3}{6}\rho_\mathrm{p}}{\sigma_\mathrm{p}} \tag{4.1}$$

where L_s is the centre-to-centre particle separation distance assuming an evenly spaced cubic array and σ_p is the dust concentration. Taking the cube root of both sides of Equation 4.1 gives the following for the separation distance:

$$L_s = d_\mathrm{p}\left(\frac{\pi\rho_\mathrm{p}}{6\sigma_\mathrm{p}}\right)^{1/3} \tag{4.2}$$

This relation can also be arranged to give the normalized length-to-diameter ratio (L_s/d_p) in the particle cloud. This parameter is used to explore the impact of discrete particle combustion in hybrid flames in Section 7.4 of this work.

4.1.1 Boundary Conditions

The upstream and downstream boundary conditions are given in Table 4.1, and are set so the flame propagates upstream into a quiescent gas and particle mixture. The burned gas and particles are ejected from the downstream boundary due to expansion behind the flame front.

Table 4.1: Boundary conditions for one-dimensional flame simulation.

Variable	**Upstream Boundary**	**Downstream Boundary**	**Value**
Pressure	zeroGradient	fixedValue	101,325 Pa
Temperature	fixedValue	zeroGradient	300 K
Velocity	fixedValue	zeroGradient	0.0 m/s
Mass Fractions	fixedValue	zeroGradient	Calculated

4.2 Multiphase Discretization

In this work, the coal particles are discretized using a Lagrangian approach to facilitate future investigation at a laboratory scale with a particle size distribution. Although size distributions can be included in an Eulerian discretization using multiple sets of continuum equations, or using various closure methods such as the quadrature method of moments and direct quadrature method of moments [153], the review of Christ [151] suggests that Lagrangian models are more typically used for coal combustion applications including burners and furnaces.

The Lagrangian approach used in this investigation falls under the Discrete Particle Model (DPM) classification of van der Hoef et al. [154]. Since interaction between the particle surface and gas phase is approximated using momentum, energy, and mass transfer correlations, the model falls under the unresolved classification of their work. In the current model, particle-particle interaction (e.g., collision and agglomeration)is neglected as the mean particle spacing is generally greater than 10 diameters.

4.2.1 Gas Phase Exchange

Interaction between the gas and particle phases is modeled using a particle-source-in-cell method [151, 155], where the particles act as point sources and sinks within the cell in which their centre resides. As called for by van der Hoef et al. [154], the computational grid is several orders larger than the particles by volume, with the volume fraction remaining below 0.001. However, due to the rectangular control volumes, the cell size in the flame propagation direction may be on the same order as the particle diameter. With this approach, the volume of the particle within the cell and boundary layer interaction are not captured in a natural way. This could be approximated using porosity terms in the gas-phase equations [154] or using sub-grid

models. The uncertainty in using these approaches for one-dimensional, multiphase flame propagation is high and therefore they are not included here.

4.2.2 Discrete and Continuum Particle Representations

The insets in Figure 4.1 show a schematic of the discrete and continuum particle representations used in this work. In the discrete representation, $N_{\mathrm{p}} = 1.0$ and a single group represents one particle, which is consistent with the DPM approach. In this case, there are several cells containing only air between the particles. For the infinitely tall tube, this is equivalent to an infinitely tall flame passing through a three-dimensional cubic array of evenly spaced particles, as represented in the Figure 4.1 inset.

In the continuum representation, $N_{\mathrm{p}} < 1.0$ and each group is only a fraction of the mass of a single particle. This is similar to particle-in-cell models (PIC), fluid-implicit particle models (FLIP), material point methods (MPM), and smoothed particle hydrodynamics (SPH), except information does not propagate from one particle to the next, and smoothing or remapping of particle solution variables is not included.

The continuum particle representation models an infinitely tall flame passing through a cloud of particles that are not necessarily evenly spaced in the off-propagation directions. This is shown schematically in the second inset in Figure 4.1. Since the flame is infinitely tall, the one-dimensional discretization averages the particle effects in the off-propagation directions. For example, if the flame is made tall enough, each one-dimensional cell would contain at least one particle. These would then be averaged to a fraction of a particle when collapsing the system to one-dimension. This is the same conceptually as an Eulerian discretization of the particle phase as a continuum.

4.2.3 Comparison of the Two Representations

The continuum and discrete particle representations demonstrate two extremes for approximating flame propagation through a particle cloud. The continuum representation used here and the Eulerian discretization used previously in the literature, represent a theoretical maximum propagation velocity, where mass and heat diffusion in the space between the particles has the smallest impact on the burning velocity.

The discrete Lagrange approach represents a theoretical minimum velocity, where the effects of heat and mass transfer in the space between the particles have the largest possible effect.

The actual propagation velocity in a physical particle cloud likely lies between these two extremes. The case where the two approaches give similar burning velocities suggests that mass and heat transfer between the particles is truly negligible. Characterizing the limits of applicability of the continuum assumption is an important contribution for understanding dust and hybrid flames, as previous simulations used assumptions taken from droplet combustion that have not been proven to be applicable to solid particles.

4.3 Numerical Solution

The gas-phase conservation equations are solved using a segregated approach where each equation is discretized over all cells with the finite volume method [47]. The convective terms are discretized using a bounded Gaussian upwind interpolation scheme, the diffusion terms are discretized using Gaussian linear interpolation, and the time-derivative terms are discretized with an implicit first-order scheme (see [156, 157] for a discussion of discretization approaches). Solutions to the resulting symmetric matrices are calculated using a preconditioned conjugate gradient method with incomplete lower-upper factorization. Lastly, solutions to the resulting asymmetric matrices are calculated using a preconditioned bi-conjugate gradient method with diagonal incomplete-Cholesky decomposition. See [63] for more information on the linear solver algorithms and options available in OpenFOAM.

4.3.1 Pressure-Velocity Coupling

Pressure-velocity coupling is achieved using the PISO (Pressure Implicit with Split Operator) algorithm [158]. A transport equation for pressure is derived from the continuity and momentum equations [159]. This equation is solved iteratively along with a velocity correction. The benefit of the PISO algorithm over the SIMPLE (Semi-Implicit Method for Pressure Linked Equations; see Patanker [156]) algorithm is that the momentum equation only has to be solved once and under-relaxation is not required, ensuring a time-accurate solution.

The main drawback of the PISO algorithm is that it requires a low CFL (Courant-Friedrichs-Lewy) number [151]:

$$\mathrm{CFL} = \frac{u\Delta t}{\Delta x} \leq 0.1 \tag{4.3}$$

where Δt is the simulation timestep and Δx is the cell size. A cell size of 50 µm is used for the dust and hybrid flames in this work, along with a constant 5-µs timestep. Since the velocity is typically less than 1 m/s, except in the burnt products behind the flame, stability is achieved.

4.3.2 Lagrange Solution

The Lagrange solution method includes a fractional timestep approach as described by Macpherson et al. [160]. At each timestep, the numerical scheme loops through all Lagrange particles, updates their properties, calculates new velocities, positions, temperatures, and densities, and calculates the gas-phase source terms. If the particle residence time in a cell is smaller than the overall timestep, all variables are updated using the state in that cell. However, if the particle will transfer to an adjacent cell, it takes a fractional timestep to the cell face, and then a second timestep within the adjacent cell. This process occurs repeatedly until the overall outer timestep is complete.

The Lagrange momentum and energy exchange equations solved in their integrated form based on the fractional timestep. A semi-implicit Euler formulation is used to solve for velocity and an explicit exponential Euler scheme is used to solve for temperature. The particle density is updated explicitly based on the fractional timestep and the devolatilization and surface reaction models.

4.3.3 Gas-Phase Chemistry

Gas-phase combustion reactions are solved by treating each computational cell as a "perfectly stirred reactor." A set of ordinary differential equations are constructed from the species and energy solution vectors, along with the details of the chemistry reaction model. A robust solver is required to integrate this stiff system of equations, and the Seulex algorithm [161] is used in this work.

4.3.4 Equation Coupling

Coupling between the gas phase, Lagrange particles, and chemistry solutions is also completed using a segregated approach. At the start of a timestep, the Lagrange position, velocity, temperature, and density are updated along with the respective gas-phase source terms. The fluid velocity is calculated based on the momentum transport equation, followed by the calculation of the combustion reaction source terms. The species mass fraction and energy transport equations are then solved with the updated source terms and velocity. Lastly, the pressure equation and velocity corrections are solved using three PISO iteration loops.

Preliminary simulations were completed to determine the effect of more tightly coupling the governing chemistry and fluid flow equations. Both moving the chemistry calculation, species mass fraction, and energy equation solutions inside the PISO iteration loop and using a combined SIMPLE/PISO algorithm with and without under-relaxation, showed only a 2–3 % change in predicted burning velocity using the MP1 and DRM19 reaction models. This tighter coupling is not justified, as it may double or triple the overall simulation time due to the chemistry and species transfer being a large portion of the overall computational effort.

4.4 Simulation Approach

A multistep modeling procedure is used for the CFD simulations. The gas flame profile used to initialize each simulation is calculated using the Cantera Package [128] with one of the four gas reaction mechanisms (Table 3.1). This allows the initial variable profiles to be determined faster than if they are calculated using OpenFOAM.

Scripts written in the Python language are used to run the Cantera simulation, create the CFD mesh, map the Cantera solution, and place the particles in their initial positions. This process is automated such that parametric analysis can be completed with different particle concentrations and initial conditions.

4.4.1 Example Dust Flame Simulation

Results from a coal flame simulation are shown in Figure 4.2. The gas and particle temperature are shown for 4 µm particles at a concentration of 144.3 g/m^3. Note that

the continuum particle representation was used in the simulation such that a steady flame profile and propagation velocity was achieved.

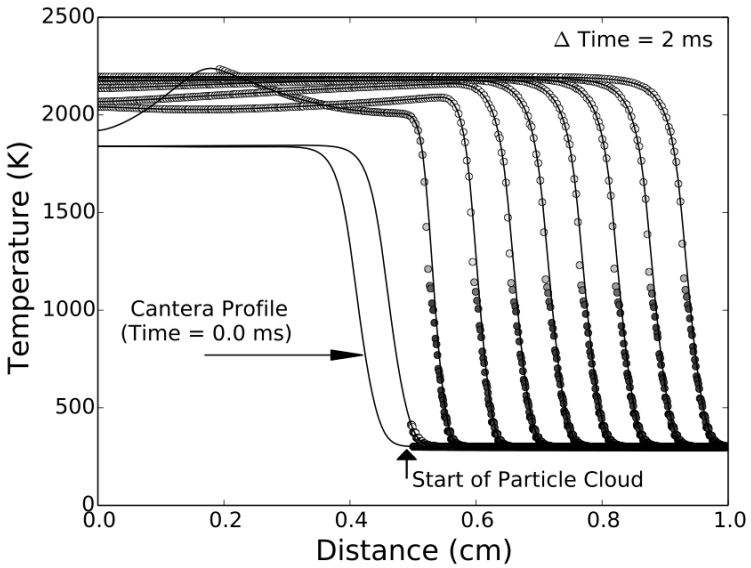

Figure 4.2: Example transient temperature profile for 4 µm coal particles at 144.3 g/m^3 concentration using the MP1 reaction mechanism and continuum particle representation. Nomenclature: lines – gas temperature; symbols – particle temperature; symbol shading – filled: 100 % volatiles and open: 0 % volatiles.

In Figure 4.2, the Cantera profile and start of the particle cloud are indicated by arrows. The flame travels from left to right, which is the same for each plot shown in this work. The time between each profile is 2 ms and the transient period as the flame enters the particle cloud is approximately 15 ms. After this time, the flame structure and velocity are constant as the flame moves through the particle cloud.

Particle devolatilization is also illustrated in Figure 4.2. The particle groups are shaded based on their volatile content, where fully black means that all of the volatiles are present, and clear means that all of the volatiles have been released. Based on Figure 4.2, the volatiles begin to be released at a particle temperature around 1100 K.

4.5 Solver Modifications

Modifications to the coalChemistryFoam solver included additional diagnostics for thermophysical parameters and routines to track the flame position and velocity during the simulation. The rest of the diagnostics were completed by post-processing the

CFD results after the simulation.

Two changes were made to the core solving routines in the CFD model. The first was to the routine that tracks particle motion through the computational domain. The original routine passes Lagrange groups through cell faces and is designed for complex, three-dimensional, unstructured meshes [160]. In the simulations completed in this work, errors were found in the trackToFace routine in particleTemplates.C, and particle tracking did not always work correctly. It was determined that this routine is not suitable for micrometric cell resolution when the cells have an aspect ratio different than unity and contain small particles. This routine was replaced with a simple approach that tracked the particle group to the cell face in one-dimensional space.

The second change to the solver was to the species mass diffusion treatment. The original coalChemistryFoam solver supplied in the OpenFOAM 3.0.1 distribution computed the gas phase diffusivity using a unity Schmidt number assumption:

$$\mathrm{Sc} = \frac{\mu}{\rho D} = 1 \tag{4.4}$$

$$D = \frac{\mu}{\rho} \tag{4.5}$$

Preliminary analysis demonstrated that replacing the unity Schmidt number assumption with the unity Lewis number assumption (see unity Lewis number approach in Section 3.1.4) improved burning velocity predictions for pure methane flames using the global MP1 and BFER2 reaction mechanisms. This change had minimal impact on burning velocity predictions using the DRM19 and GRI53 mechanisms.

Chapter 5

Methane Flames

Methane ignition delay and laminar flame simulations are used to verify the gas-phase governing equations and solution methods of the current model. Results from the simulation model are then used to measure the laminar flame thickness for methane gas at different equivalence ratios. The flame thickness is used to compute the flame reaction timescale which is proposed to govern interaction between the dust and gas in hybrid flames where the gas is above its LFL. This chapter concludes with a discussion of the implications of the flame reaction timescale on hybrid mixture burning velocity, and a discussion the overall accuracy of the CFD model.

5.1 Model Verification

Verification of the computational model is completed by comparing ignition delay, thermophysical parameters, transport parameters, flame structure, and burning velocity to results from the Cantera package [128] and experimental data. Gas-phase reaction kinetics and associated solution routines are verified by simulating ignition delay times in a constant-pressure, fixed-mass reactor (CPFMR). The model thermophysical and transport parameters as a function of temperature and species concentration are also compared to Cantera in the CPFMR.

Coupling of the gas-phase momentum, energy, and mass transport equations is verified by comparing the flame structure and burning velocity from the current model with the different Cantera approximations outlined in Table 3.3. Comparison between the multispecies approach, the current model, and the experimental data gives an evaluation of the effect of the modeling assumptions on burning velocity. Lastly, sensitivity of the predicted results to mesh resolution and domain length are explored.

In this thesis the fuel concentration is often specified in terms of equivalence ratio, Φ. This parameter is defined as the fuel-to-air ratio in the mixture on a mass basis, divided by the fuel-to-air ratio for a stoichiometric mixture. The relations between Φ,

mass concentration, and volume concentration change depending on whether the gas alone, dust alone, or hybrid mixtures are being analysed, and if only homogeneous reaction or homogeneous and heterogeneous reaction are being considered. For reference, Appendix A gives a derivation of the five equivalence ratios used in this work. In the current chapter, equivalence ratio is always that of the methane gas alone, Φ_g.

5.1.1 Ignition Delay

Simulating ignition delay in a CPFMR allows the solution routines for gas-phase chemistry to be explored in isolation from mass, momentum, and energy transport [162]. Since the reactor is homogeneous throughout, the transport equations are nullified and only terms with respect to energy release and species mass production or consumption from reactions are non-zero.

Cantera has a user-selected solution routine specifically for CPFMR simulation [128]. This condition is achieved in the OpenFOAM model by using a single-cell simulation where pressure is fixed at a constant value of 101,325 Pa. Energy and species mass are updated as the reaction occurs, and system temperature, density and thermophysical parameters are updated by coupling the governing equations.

Ignition delay of stoichiometric methane is compared between the current model and Cantera^{multi} in Figure 5.1. Simulations are presented at different initial temperatures, and results from the four reaction mechanisms outlined in Table 3.1 are given. Ignition delay is defined as the time for the reactor temperature to increase 500 K above the initial temperature.

The four reaction mechanisms predict different ignition delay times based on the initial system temperature. This is expected as the reaction kinetics in simpler mechanisms are typically correlated to achieve experimental burning velocity or flame structure observations. For example, the global reaction mechanisms do not have the same thermophysical parameters, transport parameters, and radical species formation through a burning flame, which necessitates modifying the reaction rates. In the case of the MP1 and BFER2 mechanisms, the chemistry rates must be increased to overcome slower diffusion processes in the flame. The ignition delay predicted using the current model agrees with the Cantera results, thus verifying implementation of the four reaction mechanisms and chemistry solution routines.

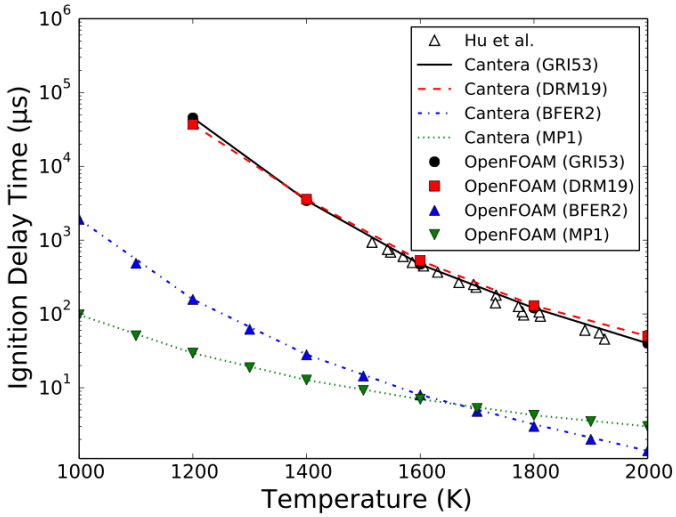

Figure 5.1: Comparison of ignition delay times in a CPFMR using the current model and Cantera$^{\text{multi}}$ with four reaction mechanisms. The equivalence ratio is 1.0 and the experimental data is from Hu et al. [163]

Temperature distribution for a specific CPFMR simulation at an initial temperature of 1600 K is given in Figure 5.2. As the simulation progresses, the mixture slowly heats due to a small degree of methane reaction. At approximately 500 µs, a run-away reaction occurs and the mixture rapidly ignites. The long-tail to reach the adiabatic reactor temperature is typical of multispecies reaction mechanisms [130] and is due to later stage reactions including CO_2 formation.

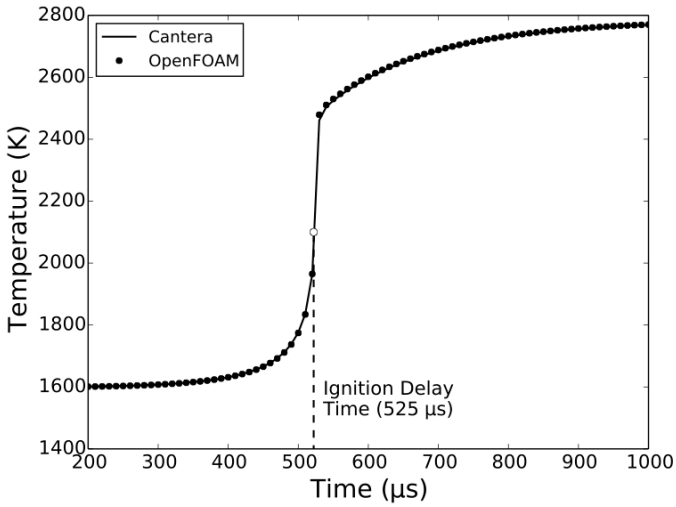

Figure 5.2: Temperature as a function of time in a CPFMR using the DRM19 reaction mechanism with stoichiometric methane initially at 1600 K.

The predicted temperature distribution from the current model agrees with Cantera, having a maximum difference of 17 K directly after ignition. This increased temperature is related to differences in the overall solution routines and is reduced to fractions of a Kelvin as the adiabatic temperature is reached.

Figure 5.3 gives the temporal mass fraction distribution of several gas species in the same CPFMR simulation. CH_4 is slowly consumed leading up to the ignition time, with an associated increase in H_2O. Ignition is indicated by a rapid depletion of CH_4 and O_2 and creation of CO_2. This is followed by a slow reaction of the later time intermediate species to reach a steady temperature after ignition.

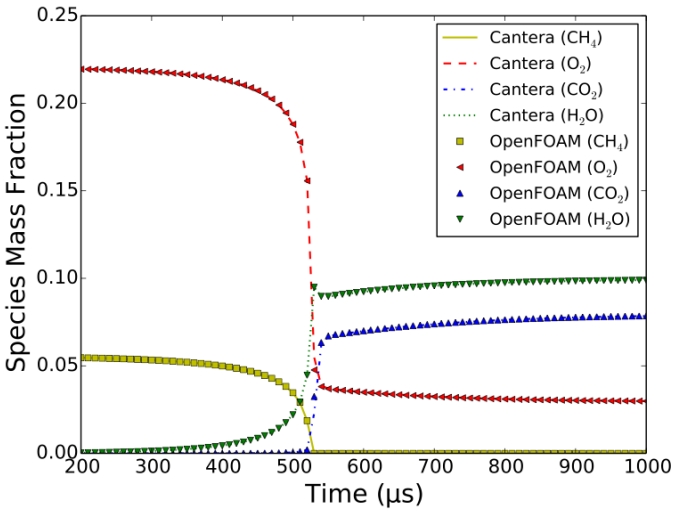

Figure 5.3: Species mass fraction as a function of time in a CPFMR using the DRM19 reaction mechanism with stoichiometric methane initially at 1600 K.

Temporal species distribution in the CPFMR simulation agrees very well between the two models in Figure 5.3, verifying the reaction mechanism and solution routines. Since both temperature and species profiles are in agreement in the current model and Cantera, this gives a good platform to compare the thermophysical and transport properties predicted. This comparison is given in the following two sections.

5.1.2 Thermophysical Parameters

Results from the CPFMR simulation are used to verify gas density and specific heat in the current model. Gas density is a transported quantity based on the mass conservation equation and is linked to pressure and temperature through the ideal gas

law. Specific heat is calculated using fitted polynomial functions to JANNAF table data. The polynomial parameters are based on input from Cantera [128] but needed to be converted to metric units for the current model input. This was completed using the chemkinToOpenfoam utility provided with the OpenFOAM 3.0.1 distribution. Since these are large tables (six parameters multiplied by 53 species), it is good practice to verify that the conversion was done correctly.

Gas density and specific heat during the CPFMR simulation are given in Figure 5.4. As the reactor ignites, the gas expands and density is reduced through ignition. The density predicted from the current model agrees with Cantera within 1 % throughout the simulation, verifying that the pressure-temperature-density relation is maintained correctly.

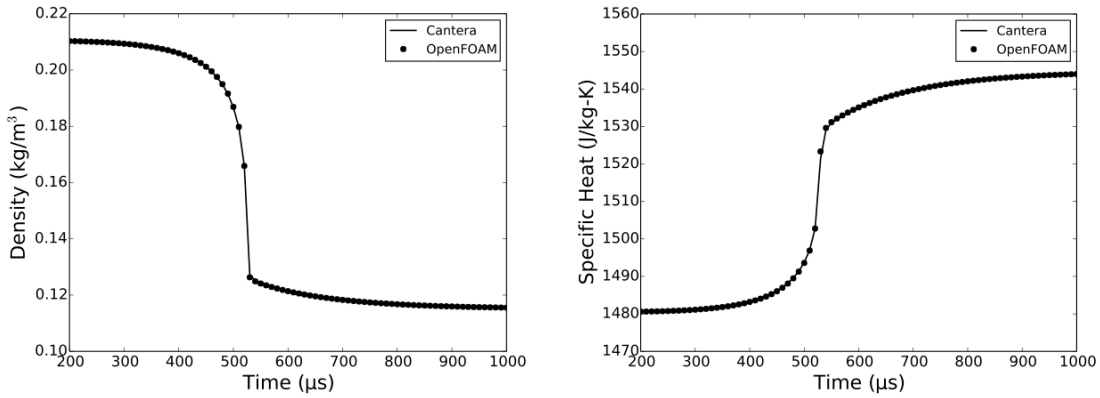

(a) Density (b) Specific Heat

Figure 5.4: Gas density and specific heat as a function of time in a CPFMR using the DRM19 reaction mechanism with stoichiometric methane initially at 1600 K.

Specific heat at constant pressure (C_p) output from the simulation model is also compared to Cantera in Figure 5.4. The specific heat ranges from 1480 J/kg-K for stoichiometric methane at 1600 K, to 1545 J/kg-K in the reaction products at the adiabatic reactor temperature. Agreement between the two models demonstrates that conversion of the JANNAF polynomial fits to metric units was completed correctly.

5.1.3 Transport Parameters

Since global approximations are used in the current model to describe gas viscosity, thermal conductivity, and mass diffusivity, it is instructive to compare the results

predicted from each equation to Cantera$^{\text{multi}}$. This comparison demonstrates the typical agreement that can be expected between the global and multispecies approach and highlights some of the limitations with respect to the current model.

Gas viscosity, thermal conductivity, and mass diffusivity during the CPFMR simulation are given in Figure 5.5. Single values at each computational cell are reported for viscosity and thermal conductivity. Mass diffusivity is reported for the most abundant (major) species and less abundant (minor) species. The mass diffusivity output for Cantera$^{\text{unity}}$ is also given in Figure 5.5 for reference.

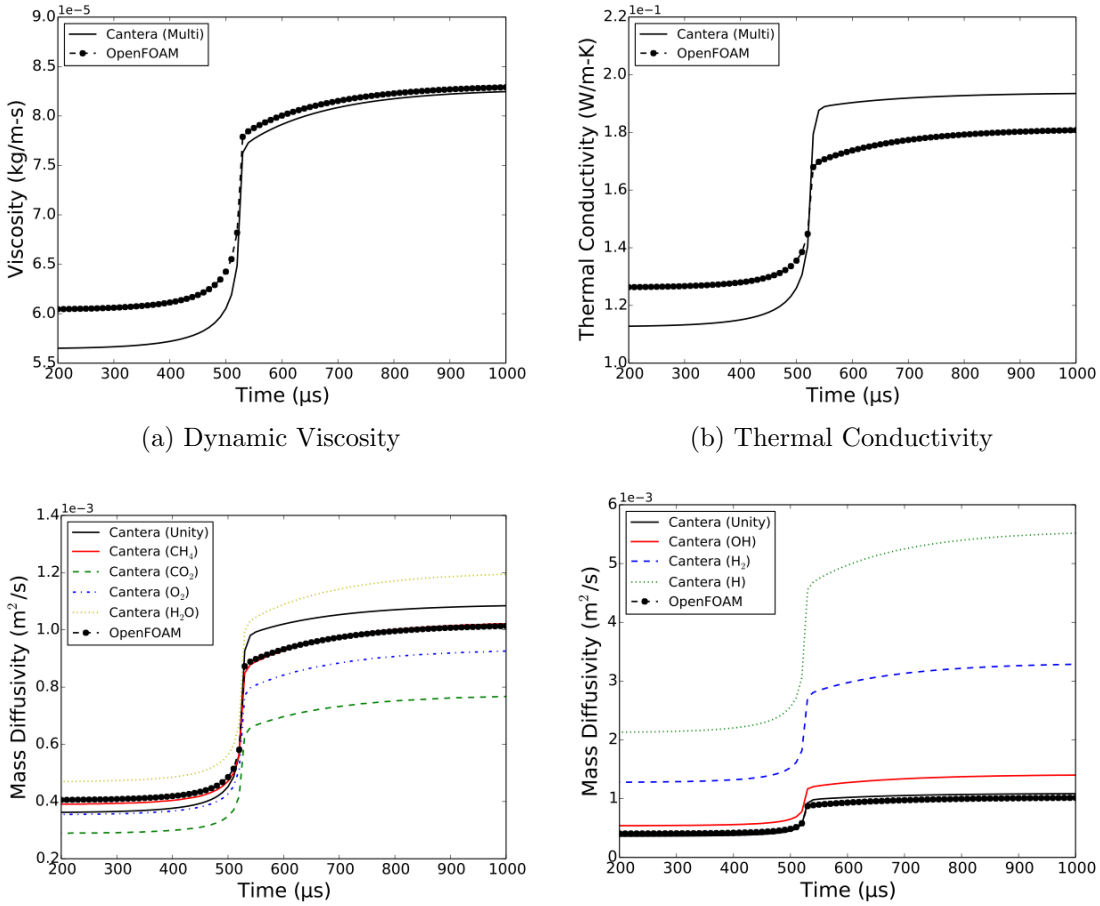

(a) Dynamic Viscosity

(b) Thermal Conductivity

(c) Major Species Diffusivity

(d) Minor Species Diffusivity

Figure 5.5: Gas viscosity, thermal conductivity, and species mass diffusivity as a function of time in a CPFMR using the DRM19 reaction mechanism with stoichiometric methane initially at 1600 K.

The global gas viscosity model is described by Sutherland's law (Equation 3.14). The global model overpredicts viscosity throughout the ignition simulation compared

to the multispecies model. The maximum difference between the two models is 6 % and occurs at 1600 K for stoichiometric methane. This difference may be acceptable in many cases as the multispecies model takes $\mathcal{O}(N_k^2)$ times longer to compute than the global model.

The global thermal conductivity is described as a function of viscosity using the Eucken model (Equation 3.18). Thermal conductivity calculated using this global approach has a more narrow range than the multispecies model. The maximum difference is 11 % and again occurs at 1600 K for stoichiometric methane. Thermal conductivity is underpredicted by approximately 7 % in the reaction products. This is due to the individual thermal conductivities of the product component species not being captured in the model.

The global mass diffusivity is described using a unity Lewis number assumption (Equation 3.31). Both the diffusivity calculated using the current model and Cantera$^{\text{unity}}$ are given in the bottom two plots of Figure 5.5. Cantera$^{\text{unity}}$ also employes a unity Lewis number assumption but uses λ^{multi} in the calculation.

The mass diffusivity comparison given in Figure 5.5 illustrates the spread of component diffusivities using the multispecies approach. For the major species, global diffusivities in the current model lie between the component values. The lowest diffusivity shown in the bottom-left of Figure 5.5 is that of H_2O, which is overpredicted by 40 % using the unity Lewis number assumption. Agreement between the current model and Cantera$^{\text{unity}}$ is within 11 %, with the difference being caused by thermal conductivity.

The final plot given in the bottom-right of Figure 5.5 compares mass diffusivity from the current model to the multispecies diffusivities of OH, H_2O, and H. This comparison highlights the main limitation of the unity Lewis number approach, in that preferential diffusion of the highly diffusive species (such as H radicals) cannot be captured. The trade-off for this assumption is that the transport parameters can be calculated with $\mathcal{O}(1)$ operations per computational cell, whereas determining multispecies transport requires constructing and inverting an $N_k \times N_k$ matrix and solving a $3N_k \times 3N_k$ system of algebraic equations [64].

5.1.4 Flame Structure

The impact of the global modeling approximations can be explored by looking at flame structure predictions from the different computational models. Flame temperature and major species profiles for a methane flame with an equivalence ratio of 0.8 are given in Figure 5.6. The flame is travelling from left to right in Figure 5.6, and the burning velocities are 29.7, 25.3, and 26.3 cm/s for Cantera$^{\text{multi}}$, Cantera$^{\text{unity}}$, and the current model, respectively. The flame position for each model has been shifted such that the temperature profile is equal to 1200 K at 0.0 mm.

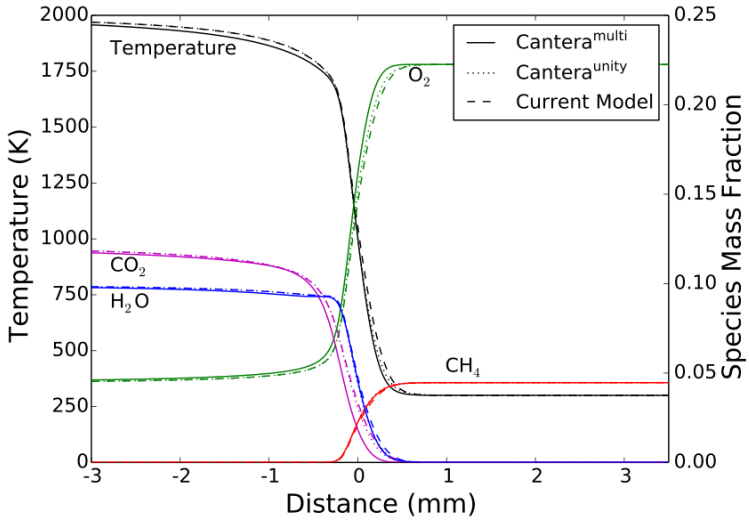

Figure 5.6: Methane flame structure with different computational models using the DRM19 reaction mechanism ($\Phi_g = 0.8$).

The flame structures of the three models are qualitatively similar with the largest quantitative differences occurring in the temperature, O_2, and CO_2 profiles. The temperature profile extends the furthest into the preheating section in front of the flame using the current model. This is due to the overprediction of thermal conductivity in the reactants as shown in Figure 5.5. This is the main reason that the current model predicts a higher burning velocity for the flame than Cantera$^{\text{unity}}$. The differences in the O_2 profile are also due to the different temperature structure.

Temperature in the preheat zone for Cantera$^{\text{multi}}$ lags behind the other two models in Figure 5.6. The CO_2 mass fraction profile is also less diffuse due to this specie having a low diffusivity compared to the mixture (see Figure 5.5). To demonstrate why Cantera$^{\text{multi}}$ has a larger burning velocity than the other models, the effect of

mass diffusivity on the minor species and chemical radicals must be explored. Species profiles for OH, H_2, and H for the same simulations as Figure 5.6 are given in Figure 5.7. In Figure 5.7, the CH_4 profile is given to illustrate the flame front location and the ordinate is given in log-scale.

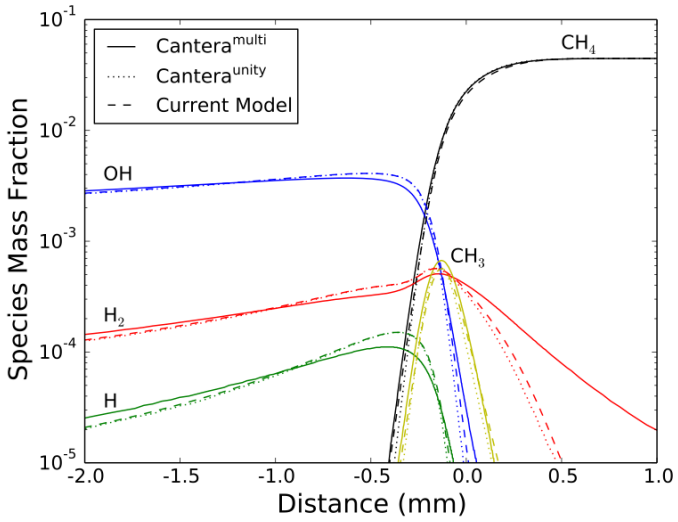

Figure 5.7: Distribution of minor species in a methane flame with different computational models using the DRM19 reaction mechanism ($\Phi_g = 0.8$).

Both H_2 and H show pronounced diffusion using Cantera^{multi} in Figure 5.7. H_2 diffuses far upstream into the flame front, which helps establish the radical pool. The diffusion of the H radical is illustrated by the reduced peak value. This radical is rapidly consumed as it diffuses forward into the flame front. Diffusion of these intermediate chemical species forward into the flame is what enhances the burning velocity when multispecies diffusion is accounted for.

The minor species distributions between the current model and Cantera^{unity} are qualitatively similar with small variations in the preheat and reaction zones due to differences in temperature. These results further verify the coupling of the transport and chemistry equations in the current model and the overall solution method.

5.1.5 Burning Velocity

The goal of the computational model is to explore burning velocity and flammability limits of hybrid mixtures. By comparing laminar flame simulation from the different models outlined in Table 3.3, the impact of the global approximations in the current

model on methane burning velocity can be explored. Burning velocity predictions from these models with the four reaction mechanisms are investigated in this section.

Figure 5.8 presents burning velocity predictions from Cantera$^{\text{multi}}$ compared to experimental data. The results are plotted as a function of equivalence ratio with values between $\Phi_g = 0.6$ and 1.4.

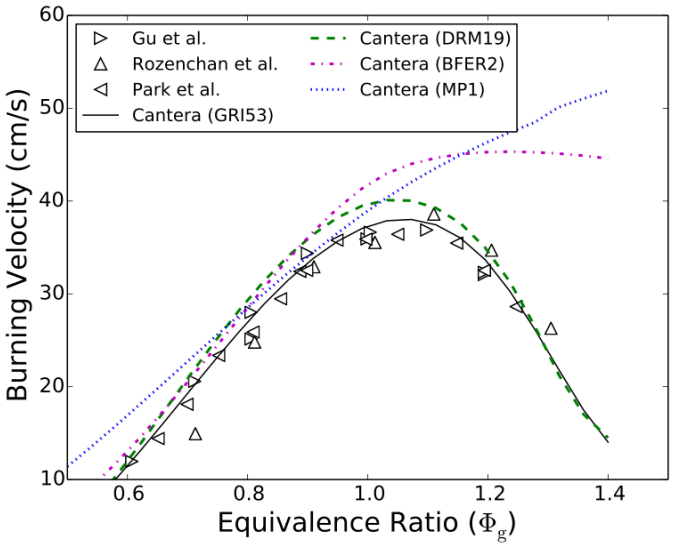

Figure 5.8: Methane burning velocity using Cantera$^{\text{multi}}$ with different reaction mechanisms compared to experimental data from Gu et al. [164], Rozenchan et al. [165], and Park et al. [166].

The burning velocity predicted with GRI53 compares well with the experimental data throughout the entire concentration range explored. DRM19 tends to overpredict the burning velocity throughout the majority of the concentration range with a maximum difference around 5 % near the stoichiometric concentration. The qualitative burning velocity profile between these two models is similar, with DRM19 demonstrating a small shift in the peak burning velocity from approximately $\Phi_g = 1.07$ to 1.03.

The global two-step and single-step reaction mechanisms are only able to capture a portion of the burning velocity curve. BFER2 compares well with the experimental data and more detailed mechanisms up to $\Phi_g = 0.9$, at which point it overpredicts the burning velocity. MP1 agrees with the experimental data between $\Phi_g = 0.75$ and 0.95 and also overpredicts the burning velocity elsewhere. Both models predict an increasing burning velocity with an equivalence ratio at low concentrations but are

unable to capture qualitative features such as a maximum burning velocity near the stoichiometric concentration and reduced burning velocity for fuel-rich concentrations. Overall, both the GRI53 and DRM19 mechanisms appear suitable for predicting the burning velocity of methane gas throughout the flammable concentration range, whereas the BFER2 and MP1 mechanisms may only give qualitative agreement under fuel-lean concentrations.

To explore the impact of the various transport modeling approaches on flame propagation, the burning velocity is presented for each approach in Figure 5.9. The top plot compares Cantera$^{\text{multi}}$ to Cantera$^{\text{mix}}$, the middle plot compares Cantera$^{\text{multi}}$ to Cantera$^{\text{unity}}$ and the bottom plot compares Cantera$^{\text{unity}}$ to the current model. Results are presented for each of the four reaction mechanisms in Figure 5.9.

The differences between Cantera$^{\text{multi}}$ and Cantera$^{\text{mix}}$ are the thermal conductivity and diffusivity modeling approaches. The mixture-averaged transport properties show a small reduction in burning velocity for the GRI53 and DRM19 mechanisms, but overall the predicted results are similar to the multispecies simulations. This demonstrates that the mixture-averaged modeling approach has a small impact when these mechanisms are used. The impact of the mixture-averaged transport properties is larger for BFER2 and MP1, especially at fuel-rich concentrations. Since intermediate chemistry and species production/consumption are not captured with these mechanisms, the transport processes have a larger impact on the burning velocity.

The difference between Cantera$^{\text{mix}}$ and Cantera$^{\text{unity}}$ is isolated to the species diffusivity alone. The comparison given in Figure 5.9 (b) illustrates that the diffusivity model has a negligible impact on burning velocity for the BFER2 and MP1 mechanisms. For these mechanisms, there are not enough species involved for preferential diffusion to impact flame propagation. This further illustrates that the differences between Cantera$^{\text{multi}}$ and Cantera$^{\text{mix}}$ shown in Figure 5.9 (a) are due to the thermal conductivity assumption. These results demonstrate that thermal conductivity is an important parameter, especially when global chemistry mechanisms are employed in the simulation.

Although the unity Lewis number assumption plays a limited role in the BFER2 and MP1 mechanisms, it has a significant impact in the GRI53 and DRM19 mechanisms, especially at equivalence ratios above 0.8. Above this concentration, the

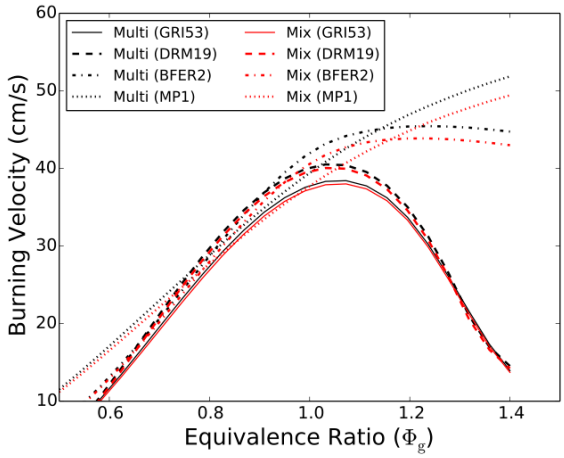

(a) Multi vs Mix

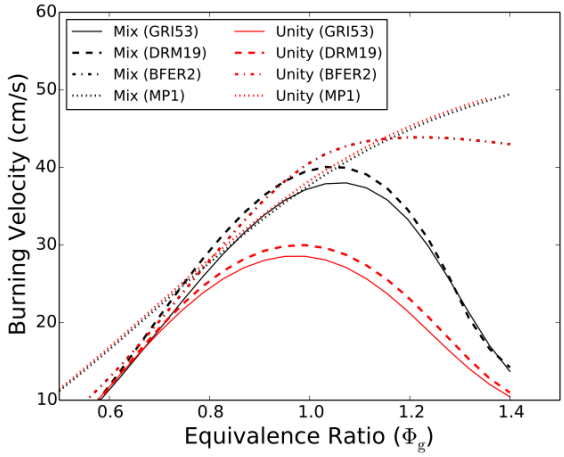

(b) Mix vs Unity

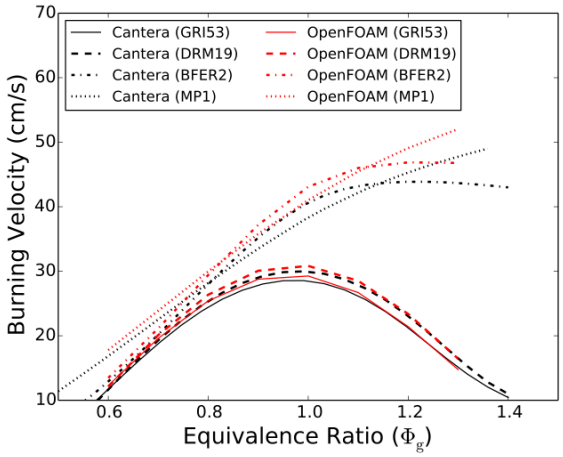

(c) Unity vs Current Model

Figure 5.9: Comparison of methane burning velocity using Cantera$^{\text{multi}}$, Cantera$^{\text{mix}}$, Cantera$^{\text{unity}}$, and the current simulation model.

burning velocity is reduced by more than 25 %. The concentration at which the maximum burning velocity occurs also shifts from slightly rich to slightly lean. These two effects are caused by a lack of diffusion of the intermediate chemical species into the flame front as illustrated in Figure 5.7.

The results presented in Figure 5.8 and Figure 5.9 (a, b) demonstrate an important conclusion for simulating gas flames. If global single-step or two-step chemistry mechanisms are used, a detailed treatment of the transport properties is generally not warranted as it does not greatly improve burning velocity predictions compared to experimental data. However, if complex chemistry mechanisms are used, then at least mixture-averaged transport properties are needed to quantitatively predict the burning velocity. This is difficult because many-step chemistry mechanisms increase the time required to complete the simulation by 10–100 times that of the global mechanisms. With the added cost of determining component thermal conductivities and binary diffusion coefficients for the individual species, the quantitatively accurate simulations may take more than 1000 times longer than the approximate solutions achieved with global models. With the computational resources that are generally available, it does not appear that simulations using detailed chemistry and multispecies or mixture-averaged transport properties will be possible for a parametric analysis of dust and hybrid flame propagation at the current time. This is even more critical in future studies as the model is extended to industrial scenarios and geometries.

Burning velocity from the current simulation model is compared to Cantera$^{\text{unity}}$ in Figure 5.9 (c). The main differences between these simulations are the global treatment of dynamic viscosity and thermal conductivity, and the different solution methods between the two models. The current model predicts burning velocities that are higher than Cantera$^{\text{unity}}$. This is largely due to increased thermal diffusion in the flame front due to higher predicted thermal conductivity. Dynamic viscosity has a lesser impact on the flame structure and burning velocity for planar, laminar flames.

Overall agreement between the current model and Cantera$^{\text{unity}}$ is achieved using the GRI53 and DRM19 mechanisms with burning velocities that are within 5 %. The BFER2 and MP1 mechanisms show larger differences due to the increased impact of thermal diffusion using these mechanisms, but the overall burning velocity profile is

similar. These results further verify the coupling of the governing equations and the overall solution for gas flames throughout the flammable gas concentration range in the current model.

The final methane burning velocity comparison is given in Figure 5.10 where the current model results are plotted with the experimental data. The burning velocity from Cantera^{multi} with the GRI53 mechanism is also given in Figure 5.10 for reference.

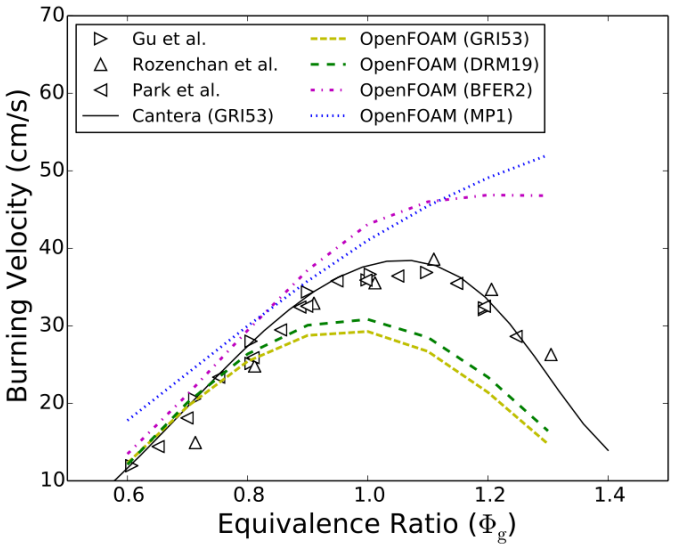

Figure 5.10: Methane burning velocity using the current model with different reaction mechanisms compared to experimental data from Gu et al. [164], Rozenchan et al. [165], and Park et al. [166].

Agreement between the current model and experimental data is similar to Cantera^{multi} up to an equivalence ratio of 0.8. At these fuel-lean concentrations, the GRI53, DRM19, and BFER2 mechanisms predict similar burning velocities, which are close to the experimental results. The MP1 mechanism tends to overpredict the burning velocity throughout the concentration range as seen using Cantera^{multi} in Figure 5.8.

The maximum burning velocity using the GRI53 and DRM19 mechanisms is lower than the experimental results and is shifted compared to the experimental data. The burning velocity decreases at fuel-rich concentrations, but is also lower than the experimental data. As shown previously, the majority of these differences are due to the unity Lewis number assumption. The burning velocity using the BFER2 and MP1 mechanisms is slightly higher than Cantera^{multi} but has the same qualitative features. This includes the inability to capture the maximum and to predict the

downturn in burning velocity at fuel-rich concentrations. A further discussion of the model accuracy is given in Section 5.4.2.

5.1.6 Flame Temperature

The methane flame temperature predicted from the current model is compared to the adiabatic flame temperature in Figure 5.11. The adiabatic temperature is calculated with a Cantera equilibrium routine specifically designed to determine concentration and temperature after combustion reactions. For the equilibrium calculation, the GRI53 mechanism is used with ambient initial temperature and pressure.

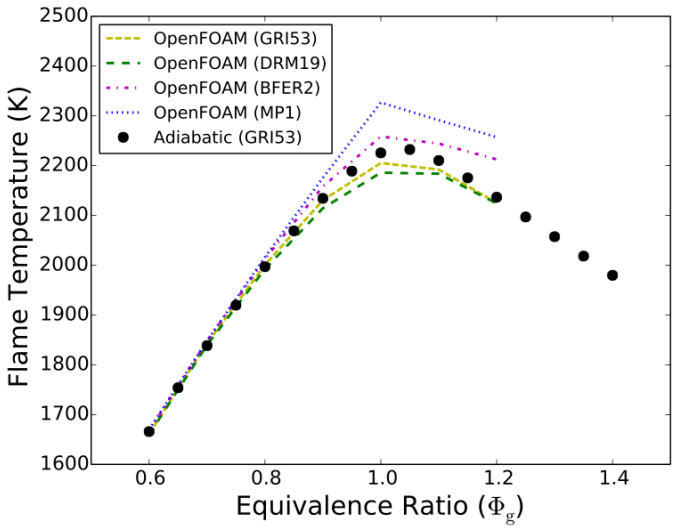

Figure 5.11: Methane flame temperature compared to adiabatic temperature calculated with Cantera using the GRI53 mechanism.

The predicted flame temperature between the four reaction models is similar below an equivalence ratio of 0.8 and agrees with the adiabatic flame calculation. At higher concentrations, BFER2 and MP1 overpredict flame temperature while GRI53 and DRM19 underpredict flame temperature. Agreement between the current model using the GRI53 mechanism and the adiabatic calculation is generally good with a maximum difference of 20 K near the maximum.

5.1.7 Effect of Modeling Parameters

To understand the impact of numerical resolution on methane burning velocity, results from simulations with different cell sizes are summarized in Figure 5.12. Figure 5.12

(a) shows the burning velocity from each simulation, while Figure 5.12 (b) shows burning velocity normalized by the value reported with the 5-µm resolution. Each line in Figure 5.12 gives the results for a different gas equivalence ratio and each symbol is an individual simulation.

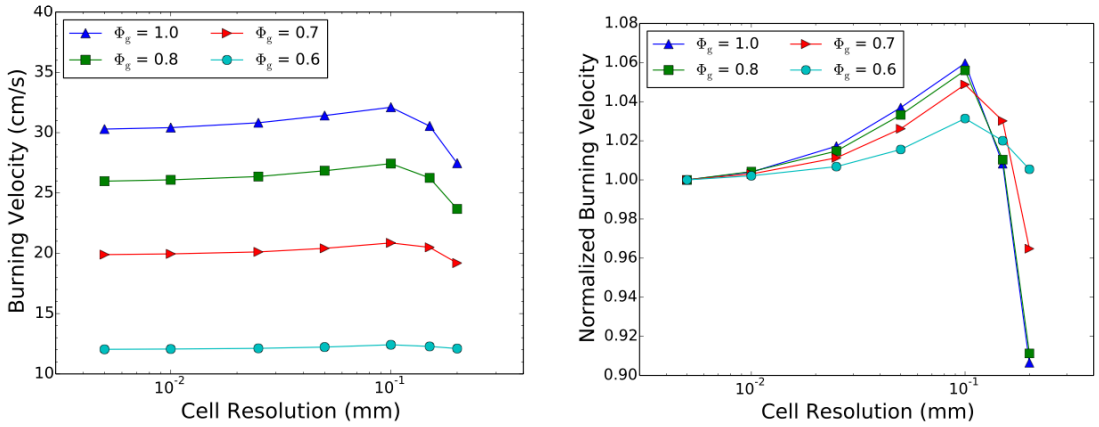

(a) Burning Velocity

(b) Normalized Burning Velocity

Figure 5.12: Methane burning velocity for varying cell resolutions and equivalence ratios. All simulations were performed using the DRM19 mechanism.

As discussed by Heravi et al. [167], the thickness of methane flames range from several millimetres at low equivalence ratios to approximately 0.2 to 0.5 mm near stoichiometric conditions. In Figure 5.12, the burning velocity results become divergent at cell resolutions above 100 µm because not enough cells are available to resolve the flame front. The results are convergent below 100 µm and are relatively grid independent below 25 µm. As a balance between accuracy and computational requirements, a cell resolution of 50 µm is used in the current thesis unless stated otherwise. A comparison with a 5 µm cell resolution shows an decrease in predicted methane burning velocity less than 4 %.

Another modeling parameter that may impact the simulation results is the length of the computational domain. If the domain is too short, fluctuations in the flame position over time are present due to pressure wave acoustics [168] from interaction with the simulation boundary. The computational domain is extended 20 m from the test section, which removes these fluctuations for the gas, dust, and hybrid flames studied. The cell size in the extended domain is increased gradually to reduce the overall computational requirement.

5.2 Flame Thickness

Gas flame thickness and burning velocity govern the time available for particle combustion to occur in hybrid mixtures and enhance the propagating gas flame in the gas-driven and dual-fuel regimes. If particle combustion is too slow, the burning velocity of the hybrid flame will be reduced by heat loss in the reaction front. If particle combustion occurs inside the reaction front, the burning velocity can be enhanced.

The gas flame simulations are analyzed to measure flame thickness in this section. The results are compared to those from the literature, and the impact of the four reaction mechanisms is explored. The flame thickness is used in Section 5.3 to determine the flame residence timescale that governs hybrid flame behaviour when compared with particle combustion.

5.2.1 Measurement Approach

The direct measurement approach described by Heravi et al. [167] is used to determine flame thickness from the current simulations. A schematic of this approach is given in Figure 5.13 where temperature, methane specie mass fraction, and heat release rate profiles are given for a methane flame with $\Phi_g = 0.8$. The lower horizontal dashed line indicates the ambient temperature of the unburned mixture, and the upper horizontal dashed line indicates the final flame temperature in the burned products. The vertical line indicates the location of the maximum heat release rate and tilted line indicates the maximum slope of the temperature profile.

The flame thickness (l_f) is determined by drawing a tangent line through the inflection point of the temperature-distance profile. In this approach, flame thickness is defined as the distance between the location where the tangent intersects the ambient temperature and where it intersects the final flame temperature. This is the horizontal distance between P1 and P2 in Figure 5.13.

The flame thickness is broken into two components: the preheat zone and the reaction zone. Following Heravi et al. [167], these zones are divided by the location of the maximum heat release rate. This is indicated by the vertical line starting at P3 in Figure 5.13. The preheat zone is defined as the distance between P1 and P3, and the reaction zone is the distance between P3 and P2.

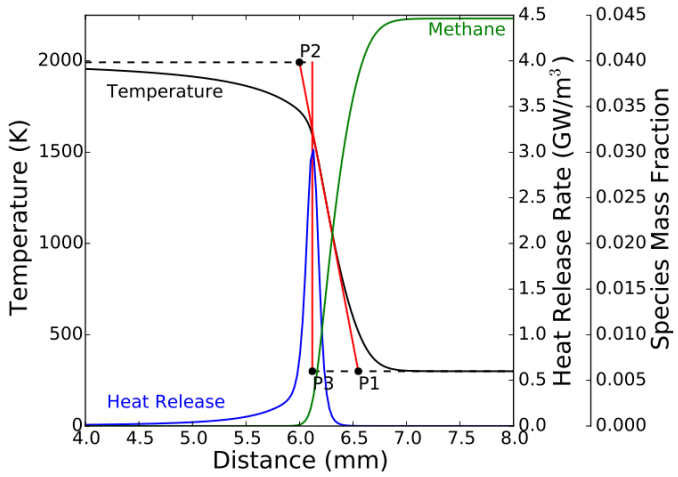

Figure 5.13: Example methane flame thickness calculation using the DRM19 reaction mechanism ($\Phi_g = 0.8$). The variables are labeled with text, and fit lines indicate the slope at the maximum $\mathrm{d}T/\mathrm{d}x$ (between P1 and P2) and the location of maximum heat release rate (P3).

5.2.2 Simulation Results

The thickness of a gas flame is challenging to measure experimentally due to the small dimensions relative to the thermocouples used and difficulties calibrating the thermocouples against losses (see findings of Kwon et al. [169] as described by Heravi et al. [167]). As such, measurements from experiments were historically larger than those reported from simulation results [167]. More recently, Lafay et al. [170] used a Rayleigh scattering technique for more precise measurements of methane flame thickness.

Example experimental and simulation measurements of methane flame thickness are given in Figure 5.14 for different equivalence ratios. The experimental results are shown as open symbols, while the simulation results are shown as closed symbols with lines connecting them.

Flame thickness starts off at a few millimeters near the LFL, decreases to a minimum value near the stoichiometric equivalence ratio, and increases again for fuel-rich mixtures. The experimental flame thickness of Andrews and Bradley [171] is 1.5–4.5 times that reported in the simulation results, while the measurements of Lafay et al. [170] are generally in agreement with the simulations. Both Gottgens et al. [172] and Heravi et al. [167] report flame thickness using the direct measurement approach

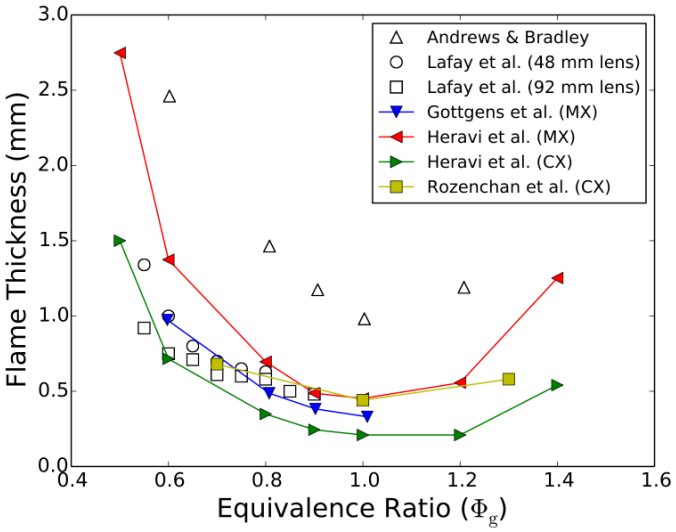

Figure 5.14: Methane flame thickness from experimental measurements and simulation models. Experimental results are from Andrews and Bradley [171] and Lafay et al. [170] with two different lens sizes. The simulation results are from Gottgens et al. [172], Heravi et al. [167], and Rozenchan et al. [165].

(MX) outlined in the previous section. Heravi et al. also report values using a calculated approach (CX) by combining simplified mass and heat transfer equations to obtain a closed form relation between flame thickness, burning velocity, and a presumed temperature profile. Rozenchan et al. [165] also appear to use a calculated approach based on the work of Sun et al. [173] and Law and Sung [174].

From the simulation models presented in Figure 5.14, flame thickness ranges from 1.5 to 2.75 mm near the LFL and from 0.2 to 0.45 mm at $\Phi_g = 1.0$. The measured and calculated flame thickness from Heravi et al. [167] bound the simulation results and are compared to flame thickness using the current model in Figure 5.15. Results from the current model are shown as symbols with lines connecting them, while the range found in the literature is illustrated by the solid lines with shading in between.

Flame thickness from the current model generally agrees with the range of simulation results reported in the literature and the experimental results of Lafay et al. [170]. The GRI53 and DRM19 mechanisms agree with the trends of Gottgens et al. [172] and Rozenchan et al. [165], while predicting a larger minimum flame thickness of 0.54 mm. Since the minimum is shifted to the fuel-lean side of stoichiometric, the larger thickness may be related to the unity Lewis number assumption.

The MP1 mechanism predicts a similar flame thickness as the detailed mechanisms

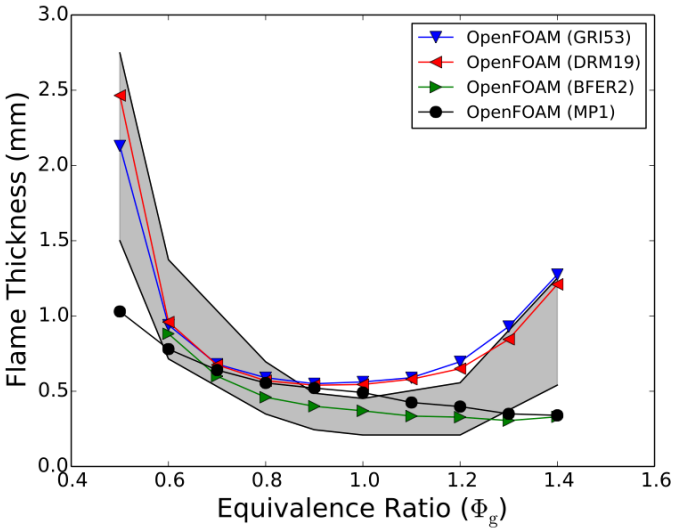

Figure 5.15: Methane flame thickness from the current model using the direct measurement approach, compared to the range predicted from Heravi et al. [167] using the direct measurement and calculated approaches (shaded region).

between equivalence ratios of 0.7 and 1.0, while predicting a small flame thickness near the LFL due to the higher burning velocity compared to the other models. Cantera simulation results could not be achieved for the BFER2 mechanism at $\Phi_g = 0.5$ and as such no profile could be used to initialize the simulation with the current model. Both MP1 and BFER2 are unable to predict the increase in flame thickness for fuel-rich methane gas mixtures.

5.3 Flame Reaction Timescale

The flame reaction timescale represents the residence time for a fluid element passing through the flame. Similarly, this timescale can be used to approximate the time a particle passing through the flame has to react and contribute to enhancing the burning velocity. As such, the flame reaction timescale is also referred to in this work as the flame residence time. This value is calculated from the simulations using the different reaction mechanisms in the following sections.

5.3.1 Calculation Approach

The residence time (τ_f) is characterized by the flame thickness and laminar burning velocity (S_L). If a stationary fluid element or particle is placed in front of the flame,

the time that they are in the reaction front is defined as:

$$\tau_{\mathrm{f}} = \frac{l_{\mathrm{f}}}{S_{\mathrm{L}}} \tag{5.1}$$

where l_{f} and S_{L} are determined from the simulation results.

5.3.2 Simulation Results

A summary of the burning velocity, flame thickness, flame reaction timescale, and preheat flame fraction is given in Table 5.1 for the simulation results presented in this chapter. Burning velocity and flame thickness are determined from the simulations, and the flame reaction timescale is calculated based on Equation 5.1. Values are presented for each of the four reaction mechanisms in Table 5.1.

Table 5.1: Summary of methane flame characteristics with four reaction mechanisms. Units are as follows: S_{L} (cm/s), l_{f} (mm), and τ_{f} (ms).

	MP1				**BFER2**				**DRM19**				**GRI53**			
$\boldsymbol{\Phi_{\mathrm{g}}}$	$\boldsymbol{S_{\mathrm{L}}}$	$\boldsymbol{l_{\mathrm{f}}}$	$\boldsymbol{\tau_{\mathrm{f}}}$	$\boldsymbol{l_{\mathrm{ph}}/l_{\mathrm{f}}}$	$\boldsymbol{S_{\mathrm{L}}}$	$\boldsymbol{l_{\mathrm{f}}}$	$\boldsymbol{\tau_{\mathrm{f}}}$	$\boldsymbol{l_{\mathrm{ph}}/l_{\mathrm{f}}}$	$\boldsymbol{S_{\mathrm{L}}}$	$\boldsymbol{l_{\mathrm{f}}}$	$\boldsymbol{\tau_{\mathrm{f}}}$	$\boldsymbol{l_{\mathrm{ph}}/l_{\mathrm{f}}}$	$\boldsymbol{S_{\mathrm{L}}}$	$\boldsymbol{l_{\mathrm{f}}}$	$\boldsymbol{\tau_{\mathrm{f}}}$	$\boldsymbol{l_{\mathrm{ph}}/l_{\mathrm{f}}}$
0.5	12.1	1.03	8.5	0.84					3.3	2.47	74.3	0.92	4.5	2.13	47.7	0.92
0.6	18.0	0.78	4.3	0.82	13.6	0.88	6.5	0.95	12.2	0.96	7.8	0.86	12.4	0.94	7.6	0.86
0.7	24.3	0.64	2.6	0.79	21.5	0.60	2.8	0.96	20.4	0.68	3.3	0.80	19.8	0.68	3.4	0.82
0.8	30.6	0.56	1.8	0.77	30.0	0.46	1.5	0.94	26.8	0.57	2.1	0.77	25.8	0.59	2.3	0.78
0.9	36.7	0.52	1.4	0.73	38.0	0.40	1.1	0.91	30.7	0.54	1.8	0.74	29.2	0.55	1.9	0.76
1.0	42.3	0.49	1.2	0.70	44.2	0.37	0.8	0.88	31.4	0.55	1.7	0.76	29.7	0.56	1.9	0.77
1.1	47.0	0.43	0.9	0.73	47.3	0.34	0.7	0.91	29.0	0.58	2.0	0.78	27.1	0.59	2.2	0.79
1.2	50.9	0.40	0.8	0.76	48.2	0.33	0.7	0.92	23.7	0.65	2.7	0.83	12.7	0.70	3.2	0.86
1.3	54.1	0.35	0.6	0.80	48.1	0.31	0.6	0.99	16.7	0.85	5.1	0.89	15.0	0.93	6.2	0.91
1.4	56.7	0.34	0.6	0.77	47.5	0.33	0.7	0.98	10.9	1.21	11.2	0.92	10.1	1.28	12.6	0.91

The values in Table 5.1 give a summary of the flame characteristics that can be expected using the OpenFOAM model with a unity Lewis number assumption. As illustrated in Figure 5.10, the BFER2, DRM19, and GRI53 mechanisms demonstrate agreement within 15 % in the burning velocity below an equivalence ratio of 0.8, while MP1 overpredicts the burning velocity throughout the concentration range. As shown in Figure 5.15, flame thickness agrees within 15 % between equivalence ratios of 0.7 and 1.0. The ratio of preheat zone thickness (l_{ph}) to flame thickness is an average of 0.77, 0.93, 0.83, and 0.84 for MP1, BFER2, DRM19, and GRI53 mechanisms, respectively. This is higher than the values of Heravi et al. [167], which range from 0.57 to 0.63, and of Gottgens et al. [172] as reported by Hervai et al. [167], which range from 0.57 to 0.71.

Flame reaction timescales from the four reaction mechanisms are summarized in Figure 5.16. For each reaction mechanism, the calculated results from a single simulation is shown as a closed symbol with lines connecting them.

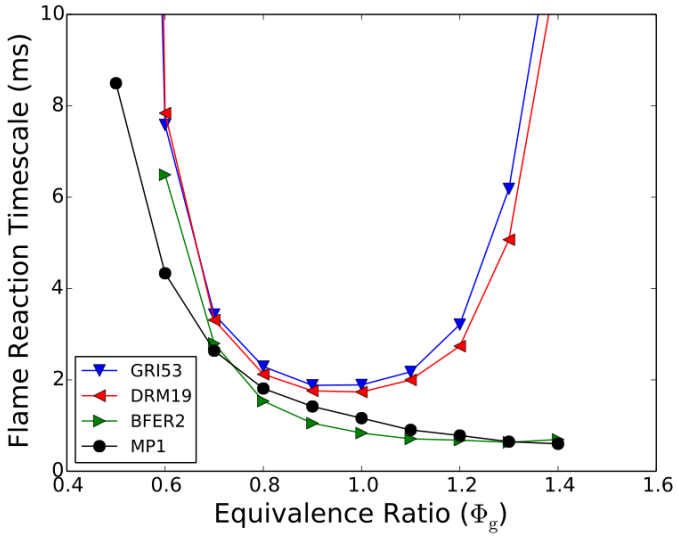

Figure 5.16: Methane flame reaction timescale calculated with four reaction mechanisms with the current model.

All four reaction mechanisms predict timescales that decrease from the LFL toward the stoichiometric concentration. These values vary by an order of magnitude near the LFL to 65 % at $\Phi_g = 0.9$. GRI53 and DRM19 capture an increase in the flame reaction timescale for fuel rich mixtures whereas BFER2 and MP1 do not.

5.4 Discussion of Results

Methane flame simulations provided a mechanism to measure flame reaction timescales at different equivalence ratios, to evaluate the impact of individual modeling assumptions, and to gauge the overall accuracy of the CFD model under gas flame conditions. Ignition delay simulations were used to validate the reaction solution routines in the absence of mass, momentum, and energy transport, and to illustrate thermophysical and transport properties predicted with the current model. Flame structure, burning velocity and flame thickness were compared to results from the literature, verifying coupling between reaction and transport solution routines and the impact of different reaction mechanisms with the unity Lewis number assumption.

5.4.1 Implications for Hybrid Mixtures

CFD simulation measurements indicate that methane flame thickness has a maximum value near the LFL, on the order of a few millimetres. The flame thickness decreases to a minimum value around 0.75 mm using the DRM19 and GRI53 reaction mechanisms. Flame thickness for the global MP1 and BFER2 mechanisms compared well with the more detailed mechanisms between equivalence ratios of 0.6 and 1.0, but continued to decrease for fuel-rich mixtures. The flame thickness for MP1 at $\Phi_g = 0.5$ was more than half that of the other mechanisms.

Flame reaction timescales were calculated from the burning velocity and flame thickness measurements; these ranged across almost three orders of magnitude. Between equivalence ratios of 0.6 and 1.0, the range was smaller, falling between 1 and 8 ms for all four reaction mechanisms. The MP1 and BFER2 reaction mechanisms had the smallest timescales at magnitudes approximately half those of the detailed mechanisms.

Analysis of the gas flame reaction timescale indicates that the time available for a particle to contribute to energy release in the flame front of a hybrid mixture when the gas is above the flammability limit (i.e., the dual-fuel or gas-driven explosion regime). If the particle reacts slower than this timescale, it will only serve to take energy away from the propagating flame and lower the burning velocity. If it reacts faster than this timescale, it will contribute to energy release and enhance the burning velocity in the hybrid mixture.

In this sense, the flame reaction time can also be called the "flame residence time," or the maximum time a particle has to contribute to the flame during its passage. Since particle heating and reaction is explicitly linked to particle size, hybrid enhancement and the resulting combustion regimes will be a strong function of the particle diameter. This feature is not currently captured in the hybrid explosion regimes available in the literature.

5.4.2 Accuracy of the CFD Model

Ignition delay time, species distribution, and temperature comparisons for the CPFMR given in Section 5.1.1 verify the reaction mechanisms and chemistry solution methods in the current computational model. Flame structure comparisons given in Figure 5.6

and Figure 5.7 further verify the transport equation coupling and overall solution routines for gas flames. The impact of the thermophsyical and transport modeling assumptions is highlighted by comparing the burning velocity between Cantera$^{\text{unity}}$and the current model in Figure 5.9 (c). These assumptions have a limited impact using the DRM19 and GRI53 reaction mechanisms. Burning velocity with the MP1 and BFER2 mechanisms is overpredicted compared to Cantera$^{\text{unity}}$, due to the higher thermal conductivity with the current model.

Simulations using Cantera$^{\text{multi}}$ in Figure 5.8 and Cantera$^{\text{mix}}$, Cantera$^{\text{unity}}$ and the current model in Figure 5.9 and Figure 5.10 demonstrate that both detailed reaction kinetics and component diffusion velocities are required to quantitatively predict methane burning velocity throughout the entire flammable gas concentration range. The difficulty is that the computational requirements may hinder extension of the CFD model to investigate more practical systems at larger geometries and once particles are added. For example, the computer time required to calculate a single timestep for a methane flame simulation with the current model are 0.02, 0.07, 2.6 and 7.6 s using the MP1, BFER2, DRM19, and GRI53 mechanisms, respectively (Dell XPS L501X laptop, 1.73 GHz Intel Core i7 processor, and 8 GB of RAM). Furthermore, the impact of using multispecies diffusion can be evaluated by comparing Cantera with the single-step mechanism to the multistep mechanisms. Cantera$^{\text{mix}}$ with MP1 takes less than 1 s to simulate the methane flame, while DRM19 takes 13.4 s and GRI53 takes 69.9 s. These times increase by a factor of 2 to 4, when using Cantera$^{\text{multi}}$. Altogether, the DRM19 mechanism with the mixture-averaged diffusion approach would take at least 1500 times longer to run than the MP1 mechanism with the unity Lewis number assumption. This would be increased by a further factor of at least 10 using the GRI53 mechanism and Cantera$^{\text{multi}}$.

Simulation results from the current model presented in Figure 5.10 demonstrate that the BFER2, DRM19, and GRI53 reaction mechanisms with the unity Lewis number assumption are in reasonable agreement with the experimental data below $\Phi_{\text{g}} = 0.8$. Furthermore, the MP1 mechanism overpredicts the burning velocity by a maximum of 45 % at these concentrations. The DRM19 mechanism appears to be a reasonable balance between computational cost and accuracy and is recommended to simulate gas flames under the unity Lewis number assumption.

Chapter 6

Coal Dust Flames

In the previous chapter, reaction timescales for methane flames were determined which are proposed to govern hybrid flame interaction when the gas is above its LFL. When the gas is below its LFL, the flame structure and combustion process may more-closely resemble that of a laminar dust flame propagating in a particle cloud. In the current chapter, results from coal dust flame simulations are verified by comparing to previous experimental and numerical studies in the literature. This is followed by an analysis of the role of gas-phase reaction mechanisms, the role of discrete particle combustion, and the flame structure of coal dust flames. This chapter concludes with the development of coal dust combustion regimes for laminar flame propagation and a discussion of the overall results.

6.1 Model Verification

Coal dust flame results from the current model are verified by comparing the flame structure and burning velocity to simulation results from the literature and experimental data. Heat and momentum exchange are compared to analytical solutions, followed by an analysis of flame structure and burning velocity. The impact of initial temperature on the burning velocity is presented and the sensitivity of the results to modeling parameters is explored.

6.1.1 Momentum and Heat Exchange

To verify particle momentum and heat exchange, simplified single computational cell simulations were completed and compared to analytical solutions of the governing equations. This comparison demonstrates that the equations are implemented correctly in the simulation model and that the solution and coupling methods produce the expected results. This comparison also demonstrates the role of particle relaxation timescales on velocity and heating of individual particles. The particle timescales play

an important role in coupling in the dual-fuel and gas-driven explosion regimes [65], and are explored later in this thesis.

The velocity of a single particle placed into a 1 m/s airflow is given in Figure 6.1. The particle has a 10 µm diameter and is initially at rest. Drag force on the spherical particle causes acceleration, increasing the particle velocity until it reaches equilibrium with the gas flow. Also given in Figure 6.1 are analytical solutions calculated by solving Equation 3.60 using constant and variable $C_{\mathrm{D}}\mathrm{Re}_{\mathrm{p}}$.

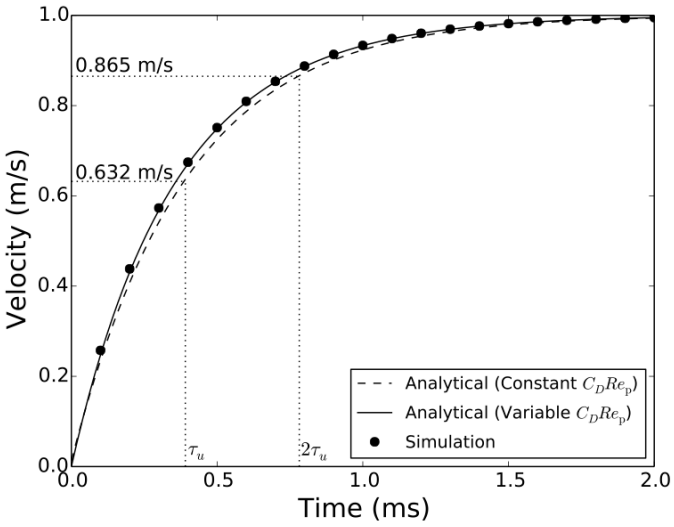

Figure 6.1: Velocity of a 10 µm particle placed in air flowing at a constant velocity of 1 m/s. The times indicated with τ_u and $2\tau_u$ represent a single momentum relaxation timescale and two relaxation timescales, respectively.

In the first analytical result, $C_{\mathrm{D}}\mathrm{Re}_{\mathrm{p}}$ is held at a constant value of 24.0 when evaluating the relaxation timescale. In the second result, $C_{\mathrm{D}}\mathrm{Re}_{\mathrm{p}}$ is evaluated using Equation 3.58 and Equation 3.59, assuming that $\rho = 1.168\,\mathrm{kg/m^3}$, $\rho_{\mathrm{p}} = 1300\,\mathrm{kg/m^3}$, and $\mu_{\mathrm{s}} = 1.846 \times 10^{-5}\,\mathrm{Pa\,s}$. Particle velocity from the simulation model agrees with the analytical results using the variable parameters.

Also given in Figure 6.1 are the times associated with a single drag relaxation timescale and two relaxation timescales calculated with the constant $C_{\mathrm{D}}\mathrm{Re}_{\mathrm{p}}$ assumption. Equation 3.61 indicates that the particle velocity increases to 63 % of the gas velocity when $t = \tau_u$, and to 83 % of the gas velocity when $t = 2\tau_u$. This behaviour is reproduced in the analytical results and simulation model.

The temperature of a 10 µm particle immersed in 2000 K air is shown in Figure 6.2.

Both the particle and gas are stationary. The particle temperature increases with time due to heating from the air, reaching the air temperature at approximately 0.8 ms.

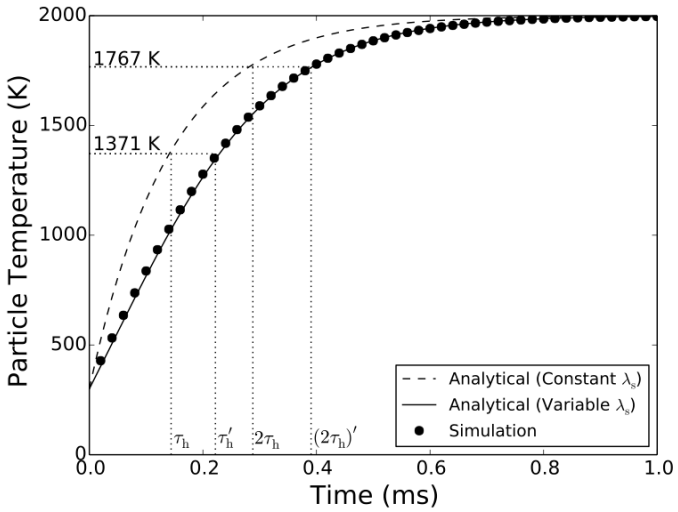

Figure 6.2: Temperature of a 10 µm particle placed in a stationary gas at a temperature of 2000 K. The times indicated with τ_h and $2\tau_h$ represent a single heating relaxation timescale and two relaxation timescales, respectively. τ_h' and $(2\tau_h)'$ indicate the change in timescale associated with temperature dependent gas conductivity at the surface of the particle.

The analytical results presented in Figure 6.2 are calculated by solving Equation 3.52 and Equation 3.63. Devolatilization and surface reaction are not included in this calculation, and the integrated equation takes the same exponential form as the momentum transfer:

$$T_p(t) = T + \left(T_p^\circ - T\right) e^{-t/\tau_h} \tag{6.1}$$

where $T_p(t)$ is the particle temperature at a given instance in time, T is the gas temperature, T_p° is the initial particle temperature, and τ_h is the particle heating relaxation timescale from Equation 3.67.

The same parameters as the momentum transfer example are used in the analytical solution along with $C_s = 1650$ J/kg-K and Nu = 2.0. As in the momentum transfer example, two analytical results are presented in Figure 6.2. In the first, thermal conductivity at the surface of the particle is held constant at $\lambda_s = 0.124$ W/m-K. In the second, thermal conductivity increases linearly with particle surface temperature calculated using a 1/3 weighting of the gas and particle temperature [147].

Comparing the constant and variable λ_s solutions in Figure 6.2 demonstrates that particle heating is impacted more by thermal conductivity than the momentum transport is by viscosity. Including variable thermal conductivity causes a delay in heating represented by τ_h' and $(2\tau_h)'$ in Figure 6.2. Agreement between the current model and the analytical solution verifies particle heating in the current model.

6.1.2 Flame Structure

Little data is available on the flame structure of planar propagating coal dust flames at ambient pressure and temperature. According to the simulation models outlined in Table 3.4, Bradley et al. [60] reported a flame structure for 4 µm coal particles with 40 % volatiles and 144.3 g/m^3 concentration, and Smoot and Horton [78] reported a flame structure for 30 µm particles with 50 % volatiles and 300 g/m^3 concentration. The model of Bradley et al. [60] is most similar to the current model using the same devolatilization approach. Differences between the models include a molecular-based surface reaction model which produces CO instead of CO_2, and multispecies treatment for diffusivity, viscosity, and conductivity.

Flame structure predictions from Bradley et al. [60] are given in Figure 6.3 and compared to the current model. Temperature is presented along with mole fraction of various species throughout the flame. The mole fractions are determined on a dry basis where H_2O is subtracted from the mixture and the flames have been shifted so that the maximum methane concentration is located at 0 mm. The burning velocity is 23.5 and 19.5 cm/s for the current and literature models, respectively.

At 144.3 g/m^3, the overall equivalence ratio including the volatile release and surface reaction is 1.68, while the volatile component equivalence ratio is 0.84. The current model predicts a higher burning velocity and thinner flame front than Bradley et al. [60]. This is accompanied by a lower maximum methane gas concentration in the flame front. These results suggest that methane gas is reacting faster in the flame front in the current model than the literature model. This may be due to a combination of higher thermal conductivity, different surface reaction rates, and the specific gas-phase reaction mechanism.

The current model predicts a higher CO_2 concentration and a lower CO concentration than Bradley et al. [60]. This is likely due to differences in the heterogeneous

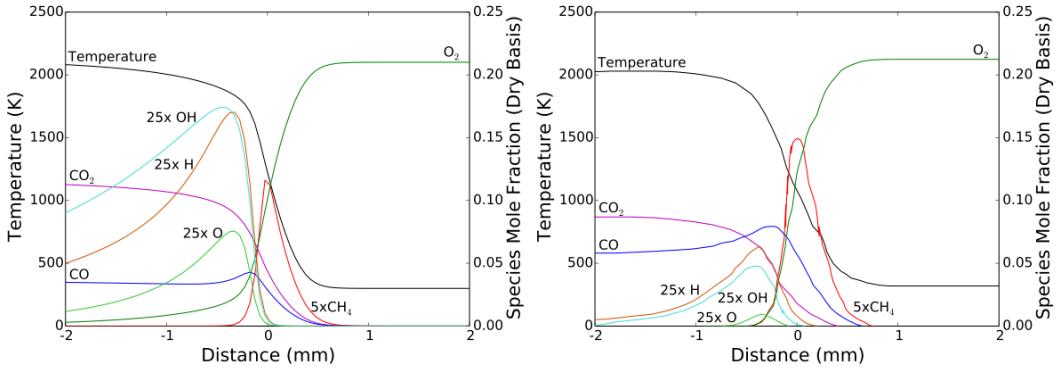

(a) Current Model (b) Literature Model

Figure 6.3: Coal dust flame structure with 4 µm particles and 144.3 g/m^3 concentration at ambient temperature and pressure. Results from the current simulation model are presented using the DRM19 mechanism and the literature model is digitized from Bradley et al. [60].

surface reaction model. The current model assumes that the product species from surface reaction is CO_2, while Bradley et al. [60] assume that CO is produced first and reacts in the gas-phase further downstream from the flame. The maximum concentration of OH, H, and O predicted by the current model is also higher than Bradley et al. [60]. This is due to the unity Lewis number assumption. This assumption prevents preferential diffusion of these species into the flame front where they would be consumed more rapidly with oxygen.

The volumetric heat release rate throughout the 144.3 g/m^3 coal dust flame is presented in Figure 6.4 for the current and literature simulation models. The heat release rate rapidly increases in the flame front, reaches a maximum value, and decreases downstream from the reaction zone. The ordinate in Figure 6.4 has the same scale as Figure 6.3 so that the heat release rate profile can be compared to the overall flame structure.

The heat release rate in the current model is steeper and reaches a higher maximum value than Bradley et al. [60]. The maximum occurs 0.14 mm behind the maximum methane concentration for the current model and 0.24 mm behind the maximum methane concentration for Bradley et al. [60]. These differences are again due to a combination of the unity Lewis number assumption, differences in gas-phase combustion mechanisms, and the transport property models used.

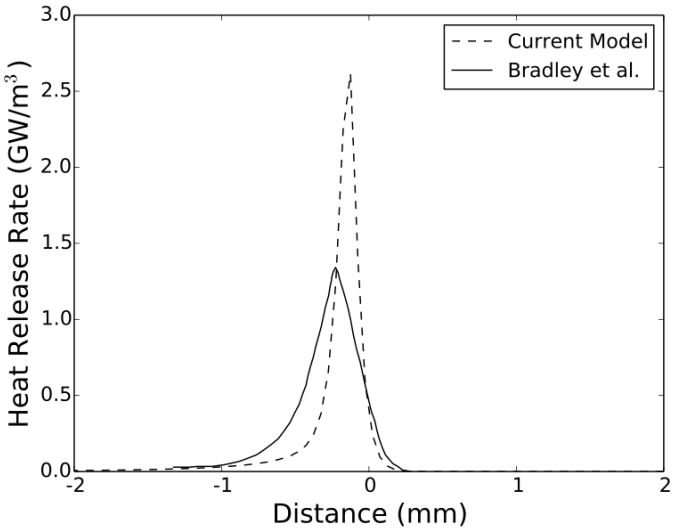

Figure 6.4: Heat release rate for a coal dust flame with 4 µm particles and 144.3 g/m^3 concentration at ambient temperature and pressure. Results are presented from the current simulation model using the DRM19 mechanism and the literature model is digitized from Bradley et al. [60].

6.1.3 Burning Velocity

The effect of particle diameter on coal dust burning velocity was explored by Smoot and Horton [78], who reviewed the experimental literature and performed numerical simulations. As outlined in Table 3.4, their simulation model included an Arrhenius devolatilization mechanism with several volatile products, a kinetic/diffusive surface reaction, and a unity Lewis number diffusion assumption. They also assumed the particles contained 50 % volatile content.

Burning velocity predictions from the current model are presented in Figure 6.5 and compared to simulation results of Smoot and Horton [78]. Simulations are performed for monodisperse particle sizes of 10 and 33 µm. For each of the current simulations, burning velocities are measured after the flame reached steady propagation, and the MP1 reaction mechanism was used.

The two simulation models predict similar burning velocities for 10 µm particles up to a concentration of 300 g/m^3. At this concentration, the current model predicts a maximum value of 25.8 cm/s. The burning velocity of Smoot and Horton [78] increases to a concentration of 625 g/m^3, where it reaches a maximum value of 29.3 cm/s. The trend in burning velocity between the two models is similar for 33 µm particles,

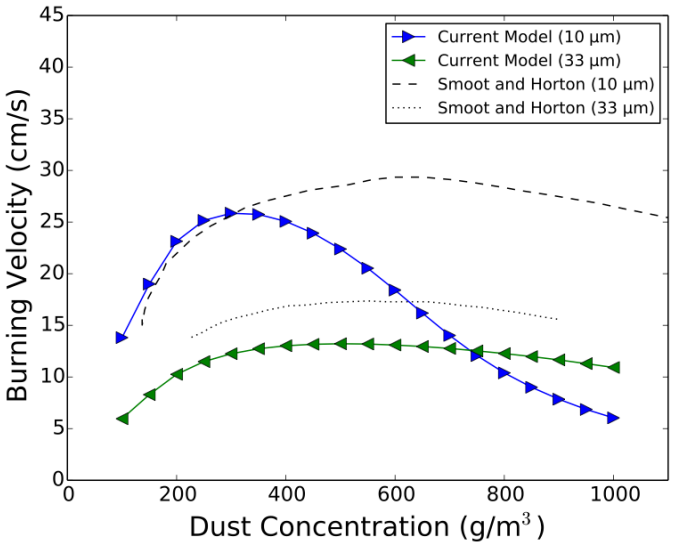

Figure 6.5: Coal dust burning velocity at ambient temperature and pressure compared to simulation results of Smoot and Horton [78]. Current simulations are performed using the MP1 reaction mechanism.

with the current model predicting burning velocities that are lower by approximately 25 %. The maximum burning velocity of 33 µm particles for the current model occurs at 500 g/m^3 with a value of 13.2 cm/s, while the maximum velocity for Smoot and Horton [78] occurs at 550 g/m^3 with a value of 7.4 cm/s.

In their review of the experimental data, Smoot and Horton [78] state several summary observations for coal dust flames. Two of these observations are that finer coal dust particles shift the peak burning velocity to leaner dust concentrations and that coarser dust particles have a higher burning velocity for very rich concentrations. Smoot and Horton [78] acknowledge that their simulation model is unable to capture either of these effects in their presented work. This is also shown in Figure 6.5.

It is interesting to note that both of these features are present in the current model using a simpler devolatilization approach with a single fuel specie, and with the single-step MP1 reaction mechanism. This suggests that one of these changes may be responsible differences shown by Smoot and Horton [78]. It also demonstrates that these qualitative observations can be reproduced with the unity Lewis number assumption for species diffusion.

Burning velocity predictions from the current model are compared to experimental data from Horton et al. [77] in Figure 6.6. The simulations again have a uniform

particle diameter, while the experimental results have a size distribution with a cumulative mass fraction of 50 % below the particle diameter indicated. Burning velocity predications from the current model are presented for 4, 10, and 33 µm particles using the MP1 reaction mechanism.

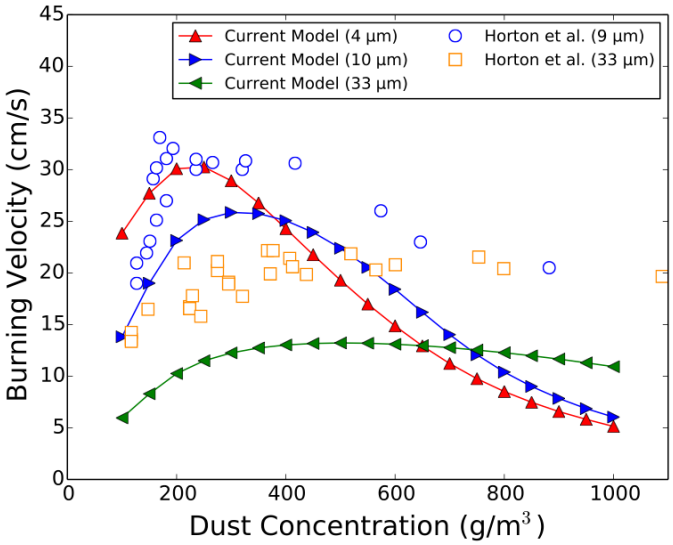

Figure 6.6: Coal dust burning velocity at ambient temperature and pressure compared to experimental data of Horton et al. [77]. Current simulations are performed using the MP1 reaction mechanism.

The experimental results of Horton et al. [77] further illustrate the two summary observations highlighted by Smoot and Horton [78]. The peak burning velocity is shifted to leaner dust concentrations as the average particle size is decreased, and the burning velocity for coarser particles is higher at very rich concentrations (greater than 900 g/m^3; not shown in Figure 6.6). The predicted burning velocity for 4 µm particles with the current model also further demonstrates this observation with a peak value of 30.2 cm/s at 250 g/m^3.

Although the qualitative burning velocity trends are well produced with the current model, the magnitude of the burning velocity is underpredicted overall. This underprediction is due to two factors that are not included in the simulation. The first of these is the particle size distribution. Having a polydisperse particle cloud tends to increase the maximum flame propagation velocity towards the smaller particle size range [175]. In Figure 6.6, this is demonstrated by the 4 µm particle simulations which have a similar maximum burning velocity as the experimental 9 µm size distribution.

The second factor not included in the simulations is the impact of preheating in the experimental apparatus. Bradley et al. [37] reviewed ten experimental studies and argued that preheating by hot walls, flame holders, and flame screens influences experimental burning velocity measurements. Specifically, they suggested that the experimental apparatus of Horton et al. [77] may have caused preheating of several hundred Kelvin near the screen used to anchor the dust flame.

6.1.4 Effect of Initial Temperature

The effect of initial temperature on coal dust burning velocity using the current model was explored in Cloney et al. [36]. The results are compared to the experimental data of Horton et al. [77] and the comprehensive simulation model of Park and Park [38]. The literature model of Park and Park [38] is summarized in Table 3.4 and includes a multispecies evaluation of gas-phase transport properties, thermal radiation, multi-step heterogeneous surface reactions including tar formation and decomposition, and multispecies devolatilization. This comparison demonstrates the possible impact of preheating on the experimental results, as well as the performance of the current model against the comprehensive modeling approach.

The burning velocity for 10 µm and 33 µm coal dust particles using the MP1 reaction mechanism is given in Figure 6.7 and compared to the experimental and simulation literature data. The experimental data is the same as Figure 6.6. For their simulations, Park and Park [38] used a global Arrhenius devolitization model ($A_{\mathrm{v}} = 5.5{\times}10^5$ kg/s and $E_{\mathrm{a,v}}/R = 8{,}907\,\mathrm{K}$) and a "speciated" model in which rates were derived for each of the seven devolatilization species separately.

As suggested by Bradley et al. [37] and Park and Park [38], increasing the initial system temperature provides better agreement between the simulation results and the experimental data. Using the current model, an initial cloud temperature of 373 K provides very good agreement with the experimental data for 10 µm particles up to a concentration of $600\,\mathrm{g/m^3}$ [36]. At this point, a drop in the burning velocity is captured, with a magnitude larger than the experimental results. At this initial temperature, the burning velocity for 33 µm particles is underpredicted by 10 % to 30 % throughout the concentration range, although the correct profile versus particle concentration is maintained.

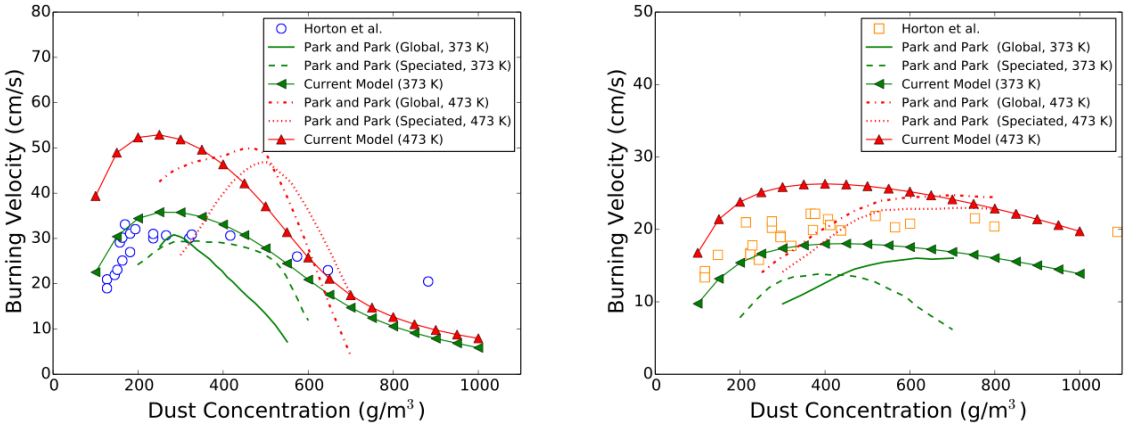

(a) $d_p = 10\,\mu m$ (b) $d_p = 33\,\mu m$

Figure 6.7: Coal dust burning velocity at elevated initial temperatures compared to the experimental data of Horton et al. [77] and simulation model of Park and Park [38]. The current model uses the MP1 reaction mechanism.

The impact of changing the initial temperature in the current model is quite different than seen in the model of Park and Park [38]. In the current model, increasing the initial temperature increases the maximum burning velocity and reduces the concentration at which this maximum occurs. It also appears to generally broaden the overall burning velocity profile. This is in contrast to the results of Park and Park [38], where the concentration at which the maximum burning velocity occurs is higher at increased initial temperatures. The model of these authors [38] also appears to shift the overall burning velocity profile, rather than broadening it, for all simulations except the global devolatilization model with 33 µm particles.

The amount of literature available on the impact of initial temperature for coal dust flames is insufficient at the current time to determine which model behaviour is correct. However, it is worth noting that the experimental burning velocity profile of Horton et al. [77] and behaviour towards the fuel lean and rich limits more closely matches the current model than that of Park and Park [38]. It is also worth noting that increasing the system temperature typically leads to the broadening of burning velocity profiles and flammability limits for methane gas flames, rather than shifting them (see Chapter 5, Section 8.1 of Kuo [130]).

Lastly, Park and Park [38] explain that flame propagation could not be achieved with their model in ambient temperature clouds and argue that preheating must

be needed in experimental systems. However, experiments under microgravity conditions with lycopodium [176] and iron [177] are able to propagate a flame. With this in mind, it seems reasonable to conclude that coal dust would also sustain flame propagation under laminar microgravity conditions at ambient temperature. Although not conclusive, these qualitative observations suggest that the current model may better capture burning velocity in coal dust clouds, even though a simplified treatment of the physical and chemical processes is employed.

6.1.5 Effect of Modeling Parameters

The effect of changing the diffusion coefficient for heterogeneous reactions on flame structure is illustrated for 4 µm particles at 144.3 g/m^3 in Figure 6.8. Temperature, oxygen, and methane mass fraction profiles are shown in the figure. Laminar burning velocities are 19.9, 27.3, and 34.1 cm/s for 0, 100, and 500 mm^2/s, respectively.

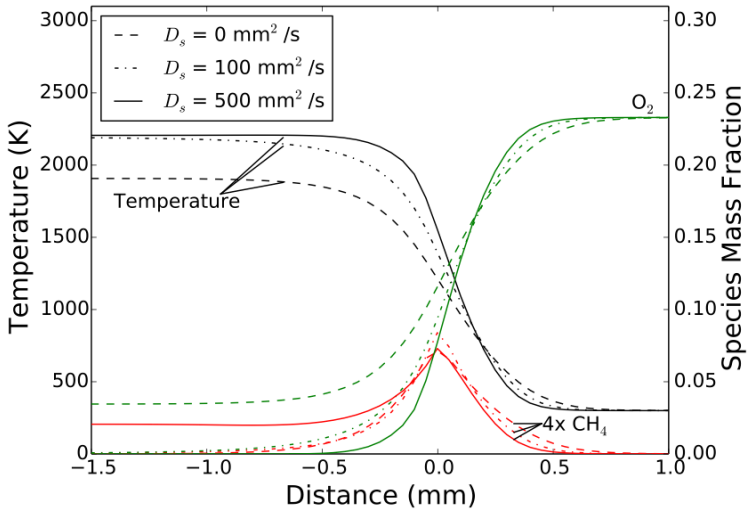

Figure 6.8: Flame profile using MP1 chemistry model with surface reactions and different diffusivity constants. Particle concentration is 144.3 g/m^3 and the particle diameter is 4 µm.

The results presented in Figure 6.8 show that flame structure and burning velocity are sensitive to the choice of diffusion coefficient at this dust concentration. Increasing the diffusion coefficient causes the flame temperature and burning velocity to increase and oxygen concentration behind the flame to decrease due to the heterogeneous reaction. At large diffusion coefficients (e.g., 500 mm^2/s), surface reaction starts

to compete with the gas-phase reaction for oxygen, leaving unburned methane gas behind the flame front. A fixed diffusion coefficient (D_s) of 100 mm^2/s was used in the current work unless specified otherwise.

The effect of changing the devolatilization rate was not explored in the current work. However, Dixon-Lewis et al. [150] state that the burning velocity was insensitive to decreasing the devolatilization rate by up to three orders of magnitude using the same devolatilization model. This suggests that the current devolatilization rate occurs nearly instantaneously once the activation energy is reached during particle heating. As such small changes in the rate parameters are unlikely to impact the results.

The burning velocity and normalized burning velocity at multiple cell resolutions are given in Figure 6.9. Two different groups of simulations are presented: 4 µm particles using the continuum Lagrange representation and 33 µm particles using the discrete representation.

For 4 µm particles using the continuum representation, a similar trend as methane flames where the burning velocity moderately increases with cell resolution is seen. Burning velocity becomes divergent past 100-µm cell resolution for this small particle size, suggesting that the flame thickness may be similar to methane gas. The burning velocity results are again convergent below 100-µm cell resolution, and decreasing from 50 to 25-µm resolution gives a drop in burning velocity of less than 2.5 %.

For 33 µm particles using the discrete representation, the average error for the 50-µm cell resolution is similar to 4 µm particles, but the scatter simulation-to-simulation is larger. This larger scatter is due to the difficulty in determining the mean burning velocity from fluctuating distance-time traces using the discrete particle representation. The results presented in Figure 6.9 are from a single pass using an automated Python algorithm. For the discrete results presented in the remainder of this thesis, multiple passes at the data were completed with manual adjustment of the distance-time trace fits. Therefore, the scatter in Figure 6.9 represents the largest magnitude that could apply to the results presented.

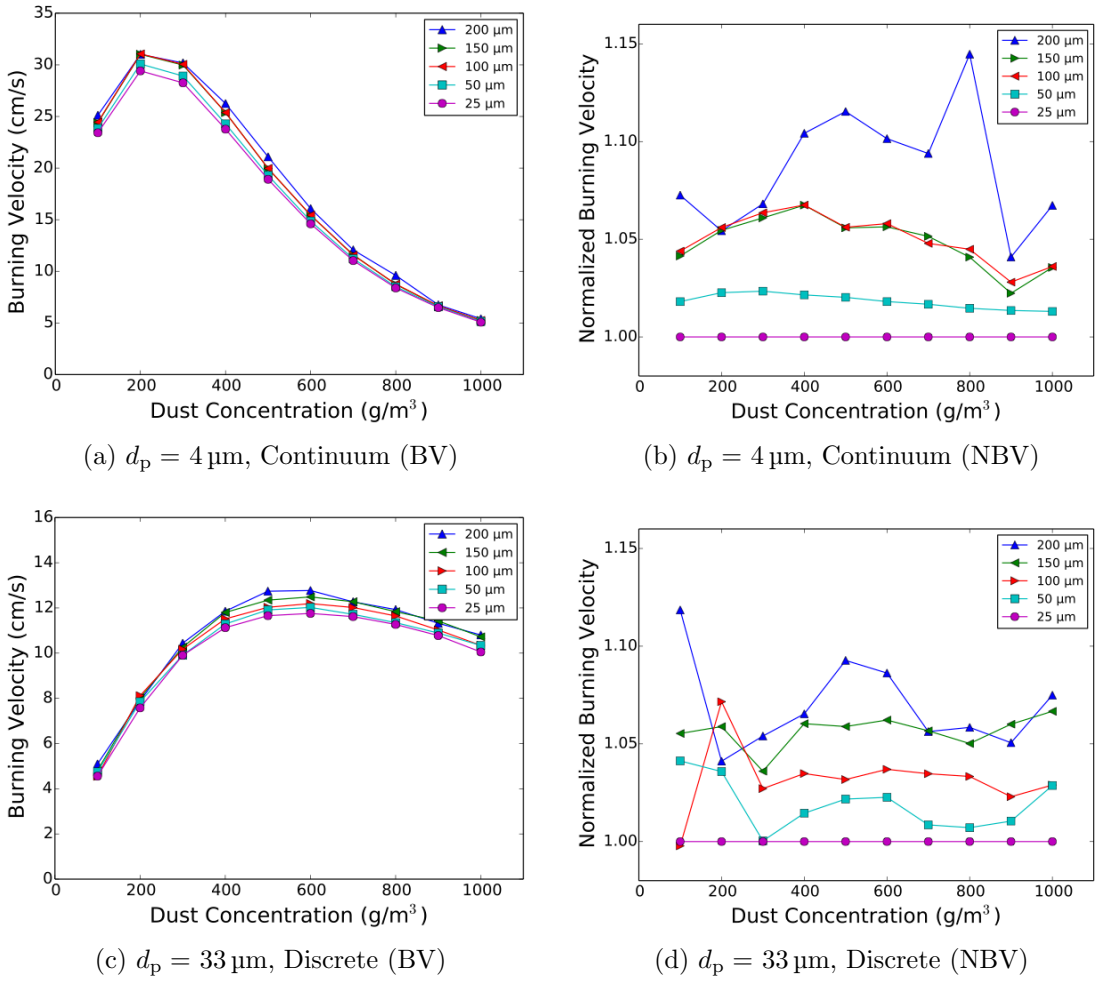

(a) $d_p = 4\,\mu m$, Continuum (BV)

(b) $d_p = 4\,\mu m$, Continuum (NBV)

(c) $d_p = 33\,\mu m$, Discrete (BV)

(d) $d_p = 33\,\mu m$, Discrete (NBV)

Figure 6.9: Burning velocity (BV) and normalized burning velocity (NBV) as a function of coal dust concentration at different cell resolutions using the continuum and discrete particle representations.

6.2 Role of Reaction Mechanism

Although the investigations outlined in Section 2.3.1 and models outlined in Table 3.4 cover many variations in transport modeling approaches, devolatization, and surface reaction, none cover the impact of using different gas-phase chemistry mechanisms within the same modeling framework. As discussed in the introduction to this thesis, global reaction models may be necessary for systems with three dimensional geometry at industrial scales. Furthermore, the degree of accuracy in using different reaction mechanisms for coal dust flames remains to be determined, and there is little guidance on which models may be appropriate under different conditions. To this end, the

impact of the four reaction mechanisms outlined in Table 3.1 on flame propagation, flame temperature, and burning velocity is explored in this section.

6.2.1 Flame Propagation

In addition to increasing the computational effort on a per timestep basis, using more complex mechanisms also makes it difficult to achieve steady flame propagation and analyze coal dust flames. As the particle concentration increases, simulations may have to be run longer to achieve steady state, especially with the DRM19 and GRI53 mechanisms. Furthermore, the flames may become physically unstable due to coupling between heating, devolatilization, and gas-phase kinetics. In some concentration ranges, flames could not be achieved with multi-step reaction mechanisms. This difficulty in achieving steady flame propagation with detailed mechanisms has been demonstrated previously in the literature (e.g., see [38, 49]). Furthermore, from the results presented in Section 6.1.3, it is not clear that more detailed reaction mechanisms provide a better prediction of burning velocity when flame propagation is achieved.

Coal dust flame propagation is explored in Figure 6.10 where distance is plotted against time using different reaction mechanisms, particle sizes, and dust concentrations. The flame position is specified based on a point on the flame front where it reaches 1000 K. In some cases (e.g., 33 µm particles at high concentrations), this value had to be reduced to 750 K as the dust flame temperature decreased. The short solid black lines overlaid on the flame propagation profile indicate the steady-flame fit for that simulation. The slope of this line is defined as the burning velocity.

Burning velocity for 10 µm particles using the MP1 mechanism increases in the concentration range between 160 and 200 g/m^3. This is also shown in the burning velocity trends presented in Figures 6.6 and 6.5. In Figure 6.10, the burning velocity for 10 µm particles using the BFER2 mechanism reaches the maximum burning velocity at 190 g/m^3 and then starts to decrease at higher concentrations.

The DRM19 mechanism required longer simulation times than the MP1 and BFER2 mechanisms to achieve steady propagation. As the initiating methane flame enters the particle cloud, it is partially quenched by heat loss to the dust, and the flame must propagate a certain distance before it reignites. This distance increases

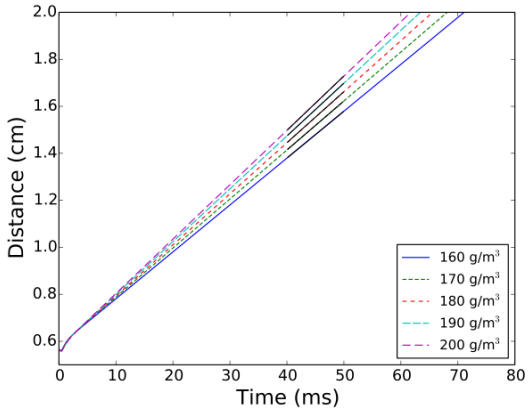

(a) MP1, $d_\mathrm{p} = 10\,\mu\mathrm{m}$

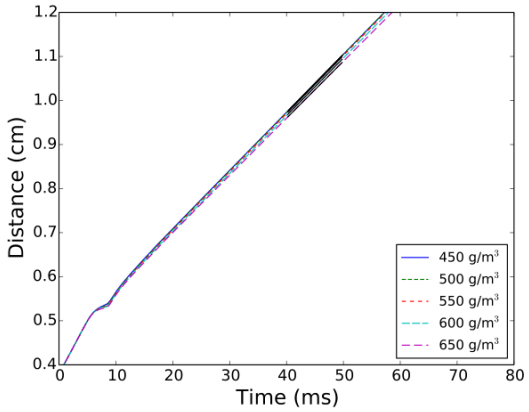

(b) MP1, $d_\mathrm{p} = 33\,\mu\mathrm{m}$

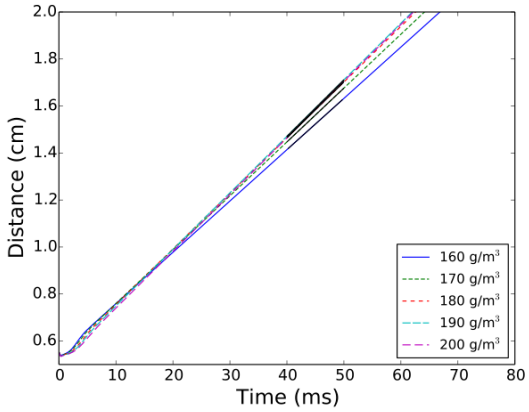

(c) BFER2, $d_\mathrm{p} = 10\,\mu\mathrm{m}$

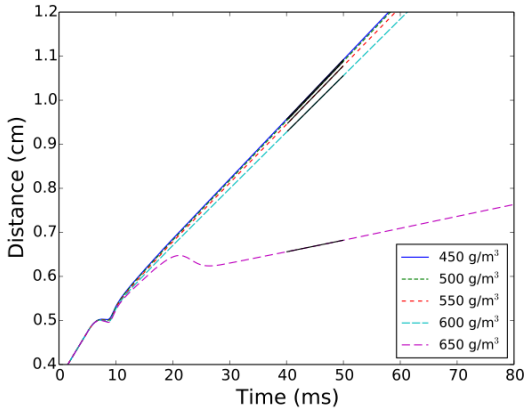

(d) BFER2, $d_\mathrm{p} = 33\,\mu\mathrm{m}$

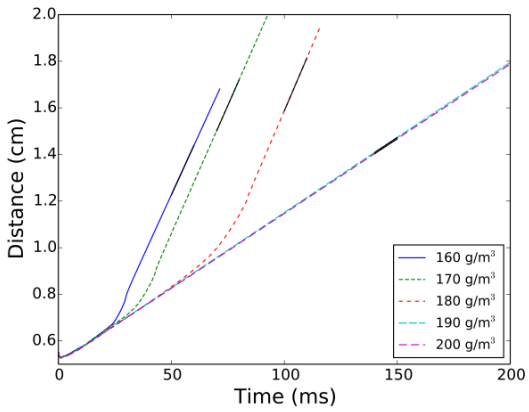

(e) DRM19, $d_\mathrm{p} = 10\,\mu\mathrm{m}$

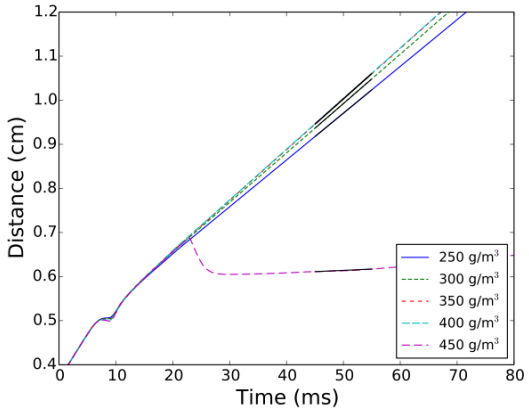

(f) DRM19, $d_\mathrm{p} = 33\,\mu\mathrm{m}$

Figure 6.10: Coal dust flame propagation for 10 and 33 µm particles at various concentrations using different reaction mechanisms.

with particle concentration, and reignition could not be achieved above a concentration of 180 g/m^3. The temperature front is still driven forward under these conditions due to conduction from the hot reaction products, but at a fraction of the velocity of the propagating flames. The GRI53 mechanism had a similar flame propagation profile as DRM19 for both particle sizes.

Flame propagation profiles for the 33 µm particles were less steep than 10 µm particles as indicated by the change in the ordinate scale on the right side of Figure 6.10. The BFER2, DRM19, and GRI53 mechanisms all had a maximum dust concentration beyond which the flame quenched prior to reaching steady state. This occurred at a concentration of 650 g/m^3 for the BFER2 mechanism and 450 g/m^3 for the DRM19 and GRI53 mechanisms. Again, the temperature fronts were driven forward by conduction above these concentrations, but flame propagation was not achieved.

The flame ignition process for 10 µm particles at a concentration of 180 g/m^3 using the DRM19 mechanism is explored in Figure 6.11. The times shown demonstrate flame structure before ignition (60 ms) and after ignition (100 ms). Flame temperature and species profiles are indicated with lines, while Lagrange groups are indicated with circles. The Lagrange groups circles are shaded, based on the amount of volatiles remaining: solid circles indicate all of the volatiles are present and clear circles indicate all of the volatiles have been released.

Prior to ignition, the temperature front was driven into the particle cloud by conduction from the products of the methane flame and a small degree of methane combustion. Methane was released by the particles during devolatilization and diffused from the reaction front. The intermediate species concentration grew behind the reaction front, but was too low to establish prompt combustion in the flame.

At approximately 75 ms (see Figure 6.10) the 180 g/m^3 flame simulation with the DRM19 mechanism promptly ignited. Particle heating, devolatilization, methane consumption, and intermediate species reaction coupled in the flame front. At 100 ms, the flame reached the steady flame propagation profile shown in Figure 6.11 (b). The methane was almost completely consumed at the rate it was released by the particles, and the concentration of intermediate species and radicals increased behind the flame front. At concentrations above 180 g/m^3 the DRM19 and GRI53 mechanisms had little or no intermediate specie formation, and flame ignition did not occur.

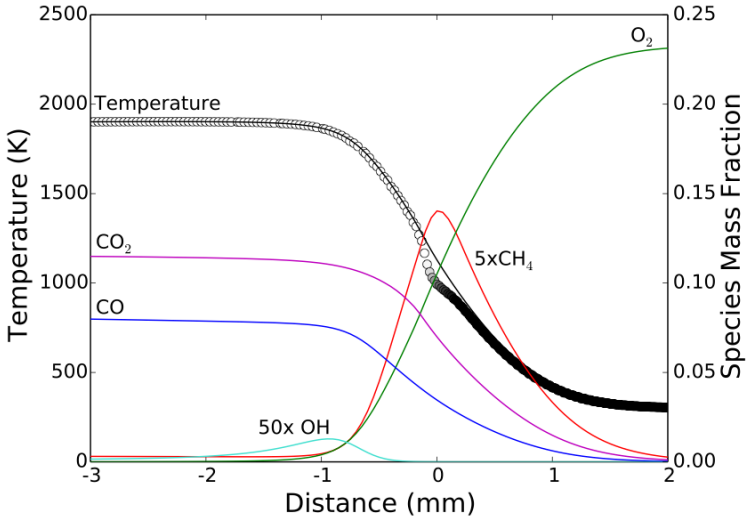

(a) Time = 60 ms, before ignition

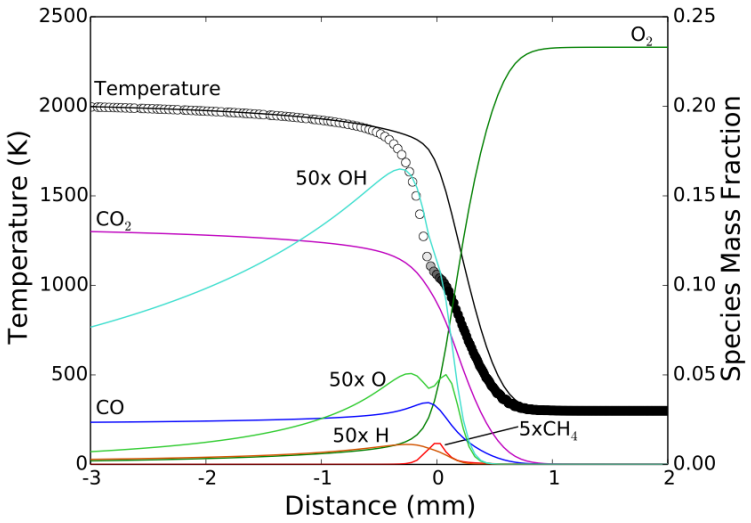

(b) Time = 100 ms, after ignition

Figure 6.11: Flame ignition process in 10 µm particles at a concentration of 180 g/m^3 using the DRM19 mechanism. Nomenclature: lines – gas temperature; symbols – particle temperature; symbol shading – filled: 100 % volatiles and open: 0 % volatiles.

The flame quenching process with the BFER2 mechanism with 33 µm particles at a concentration of 650 g/m^3 is explored in Figure 6.12. Lines indicate temperature profiles at each of the times specified, and the symbols indicate the Lagrange particle groups. The lines and symbols are shaded with the same color as the specified simulation time. The flame has not been scaled in the figure, such that the abscissa is the same as the ordinate in Figure 6.10.

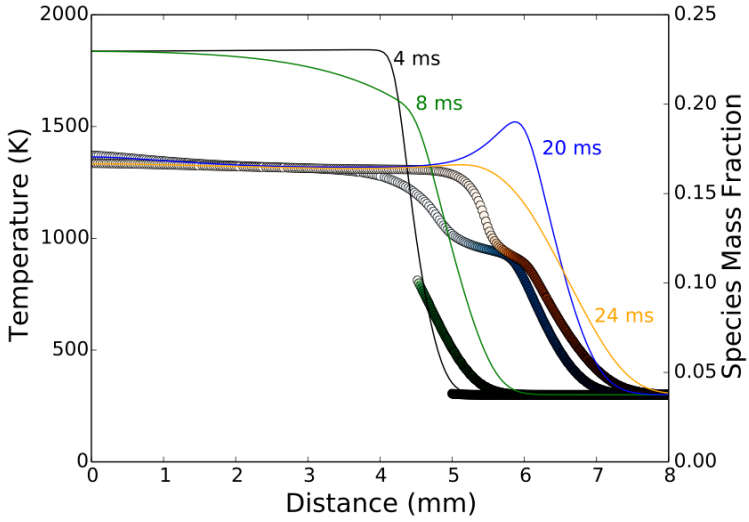

Figure 6.12: Flame quenching process in 33 µm particles at a concentration of 650 g/m^3 using the BFER2 mechanism. Nomenclature: lines – gas temperature; symbols – particle temperature; symbol shading – filled: 100 % volatiles and open: 0 % volatiles.

The flame profiles shown in Figure 6.12 and the distance-time trace in Figure 6.10 illustrate the flame propagation process during quenching. At 4 ms, the methane flame has just reached the edge of the particle cloud and at 8 ms it begins to enter the cloud. By 20 ms, the dust flame profile has almost reached steady propagation, although the flame temperature is still decreasing slightly with time. This is indicated by the curvature of the distance-time trace between 10 and 20 ms in Figure 6.10. At 24 ms, the flame abruptly extinguishes and no more reaction occurs in the flame front. Beyond this time, the temperature front is propelled forward by conduction alone.

The same quenching process occurs for the DRM19 mechanism at dust concentrations of 450 g/m^3 and above. Above this concentration, the flame temperature is too low to sustain coupling between heating, devolatilization, and gas-phase reaction in the flame front. To explore this further, the flame structure for the propagating 400 g/m^3 flame is given in Figure 6.13. Since the flame is fuel rich, not all of the methane is consumed. In Figure 6.13, the flame is shifted such that the maximum OH concentration is located at 0 mm on the abscissa.

Although the 400 g/m^3 coal dust flame in Figure 6.13 is propagating at a velocity of 11.5 cm/s, it appears to be close to the stability limit for the DRM19 reaction

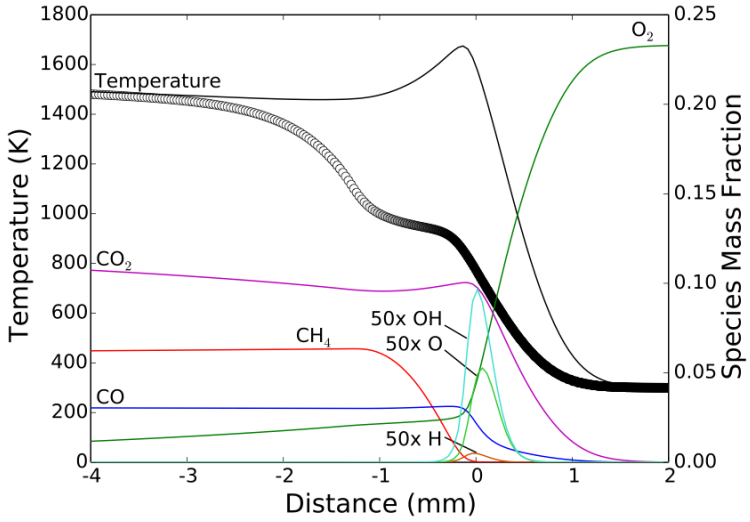

Figure 6.13: Flame structure for 33 µm particles at a concentration of 400 g/m^3 using the DRM19 mechanism. Nomenclature: lines – gas temperature; symbols – particle temperature; symbol shading – filled: 100 % volatiles and open: 0 % volatiles.

mechanism. Devolatilization and gas-phase reaction occur in the flame front as indicated by the OH, H, and O species concentrations. However, unreacted oxygen and methane also exist behind the flame front. At these locations behind the flame front, the flame temperature is insufficient to cause further reaction using the DRM19 mechanism.

6.2.2 Flame Temperature

Maximum temperature for coal dust flames using the four reaction mechanisms is presented in Figure 6.14. The temperature is only shown for concentrations where a steady flame could be achieved. The maximum concentrations for these flames are 180 and 400 g/m^3 for the DRM19 and GRI53 mechanisms with 10 and 33 µm particles and 600 g/m^3 for the BFER2 mechanism with 33 µm particles. Temperatures are not reported between 90 and 180 g/m^3 as the full flame profile takes a long time to form when $\Phi_p^t > 1.0$ but $\Phi_p^v < 1.0$, and could not be measured from the simulations.

Considering the MP1 and BFER2 results presented in Figure 6.14, the maximum flame temperature is lower for 33 µm particles than 10 µm particles when the concentration is below 180 g/m^3. At higher concentrations, the maximum flame temperature

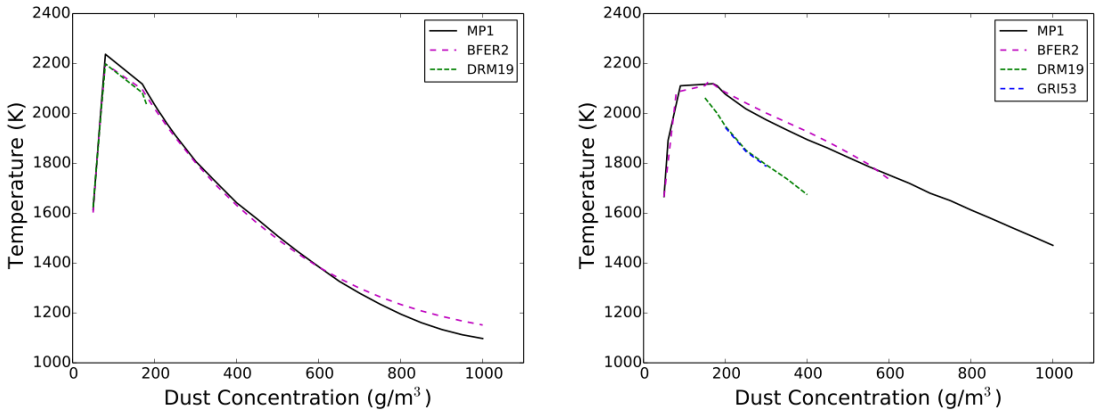

(a) $d_p = 10\,\mu m$ (b) $d_p = 33\,\mu m$

Figure 6.14: Coal dust flame temperature for 10 and 33 µm particles with different reaction mechanisms.

is higher for 33 µm particles. This is caused by the slower heating of the larger particles in the reaction front. This slower heating allows the maximum flame temperature to rise above the adiabatic temperature behind the reaction front as shown in Figure 6.13. This feature is not present for smaller particles as shown in Figure 6.3 and Figure 6.11, and is the mechanism by which larger particles have higher burning velocity than smaller particles at high dust concentrations, as observed by Smoot and Horton [78].

Figure 6.14 demonstrates that the four reaction mechanisms predict similar flame temperatures for 10 µm particles, with the largest difference of approximately 40 K occurring at the maximum. The DRM19 and GRI53 mechanisms are unable to form steady flames once the temperature drops below 2040 K. The DRM19 and GRI53 mechanisms predict a lower flame temperature than the MP1 and BFER2 mechanisms for 33 µm particles. This is due to the incomplete oxidation of methane as shown in Figure 6.13. Both the DRM19 and GRI53 mechanisms are unable to form steady flames once the temperature drops below 1640 K, and the BFER2 mechanism is unable to form a steady flame below 1740 K.

6.2.3 Burning Velocity

The burning velocity for coal dust flames with different reaction mechanisms is presented in Figure 6.15 for 10 and 33 µm particles. For 10 µm particles, simulations were

performed between 50 and 1000 g/m^3 at increments of 10 g/m^3 up to the maximum burning velocity and 50 g/m^3 intervals thereafter. For 33 µm particles, simulations were performed between 100 and 1000 g/m^3 at increments of 50 g/m^3. The experimental data of Horton et al. [77] is given in Figure 6.15 for reference.

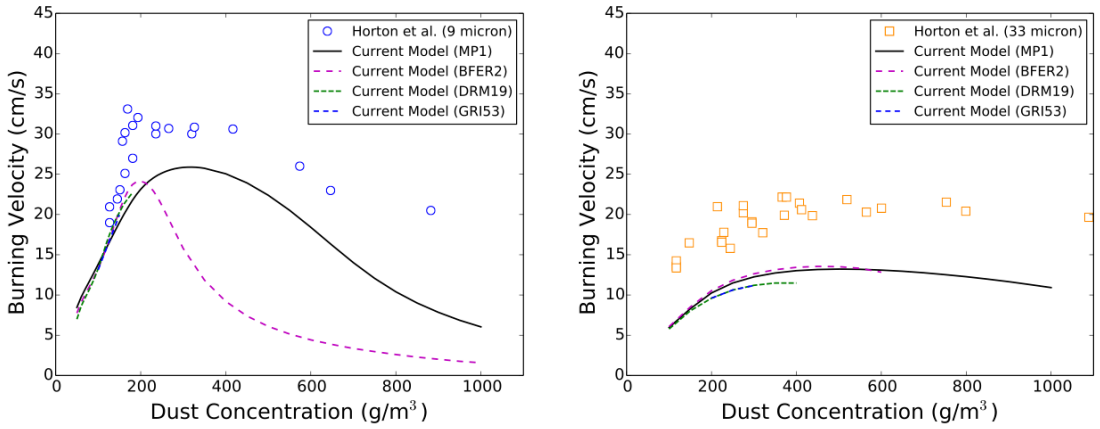

(a) $d_p = 10\,\mu m$ (b) $d_p = 33\,\mu m$

Figure 6.15: Coal dust burning velocity at ambient temperature with different reaction mechanisms compared to the experimental results of Horton et al. [77].

For 10 µm particles, the burning velocity agrees within 10 % for all reaction mechanisms up to a dust concentration of 180 g/m^3, except at the lowest concentration near the LFL. The 180 g/m^3 concentration represents equivalence ratios of $\Phi_p^t = 2.11$ and $\Phi_p^v = 1.05$. Beyond this concentration, the burning velocity with the BFER2 mechanisms drops rapidly and the DRM19 and GRI53 mechanisms do not produce propagating flames.

For 33 µm particles, the burning velocity using the BFER2 and MP1 mechanisms is similar up to 600 g/m^3. GRI53 and DRM19 mechanisms predict lower burning velocities due to incomplete methane consumption in the flame. All mechanisms agree within 10 % of each other under the conditions for which each could produce a propagating flame.

Comparing the 10 and 33 µm burning velocities presented in Figure 6.15 shows that reaction chemistry plays a more important role in the propagating flames as the particle diameter is reduced. Figure 6.15 also shows relatively good agreement between the reaction mechanisms up to volatile equivalence ratios of 1.0 ($\sigma_p = 170$ g/m^3). Overall, the MP1 reaction model shows the best agreement with the experimental data and is

able to capture the qualitative burning velocity trends throughout the full concentration range. Although increasing the initial system temperature increases the predicted burning velocity, it does not alter the agreement between the reaction mechanisms, the qualitative behaviour of the BFER2 mechanism for 10 µm particles, or the limits for which the multistep mechanisms are able to sustain flame propagation.

6.3 Role of Discrete Combustion

The literature simulation models outlined in Table 3.4 employ a Eulerian discretization of the particles in which the coal dust cloud is treated as a continuous medium. This is typically justified using an analogy to droplet flames that illustrates continuum behaviour above equivalence ratios of 0.7 [178], although applicability to solid particles has not been demonstrated, and the effect of particle diameter is not taken into account.

Since the current simulation model uses a Lagragian discretization, a discrete representation of the particles can be achieved by letting each Lagrange group be equivalent to a single particle. This approach is described further in Section 4.2.2. Comparing flame propagation between the continuum and discrete representations allows the applicability of the continuum assumption to be explored and the impact of discrete combustion on burning velocity to be quantified.

6.3.1 Flame Propagation

Cloney et al. [36] performed simulations using the continuum and discrete particle representations to explore the applicability of the continuum assumption. Based on this work, the transient flame position as a function of time is shown in Figure 6.16 for 4 µm particles at a 144.3 g/m^3 concentration using the MP1 and DRM19 reaction mechanisms. The dashed lines in Figure 6.16 indicate steady flame fits for each simulation. These fits give burning velocities of 27.3, 24.5, 23.5, and 21.2 cm/s for the MP1 continuum, MP1 discrete, DRM19 continuum, and DRM19 discrete models, respectively.

A decrease in the burning velocity is observed when using the discrete representation of the particles compared to the continuum representation. The inserts in Figure 6.16 demonstrate the reason for this velocity deficit. When the particles are

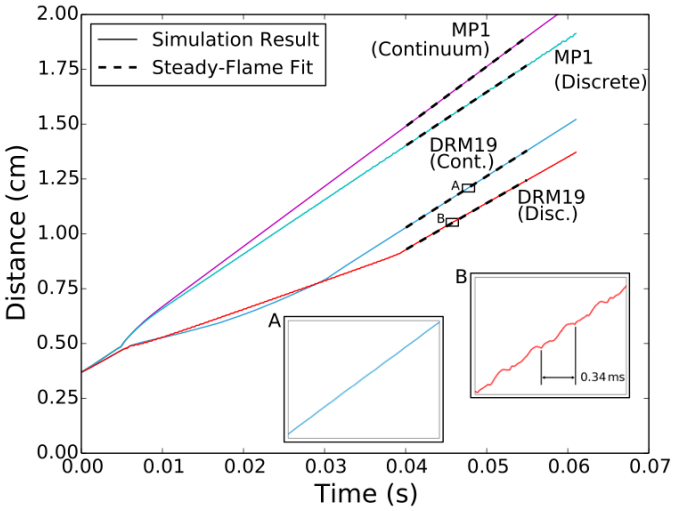

Figure 6.16: Flame position versus time using MP1 and DRM19 mechanisms and continuum and discrete particle representations. Particle diameter is 4 µm and concentration is 144.3 g/m^3. The insets "A" and "B" show a close-up of the DRM19 flame position using the continuum and discrete particle representations, respectively.

modeled discretely, the flame accelerates as each particle undergoes devolatilization, ignition, and later surface reaction, and then decelerates in between the particles. The oscillations have a repeated structure with a large increase in displacement due to particle devolatilization and ignition, and a second smaller increase in displacement due to surface reaction. This double oscillation structure is demonstrated in insert "B" in Figure 6.16 where a single oscillation period is highlighted.

For a particle concentration of 144.3 g/m^3, the normalized particle spacing (L_s/d_p) is computed in Equation 4.2 as 16.8. This gives a centre-to-centre spacing between adjacent particles of 67.1 µm for a 4 µm particle diameter. At this spacing, the flame takes an average of 0.43 ms to cross between particles which is close to the oscillation period shown in the Figure 6.16 insert "B". The MP1 flame position for the discrete simulation also oscillates at a period of approximately 0.57 ms (not shown in the figure).

Flame structure from the DRM19 simulation with the discrete particle representation is presented in Figure 6.17. Figure 6.17 highlights the time at which particle ignition occurs (61.06 ms) and a time in between particle ignition (61.28 ms). These two times are separated by 0.22 ms, which is approximately half of the oscillation period shown in Figure 6.16.

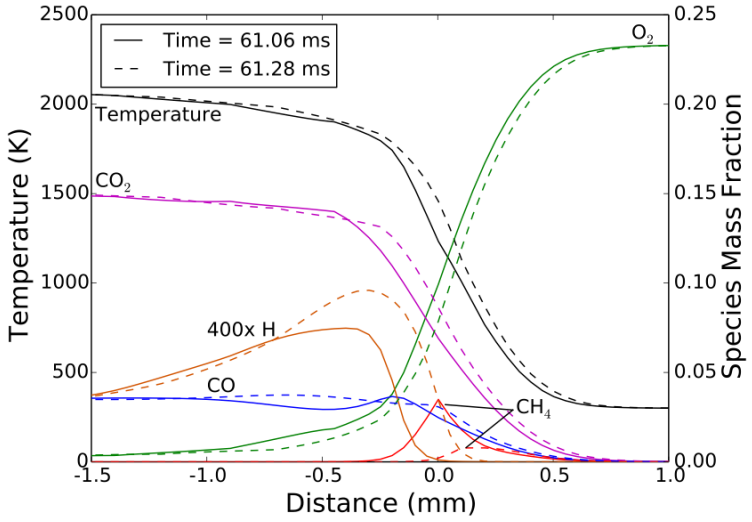

Figure 6.17: Flame profile using DRM19 chemistry model and a discrete particle representation. The two times shown represent the time at which the highest methane concentration is reached (61.06 ms) and the time at which the lowest methane concentration is reached (61.28 ms) throughout one flame crossing cycle.

The local spikes in species mass fraction and temperature in Figure 6.17 demonstrate the positions where the particles act as point sources during surface reaction and devolatilization. The spike in methane concentration in the reaction zone at 61.06 ms is from particle devolatilization and ignition. At 61.28 ms the methane specie profile is more diffuse as the flame moves forward into the particle cloud. Along with mass diffusion between methane and oxygen, thermal diffusion drives the flame forward to the next particle. This process limits flame propagation and causes the overall burning velocity to decrease when the particles are modeled discretely.

It is interesting to note that the centre-to-centre particle spacing changes throughout the flame and behind the reaction zone. This spacing can be inferred in Figure 6.17 by comparing the local peak in CH_4 and the local peak in CO_2 for 61.06 ms. These peaks correspond to two adjacent particles, where the first one at 0.0 mm is undergoing devolatilization and the second one at -0.45 mm is undergoing surface reaction. In Figure 6.17, these particles are separated by 450 µm, which is almost seven times larger than the initial particle spacing. It can not be seen in Figure 6.17, but the final centre-to-centre particle spacing behind the flame is actually closer to 515 µm. This expansion of the reacting particle cloud may further increase the impact of discrete combustion on propagating dust flames.

6.3.2 Burning Velocity

The burning velocity for 10 and 33 µm particles using the discrete particle representation is compared to the continuum representation in Figure 6.18. The MP1 reaction mechanism is used in these simulations and results are presented at various initial system temperatures.

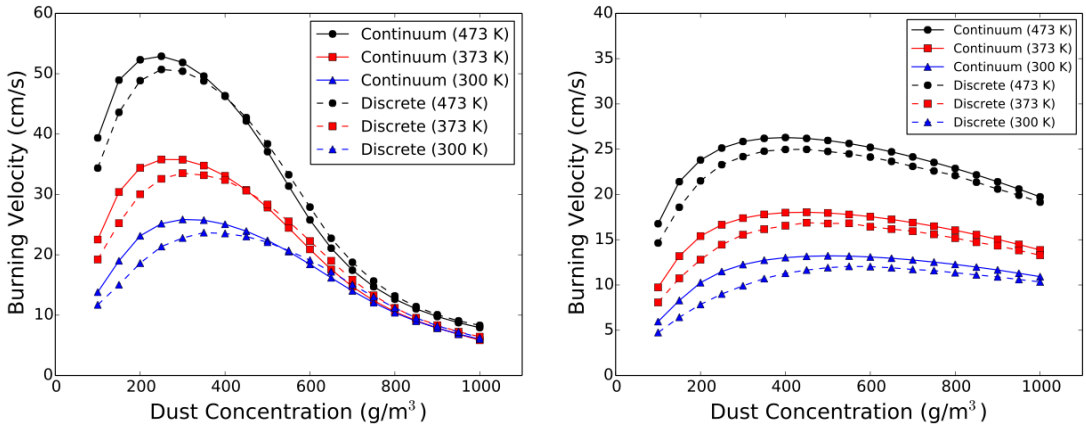

(a) $d_p = 10\,\mu m$ (b) $d_p = 33\,\mu m$

Figure 6.18: Coal dust burning velocity using the continuum and discrete particle representations at different initial temperatures with the MP1 reaction mechanism.

For 10 and 33 µm particles, the continuum modeling assumption resulted in a 25 % increase in burning velocity at low dust concentrations [36]. The current model also predicts a 5 to 10 % decrease in burning velocity at higher dust concentrations for 10 µm particles. At fuel-rich concentrations above 170 g/m^3, the flame may accelerate in the spacing between the particles due to the leaner fuel concentration and lower heat loss than when a continuum representation is assumed.

As discussed above, most theoretical modeling work for dust flames uses the assumption from droplet combustion that interaction between the flame and particle cloud can be treated as a continuum for equivalence ratios greater than 0.7 [178]. This equivalence ratio gives a dust concentration around 120 g/m^3 for the coal particles modeled in this work, taking only the volatile content into consideration.

The simulation results presented in Figure 6.15 demonstrate that discrete particle effects decrease the burning velocity up to 400 g/m^3 for 10 µm particles. This gives an equivalence ratio greater than 2, which is much larger than the value used for droplet

combustion. Furthermore, discrete combustion lowers the burning velocity for 33 µm particles throughout the entire concentration range, demonstrating that the limits of applicability of the continuum assumption depend on the particle diameter. These results suggest a need to revisit the magnitude and limits of the continuum modeling assumption traditionally used for theoretical modeling of dust flame propagation.

6.4 Flame Structure

Simulations from the MP1 reaction mechanism with 10 µm particles are analyzed to determine the different coal dust flame structures. These are used to identify flame characteristics at different equivalence ratios and to produce combustion regimes relevant to hybrid mixtures in the dust-driven explosion regime.

6.4.1 Simulation Results

Temperature and species mass fraction profiles predicted using the MP1 reaction mechanism are shown in Figure 6.19 for different dust concentrations. All of the flame profiles are taken 50 ms into the simulation, at which time the flame propagation is steady and the profile and burning velocity do not change with time.

Figure 6.19 (a) illustrates the flame structure at $50\,\mathrm{g/m^3}$. The total equivalence ratio ($\Phi_\mathrm{p}^\mathrm{t}$) at $50\,\mathrm{g/m^3}$ is 0.57. Since the overall stoichiometry is fuel lean, all of the dust is consumed close to the reaction front. This is indicated by the arrow in Figure 6.19 (a), where the dust is completely consumed and the temperature and species profiles are constant downstream from this location. The maximum temperature at this dust concentration is 1600 K.

Although the maximum temperature and burning velocity increases with dust concentration, the flame structure remains similar to $50\,\mathrm{g/m^3}$ until $\Phi_\mathrm{p}^\mathrm{t}$ approaches 1.0. Figure 6.19 (b) illustrates the flame structure at $90\,\mathrm{g/m^3}$, which is slightly higher than the stoichiometric value of $85\,\mathrm{g/m^3}$. At this concentration, a thickened flame forms, where the temperature continually increases to an asymptomatic value several millimetres downstream from the reaction front.

The thickened flame structure occurs due to the diffusion limited nature of the coal dust surface reaction. The surface reaction rate is dependent on the diffusion of oxygen toward the particle surface, which in turn depends on the mass fraction

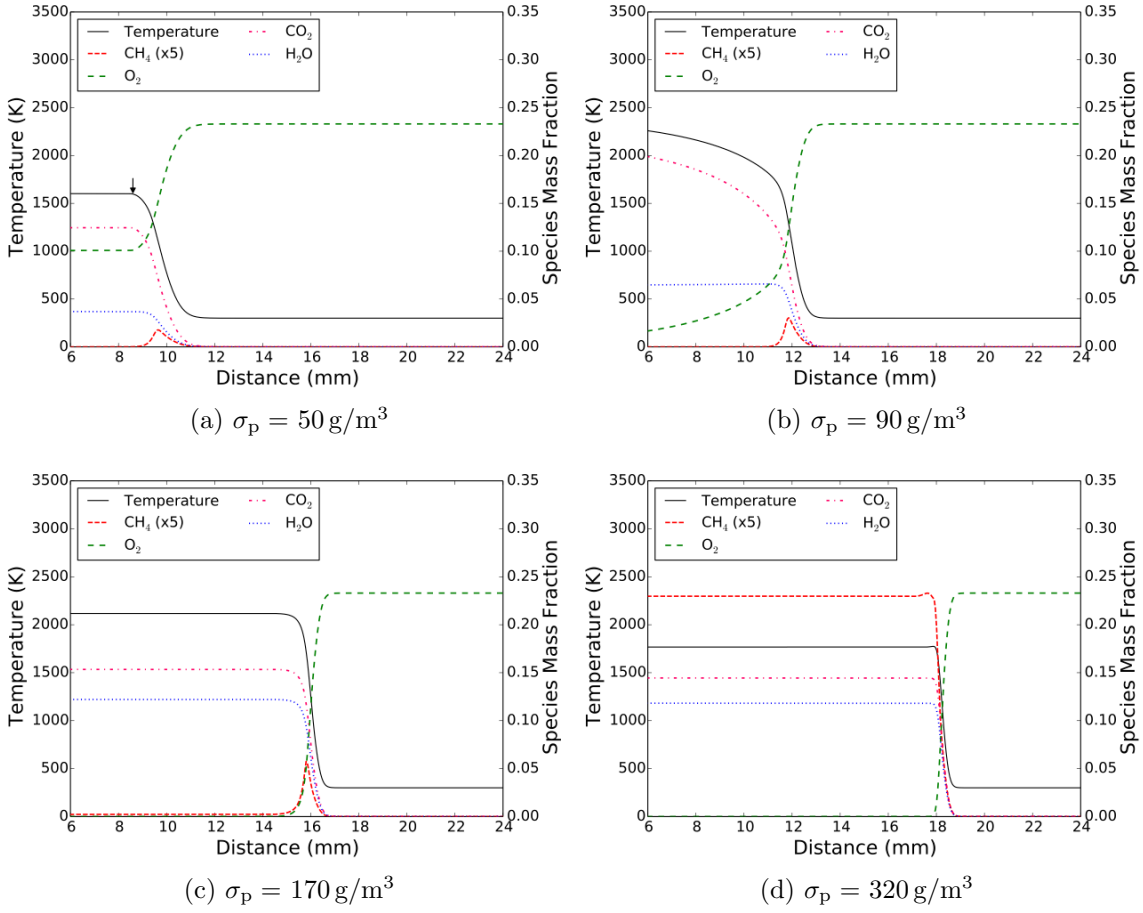

(a) $\sigma_p = 50\,g/m^3$ (b) $\sigma_p = 90\,g/m^3$

(c) $\sigma_p = 170\,g/m^3$ (d) $\sigma_p = 320\,g/m^3$

Figure 6.19: Coal dust flame structure at ambient temperature with different dust concentrations and using the MP1 mechanism and continuum particle representation.

of oxygen in the vicinity of the particle. As the particle moves downstream more oxygen is consumed. This in turn decreases the surface reaction rate. This process occurs continuously and causes the long, slow increase in temperature behind the initial reaction front.

Although the flame continually increases towards the adiabatic temperature in the thickened flame, the reaction kinetics depends on temperature near the flame front. As the dust concentration increases, more volatiles are available in the flame front, which react promptly instead of the slower burning carbon. This causes an increase in the burning velocity with dust concentration in the thickened flame region.

The thickened flame region terminates near $170\,g/m^3$, where the volatile component equivalence ratio (Φ_p^v) is equal to 1.0. At this concentration, all of the oxygen is consumed near the reaction front, and the maximum flame temperature of 2120 K

occurs. The predicted flame structure at 170 g/m^3 is illustrated in Figure 6.19 (c). As seen in Figure 6.19 (c), some methane remains downstream from the flame at 170 g/m^3, suggesting that a small amount of carbon burning occurs through the flame thickness.

Unlike gas flames, the maximum burning velocity for the dust flame does not occur at the stoichiometric concentration considering only the volatiles, but at a higher concentration of 320 g/m^3. As the dust concentration increases, the amount of methane remaining in the flame products increases, the maximum flame temperature decreases, and the maximum burning velocity increases.

The flame structure at 320 g/m^3 is shown in Figure 6.19 (d). Note that the amount of volatiles in the flame products is quite high at 4.6 % by mass, and that the flame temperature is reduced to 1760 K.

6.4.2 Combustion Regimes

The flame structure analysis leads to the definition of four coal dust flame types or combustion regimes. Figure 6.20 shows the burning velocity calculated with the MP1 reaction mechanism. The plot is subdivided by vertical lines to demonstrate the extent of each of the combustion regimes, labeled using the Roman numerals I through IV. The characteristics of each regime are outlined in the following.

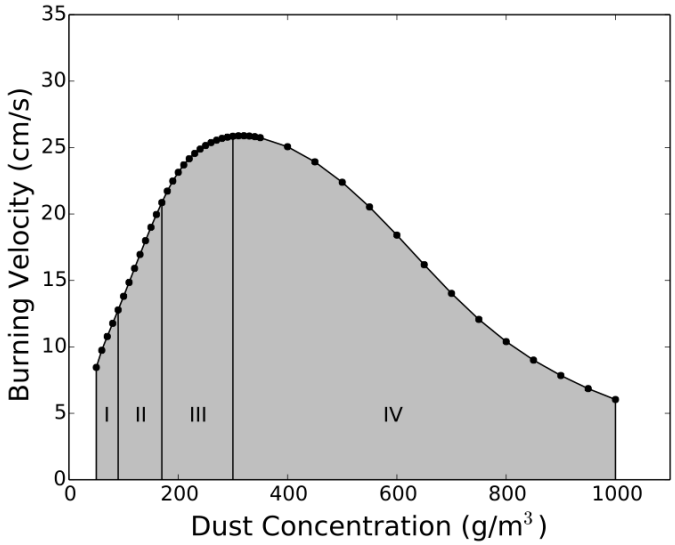

Figure 6.20: Coal dust combustion regimes predicted from flame structure analysis.

Type I (Fuel-Lean Flames)

Type I flames occur when the total dust concentration is below stoichiometric. As shown in Figure 6.19 (a), both the carbon and volatile components of the dust are consumed in the vicinity of the reaction front for 10 µm particles and oxygen is transported downstream into the flame products. Burning velocity and flame temperature increase with dust concentration, and the predicted values for the different gas-phase reaction models are similar, as shown in Section 6.2.3.

Type II (Volatile-Lean or Thickened Flames)

Type II flames lie in the region between the total stoichiometric dust concentration ($\Phi_p^t = 1.0$) and volatile component stoichiometric concentration ($\Phi_p^v = 1.0$). Under the diffusion-limited surface reaction assumption, these flames demonstrate a very thick temperature profile, with oxygen being completely consumed far downstream from the reaction front. Like Type I flames, burning velocity and flame temperature increase with dust concentration, and similar values are predicted for each mechanism.

Type III (Volatile-Rich Flames)

Type III flames lie between the volatile component stoichiometric dust concentration ($\Phi_p^v = 1.0$) and the maximum burning velocity. All of the oxygen is consumed near the reaction front and excess volatiles are transported into the reaction products downstream. The flame temperature decreases from a maximum value at the volatile component stoichiometric concentration, but the burning velocity increases.

Type IV (Transition Flames)

Type IV flames lie above the maximum burning velocity. Flame structure is similar to Type III flames, but heat loss to the particles and excess volatiles overcome the energy provided by surface and gas-phase reactions. Both flame temperature and burning velocity decrease with increased dust concentration. The simulations presented in Section 6.2.3 suggest that reaction chemistry plays a critical role in Type III and IV flames.

6.5 Discussion of Results

Coal dust flame simulations allowed flame structure, the role of discrete combustion, the role of reaction mechanism, and the accuracy of the CFD model for coal flames to be explored. Analysis of flame structure at different dust concentrations allowed four combustion regimes to be identified: fuel-lean flames, volatile-lean flames, volatile-rich flames, and transition flames. Each flame type has specific characteristics with respect to burning velocity, flame temperature, and fuel or oxidizer species concentration downstream from the flame front. Discrete combustion lowered the burning velocity of coal dust flames up to dust concentrations of $400\,\mathrm{g/m^3}$ for $10\,\mu\mathrm{m}$ particles and through the full concentration range simulated for $33\,\mu\mathrm{m}$ particles.

6.5.1 Implications for Hybrid Mixtures

The four combustion regimes identified for coal dust are anticipated to be present for hybrid mixtures with methane gas at low concentrations. These mixtures correspond to the dust-driven explosion regime proposed by Garcia-Agreda et al. [29]. The dust-only results demonstrate the importance of the volatile component and total equivalence ratio on flame structure. As methane gas is added, this equivalence ratio will change, reducing the dust range over which each regime applies.

The results from the discrete combustion simulations also provide insight into potential hybrid flame structures. Previously, Cloney et al. [65] proposed that burning velocity enhancement from adding small amounts of methane gas to coal dust would be larger in the discrete combustion regime. The results from this chapter demonstrate that this regime is wider than predicted from spray droplet analysis and that the limits depend on particle diameter.

6.5.2 Practical Implications

In addition to providing insight into hybrid flame structure, the coal dust combustion regimes provide a way to classify experiments performed in open tubes and burners. By comparing measurements of the flame temperature, burning velocity, and species concentrations behind the flame at increasing dust concentrations, the different flame structures can be identified for a given dust.

For example, the four combustion regimes identified in this chapter are summarized in Table 6.1. Three flame characteristics are identified: the maximum flame temperature, the burning velocity, and the species mass fraction of oxygen or methane behind the flame front.

Table 6.1: Summary of coal dust combustion regimes and flame characteristics with increasing dust concentration. T_f is flame temperature, S_L is burning velocity, and $Y_{k,\mathrm{f}}$ is mass fraction of species k downstream from the reaction front.

Regime	**Flame Type**	**Upper Limit**	$\boldsymbol{T_\mathrm{f}}$	$\boldsymbol{S_\mathrm{L}}$	$\boldsymbol{Y_{k,\mathrm{f}}}$
Type I	Fuel-Lean Flame	$\Phi_\mathrm{p}^\mathrm{t} = 1.0$	$\uparrow$	$\uparrow$	$Y_{\mathrm{O}_2} > 0.0$
Type II	Volatile-Lean Flame	$\Phi_\mathrm{p}^\mathrm{v} = 1.0$	-	$\uparrow$	$Y_{\mathrm{O}_2} = 0.0$
Type III	Volatile-Rich Flame	Max S_L	$\downarrow$	$\uparrow$	$Y_{\mathrm{CH}_4} > 0.0$
Type IV	Transition Flame	-	$\downarrow$	$\downarrow$	$Y_{\mathrm{CH}_4} > 0.0$

In comparing measured flame temperature, burning velocity, and species mass fractions to the combustion regimes given in Table 6.1, the concentration at which $\Phi_\mathrm{p}^\mathrm{t} = 1.0$ and $\Phi_\mathrm{p}^\mathrm{v} = 1.0$ can be determined for coal with an unknown composition. Furthermore, these parameters can be determined for any dust that reacts through homogeneous and heterogeneous processes, even when the stoichiometry is hard to define. This provides information that is not easily available for dust where the chemistry reactions are not well known and insight into the flame propagation process or interaction in hybrid mixtures.

6.5.3 Accuracy of the CFD Model

The results presented in Section 6.2.3 demonstrate that the different reaction mechanisms play a lesser role in coal dust flames than in methane flames when flame propagation is achieved. The maximum difference in laminar burning velocity is approximately 10 % for 10 and 33 µm particles as shown in Figure 6.15, compared to 50 % for methane flames (see Figure 5.10). Distance-time plots presented in Figure 6.10 demonstrate that flame propagation cannot be achieved for the multistep mechanisms at high dust concentrations. Under these conditions, the flame temperature is reduced such that intermediate reactions are arrested in the flame front.

Even with the unity Lewis number assumption and the single-step MP1 reaction mechanism, coal dust burning velocity compared more favourably to the available experimental data than previous CFD models in the literature. The results in Figure 6.5,

Figure 6.6, and Figure 6.7 demonstrate that the current model is able to capture qualitative burning velocity features such as finer coal particles shifting peak burning velocity to leaner dust concentration, coarser dust particles having a higher burning velocity at very rich concentrations, and increasing system temperature widening the overall flammability limits. Furthermore, quantitative agreement between burning velocities may be achieved once preheating in the experimental system is accounted for, as shown in Figure 6.7. Overall, the CFD models of Smoot and Horton [78] and Park and Park [38] failed to capture these qualitative and quantitative features to the same degree as the current model even though more detailed approaches were used for devolatilization, surface reaction, mass diffusion, and radiation.

Determining the effect of the unity Lewis number assumption on the results of the current model is not straight forward due to insufficient experimental or simulation results for comparison. Comparison of flame structure using the DRM19 reaction mechanism for 4 µm particles to the CFD model of Bradley et al. [60] shows reduced consumption of intermediate gaseous species in the flame front. However, this is combined with an increased burning velocity from the current model, which is the opposite of that seen for gas flames. Direct comparison between the two models is made more difficult by differences in the transport models, thermophysical parameters, and solution routines used in each.

Overall, these results suggest a need for more research into the fundamental flame propagation processes for dust flames. Investigation into detailed reaction models at high fuel concentrations and low temperatures may be needed to determine the correct mechanisms for dust flames. Furthermore, the role of multispecies diffusion and radiation at the scale of the flame front is not well understood. Although it would be tempting to state outright that more detailed modeling of devolatilization, surface reaction, gas-phase kinetics, and radiation would provide a better prediction of burning velocity, comparison to the experimental observations given in this chapter leaves room for this statement to be questioned. The current CFD model gives a novel platform not available in the literature from which the effects of these models can be explored individually in the future.

Chapter 7

Hybrid Flames

This chapter presents the investigation of hybrid mixture burning velocity. After verification of the computational model, an analysis of the dust and gas timescales involved in hybrid flames, the role of volatile and total equivalence ratio on burning velocity, and the impact of discrete particle combustion are given. Novel combustion regime diagrams are developed illustrating interaction between the coal dust and methane gas combustion processes in hybrid mixtures. This chapter concludes with a discussion of the newly developed combustion regime diagrams, practical implications compared to closed-chamber explosion regimes, the role of discrete combustion in hybrid flames, and verification of the CFD model.

7.1 Model Verification

Hybrid flame results from the current model for mixtures of coal dust and methane gas are verified by comparing burning velocity predictions to the experimental data of Xie et al. [80], Lee et at. [82], and Horton et al. [77]. Coupling between gas and dust flames at different particle diameters is demonstrated in the dual-fuel regime of Garcia-Agreda et al. [29], followed by heat loss to large particles (75–95 µm) at different system temperatures. Lastly, burning velocity enhancement in the dust-driven regime from small amounts of methane gas is explored. The MP1 reaction mechanism is used for all of the simulations presented in this section.

7.1.1 Coupling Interaction

Coupling interaction in the dual-fuel regime of Garcia-Agreda et al. [29] is explored by comparing simulation results to the experimental work of Xie et al. [80]. In their work, Xie et al.[80] used an experimental dust burner apparatus and shadowgraph technique to measure the burning velocity of methane gas and Pittsburgh seam coal with different particle size ranges.

Figure 7.1 presents normalized burning velocity from the experimental work of Xie et al. [80] compared to current simulation results. In each case, the burning velocity under hybrid conditions is normalized by the burning velocity of the gas flame. This is required because the experimental apparatus tends to underpredict the burning velocity due to heat loss, while the current simulation model overpredicts it. For example, Xie et al. [80] predicted a methane flame burning velocity of 18 cm/s at an equivalence ratio of 0.8, where the current model predicts 31 cm/s. This is compared to the experimental data [164, 165, 166] reported in Figure 5.10, which gives a burning velocity of approximately 27 cm/s at this concentration.

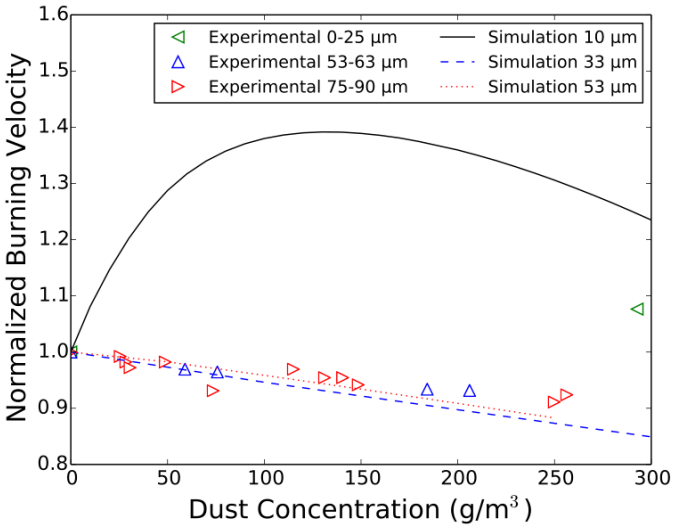

Figure 7.1: Comparison of hybrid flame normalized burning velocity for coal dust and methane gas to the experimental data of Xie et al. [80]. The 0–25 µm experimental results and 10 µm simulations have an initial gas phase equivalence ratio of 0.75, while the remainder of experiments and simulations have an initial gas phase equivalence ratio of 0.8.

Once normalized by the gas burning velocity, the results of Xie et al. show that particle sizes ranging from 53 to 90 µm only tend to reduce the burning velocity of the gas flame. On the other hand, the experiment with a particle size less than 25 µm shows an increase in burning velocity. This increase in burning velocity is predicted with the current model where uniform sizes of 33 µm and 53 µm only act to reduce the burning velocity, while a particle size of 10 µm enhances it. These results demonstrate that interaction between the premixed gas flame and particle combustion in the dual-fuel regime is qualitatively captured using the current model.

Quantitative comparisons are difficult due to differences in the coal particle properties and particle size distribution, and experimental effects not captured in the simulation model, including heat loss to the apparatus.

7.1.2 Effect of Initial Temperature

Burning velocity in the dual-fuel regime is further explored by comparing simulation predictions to the experimental results of Lee et al. [82]. These authors modified the burner apparatus of Xie et al. [80], and investigated burning velocity of hybrid mixtures of methane gas and Pittsburgh seam coal at different initial temperatures. The methane gas equivalence ratio was varied between 0.9 and 1.2 and particle concentration was less than $150\,\mathrm{g/m^3}$. A single particle size distribution between 75 and 90 µm was investigated in their work. Figure 7.2 presents normalized burning velocity from the experimental work of Lee et al. [82] compared to the current model with a fixed particle size of 75 µm. Burning velocity is again normalized to methane burning velocity, to account for underprediction in the experiments due to heat loss and overpredication in the simulations due to the MP1 reaction mechanism. Once burning velocity is normalized, the 400-K results are offset by positive 0.2 on the ordinate and the 300-K results are offset by negative 0.2 on the ordinate, so that they can be visualized on the same plot along with the 350 K results, which are not offset.

Overall, the results presented in Figure 7.2 demonstrate relatively little impact on methane burning velocity from adding coal dust in the 75 to 90 µm size range. The maximum increase in burning velocity is around 7 % for $\Phi_\mathrm{g} = 1.0$ and $\sigma_\mathrm{p} = 50\,\mathrm{g/m^3}$, and the maximum decrease is around 11 % for $\Phi_\mathrm{g} = 1.2$ and $\sigma_\mathrm{p} = 150\,\mathrm{g/m^3}$. This relatively insensitive burning velocity with respect to particle concentration is captured in both the experimental and simulation results.

Burning velocity shows a slight increase at $50\,\mathrm{g/m^3}$ followed by a decrease at higher concentrations for $\Phi_\mathrm{g} = 0.9$ (Figure 7.2 (a)). The burning velocity profile tends to level out at a higher initial temperature, with coal dust having very limited impact at 400 K. These effects are relatively well captured in the simulation results. At $\Phi_\mathrm{g} = 1.0$ (Figure 7.2 (b)), the same trends generally hold, with the predicted burning velocity showing less agreement for 50 and $100\,\mathrm{g/m^3}$ at ambient temperature.

The experimental results for $\Phi_\mathrm{g} = 1.2$ (Figure 7.2 (c)) demonstrates monotonically

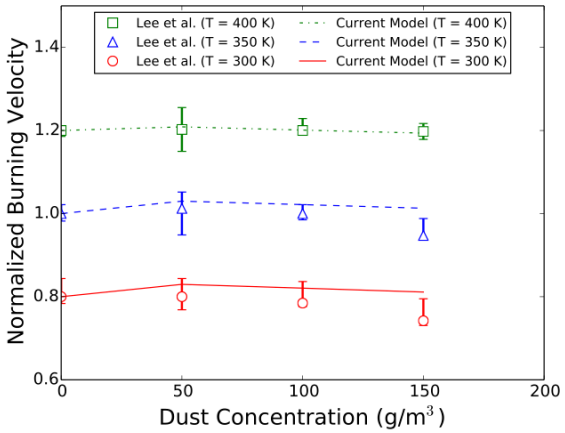

(a) $\Phi_g = 0.9$

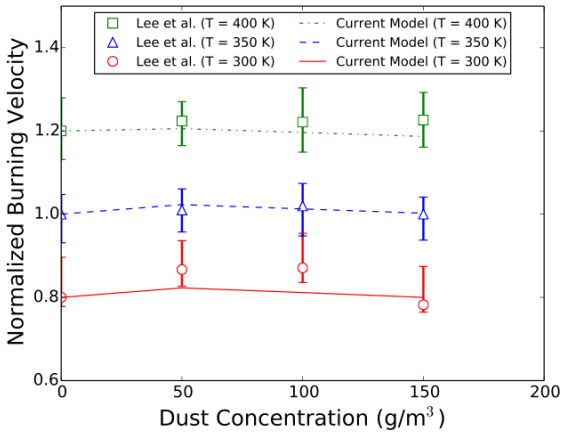

(b) $\Phi_g = 1.0$

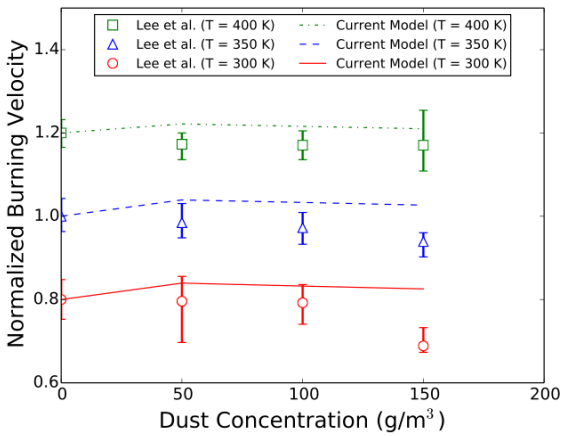

(c) $\Phi_g = 1.2$

Figure 7.2: Comparison of hybrid flame normalized burning velocity to the experimental data of Lee et al. [82] at different gas equivalence ratios and initial temperatures. Particles have a size distribution between 75 and 90 µm for the experimental results and fixed size of 75 µm for the simulations. Once normalized, the 300 and 400-K results are offset by negative 0.2 and positive 0.2 on the ordinate, respectively.

decreasing burning velocity with the addition of coal dust. Comparison with the simulation results demonstrate a limitation of the MP1 reaction mechanism, which predicts a small increase in burning velocity at low dust concentrations. Furthermore, the extent of the burning velocity reduction at 100 and 150 g/m^3 is not as large as the experimental results. These findings, as well as the burning velocity comparison given for methane flames in Figure 5.10, suggest that the MP1 reaction mechanism may not correctly capture burning velocity for hybrid mixtures with the initial methane concentration near stoichiometric or fuel-rich concentrations.

7.1.3 Burning Velocity

To the author's knowledge the only hybrid burning velocity measurements for mixtures of methane gas and coal dust throughout a larger dust concentration range are provided in the experimental work of Horton et al. [77]. In addition to exploring the impact of particle diameter as outlined in Section 6.1.3, Horton et al. [77] did one set of experiments with the addition of 2 % methane gas. These concentrations fall under the dust-driven regime of Garcia-Agreda et al. [29]. The particle size distribution for the experiments had a cumulative mass fraction of 50 % below 33 µm.

Figure 7.3 presents the experimentally determined burning velocities of Horton et al. [77] compared to predictions from the simulation model. As discussed in the literature by Bradley et al. [37] and demonstrated in Section 6.1.4, the experimental measurements from Horton et al. [77] may be artificially high due to preheating of the fuel mixture by the flame-holding screen. As such, the simulations presented in Figure 7.3 are completed at an initial temperature of 373 K.

As shown previously in Figure 6.7, the burning velocity of 33 µm particles at 373 K is underpredicted between 10 and 30 % throughout the concentration range presented. A similar underprediction is present for the hybrid mixture with 2 % methane.

The simulation results presented in Figure 7.3 capture a shift in maximum burning velocity to lower dust concentrations for hybrid mixtures, along with a decrease in enhancement effects at high dust concentrations above 700 g/m^3. Overall, the maximum increase in the burning velocity is 20–25 % for both the simulation results and experimental measurements over the concentration range presented. Although the scatter data in Figure 7.3 appears to suggest that the burning velocities may cross

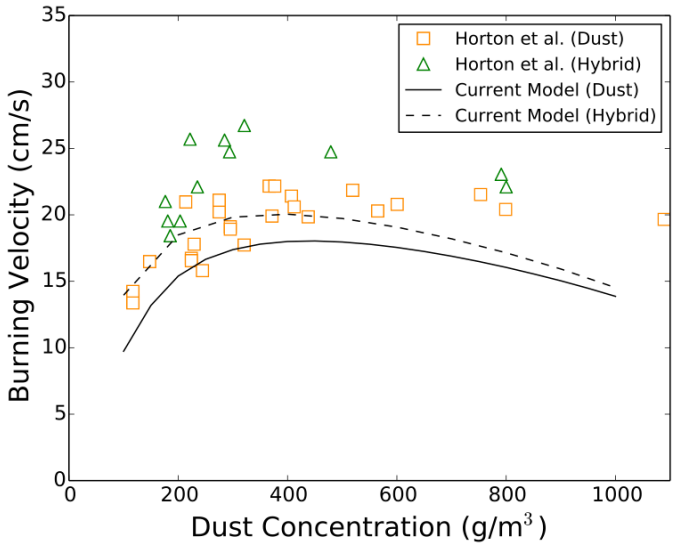

Figure 7.3: Comparison of hybrid burning velocity for 33 µm coal particles with methane gas to the experimental data of Horton et al. [77] with a particle size distribution (cumulative mass fraction of 50 % below 33 µm). Simulations are performed at an initial system temperature of 373 K using the MP1 reaction mechanism.

when extrapolated to lower dust concentrations, this does not occur for the lines of best-fit to the data presented by Horton et al. [77] (not reproduced here) or the simulation results.

7.2 Timescale Analysis

In order for dust particles to contribute to energy release within the hybrid flame, they must be sufficiently heated to cause devolatilization or surface reaction within the reaction front. Furthermore, heating must occur before devolatilization or surface reaction as these are serial processes. Interaction between these processes is characterized by their associated timescales and has a critical impact in the gas-driven and dual-fuel regimes of flame propagation.

The timescales for dust heating, devolatlization, surface reaction and gas flame reaction are described by Equation 3.67, Equation 3.71, Equation 3.79 and Equation 5.1, respectively. The particle diameter has a large impact on both heating and surface reaction, and the impact on hybrid flame burning velocity is explored in the following sections.

7.2.1 Calculated Timescales

Figure 7.4 presents the particle heating, devolatilziation, and surface reaction timescales as a function of particle diameter. Particle heating is calculated assuming $C_s^* = 1650\,\mathrm{J/kg\text{-}K}$, $\rho_p = 1300\,\mathrm{kg/m^3}$, $\lambda_s = 0.13\,\mathrm{W/m\text{-}K}$, and $\mathrm{Nu} = 2.0$. Particle devolatilziation is calculated assuming $T_p = 1000\,\mathrm{K}$. Particle surface reaction is calculated assuming $D_s = 0.0001\,\mathrm{m^2/s}$, $Y_{O_2} = 0.2$, $\rho = 1.168\,\mathrm{kg/m^3}$, and $\frac{T_p+T}{T_p} = 2.0$. The devolatlization timescale is independent of particle diameter but depends exponentially on particle temperature. The gas flame residence time at equivalence ratios of 0.6, 0.8, and 1.0 from Table 5.1 are also presented as horizontal lines in Figure 7.4.

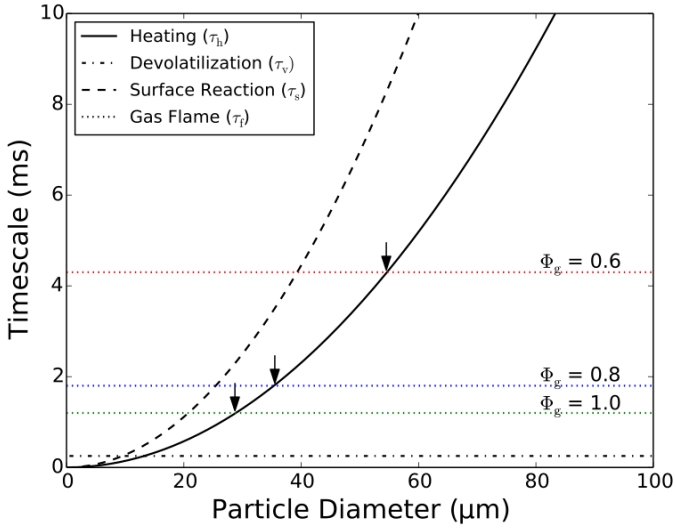

Figure 7.4: Particle heating, devolatilization, and surface reaction timescales compared to flame residence time measured from the gas flame simulations. The symbols and arrows show the cross-over particle diameters below which heating is faster than flame residence timescale.

In order for hybrid enhancement to occur, the particle must heat up enough that devolatilization and gas-phase reaction can take place or surface reaction occurs in the flame residence time. In Figure 7.4, particle surface reaction is much slower than devolatilization and therefore homogeneous reaction will be the main contributor to flame propagation. Furthermore, particle devolatilization is fast with a timescale of 0.25 ms at 1000 K. This timescale further decreases by an order of magnitude if the particle temperature is increased to 1100 K.

These results demonstrate that the particle reaction process in hybrid mixtures

is dominated by the heating timescale under the conditions assumed in this work. In Figure 7.4, the particle diameters below which particle heating is faster than the gas flame residence time are indicated with arrows. These diameters represent the minimum particle size required to have hybrid flame enhancement from this timescale analysis. The specific values are 57, 36, and 29 µm for equivalence ratios of 0.6, 0.8, and 1.0, respectively.

7.2.2 Simulation Results

To illustrate the impact of the particle time scales on hybrid flame propagation, simulations are performed at a fixed dust concentration of 100 g/m^3 with different particle diameters. This concentration represents a total equivalence ratio of 1.17 and volatile component equivalence ratio of 0.59.

The results of the hybrid flame analysis are summarized in Figure 7.5. Each symbol in the figure indicates a burning velocity measured from one simulation. Closed symbols indicate results with nonreacting particles where only heat loss is included, and open symbols indicate reacting particles with devolatilization and surface reaction. The black arrow denotes the cross-over particle diameters from the timescale analysis, where particle heating is faster than the gas flame residence time.

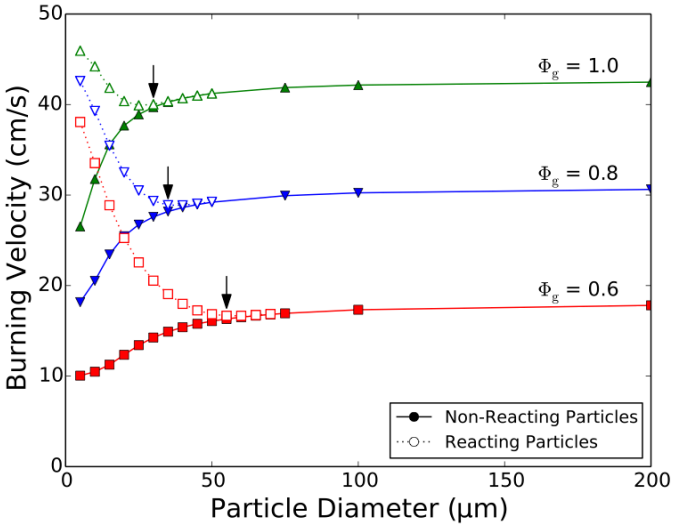

Figure 7.5: Effect of particle size on the burning velocity for hybrid mixtures of reacting and nonreacting particles. The particle concentration is 100 g/m^3 and the arrows indicate particle cross-over diameters from the timescale analysis.

At large particle diameters above 100 µm, dust heating is slow and the presence of the particles has a limited impact on gas burning velocity. As the particle diameter is reduced towards the cross-over diameter, heat loss to the dust begins to decrease the burning velocity. Following the closed symbols in Figure 7.5, the extent of the particle heat loss effect on the gas flame is demonstrated.

The open symbols in Figure 7.5 show the enhancement effect of reacting particles on the hybrid flame. Open symbols are not shown for 75, 100, and 200 µm particles, but the burning velocity is identical to the nonreacting particle case. The burning velocity is also similar in the reacting and nonreacting particle simulations at all particle sizes above the cross-over diameter. Under these conditions, the particles do not heat up fast enough to release volatiles or react in the flame.

Once the particle size is reduced below the cross-over diameter, enhancement of the gas flame burning velocity occurs. Under these conditions, the particles heat up fast enough to release their volatiles in the flame front. As demonstrated in Section 7.1.2, overall burning velocity enhancement at $\Phi_g = 1.0$ may be overpredicted with the MP1 reaction mechanism. However, agreement between the simulation results and timescale analysis demonstrates that coupling between the gas flame and particle combustion plays an important role in hybrid flame propagation behaviour and is captured in the model.

7.3 Role of Equivalence Ratio

There are several difficulties in evaluating the role of equivalence ratio in dust and hybrid flames. Firstly, reaction chemistry of the dust is often difficult to determine, and mechanisms are generally unavailable. Furthermore, some dusts such as coal undergo both homogeneous gas-phase reaction and heterogeneous surface reaction, and therefore have multiple ways to define equivalence ratio. Lastly, the role of the equivalence ratio changes as the dust particle size is increased, further complicating the underlying effects.

An explanation of the different equivalence ratios that are involved in hybrid mixtures of the coal dust, assuming methane gas is the only volatile and the remainder of the particle is carbon, is given in Appendix A. In the following, burning velocity results are analyzed to determine the role of the equivalence ratio when only the

volatiles in the coal dust are considered in hybrid mixtures with methane, and when both the volatiles and surface reaction are considered. This is followed by a discussion of the effect of particle diameter on these results.

7.3.1 Volatile Component Alone

The volatile component equivalence ratio for hybrid mixtures (Φ_h^v) is determined by including the initial methane gas and volatiles released from the particle. The burning velocity as a function of Φ_h^v for various hybrid mixtures is given in Figure 7.6. The simulations are performed for 10 µm particle using MP1 and BFER2 reaction mechanisms. Each burning velocity line is determined for a fixed methane concentration with coal dust between 50 and 1000 g/m^3.

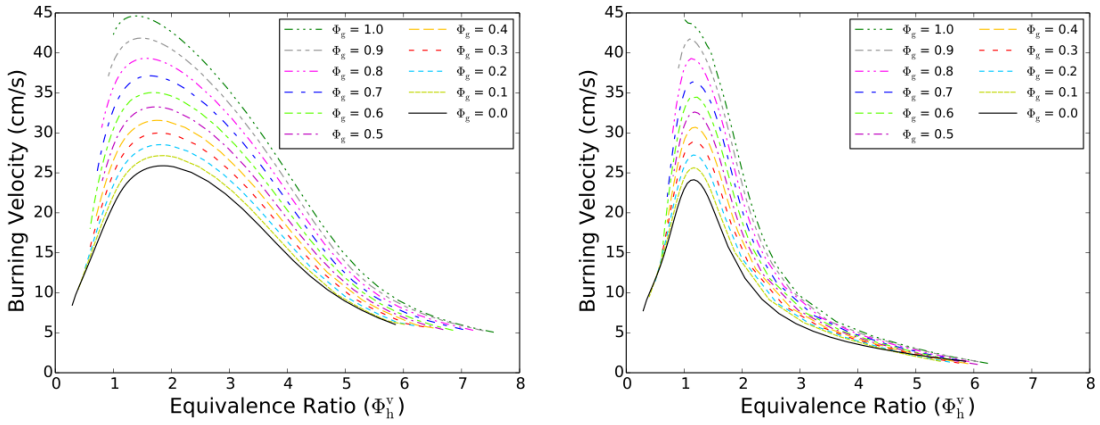

(a) MP1 (b) BFER2

Figure 7.6: Hybrid burning velocity as a function of volatile component equivalence ratio (methane gas and dust volatiles) for MP1 and BFER2 mechanisms with 10 µm coal particles.

When plotted as a function of Φ_h^v, the burning velocity monotonically increases with the initial methane gas equivalence ratio for all simulations except very high dust concentrations using the BFER2 mechanism. A noteworthy feature is that the maximum burning velocity at each initial methane concentration occurs at dust concentrations that give a relatively constant volatile component equivalence ratio. For the BFER2 mechanism, the maximum occurs near $\Phi_h^v = 1.15$. For the MP1 mechanism, the maximum occurs in the range between $\Phi_h^v = 1.37$ and 1.87. These are close to the equivalence ratios that produce the maximum burning velocity for the methane

flame alone, using each mechanism. This suggests that the "worst-case" dust concentration for small particles at a given initial gas concentration may be determined from knowing the equivalence ratio chemistry and overall reaction mechanism.

7.3.2 Volatile and Surface Reaction

The total equivalence ratio (Φ_h^t) is determined from the initial methane gas, volatile component of the dust, and solid-phase fuel. Burning velocity as a function of Φ_h^t for various hybrid mixtures is given in Figure 7.7. Again, the simulations are performed for 10 µm particles and using the MP1 and BFER2 reaction mechanisms.

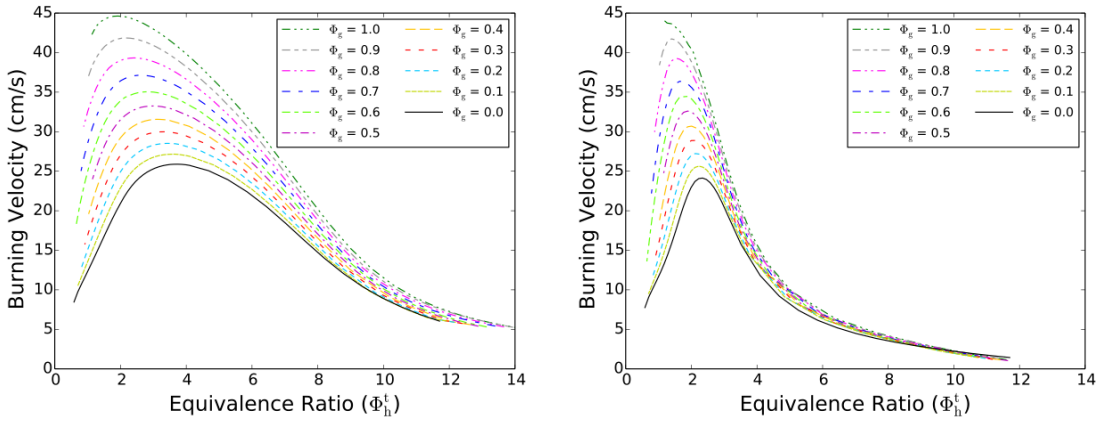

(a) MP1 (b) BFER2

Figure 7.7: Hybrid burning velocity as a function of the total equivalence ratio (methane gas with coal dust volatiles and surface reaction) for MP1 and BFER2 mechanisms with 10 µm particles.

When plotted as a function of Φ_h^t, the burning velocity becomes relatively independent of the initial methane concentration in the gas phase at fuel-rich concentrations. This can be interpreted as meaning the burning velocity does not change if the fuel initially starts in the gas phase or in the particle phase, and suggests that dust heating and devolatilization is fast compared to the gas-phase reaction. For the BFER2 mechanism, burning velocity agrees within 10 % for all Φ_g except $\Phi_g = 0$, when Φ_h^t is greater than 5.5. For the MP1 mechanism, the same trend is seen, although agreement between all Φ_g never gets closer than 10 %.

These results suggest an upper dust concentration limit, where the flame is cooled enough that gas-phase reaction becomes the limiting combustion step. The reason for

the difference between BFER2 and MP1 is the different ignition delay times and flame reaction timescales between these mechanisms. This is important as both times are larger for more detailed mechanisms such as DRM19 and GRI53, which would force the kinetic limit to occur at lower dust concentrations. Although not conclusive, these findings suggest that the rich kinetic limit of the reaction mechanisms is important for understanding rich dust flames with small particles. This is further highlighted by the results in Section 6.2.1 demonstrating difficulties with detailed reaction mechanisms predicting experimental coal dust flame behaviour.

7.3.3 Effect of Particle Diameter

The equivalence ratio effects illustrated in the previous subsections are related to the gas-phase reaction kinetics and their interaction with particle combustion. As the particle diameter is increased, these effects are anticipated to decrease. This is illustrated in Figure 7.8, in which the burning velocity is plotted as a function of the volatile component equivalence ratio and total equivalence ratio for 33 µm particles using the MP1 reaction mechanism. The BFER2 mechanism is not used, as flame propagation could not be achieved at high dust concentrations as explained in Section 6.2.3.

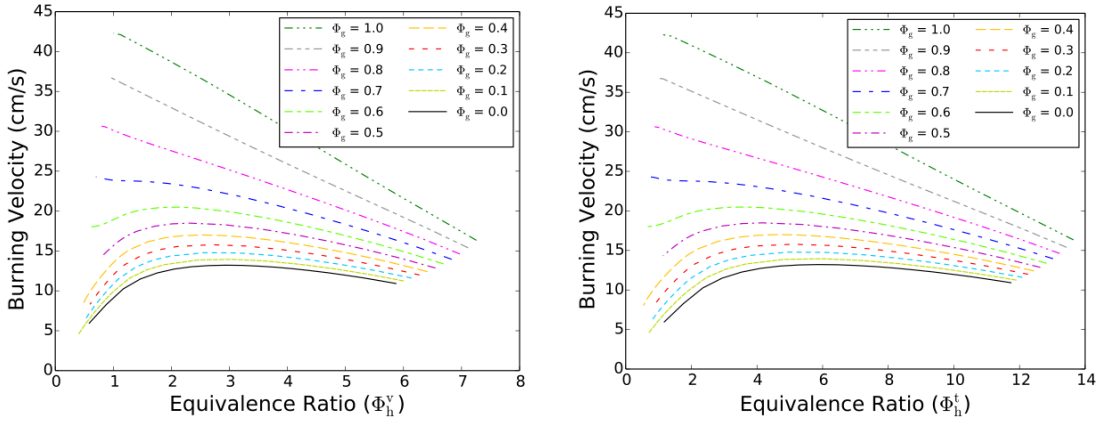

(a) Volatile Component

(b) Volatile and Surface Reaction

Figure 7.8: Hybrid burning velocity for 33 µm coal particles with methane as a function of the volatile component and total equivalence ratios using the MP1 reaction mechanism.

Plotting burning velocity as a function of the volatile component or total equivalence ratio does not provide any insight into flame propagation phenomena for 33 µm particles. The maximum burning velocity does not occur at a fixed equivalence ratio and no kinetic upper limit is exhibited. For these larger particles, gas-phase reaction is still fast compared to particle heating and subsequent devolatilization. Given these results, the equivalence ratio may only have a direct impact on hybrid flame propagation for relatively small particle sizes in the dual-fuel and gas-driven regimes.

7.4 Role of Discrete Combustion

As proposed in Section 2.1.4, discrete particle combustion may play an important role in hybrid burning velocity enhancement at low gas concentrations. Two modes of flame propagation were suggested based on the experimental observations: isolated dust combustion where the addition of flammable gas has a large impact on burning velocity and group dust combustion where gas addition has a smaller impact.

The results presented in Section 6.3 for coal dust flames demonstrate that the impact of discrete combustion on burning velocity persists up to much larger equivalence ratios than suggested using data from droplet combustion literature (see work of Seshadri et al. [178] that suggests a limit of $\Phi = 0.7$). For 10 µm particles, discrete combustion lowered the burning velocity up to concentrations of 400 g/m^3 ($\Phi_p^v = 2.3$, $\Phi_p^t = 4.5$), while the burning velocity of 33 µm particles was lowered at concentrations higher than 1000 g/m^3 ($\Phi_p^v = 5.9$, $\Phi_p^t = 11.4$).

The role of discrete combustion in hybrid mixtures is explored in the following sections. Burning velocity is presented for 10 and 33 µm particles in hybrid mixtures with $\Phi_g = 0.2$ and $\Phi_g = 0.4$. Length-to-diameter ratio is presented as an alternative approach to delineate the impact of discrete combustion and the onset of hybrid burning velocity enhancement in the dust-driven regime.

7.4.1 Burning Velocity

Burning velocity for hybrid mixtures with methane gas below the LFL is presented for 10 and 33 µm coal dust particles in Figure 7.9. Solid lines indicate simulations using the continuum particle representation and dashed lines indicate simulations using the discrete representation. A difference between the two representations indicates

that discrete particle combustion plays a role in flame propagation, while agreement indicates that the flame is propagating through the fuel as a continuum.

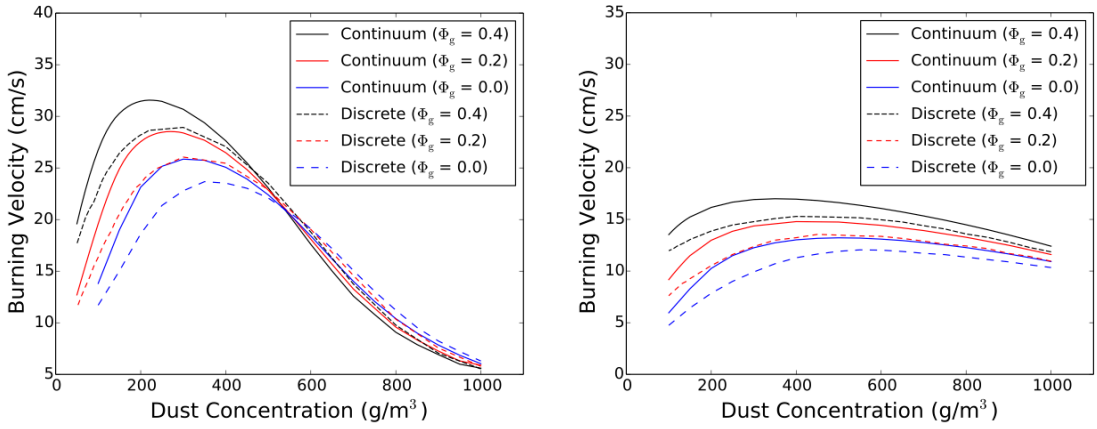

(a) 10 µm (b) 33 µm

Figure 7.9: Hybrid burning velocity for 10 and 33 µm coal dust particles with the addition of flammable gas using the continuum and discrete particle representations and the MP1 reaction mechanism.

Similar to coal dust flames, discrete representation of the particle cloud decreases burning velocity for hybrid mixtures with 10 µm particles when compared to the continuum model, up to a large dust concentration. After this concentration, the discrete representation has a small increase over the continuum model with a maximum value around 5 %. The concentration at which this occurs decreases with the addition of methane gas moving from 530 g/m^3 for the coal dust flame to 500 and 460 g/m^3 when Φ_g is equal to 0.2 and 0.4, respectively.

Also similar to coal dust flames, discrete particle representation decreases the burning velocity throughout a wide range of dust concentrations for 33 µm particles. As the particle diameter increases, the spacing between the particles at the same concentration also increases. From this larger spacing, the effect of isolated particle combustion persists to higher dust concentrations.

7.4.2 Length-to-Diameter Ratio

Using a one-dimensional model where both the condensed-phase fuel and surrounding gas are discretized with a very fine mesh, Cloney et al. [68] demonstrated that the initial flame diameter at ignition is 5–13 times the condensed phase diameter for solid

octadecane particles, and 3–8 times the condensed phase diameter for liquid heptane droplets. To achieve group combustion, the ignition flame diameter of adjacent particles must overlap. Therefore, the ignition diameter must be larger than the individual particle spacing. The simulation results of Cloney et al. [68] suggest that this will occur at concentrations where L_s/d_p is larger than 10.

The burning velocity results presented in Figure 7.9 are replotted in terms of normalized centre-to-centre particle spacing (L_s/d_p) in Figure 7.10. The abscissa in the figure has been scaled from dust concentration using Equation 4.2. More simulations were completed with 33 µm diameters at higher dust concentrations so that lower normalized particle spacing could be explored.

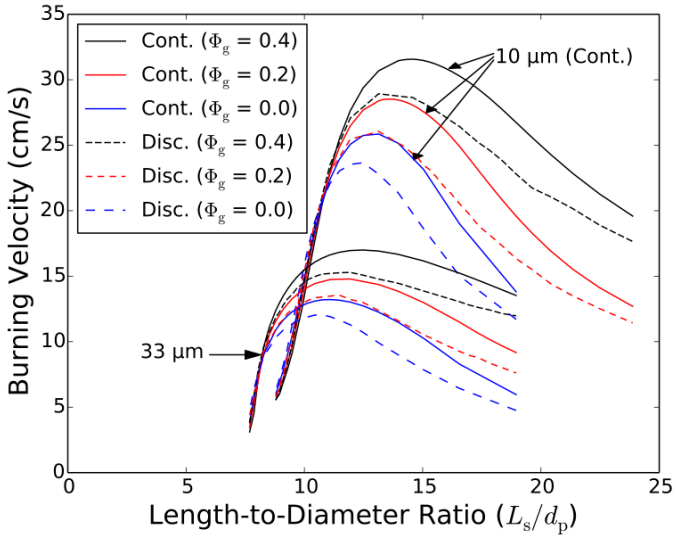

Figure 7.10: Hybrid burning velocity as a function of length-to-diameter ratio for 10 and 33 µm coal dust particles using the MP1 reaction mechanism.

The burning velocity curves in Figure 7.10 are inverted from Figure 7.9 as the normalized particle spacing decreases with increasing dust concentration. At larger normalized spacing, both isolated particle combustion and hybrid burning velocity enhancement play a role in flame propagation. The limit of isolated droplet combustion and the start of group combustion occurs at centre-to-centre normalized particle spacing of approximately 10.8 and 8.1 for 10 and 33 µm particles, respectively, which are consistent with the ranges found by Cloney et al. [68] for octadecane particles.

7.5 Combustion Regimes

Although the original hybrid explosion regimes identified by Garcia-Agreda et al. [29] provide a useful way to categorize closed volume explosion data (see Figure 2.1), they do not provide insight into the underlying flame structure involved. Furthermore, interaction between particle combustion and the propagating gas or hybrid flame is not well delineated. This makes it difficult to anticipate burning velocity enhancement effects in hybrid mixtures and to design experimental testing programs.

Parametric analysis is performed for hybrid mixtures of coal dust and methane gas to extend the combustion regime diagrams currently available in the literature. Flame structure, coupling effects between the dust and gas, and the limits of hybrid flame enhancement are explored for 10 and 33 µm particles. For both particle sizes, simulation results are presented with initial gas equivalence ratios ranging from 0.0 to 1.0. Dust concentration is varied between 50 and 1000 $\mathrm{g/m^3}$ when the gas equivalence ratio is below 0.5, and between 0 and 1000 $\mathrm{g/m^3}$ when the gas equivalence ratio is 0.5 and above. These fuel mixtures equate roughly to the dust-driven, dual-fuel, and gas-driven regimes proposed by Garcia-Agreda et al. [29].

7.5.1 10 µm Particles

The burning velocity for 10 µm particles from Figure 7.6 (a) and Figure 7.7 (a) is replotted as a function of dust concentration for different initial gas equivalence ratios in Figure 7.11. Simulations are presented in 10 $\mathrm{g/m^3}$ increments up to the maximum velocity for a given Φ_g and 50 $\mathrm{g/m^3}$ increments thereafter.

The addition of methane gas causes an overall increase in burning velocity for dust concentrations below 400 $\mathrm{g/m^3}$. It also causes the maximum burning velocity to shift to lower dust concentrations. This is consistent with observations from closed-chamber experiments in the literature [17, 179]. Beyond 400 $\mathrm{g/m^3}$, the curves invert and those with the highest initial gas concentration have the lowest burning velocities. When combined with the fast-devolatilizing 10 µm particles, these mixtures are very fuel rich in the reaction front, which causes the decrease in burning velocity.

The overall maximum burning velocity at each Φ_g is indicated with a white circle in Figure 7.11. The decrease in concentration at which the maximum burning velocity

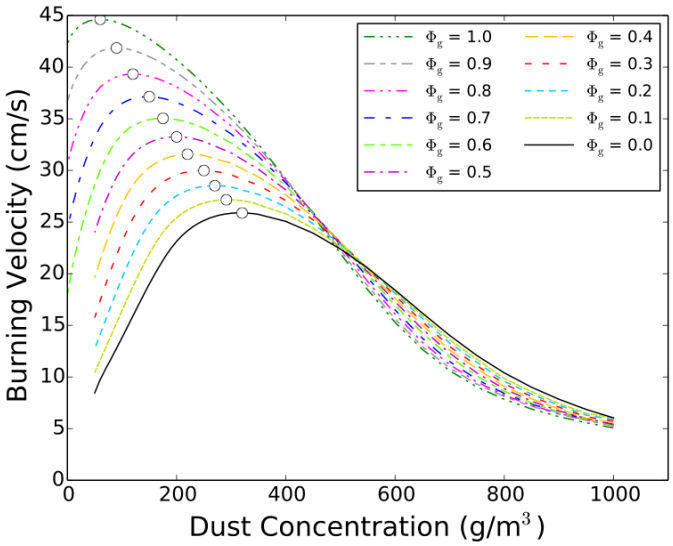

Figure 7.11: Hybrid mixture burning velocity for 10 µm coal particles at different initial methane gas equivalence ratios using the MP1 reaction mechanism.

occurs shows a relatively linear trend with the addition of methane gas. It is unclear whether burning velocity with $\Phi_g = 1.0$ should show as much of an increase with the addition of coal dust as shown in Figure 7.11. This is likely an artifact of the MP1 reaction mechanism and the associated behaviour for fuel-rich flames.

The burning velocity results from Figure 7.11 are replotted in terms of a combustion regime diagram in Figure 7.12. In Figure 7.12, the burning velocity is denoted by the contour colouring where dark red is 45 cm/s and dark blue is 0 cm/s. Solid lines denote specific contours starting at 40 cm/s at the far right and decreasing at 5 cm/s increments. The white circles in Figure 7.12 are taken at the same dust concentrations as shown in Figure 7.11, indicating the maximum burning velocity at each Φ_g.

Analysis of hybrid flame structure in the dust-driven regime indicates the same flame divisions demonstrated for coal dust flames in Section 6.4.2. These are delineated in Figure 7.12 by the dashed lines which divide Types I, II, III, and IV flame structures. The kinetic limited regime (Type V flame) from Section 7.3.2 has also been added to Figure 7.12 (upper right-hand corner). Burning velocity and flame temperature increase with the addition of coal dust in the Type I regime (fuel-lean flame, $\Phi_h^t < 1.0$) and Type II regime (volatile-lean flame, $\Phi_h^v < 1.0$). In the Type III regime (volatile-rich flame, $\Phi_h^t > 1.0$), the temperature decreases with the addition

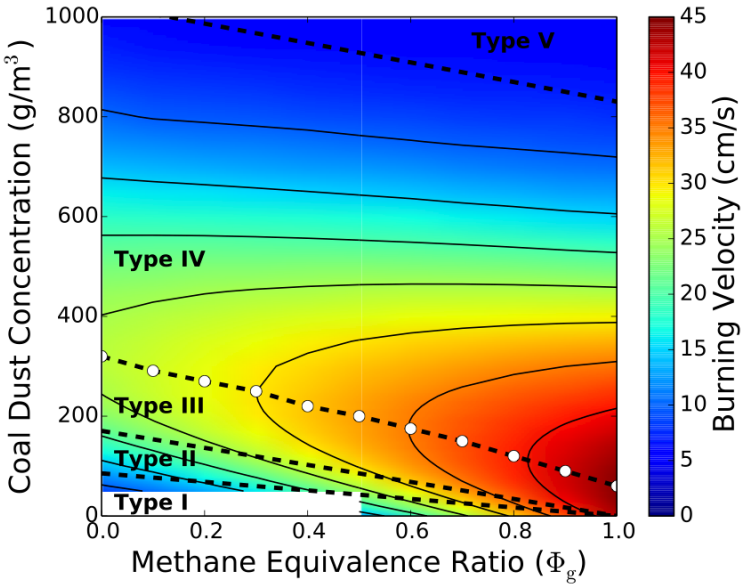

Figure 7.12: Burning velocity and combustion regime diagram for hybrid mixtures of 10 µm coal dust particles and methane gas using the MP1 reaction mechanism.

of coal dust but burning velocity increases.

The Type III regime terminates at the dust concentration where the maximum burning velocity for a given initial gas equivalence ratio is reached. Past this concentration, burning velocity and flame temperature decrease with further dust addition in the Type IV regime (transition flame). Lastly, at rich dust concentrations, the flame temperature is low enough that reaction chemistry becomes the slowest process, resulting in the Type V regime (kinetic-limited flame). When using the MP1 reaction mechanism, this occurs at high values of Φ_h^t due to the low ignition delay and flame reaction timescales. In Figure 7.12, $\Phi_h^t = 12.0$ is selected as the boundary of the kinetic-limited flame based on the burning velocity results given in Figure 7.7 (a). When using a multistep reaction mechanism, the simulation results suggest that the equivalence ratio at which the flame is limited by reaction kinetics may be lower than shown in Figure 7.12.

7.5.2 33 µm Particles

Burning velocity for 33 µm particles is plotted as a function of dust concentration for different initial gas equivalence ratios in Figure 7.13. Simulations are presented in 10 g/m^3 increments up to 150 g/m^3 and 50 g/m^3 increments thereafter.

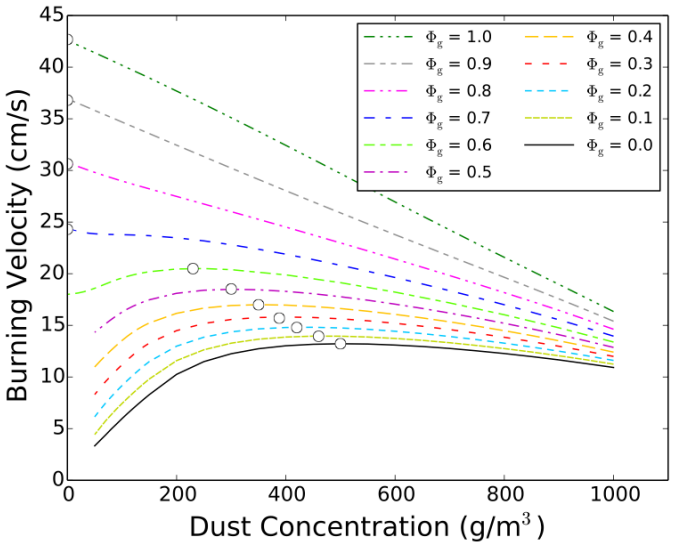

Figure 7.13: Hybrid mixture burning velocity for 33 µm coal particles at different initial methane gas equivalence ratios using the MP1 reaction mechanism.

The burning velocity behaviour for 33 µm particles is noticeably different than 10 µm particles. At initial gas equivalence ratios (Φ_g) less than 0.68, an increase in burning velocity as dust concentration increases is demonstrated. This is similar to the 10 µm particles, except the overall maximum is lower and occurs at a higher dust concentration.

At initial gas equivalence ratios higher than 0.68, the addition of coal dust only acts to reduce the overall burning velocity. As the gas equivalence ratio is increased, the flame thickness decreases and burning velocity increases. Above an equivalence ratio of 0.68, the gas flame residence time is reduced below the particle heating timescale, and the dust no longer contributes to hybrid burning velocity enhancement. Under these conditions, the particles react behind the flame front and do not contribute to energy release in the flame.

The combustion regime diagram for 33 µm particles is given in Figure 7.14 based on the results presented in Figure 7.13. The white circles illustrate the concentrations at which the maximum burning velocity occurs for each Φ_g. More simulations were completed near the drop-off equivalence ratio of 0.68, shown by the additional white circles in Figure 7.14.

The overall hybrid mixture burning velocity enhancement is lower for 33 µm particles than for 10 µm particles. Furthermore, the constant-velocity contours are much

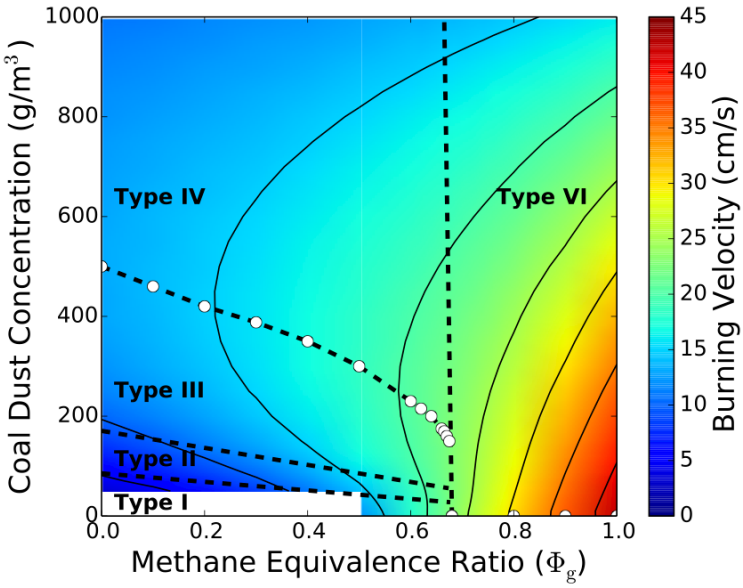

Figure 7.14: Burning velocity and combustion regime diagram for hybrid mixtures of 33 µm coal dust particles and methane gas using the MP1 reaction mechanism.

broader. In the dust-driven regime, Type I, Type II, Type III, and Type IV flames are demonstrated. Kinetic-limited (Type V) flames are not found for 33 µm particles in the concentration ranges investigated. It appears from these results that the lower heat loss for 33 µm particles does not reduce the flame temperature enough that chemistry reactions become the limiting combustion step.

By tracing out the maximum burning velocity for each Φ_g in Figures 7.13 and 7.14, the extent of the hybrid flame enhancement can be identified. From the simulations presented in Figure 7.13, hybrid flame enhancement terminates at $\Phi_g = 0.68$. Below this value, the dust enhances the burning velocity. Above this Φ_g, the dust only acts to reduce the burning velocity of the premixed gas flame. This regime is labeled Type VI (impeded gas flame) as shown in Figure 7.14.

7.6 Discussion of Results

Hybrid flame simulations facilitated combustion regime diagrams to be defined in terms of flame structure, volatile component and total equivalence ratios, and the interaction between dust combustion timescales and gas flame residence time. Equivalence ratio analysis demonstrated that maximum burning velocity for hybrid mixtures

may occur along lines of constant Φ_h^v for small particle sizes and that a kinetic-limited combustion regime may be present for Φ_h^t. The timescale analysis demonstrated an impeded gas flame regime where the dust could not react fast enough to contribute to energy release in the flame front.

7.6.1 Comparison to Explosion Regime Diagrams

The regime diagram proposed by Garcia-Agreda et al. [29] is compared to those developed in the current work in Figure 7.15. Figure 7.15 (a) is an example of the literature regime diagram, while Figure 7.15 (b) and (c) are from the current work for 10 and 33 µm particles, respectively.

The comparison of combustion regimes given in Figure 7.15 further demonstrates that the dust-driven regime of Garcia-Agreda et al. [29] actually contains several different regimes where each flame structure depends on the volatile component and total equivalence ratio. The specific flame structures are similar for both particle sizes in this area of the diagram, although the concentration at which the maximum burning velocity occurs increases with the larger particle diameter.

Flame structure and burning velocity in the gas-driven and dual-fuel regimes are greatly impacted by the combustion timescales of the dust and the gas. Small particle diameters are able to enhance the burning velocity at all gas concentrations below stoichiometric. At larger particle diameters, the dust may be unable to contribute to energy release in the flame front and acts only as a heat sink to reduce burning velocity.

7.6.2 Practical Implications

In the literature review presented in Section 2.1.4, single-stage, two-stage, and gas-only explosion regimes were proposed based on the experimental analysis of Denkevits [18] and Denkevits and Hoess [88]. At first glance, these proposed regimes appear to conflict with those developed from the simulation results in the current work. From the current results, coupling between the dust and gas (Type I – Type IV flames) occurs below some minimum initial gas equivalence ratio (e.g., 0.68 for 33 µm particles). In the literature, these are reversed and gas-only or uncoupled explosions occur at low gas concentrations, and coupled single-stage explosions occur at higher values.

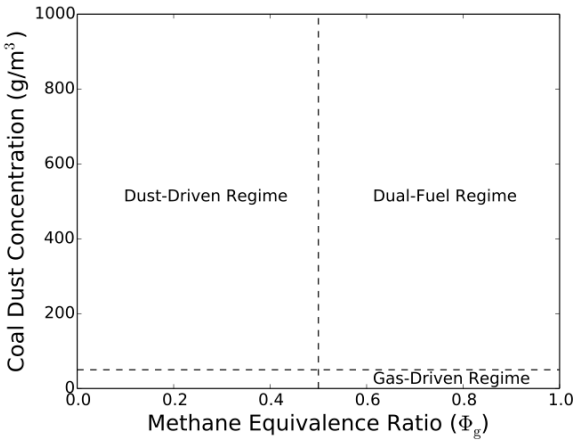

(a) Adapted from Garcia-Agreda et al. [29]

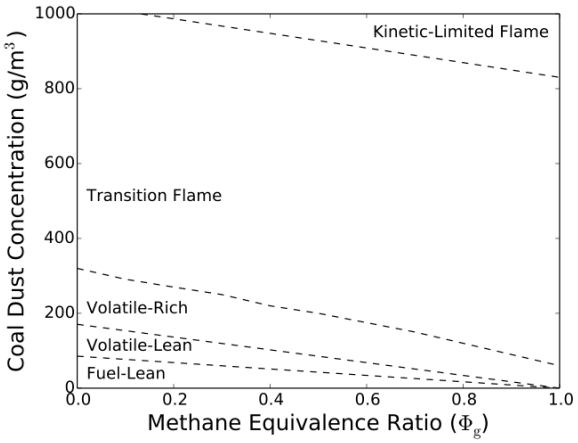

(b) Current Work, 10 µm particles

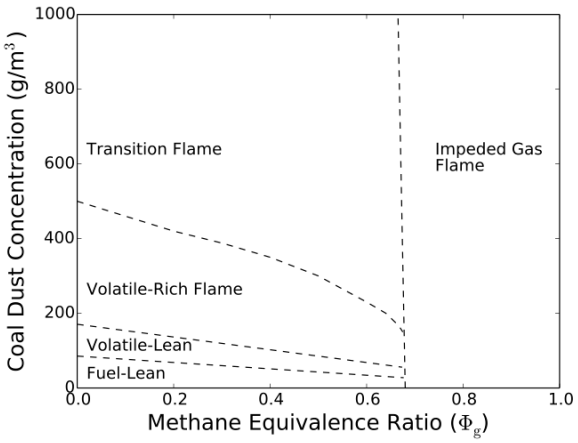

(c) Current Work, 33 µm particles

Figure 7.15: Combustion regime diagram from the literature compared to those developed in the current work.

The reason for this discrepancy is the difference in system geometry and the concepts of combustion regimes and explosion regimes. In this work, open "free flames" are being simulated, while in the experimental work, flames propagating in a closed chamber are being measured. The closed-chamber geometry adds another scale to the system, namely, the size of the experimental chamber and the time needed for the flame to reach the chamber walls.

In closed-chamber explosions, particle burning can contribute to pressure rise even if it is too slow to occur in the flame front. As long as the particle burns before the gas flame reaches the chamber walls, it will be recorded as "coupled" with the gas flame pressure rise.

Different explosion and combustion regimes are summarized in Table 7.1 along with the impact on recorded maximum pressure, size-normalized maximum rate of pressure rise, and burning velocity from adding dust to the propagating gas flame initially at lean concentrations. The parameter τ_{p} is the combustion timescale of the particle which is dominated by particle heating under the conditions simulated ($\tau_{\mathrm{p}} \approx \tau_{\mathrm{h}}$), τ_{vol} is the time required for the gas flame to reach the vessel walls, and τ_{f} is the gas flame residence time.

Table 7.1: Comparison between explosion regimes proposed from the literature and combustion regimes presented in the current work. P_{m}, K_{m}, and S_{L} are the maximum pressure, sized-normalized maximum rate of pressure rise, and burning velocity as dust is added to the flammable gas at lean concentrations.

Timescales	**Explosion Regime**	**Combustion Regime**	$\boldsymbol{P_{\mathrm{m}}}$	$\boldsymbol{K_{\mathrm{m}}}$	$\boldsymbol{S_{\mathrm{L}}}$
$\tau_{\mathrm{p}} \gg \tau_{\mathrm{vol}}$	Gas-Only Explosion	Impeded Gas Flame	↓	↓	↓
$\tau_{\mathrm{p}} \approx \tau_{\mathrm{vol}}$	Two-Stage Explosion	Impeded Gas Flame	↑	↓	↓
$\tau_{\mathrm{p}} \ll \tau_{\mathrm{vol}}$	Single-Stage Explosion	Impeded Gas Flame	↑	↑	↓
$\tau_{\mathrm{p}} \gg \tau_{\mathrm{f}}$	Single-Stage Explosion	Impeded Gas Flame	↑	↑	↓
$\tau_{\mathrm{p}} \approx \tau_{\mathrm{f}}$	Single-Stage Explosion	Coupled Flame	↑	↑	↑
$\tau_{\mathrm{p}} \ll \tau_{\mathrm{f}}$	Dust-Only Explosion	Dust-Driven Flame	↑	↑	↑

The top three rows in Table 7.1 present the proposed explosion regimes from analysing the work of Denkevits [18] (see Figure 2.4). The bottom three rows show the combustion regimes from the simulation model and the additional dust-only explosion regime from Denkevits and Hoess [88] (see Figure 2.5). Together these results demonstrate the role of particle combustion time on the flame combustion and explosion regimes. If the particle reacts fast enough to interact with the gas flame reaction

front, a single-stage explosion is registered by the experimental pressure rise. On the other hand, if the particle reacts too slowly to couple with the reaction front, an impeded gas flame occurs, but this may be registered as a single-stage, two-stage, or gas-only explosion. The change in explosion regimes in the top three cases in Table 7.1 is due to the flame temperature. As the gas concentration is increased, the flame temperature increases. This increases the particle heating rate, allowing the particles react before the gas flame reaches the vessel walls.

To the current author's knowledge, the difference between explosion regimes and combustion regimes as highlighted in Table 7.1 has not been explored in the literature to date. Care must be taken when drawing conclusions on flame-front scale phenomena from closed-chamber pressure-time traces. This may have an important impact on scaling between vessels and time-sensitive safety equipment such as suppression systems. With this is mind, it is important to also note that the closed-chamber measurements may be more representative of explosions in industrial vessels than the free-flame measurements. Overall, both types of measurements are needed to characterize flame propagation over a large set of industrially relevant conditions.

7.6.3 Discrete Particle Combustion

The simulation results presented in Section 6.3 demonstrate that discrete particle combustion lowers burning velocity over the continuum assumption up to high dust concentrations. Both hybrid and dust-only simulations appear to correlate well with normalized particle spacing with discrete effects impacting a burning velocity above $L_s/d_\mathrm{p} = 10.8$ for 10 µm particles and above $L_s/d_\mathrm{p} = 8.1$ for 33 µm particles.

These results demonstrate the potential reduction in burning velocity from discrete combustion under the conditions where it can have the largest effect – namely, when the particles are evenly spaced in all directions with a fixed particle diameter. In reality, the burning velocity likely falls between the values predicted with the discrete and continuum representations due to randomized particle distribution in the cloud and preferential flame travel in directions with higher dust concentrations. Future simulations in multidimensional space using randomly scattered particles are needed in addition to a statistical analysis to predict the overall impact of discrete combustion in dust and hybrid flames.

7.6.4 Accuracy of the CFD Model

Verifying the accuracy of the computational model for hybrid mixtures is challenged by the limited experimental and numerical investigations available in the literature. Burning velocity comparisons given in Figure 7.1 and Figure 7.2 show that the coupling interaction and conditions under which burning velocity is enhanced over the gas flame are captured using the current model. They also demonstrate that agreement with the experimental data may decrease as Φ_g approaches stoichiometric concentrations. This may be due to the MP1 reaction mechanism being unable to capture the decrease in burning velocity for fuel-rich gas concentrations. Comparison to the results of Horton et al. [77] in the dust-driven regime as shown in Figure 7.3 shows reasonable agreement with burning velocity enhancement.

The of impact reaction mechanisms on hybrid flame burning velocity could not be explored fully due to detailed mechanisms being unable to produce propagating flames at high dust concentrations. As these models become available, it would be instructive to compare flame behaviour to those predicted with the current model as the initial gas concentration approaches the stoichiometric concentrations ($\Phi_g = 1.0$). Investigation into the kinetic-limited regime with these new mechanisms may also be helpful to understand the dynamics of hybrid flames at high dust concentrations.

Chapter 8

Lower Flammability Limits

The lower flammability limits of hybrid mixtures are an important component of explosion prevention practices. This chapter begins by exploring the flame structure and role of reaction mechanism on near-limit methane and coal dust flames. Specific attention is given to the impact of particle diameter and discrete combustion on the coal dust flammability limits. The LFLs of the methane gas and coal dust alone are then compared to combine LFLs of hybrid mixtures. These results are used to evaluate existing LFL mixing rules in the literature and to explore their applicability for the free-flames simulated in this work. This chapter concludes with an overall discussion of hybrid LFL mixing rules and implications for experimental testing.

8.1 Methane Gas

Simulation results from the computational model are analyzed to determine the predicted LFL for methane gas. Flame structure near the LFL is explored, along with the role of reaction mechanisms and flammability criteria. The methane gas LFL predicted numerically is used in later sections to explore mixing rules for hybrid mixtures.

8.1.1 Flame Structure

As discussed in Section 2.2.1, quantitatively capturing the LFL for gas flames is difficult in both experiments and computational models as heat loss plays an important role. Physically, the LFL occurs when heat loss from the flame front increases above the heat generated by the reaction [180]. In experimental investigations, this makes the limit dependent on the size and shape of the experiential apparatus and orientation of the flame [104]. For computational models, the specific approach used for the gas-phase reaction mechanism, thermal conductivity, and the assumptions used for radiative heat loss, may become important when approaching the LFL and capturing

its value.

In the current simulation model, radiation and other heat loss effects to the surroundings are neglected. This tends to result in predictions of LFL boundaries that are lower than would be seen in a physical experimental system. As an example, flame temperature, CH_4 mass fraction, and CO_2 mass fraction profiles are given in Figure 8.1 for gas concentrations near the flammability limit, using the DRM19 mechanism. Each column from left to right shows the flame profile at a different time in the simulation, and each row is at a different equivalence ratio (top is 0.5, middle is 0.45, and bottom is 0.40).

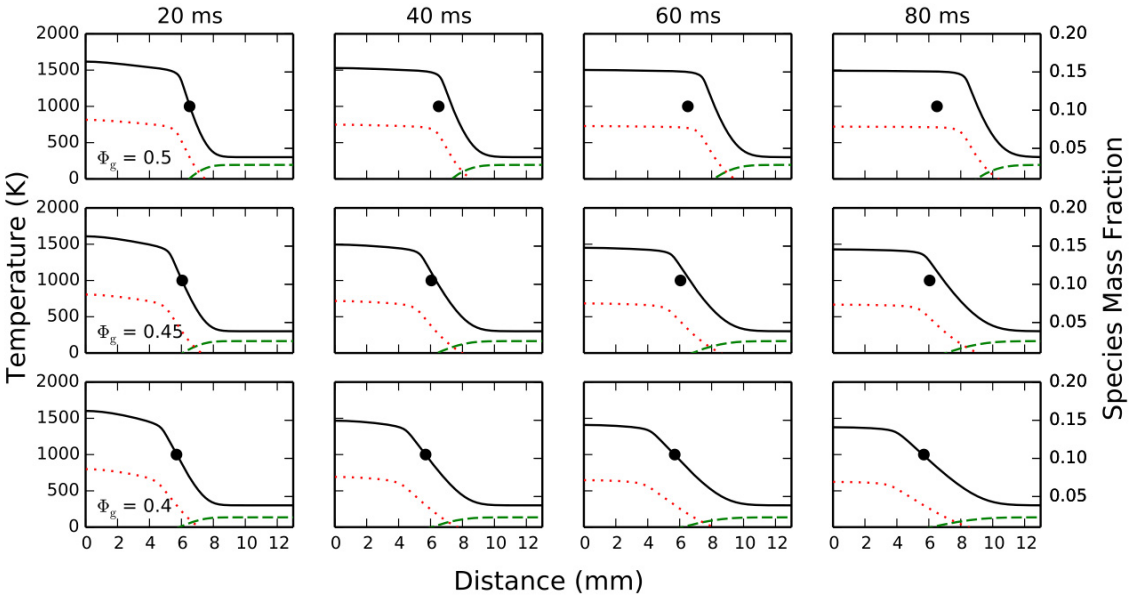

Figure 8.1: Methane flame structure at equivalence ratios of 0.5 (top), 0.45 (middle), and 0.40 (bottom) using the DRM19 reaction mechanism. The lines and symbols in the figure are as follows: temperature – black solid line; methane mass fraction – long-dash green line; carbon dioxide mass fraction – short-dash red line; and black circle – flame location at 20 ms.

The black circles in Figure 8.1 show the flame location 20 ms into each simulation. The flame location is defined as the position where the flame temperature is 1000 K; comparing this to the later flame profile demonstrates propagation of the flame into the unburned methane gas. The top and middle rows in Figure 8.1 ($\Phi_g = 0.5$ and $\Phi_g = 0.45$) show propagating flames, while the lowest equivalence ratio of 0.4 does not propagate a flame. Instead, the flame location does not change and temperature and

species gradients diffuse with time.

The burning velocities for propagating flames in Figure 8.1 are 4.4 and 1.5 cm/s for equivalence ratios of 0.5 and 0.45, respectively. Although this range agrees with the experimental literature cited in Section 2.2.1, it is not clear that a gas flame in a physical system would be able to propagate at 1.5 cm/s. Instead, instabilities or energy loss in the reaction front may prevent flame propagation and increase the LFL. These flames may be similar to those described by Coward and Jones [107] that propagate some distance away from the ignition point but are unable to self propagate down a long tube and as such are actually below the fuel LFL.

8.1.2 Role of Reaction Mechanism

To further explore gas flame behaviour near the LFL, simulations are presented with the four different reaction mechanisms outlined in Table 3.1. Burning velocities for gas equivalence ratios between 0.4 and 0.6 are given in Figure 8.2 for these simulations. Results are presented at equivalence ratios with increments of 0.01 in Figure 8.2.

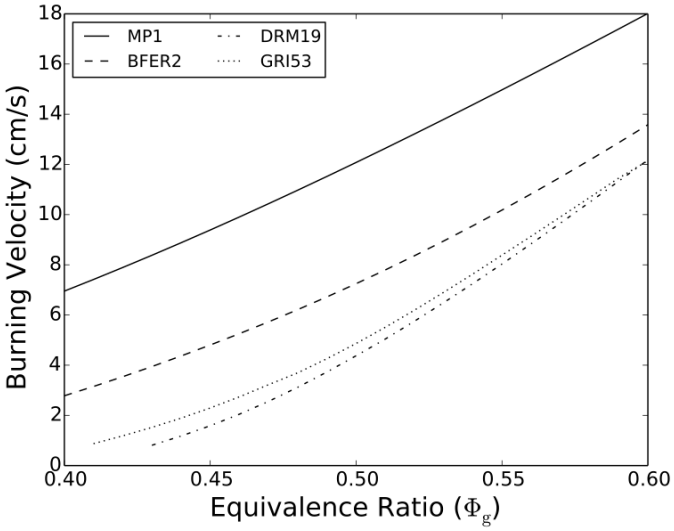

Figure 8.2: Methane burning velocity near the LFL using different reaction mechanisms.

The first measurable burning velocity for DRM19 and GRI53 is approximately 0.8 cm/s and occurs at $\Phi_g = 0.43$ and $\Phi_g = 0.41$, respectively, for each mechanism. Again, this equivalence ratio may be lower than could be achieved for gas flames in a physical system due to heat loss [104]. The BFER2 mechanism predicts a higher

burning velocity than the detailed mechanisms, with the three models agreeing within 1.5 cm/s at $\Phi_g = 0.6$. The MP1 mechanism overpredicts burning velocity throughout the entire range shown in Figure 8.2. Both BFER2 and MP1 are unable to capture a methane LFL above $\Phi_g = 0.4$.

Maximum flame temperature for gas equivalence ratios near the LFL are illustrated in Figure 8.3. Results are presented using MP1, BFER2, and DRM19. Flame temperature was taken as the highest value in the flame 100 ms into the simulation. Most of the GRI53 simulations were only completed for 40 ms and therefore it is excluded from Figure 8.3.

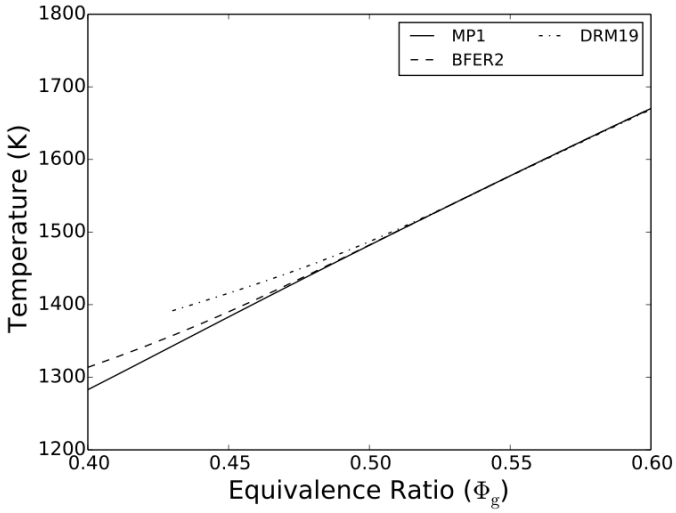

Figure 8.3: Methane flame temperature at 100 ms into the simulation near the LFL using different reaction mechanisms.

Maximum flame temperature at 100 ms between the three reaction mechanisms agrees within 5 K at equivalence ratios of 0.5 and higher. At lower equivalence ratios, the more detailed reaction mechanisms report higher maximum temperatures than the single-step mechanism. This is due to the full flame structure not yet reaching steady state with these mechanisms. Behind the flame, but before the simulation boundary, later time reactions are still creating CO_2, which is lowering the flame temperature. If the simulations are run for a longer time such that the flame develops further, all mechanisms would predict similar maximum temperatures to MP1. Note that the burning velocity of the flame front is unchanging at 100 ms and is unaffected by these later-time reactions downstream.

Although the methane flame simulations with detailed reaction mechanisms would eventually predict similar flame temperatures, the results presented in Figure 8.3 raise an important point with regard to flammability limits. Not only do the very low equivalence ratios produce a low burning velocity and flame temperature, but they also take longer to form. Any heat loss or instabilities in the physical system would then have a larger impact on these flames.

8.1.3 Flammability Criteria

From the results presented in the previous section, the simplified MP1 and BFER2 reaction mechanisms are unable to capture the flammability limit behaviour of methane gas. The reduced DRM19 mechanism gives similar results to GRI53 and is a suitable alternative in the current computational model. However, weak flames that may not self-propagate in physical systems with heat loss are predicted with these mechanisms.

A similar problem arises when selecting LFL criteria for Calculated Adiabatic Flame Temperature (CAFT) models used to predict flammability envelopes [181, 114]. Typically, a fixed limit flame temperature is selected in the range of 1000 to 1500 K (e.g., see Coward and Jones [107] as described by Dastidar and Amyotte [182]). Mashuga and Crowl [114] selected 1200 K for their investigation into mixtures of methane and ethylene, while Du et al. [181] selected 1450 K for methane alone. In their review and investigation, Dastidar et al. [182] also selected 1450 K as the limit flame temperature for Pittsburgh coal dust based on MEC data of 80 g/m^3 [25].

The burning velocity and flame temperature from the simulation model near the LFL are given in Table 8.1. The DRM19 mechanism is used and the flame characteristics are measured 100 ms into the simulation. As shown in Figure 8.3, the flame temperature for low equivalence ratios may not have reached steady state; however, the burning velocity is constant when measured.

For the hybrid analysis subsequently presented in Section 8.3, an equivalence ratio of 0.5 is selected as the methane LFL. This gives a limit flame temperature of 1480 K, which is slightly higher than the values used by Du et al. [181] and Dastidar and Amyotte [182] and is consistent with the range outlined by Coward and Jones [107]. This equivalence ratio also gives a prompt reacting flame with agreement in flame temperature within 100 ms between the reaction mechanisms.

Table 8.1: Flame characteristics near the methane gas LFL using the DRM19 reaction mechanism. Units are as follows: S_{L} (cm/s) and T_{f} (K).

$\Phi_{\mathbf{g}}$	$S_{\mathbf{L}}$	$T_{\mathbf{f}}$	$\Phi_{\mathbf{g}}$	$S_{\mathbf{L}}$	$T_{\mathbf{f}}$
0.56	8.8	1595	0.50	4.4	1485
0.55	8.0	1575	0.49	3.7	1470
0.54	7.2	1560	0.48	3.1	1455
0.53	6.5	1540	0.47	2.5	1440
0.52	5.7	1525	0.46	2.0	1430
0.51	5.0	1510	0.45	1.5	1415

8.2 Coal Dust

Coal dust flames have an inherent heat loss mechanism as the dust itself removes energy from the flame front. As such, simulations showing the lean limits may have more distinct concentration boundaries than methane flames. The general flame structure, role of reaction mechanism, role of particle size, and role of discrete combustion are explored in the following. Although the lean limit for dust explosions is typically specified as the MEC, this term is used interchangeably with the LFL for dust and hybrid flames in the following sections.

8.2.1 Flame Structure

The flame structure for coal dust concentrations near the LFL and using the DRM19 mechanism are given in Figure 8.4 for 10 µm particles. Each column shows the flame profile at a different time in the simulation, and each row is a different dust concentration (top is 50 g/m^3, middle is 45 g/m^3, and bottom is 40 g/m^3). Black circles indicate the flame position 20 ms into the simulation and can be used to illustrate the flame propagation rate. The methane mass fraction is multiplied by a factor of 10 in Figure 8.4 so that it shows up more clearly in the plots.

Comparing the later-time temperature profiles to the initial flame location indicated by the black circles shows that the flame propagates at 45 and 50 g/m^3. Burning velocities for these simulations are 6.0 and 7.2 cm/s, respectively. The flame does not propagate at a dust concentration of 40 g/m^3. This flammability limit is consistent with the reported literature data outlined in Section 2.2.2 for high-volatile content coal with low moisture and ash content.

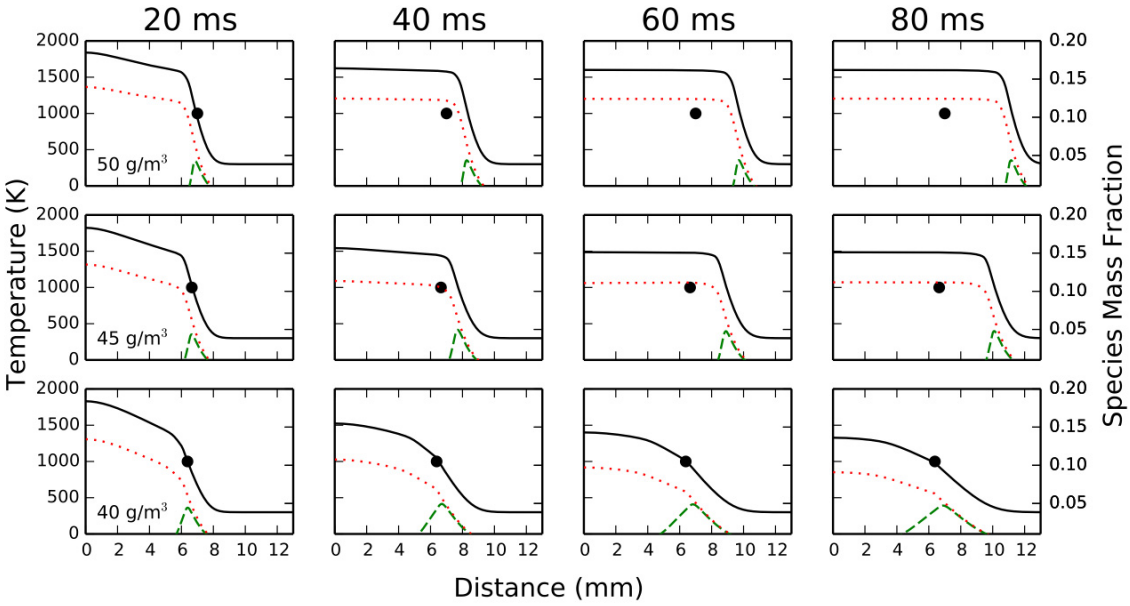

Figure 8.4: Coal dust flame structure at concentrations of 50 g/m^3 (top), 45 g/m^3 (middle), and 40 g/m^3 (bottom) using the DRM19 reaction mechanism for 10 µm particles. The lines and symbols in the figure are as follows: gas temperature – black solid line; ten times methane mass fraction – long-dash green line; carbon dioxide mass fraction – short-dash red line; and black circle – flame location at 20 ms.

8.2.2 Role of Reaction Mechanism

Gas-phase chemistry has a lesser impact on coal dust burning velocity near the LFL than for methane flames. Figure 8.5 shows the burning velocity for 10 µm particles using the four reaction mechanisms outlined in Table 3.1. Simulations are completed at 5 g/m^3 increments near the LFL for each mechanism and 10 g/m^3 increments elsewhere. The data point at the lowest dust concentration indicates the burning velocity at the LFL for each reaction mechanism.

The MP1 mechanism has the largest burning velocity at low dust concentrations. These concentrations lie in the Type I combustion regime (fuel-lean flame). The burning velocities of the different reaction mechanisms agree within 1 cm/s for 10 µm particles in Figure 8.5. This is much less than methane flames, which had a difference around 8 cm/s near the LFL.

Although the burning velocities of the different reaction mechanisms are similar near the LFL in Figure 8.5, the limit itself is different. Both DRM19 and GRI53 models predict a flammability limit of 45 g/m^3, while BFER2 predicts a limit of

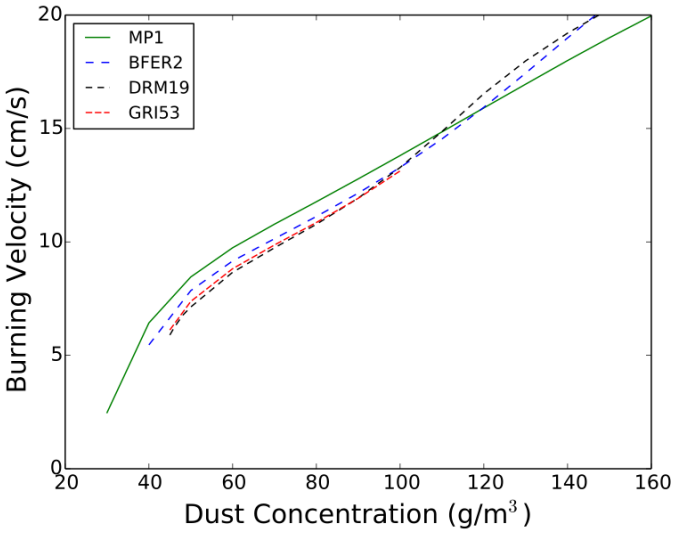

Figure 8.5: Coal dust burning velocity near the LFL for 10 µm particles using four reaction mechanisms.

40 g/m^3 and MP1 predicts a limit of 30 g/m^3. These differences can be explained by analyzing the flame temperature compared to the physical processes responsible for propagation with each mechanism.

Table 8.2 summarizes the flame characteristics at the LFL for each reaction mechanism. At each concentration, the total equivalence ratio and volatile component equivalence ratio are given. The burning velocity and flame temperature at the LFL are also given in Table 8.2. Flame temperature for GRI53 was determined 60 ms into the simulation at which time the flame profile was not fully developed.

Table 8.2: Coal dust flame characteristics for 10 µm particles near the LFL using different reaction mechanisms. Units are as follows: σ_p (g/m^3), S_L (cm/s), and T_f (K).

Model	$\boldsymbol{\sigma_p}$	$\boldsymbol{\Phi_p^t}$	$\boldsymbol{\Phi_p^v}$	$\boldsymbol{S_L}$	$\boldsymbol{T_f}$
MP1	30	0.35	0.18	2.6	1130
BFER2	40	0.47	0.23	5.8	1375
DRM19	45	0.53	0.29	6.0	1485
GRI53	45	0.53	0.29	6.2	∼1490

The results given in Table 8.2 show that the flammability limit with the MP1 model occurs at 1130 K. This is close to the temperature at which the particles begin to devolatilize in the flame front (e.g., see Figure 4.2). Below this concentration, not enough volatiles are released to increase the flame temperature to a point where

it can cause successive particles to devolatilize. This concentration limit is likely constant for all rapid single-step reaction mechanisms, as they are limited by the particle devolatilization model.

The multistep reaction mechanisms illustrate higher flammability limits than MP1 in Table 8.2. This demonstrates that gas-phase chemistry plays an important role in the LFL under the conditions simulated. Since particle devolilization is fast compared to multistep kinetics, gas-phase reaction tends to limit the flame propagation process.

The flammability limit for the DRM19 and GRI53 reaction mechanisms is $45\,\mathrm{g/m^3}$. In both cases, the flame temperature at the limit is 1485 K. This is close to the temperature of methane flames at an equivalence ratio of 0.5. This further demonstrates that gas-phase reaction kinetics play an important role in the flammability limits of the dust. It also indicates that Le Chatelier's Law (LCL) may hold for high-volatile coal dust and methane gas mixtures, as having the same flame temperature at the propagation limits is an assumption used in the LCL derivation (See Section 2.2.3 and Mashuga and Crowl [112]).

8.2.3 Role of Particle Diameter and Discrete Combustion

Flame propagation near the LFL for coal dust with different particle diameters is illustrated by distance-time plots in Figure 8.6. Results are presented using the continuum and discrete particle representations with dust concentrations ranging from 35 to $50\,\mathrm{g/m^3}$.

The distance-time traces presented in Figure 8.6 demonstrate the role of particle diameter and discrete combustion on the dust LFL. For 10 µm particles, representing the particles discretely decreases the LFL from 45 to $40\,\mathrm{g/m^3}$. This behaviour is caused by two competing effects for isolated particle combustion. The first is that heat and mass transfer in the space between the particles tends to impede flame propagation. This was demonstrated both for coal dust particles alone in Section 6.3 and for hybrid mixtures in Section 7.4. On its own, this would tend to increase the LFL, as more fuel is needed to achieve flame propagation.

The second competing effect is that the volatiles surrounding individual particles are much higher than the mean equivalence ratio. This allows the flame to accelerate through the particle ignition process. The flame then decelerates in between the

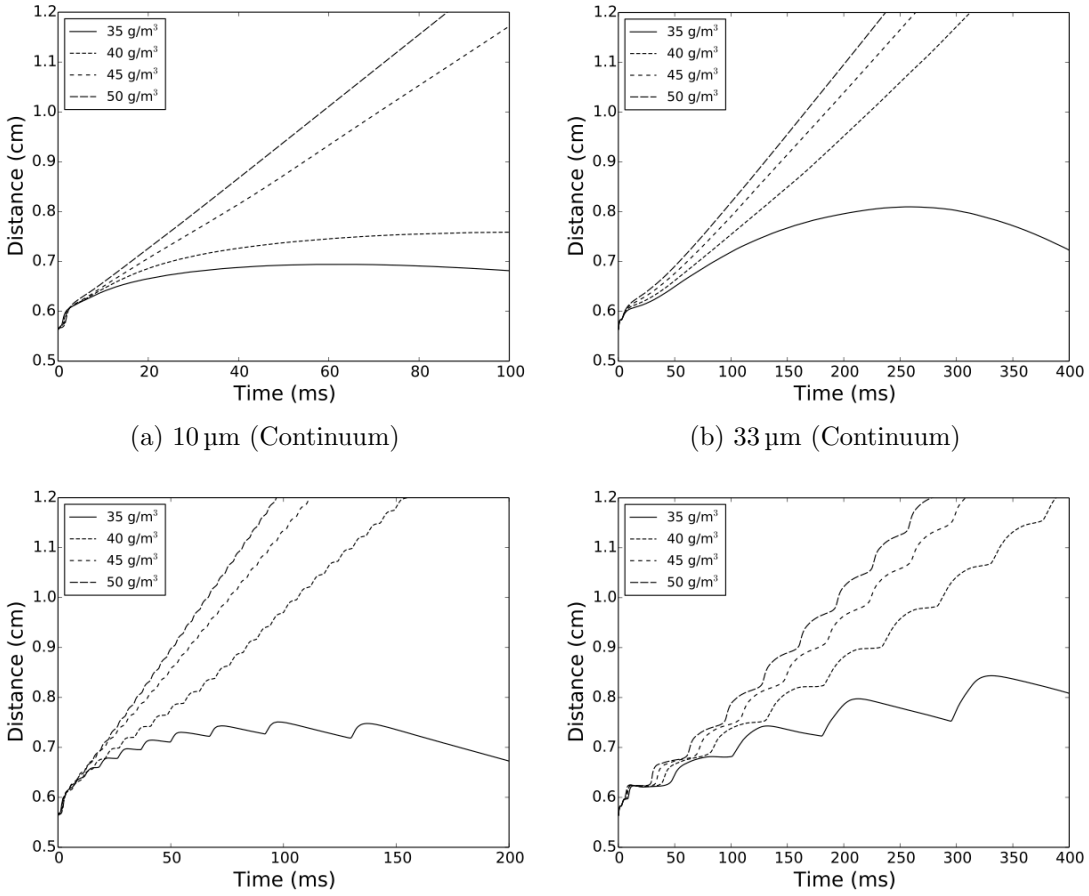

(a) 10 µm (Continuum)

(b) 33 µm (Continuum)

(c) 10 µm (Discrete)

(d) 33 µm (Discrete)

Figure 8.6: Coal dust flame propagation for 10 and 33 µm particles using the continuum and discrete Lagrange representations near the dust LFL.

particles. For 10 µm particles, this second effect outweighs the first, and the LFL is reduced when the particles are modeled discretely.

Comparing 10 µm particles to 33 µm particles using the continuum representation illustrates that the LFL decreases as the particle size is increased in this size range. This is an unexpected result but is consistent with the experimental findings of Cashdollar [117] for Pittsburgh coal with 37 % volatiles and low ash and moisture content (see Section 2.2.2). This may be explained by a decreased rate of energy absorption by the larger particles in the flame front. Discrete particle combustion does not change the LFL for 33 µm particles. Flame propagation at 35 g/m^3 for 33 µm particles decelerates overall and will quench if the simulation is run longer, indicating that this concentration is below the LFL.

The burning velocity near the coal dust LFL for the continuum and discrete representations with 10 and 33 µm particles is summarized in Figure 8.7. In all simulations, the DRM19 reaction mechanism was used. Simulations were completed at 5 g/m^3 increments near the LFL for each mechanism and 10 g/m^3 increments elsewhere.

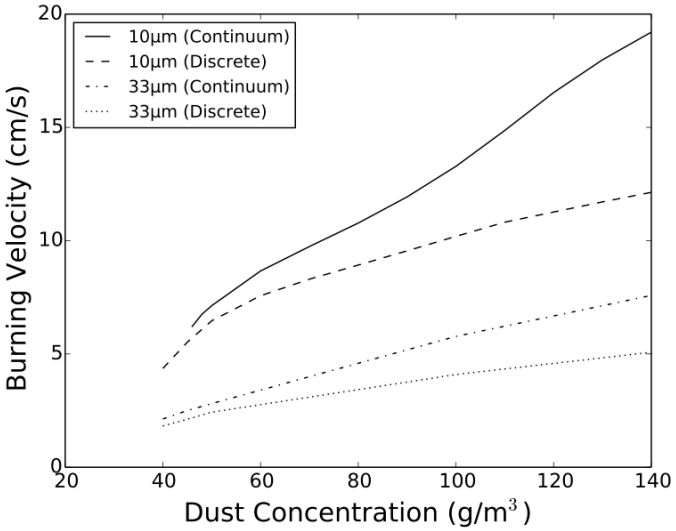

Figure 8.7: Coal dust burning velocity near the LFL for different particle sizes using the DRM19 reaction mechanism with continuum and discrete particle representations.

The burning velocity results presented in Figure 8.7 illustrate that the discrete particle representation predicts a reduction in the burning velocity of more than 1 cm/s at dust concentrations above 60 g/m^3 compared to the continuum representation. However, this difference decreases approaching the LFL. This again illustrates the two competing effects for isolated particle combustion. The decrease in burning velocity from inter-particle spacing is counterbalanced by the enhanced local equivalence ratio around the individual particles.

The burning velocity at the LFL is 6.0 and 4.2 cm/s for 10 µm particles using the continuum and discrete representations, respectively. For 33 µm particles, the burning velocity is lower at 2.4 and 1.8 cm/s using each representation. The flame temperature for the three models with an LFL of 40 g/m^3 is approximately 1425 K.

8.3 Hybrid Mixtures

A parametric analysis was performed for different dust and gas concentrations to explore the combined lower flammability limits of hybrid mixtures. Simulation results

are presented for 10 and 33 µm coal dust particles using the continuum and discrete representations. These simulations allow flame behaviour to be explored between the limits of the two fuels, and the results are compared to mixing rules outlined in Section 2.2.3.

8.3.1 10 µm Particles

To illustrate the different flame propagation processes found in the parametric analysis, distance-time plots for flame position with 10 µm coal particles and methane gas are presented in Figure 8.8. Also given in Figure 8.8 is the flame structure for the simulation with $\Phi_g = 0.1$ and $\sigma_p = 35\,g/m^3$. The flame structure is given at the specific times indicated with circles in the distance-time plot.

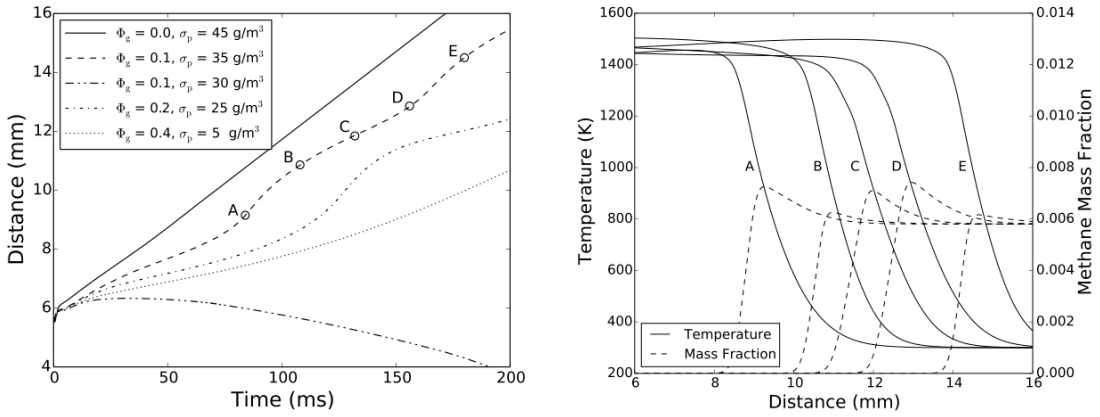

(a) Flame Propagation

(b) Flame Structure ($\Phi_g = 0.1$, $\sigma_p = 35\,g/m^3$)

Figure 8.8: Flame position as a function of time near the LFL for 10 µm particles using the continuum representation, and flame structure at different times for a single simulation. The flame structure is given at the times indicated with open circles in the flame propagation plot. All simulations use the DRM19 reaction mechanism.

Three different flame types near the hybrid LFL are demonstrated in Figure 8.8 (a). These are labeled as strong flames, weak flames, and unsteady flames in the hybrid LFL analysis. The simulation with $\Phi_g = 0.0$ and $\sigma_p = 45\,g/m^3$ illustrates a strong flame that ignites promptly and rapidly reaches a steady propagation velocity. A strong flame is defined in this work as one that has a higher burning velocity than the dust or the gas at their respective LFLs. Alternatively, the simulation with $\Phi_g = 0.1$ and $\sigma_p = 30\,g/m^3$ illustrates a nonflammable mixture in which the flame fails to

propagate.

Weak flames are defined as having a burning velocity lower than the methane or coal dust flames alone and characterized by a slower time to reach steady propagation. An example is shown in Figure 8.8 (a) for $\Phi_g = 0.4$ and $\sigma_p = 5\,g/m^3$, where the burning velocity is lower than the dust or the gas alone at their limits. The weak flame also takes approximately 150 ms to reach steady propagation. As in the case of the gas flame with an equivalence ratio of 0.45, it is not clear if these flames could physically exist with heat loss and instability mechanisms in the flow field.

Lastly, globally unsteady flames were also present in some simulations. This is illustrated in Figure 8.8 (a) by the cases with $\Phi_g = 0.1$ and $\sigma_p = 35\,g/m^3$, and with $\Phi_g = 0.2$ and $\sigma_p = 25\,g/m^3$. The first of these hybrid mixtures is explored further in Figure 8.8 (b), where temperature and methane mass fraction are given at each time indicated with a circle in the distance-time plot. As the flame moves from A to B, a period of acceleration occurs. This is accompanied by a decrease in methane gas concentration in the flame front and an increase in temperature. Moving to C and D, the flame slows down as the methane has been depleted. As the flame slows down, methane starts building up again and the process repeats moving to E. The global unsteady flames in Figure 8.8 have local burning velocities oscillating between 2 and 9 cm/s, with an average velocity between 3 and 5 cm/s. Similar to weak flames, it is not clear that these flames would propagate in a physical system without quenching due to heat loss.

To compare results from the parametric analysis to the mixing rules presented in Section 2.2.3, a value of K_{St}/K_G must be selected for Jiang's curve (JC, Equation 2.3). In this work, the ratio is taken to be equivalent to the ratio of maximum laminar burning velocities for the dust and gas alone. For 10 µm particles with the continuum representation, the maximum burning velocity could only be calculated with the BFER2 and MP1 mechanisms and had a value of 24.1 cm/s and 25.6 cm/s, respectively. For methane alone, the maximum burning velocity using the DRM19 mechanism was 30.8 cm/s. This is lower than the experimental value of approximately 37.5 cm/s given in Figure 5.10.

Using the simulation results with MP1 for the dust and DRM19 for the gas gives

$C\frac{K_{St}}{K_G} = 0.93$. This value is close to 1.0, which indicates near-linear mixing as predicted by LCL. The maximum deviation from LCL using this value in Equation 2.3 is approximately $1\,g/m^3$. This may indicate that linear mixing should be expected; however, using the experimental value of 37.5 cm/s for methane gas gives $C\frac{K_{St}}{K_G} = 0.76$. This value has a larger deviation than linear mixing and LCL with a maximum difference of $4\,g/m^3$.

Results from the parametric analysis for 10 µm particles using the continuum representation are compared to the different mixing rules in Figure 8.9. The single component limits are indicated by short dashed lines. The different mixing rules (see JC, LCL, and BC in Section 2.2.3) are indicated with solid, long-dash, and dash-dot lines, and JC is calculated from the MP1 reaction model for dust and using the experimental data for methane gas ($C\frac{K_{St}}{K_G} = 0.76$). The symbols in the figure indicate the three flame types outlined in Figure 8.8 and nonflammable mixtures.

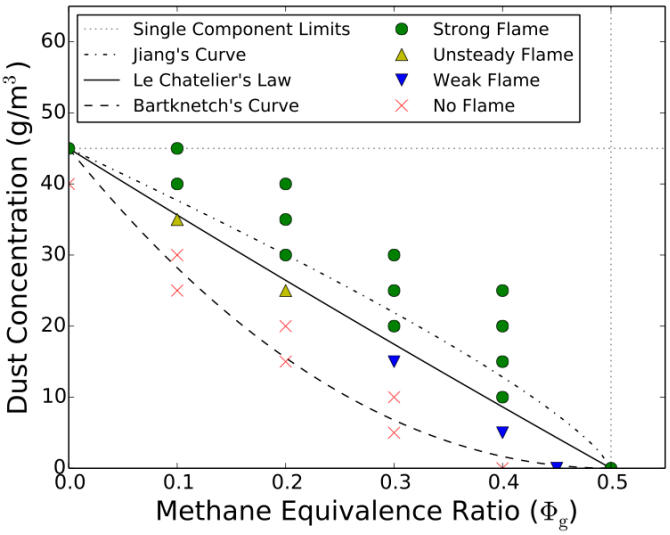

Figure 8.9: LFLs for hybrid mixtures of 10 µm coal dust using the continuum particle representation compared to mixing rules from the literature ($C\frac{K_{St}}{K_G} = 0.76$).

The results presented in Figure 8.9 demonstrate that LCL does a good job of separating strong flames from unsteady and weak flames. Nonflammable mixtures are clearly demonstrated above BC and strong ignition is clearly demonstrated below JC with $C\frac{K_{St}}{K_G} = 0.76$. Below LCL, unsteady flames are predicted at low Φ_g values, and weak flames are observed at higher methane equivalence ratios.

The same parametric analysis was performed for 10 µm particles with the discrete

Lagrange representation. Results from this analysis are summarized in Figure 8.10. The maximum burning velocity for 10 µm particles using the MP1 mechanism with the discrete approach is 23.7 cm/s (see Section 6.3.2). This gives $C\frac{K_{St}}{K_G} = 0.86$ if the simulated burning velocity for methane with DRM19 is used, and a value of 0.71 if the experimental results are used. The lower of these values is used to calculate JC as presented in Figure 8.10.

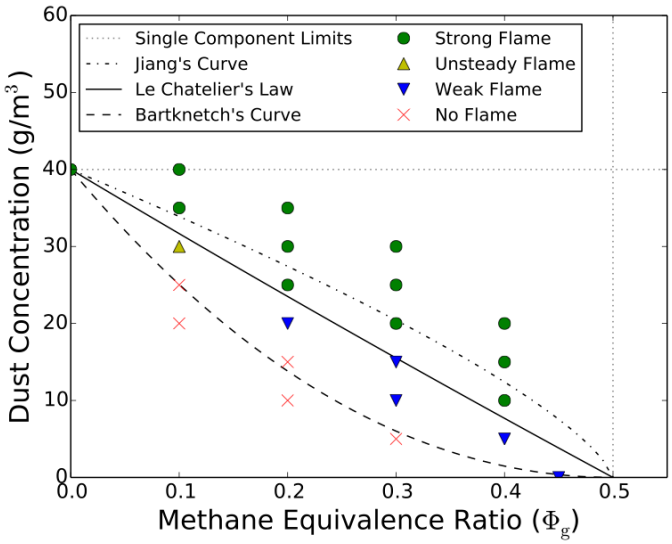

Figure 8.10: LFLs for hybrid mixtures of 10 µm coal dust using the discrete particle representation compared to mixing rules from the literature ($C\frac{K_{St}}{K_G} = 0.71$).

The hybrid LFL using the discrete representation for 10 µm particles is similar to the continuum representation with the exception that the lean limit of the coal dust is 40 g/m^3. Although all of the flame traces are unsteady due to isolated particle combustion using the discrete representation, only a single concentration demonstrates the long-time fluctuations shown in Figure 8.8. This mixture is indicated as an unsteady flame in Figure 8.10. Weak flames are present for flammable mixtures below LCL. The burning velocity at $\Phi_g = 0.3$ and $\sigma_p = 15$ g/m^3 is 3.8 cm/s, which is lower than the value of 4.2 cm/s at the coal dust LFL. From these results, LCL again reasonably separates strong flames from unsteady and weak flames, and nonflammable mixtures. Isolated particle combustion appears to allow weak flames to exist at lower hybrid concentrations approaching the limits of BC.

8.3.2 33 µm Particles

Although simulation results for 10 µm particles demonstrate nonflammable mixtures above BC, it is difficult to come to a conclusion about JC as $C\frac{K_{St}}{K_G}$ estimated from the simulation model is close to LCL. Extending the parametric analysis to 33 µm particles allows the applicability of JC to be explored further as the burning velocity at this particle size is lower. The maximum burning velocity with 33 µm particles is 13.2 and 12.0 cm/s using the continuum and discrete representations, respectively. This gives $C\frac{K_{St}}{K_G} = 0.48$ and 0.43 for these two conditions, when the numerical burning velocity is used with the DRM19 mechanism. These values deviate significantly from the LCL with maximum differences above 10 g/m^3.

Results from the parametric analysis using 33 µm particles are summarized in Figure 8.11. Simulations were completed for both the continuum and discrete particle representations. To be consistent with the previous results, JC was calculated using the experimental value for the methane burning velocity, giving $C\frac{K_{St}}{K_G} = 0.39$ and 0.36 for the continuum and discrete results presented in the figure.

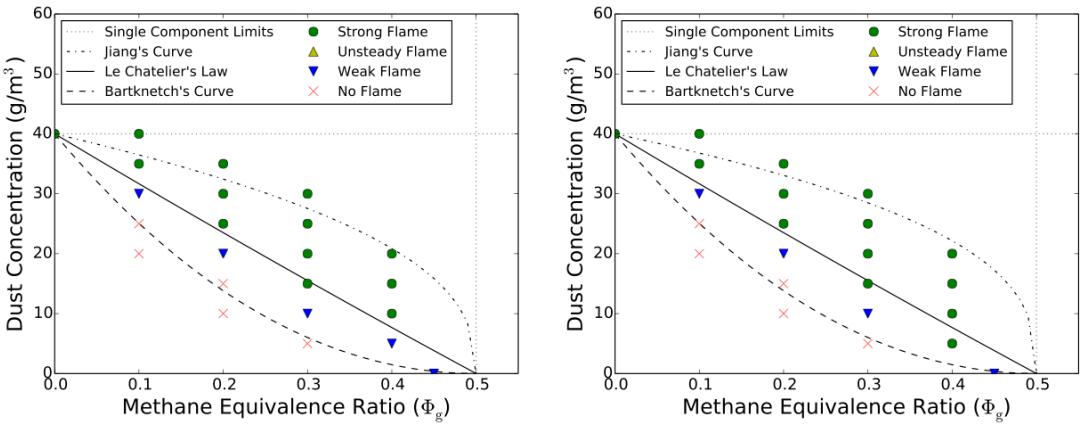

(a) Continuum Representation

(b) Discrete Representation

Figure 8.11: LFLs for hybrid mixtures of 33 µm coal dust using the continuum and discrete particle representations compared to mixing rules from the literature. Jiang's parameter $C\frac{K_{St}}{K_G}$ is equal to 0.39 and 0.36 for the continuum and discrete representations, respectively.

The global unsteady flame behaviour demonstrated for 10 µm particles was not observed for the larger 33 µm particles. This may be due to the overall slower heating and devolatilization of these particles, coupled with the reaction front. Contrary

to results from 10 µm particles, strong flames were predicted below LCL. For the continuum representation with the mixture of $\Phi_g = 0.3$ and $\sigma_p = 15\,g/m^3$ a burning velocity of 2.5 cm/s is predicted compared to 2.4 cm/s for the dust alone. For the discrete representation with mixtures of $\Phi_g = 0.3$ and $\sigma_p = 15\,g/m^3$, and $\Phi_g = 0.4$ and $\sigma_p = 5\,g/m^3$, burning velocities of 2.1 and 2.0 cm/s is predicted compared to 1.8 cm/s for the dust alone.

The results presented in Figure 8.11 also demonstrate strong flame propagation at many concentrations below JC. This suggests that JC in the form presented in Equation 2.3 is not capable of predicting hybrid mixture LFLs for methane gas and coal dust under laminar flow conditions.

8.4 Discussion of Results

Simulations at low dust and gas concentrations allowed the LFLs of methane gas, coal dust, and hybrid mixtures to be explored. Analysis of methane flame structure and burning velocity demonstrated that multistep reactions are necessary to capture the LFL and that the lack of a radiation or heat loss mechanism may tend to underpredict the values reported. A limit flame temperature of 1480 K was selected for methane gas, giving a LFL of $\Phi_g = 0.5$.

The flame structure and burning velocity of coal dust was analyzed, and the role of the reaction mechanism and particle diameter was explored. Although the impact of multistep reaction mechanisms on burning velocity was lower than demonstrated for gas flames, these mechanisms were still required to capture the dust LFL. Using the continuum particle representation, a flammability limit of $45\,g/m^3$ was found for 10 µm particles. The limit for 33 µm particles was slightly lower at $40\,g/m^3$. This decrease in LFL has been demonstrated in the literature previously for this particle size range [117] and may be caused by interaction between particle combustion and heat loss.

Isolated particle combustion demonstrated a limited role in the burning velocity approaching the LFL whereas it had a large effect at higher concentrations. This is due to flame enhancement from the local equivalence ratio in the vicinity of the particles being higher under isolated combustion conditions. This balances out the slower heat and mass transfer between isolated particles. The LFL of 10 µm particles

decreased to $40\,\mathrm{g/m^3}$ when the particles were modeled discretely, while the LFL of 33 µm remained the same at $40\,\mathrm{g/m^3}$.

The last section of this chapter explores the LFLs of hybrid mixtures and compares the results to mixing rules from the literature. Three flame types were identified near the LFL: strong flames, weak flames, and unsteady flames. Strong flames were defined as those that had burning velocities above that of the dust and gas alone at their respective LFLs, while weak flames had lower velocities. Unsteady flames showed periods of flame deceleration and methane build-up in the flame front, followed by methane consumption and acceleration. Parametric analysis was performed for hybrid mixtures with 10 and 33 µm particles under continuum and discrete modeling assumptions. This parametric analysis allowed the mixing rules outlined in Section 2.2.3 to be explored.

8.4.1 Evaluation of Mixing Rules

The simulation results presented in Section 8.3 suggest that LCL is applicable in determining the boundary of strong flame propagation for high-volatile coal dust with 10 µm diameter particles and methane gas. Under these conditions, weak and unsteady flames are predicted below LCL but nonflammable mixtures are present above BC. A mixing rule between LCL and BC may delineate these weakly flammable mixtures although it is not clear if they would be able to sustain flame propagation in a physical system with heat loss. These results indicate that LCL can be used to predict the LFL of methane gas and high-volatile coal dust with small particle diameters.

Both increasing the particle diameter and modeling isolated particle combustion shifted the LFLs slightly towards BC. For 33 µm particles, strong flames were present at concentrations below those predicted by LCL. These results indicate that LCL may not hold as the particle size is increased and that BC may provide a conservative estimate of the LFL for laminar flow conditions. However, they also indicate that the exponent in the LFL mixing rule should be variable and that a constant exponent cannot capture the correct LFL for different particle sizes.

The mixing rule proposed by Jiang et al. [32] provides a variable exponent based on the ratio of $K_{\mathrm{St}}/K_{\mathrm{G}}$. Since the current simulations represent open free-flame

propagation, the explosion parameters K_{St} and K_{G} cannot be determined directly. However, these values are related to the maximum laminar burning velocity (e.g., see relations used in macroscale simulation models [52]). In the current work, it is assumed that the ratio $K_{\mathrm{St}}/K_{\mathrm{G}}$ is equivalent to the ratio of the maximum laminar burning velocities of the dust and gas. This gives $C\frac{K_{\mathrm{St}}}{K_{\mathrm{G}}}$ in Equation 2.3, ranging from 0.36 to 1.0 for the parametric analysis. In all cases, strong flames were present below the JC mixing rule calculated with these assumptions.

There are two possibilities to explain the discrepancy between the current results and the findings of Jiang et al. [32]. The first is that some of the features not included in the model but present in the experiments caused a narrowing of the flammability limits. This could include turbulence, heat loss, radiation, particle size distribution, or chemical interaction between the different flammable gases or combustible dusts.

The second possibility is that the relation described by Jiang et al. [32] may be partially correct, but the ratio from different system parameters should be used. It seems intuitive to compare the burning velocity at the flame limits instead of the maxima, but this does not agree with the current model results. As the particle diameter is increased in the current model, the exponent decreases but the LFL becomes wider instead of narrower. The current model demonstrates that the ratio of flame temperatures at the individual limits is almost unity, ranging from 0.96–1.0. Replacing $K_{\mathrm{St}}/K_{\mathrm{G}}$ with the ratio of flame temperatures at the limits would predict hybrid LFLs that agree closely with LCL. Again, the ratio would have to be inverted to predict widening of the limits as presented seen in this work. Further investigation into JC with alternative system parameters is required in this area. Further investigation of the role of heat loss including radiation and hybrid mixtures with dusts containing volatiles dissimilar to the gas is also needed.

8.4.2 Implications for Experimental Testing

Assuming that hybrid LFLs are delineated by the limits of strong flame propagation, the parametric analysis suggests that LCL approximately divides flammable and nonflammable hybrid mixtures of methane gas and coal dust. This agrees with the experimental results of Amyotte et al. [15] but disagrees with Landman [120], who found explosion limits wider than defined by linear mixing. This discrepancy

may be due to the difference between flammability and ignitability. The flammability limit is the amount of fuel required for an already propagating flame to continue to propagate, while the ignitability limit takes into account the effects required to create the initial flame kernel including the ignition energy used. Amyotte et al. [15] demonstrated that 5 to 10 kJ ignition energy was required in a 26-L explosion chamber for the flammability limits to be determined.

In contrast, Landman [120] used a larger 40-L explosion chamber with spark ignition and a pyrotechnic 4 kJ ignitor [183]. These tests may be measuring the ignitability of the given mixture instead of its flammability. This demonstrates the importance of ensuring that the ignition kernel is fully established in order to come to conclusions about mixture flammability. It is also important to correctly characterize the limits of the dust and gas individually; otherwise no mixing rule will fit correctly.

8.4.3 Accuracy of the CFD Model

The results presented in Section 8.1.2 and Section 8.2.2 demonstrate that multistep reaction mechanisms are required to predict accurate LFL behaviour of methane gas and coal dust. Furthermore, a limit flame temperature is required to estimate the LFL for methane gas due to the absence of a heat loss mechanism in the model. A limit flame temperature of 1480 K predicted an LFL of $\Phi_g = 0.5$, which is consistent with the values reported in the literature [106, 109, 113].

The LFL for 10 µm coal dust containing 40 % volatiles and 60 % carbon was 45 g/m^3 in this work. This is on the low end of the literature values summarized in Section 2.2.2 but is consistent with coal containing moderate volatiles and low moisture and ash content. For example, Going et al. [110] found a limit ranging between 30 and 41 g/m^3 for Pittsburgh coal with 37 % volatiles and 1 % moisture content, Chawala et al. [115] found a limit ranging between 20 and 30 g/m^3 for Gilsonite with 83 % volatiles, and a value of 35 g/m^3 was found for bituminous coal with 20 % volatiles by extrapolating the analysis of Yuan et al. [116] to negligible moisture content. The current model also captures a small decrease in LFL for 33 µm particles, which is consistent with the experimental results of Cashdollar [117]. Cashdollar [117] found a decrease in LFL with particle diameters between 2 and 50 µm for Pittsburgh coal containing 37 % volatiles, 6 % ash content, and 1 % moisture content

in his work.

When strong flame propagation is assumed to delineate flammable and non-flammable mixtures, the hybrid LFLs in this work agree with the experimental results of Amyotte et al. [15]. The current model predicted a decrease in the flammable dust concentration of 40 % when 2 % methane by volume was added to the coal. This compares to the range from 30–50 % found by Amyotte et al. [15] experimentally. These results demonstrate that the current model captures physically representative hybrid LFLs within the error of the experimental results. However, the impact of radiation and system heat loss effects on these conclusions and on weak flame propagation below LCL remains to be explored.

Chapter 9

Conclusion

The overall objective of this thesis was to extend the current knowledge of burning velocity and flammability limits of hybrid mixtures of combustible dust and flammable gas. A computational fluid dynamics (CFD) model was developed based on the openly available OpenFOAM toolkit. The model included a Lewis number approximation for gas diffusion and global approaches to gas-phase viscosity and thermal conductivity. A Lagrange discretization was used for the particle phase, allowing both continuum and discrete representations of the dust to be explored. Single-step devolatilization, diffusion-limited surface reaction, and four gas-phase reaction mechanisms were employed in this work.

Burning velocities, flame structures, and coupling interactions between combustion phenomena were compared for methane gas, coal dust, and hybrid mixtures. Methane flame simulations allowed the reaction timescale, or residence time of the reaction front, to be quantified. Coal dust flame simulations allowed the flame structure to be categorized based on the equivalence ratio in the dust-driven explosion regime reported previously in the literature. Lastly, hybrid flame simulations allowed coupling between the dust and flame timescales to be explored, along with the impact of the volatile component and overall (volatile component and surface reaction) equivalence ratios. These results allowed novel combustion regimes to be identified and the role of particle diameter and discrete combustion to be explored.

Simulations of flame propagation near the LFLs for methane gas, coal dust, and hybrid mixtures allowed mixing rules from the literature to be evaluated. The roles of the gas-phase reaction mechanism and discrete combustion were investigated, and LFLs were compared to three mixing rules from the literature.

9.1 Summary of Results

The results of this work are divided into four categories based on the main contributions. A summary of each is given in the following sections, concluding with a review of the practical implications from the current findings.

9.1.1 Combustion Regimes

Simulations of coal dust flames allowed flame structure and its impact on the characteristics of the flame to be explored. These were categorized into combustion regimes that apply to both dust flames and to hybrid flames with low gas concentrations. Four combustion regimes were identified from the coal dust simulations: Type I (fuel-lean flames), Type II (volatile-lean flames), Type III (volatile-rich flames), and Type IV (transition flames). Type I flames terminated at concentrations where the equivalence ratio reached unity including both the volatile and carbon component of the fuel ($\Phi_{\mathrm{p}}^{\mathrm{t}} = 1.0$). Type II flames terminated at concentrations where the equivalence ratio reached unity, including only the volatile component of the fuel ($\Phi_{\mathrm{p}}^{\mathrm{v}} = 1.0$). Lastly, Type III flames terminated at concentrations where the maximum burning velocity occurred, moving into transition flames at higher dust concentrations.

Investigation into the effective equivalence ratio for hybrid mixtures allowed an additional combustion regime to be determined. Plotting results from the 10 µm particle simulations by total equivalence ratio including methane gas, dust volatiles, and dust surface reactions showed that burning velocity is independent of whether the fuel starts in the gas phase or solid phase at high dust concentrations. This led to the definition of a Type V (kinetic-limited flame) combustion regime. For the single-step reaction mechanism with 10 µm diameter particles, this regime occurred at very high dust concentrations; however, the limit decreased appreciably when multistep reaction mechanisms were used. The kinetic-limited regime is also dependent on particle diameter and was not present for the 33 µm particles studied.

The coupling interaction in hybrid mixtures with the gas above its LFL was explored by looking at the timescales associated with gas flame propagation and dust heating, devolatilization, and surface reaction. The flame residence timescale was determined from methane flame simulations and ranged from $\mathcal{O}(100)$ to $\mathcal{O}(1)$ ms as the

gas equivalence ratio was increased from 0.5 to 1.0. Comparing this to dust combustion timescales showed that enhancement of the gas flame due to the presence of the dust, could not occur until the particle size was below a threshold value at each gas concentration. Hybrid flame simulations predicted a coupling interaction that agreed with this timescale analysis. From this comparison, a Type VI (impeded-gas flame) combustion regime was identified in which the dust only acted to reduce the burning velocity of the propagating dust flame. This combustion regime was not present for 10 µm particles but occurred at initial gas equivalence ratios above $\Phi_g = 0.68$ for 33 µm particles.

9.1.2 Lower Flammability Limits

Simulations of methane gas, coal dust, and hybrid mixture flames at low concentrations allowed LFLs to be explored and compared to mixing rules from the literature. Methane flame results demonstrated that multistep reaction mechanisms are required to capture burning velocity near the limits and that radiation or other heat loss mechanisms are required to quantitatively capture the LFL. Using a limit flame criterion of 1480 K, a methane LFL of 5 % by volume was predicted, which is consistent with literature data.

Coal dust flame simulations also demonstrated that multistep reaction mechanisms are required to capture the LFLs. For 10 µm particles using a continuum representation, a limit concentration of 45 g/m^3 was found, while 33 µm particles had a lower limit concentration of 40 g/m^3. These values are consistent with literature data for coal dust with moderate volatiles and low ash and moisture content.

Hybrid mixture simulations demonstrated three flame structures near the LFLs: strong flames, weak flames, and unsteady flames. Strong flames were defined as having a larger burning velocity than the dust and gas at their respective limits, while weak flames did not. Unsteady flames oscillated around a mean propagation velocity due to interaction between particle heating, volatile release, and gas-phase reaction. It is not clear whether weak or unsteady flames would be able to propagate in a physical system where heat loss to the surroundings was included.

Le Chatelier's law was shown to divide the dust concentrations at which strong flame propagation occurred from weak and unsteady propagation for small particle

diameters. As the particle diameter was increased, a slight shift towards Bartknetch's curve was demonstrated. These results suggest that a constant exponent in the mixture rule cannot properly capture hybrid mixture LFLs. In all cases strong flame propagation occurred at concentrations above that predicted by Jiang's curve. It was suggested that the ratio of $K_{\mathrm{St}}/K_{\mathrm{G}}$ in Jiang's curve may need to be replaced with the ratio of some other system parameters. The ratio of limit flame temperatures for the coal dust and methane gas was nearly unity. If the inverse of this parameter was used instead of maximum rates of pressure rise, the Jiang's curve may produce LFLs that agree more closely with the simulation results.

9.1.3 Discrete Particle Combustion

Coal dust simulation results demonstrated that discrete particle combustion impacts burning velocity up to higher concentrations than previously suggested for droplet combustion. For 10 µm particles, a reduction in burning velocity from capturing discrete combustion was demonstrated up to $400\,\mathrm{g/m^3}$. For 33 µm particles, this reduction was present up to $1000\,\mathrm{g/m^3}$. Hybrid flame simulations demonstrated that the centre-to-centre normalized spacing of the particles (length-to-diameter ratio, L_s/d_{p}) is an important parameter for characterizing the concentrations at which both discrete combustion and hybrid flame enhancement occur at low gas concentrations. A limiting L_s/d_{p} of 8.1 was found for 33 µm particles and of 10.8 for 10 µm particles, above which discrete combustion and burning velocity enhancement occurred.

Simulation results for both coal dust and hybrid mixtures demonstrated a reduced role of discrete particle combustion near the LFLs. As the overall system became very fuel lean, the reduction in burning velocity from particle spacing was counterbalanced by the local equivalence ratio in the vicinity of the discrete particles being quite high. This high local volatile content in the vicinity of the particle helped to accelerate the flame during particle ignition. This tended to increase the burning velocity and reduced the LFL from conditions when the system was modeled as a continuum.

9.1.4 Accuracy of the CFD Model

Methane flame simulations demonstrated that the unity Lewis number approach could only quantitatively predict burning velocities at equivalence ratios below 0.8 using

two-step (BFER2), 19-species (DRM19), and 53-species (GRI53) reaction mechanisms. The single-step (MP1) reaction mechanism overpredicted burning velocity by up to 50 % in this concentration range. Furthermore, the DRM19 and GRI53 mechanisms were required to achieve the expected maximum burning velocity near the stoichiometric concentration and a decrease in burning velocity for fuel-rich concentrations.

To quantitatively capture the burning velocity throughout the entire flammable methane concentration range, both detailed reaction mechanisms and gas species component diffusivities were required. At a minimum, the DRM19 reaction model was necessary along with mixture-averaged gas diffusion. The main difficulty was that this increased the computational requirements by at least a factor of 1500 compared to the MP1 mechanism with global treatment of transport parameters. Moving to the GRI53 mechanism with molecular diffusion theory increased the computational requirements by an additional order of magnitude. Given the current computational resources it does not appear that these detailed simulation models will be tractable for laboratory, device, or system-scale simulations.

Coal dust flame simulations demonstrated that the multistep reaction mechanisms were less important for capturing the magnitude of the burning velocity than for gas flames when propagation could be captured. Under these conditions, the maximum difference was within 10 % for 10 and 33 µm particles up to 180 g/m^3 and 400 g/m^3, respectively. Furthermore, multistep reaction mechanisms were unable to capture flame propagation at higher dust concentrations. This difficulty appears to be related to the intermediate reaction steps and interaction with the decreased flame temperature in dust flames. It is not currently clear if the baseline reaction mechanisms for methane gas can be applied directly to laminar flame propagation of devolatilizing dust. More research is needed in this area moving forward.

Although difficulties were encountered in capturing flame propagation in dust clouds at high concentrations with the multistep reaction mechanisms, the current model with MP1 compared favourably to experimental data. Qualitative burning velocity features, such as finer particles shifting the peak burning velocity to leaner dust concentrations and coarse dust particles having a higher burning velocity at very rich concentrations, were captured. Furthermore, quantitative agreement between

the burning velocity results was achieved throughout much of the concentration range once preheating in the experimental apparatus was accounted for. Overall, the current simulation model was able to reproduce these findings, whereas more detailed models reported previously in the literature were not.

Results from the hybrid flame simulations using the MP1 reaction mechanism demonstrated that the current model is able to capture coupling interaction between the dust and gas and the impeded gas flame regime under fuel-lean conditions. Simulation results also demonstrated agreement for burning velocity enhancement in the dust-driven regime at a range of dust concentrations. Difficulties were found in capturing the burning velocity as the initial gas in the hybrid mixture approached the stoichiometric concentration, due to limitations in the MP1 mechanism. Future work is required to understand the overall impact of reaction mechanisms on the novel combustion regimes identified in this work.

9.1.5 Practical Implications

A major challenge for hybrid explosion prevention and protection is the number of tests required to characterize the fuel involved. The combustion regime diagrams developed in this work can be used to guide experimental testing programs with similar materials. For example, many coal dusts have similar volatile and carbon content and may have similar regime diagrams with only the limits of each regime changing. The current diagram can then be used as a starting point to guide which mixtures to test to characterize flame propagation. Furthermore, developing a better understanding of gas and dust combustion timescales could lead to these diagrams being created for other materials before testing occurs.

The four combustion regimes developed for low gas concentrations in this work have specific characteristics with regard to flame temperature, burning velocity, and species concentration behind the flame. This provides insight into the combustion phenomena and also a way to categorize dust of unknown chemical composition, or where the reaction mechanisms are not well-known. For example, these characteristics could be measured for an unknown dust and used to determine information about the total and volatile component stoichiometry.

The final practical implications of this work are the insights gained from comparing

free-flame combustion regimes to closed-chamber explosion regimes presented previously in the literature. This comparison demonstrated that the dust does not need to react in the flame front to be registered as coupled with the explosion pressure-time trace in a closed system. Instead, dust can react behind the gas flame but before the flame reaches the vessel walls. These findings have important implications for scaling of closed-chamber results for hybrid mixtures. Understanding both free-flame and closed-chamber explosion behaviour is needed to characterize hybrid explosion hazards under industry relevant conditions.

9.2 Recommendations

Throughout this work, several deficiencies were found in the current status of knowledge related to dust and hybrid flame propagation. Firstly, there has been only a limited investigation of gas-phase reaction mechanisms designed specifically for dust combustion and laminar burning velocity in the literature. In the current work, multistep mechanisms based on methane combustion were unable to capture flame propagation at high dust concentrations for different particle diameters. This had been demonstrated with previous CFD models, suggesting the development of gas-phase reaction mechanisms specific to dust combustion are required. The impact of multispecies diffusion in conjunction with these detailed reaction mechanisms may also be necessary to extend knowledge in this area.

Secondly, the results presented in this work demonstrate that the impact of isolated particle combustion on burning velocity may extend to higher concentrations than predicted from droplet flames. The discrete particle representation presented in this work demonstrates the "worst-case" scenario where it has the largest possible impact on flame propagation. Further investigation is required using randomly distributed particles in two-dimensional and three-dimensional space. Using statistical analysis in these systems would allow the impact of discrete combustion to be explored more thoroughly. The impact of particle size distributions and preferential flame travel through the particle cloud should also be included in this analysis.

Lastly, simulations preformed near the methane lean limits demonstrated that the LFL of small dust particles may be captured in the current model without heat loss to the external system. However, larger particles and gas flame simulations

demonstrated that both multistep reaction mechanisms and heat loss considerations may be needed to capture the LFL. Further research into the impact of radiative and system heat loss on the LFL of dust flames and hybrid mixtures is needed.

9.2.1 Future Work

Future work in this area should follow two directions. Firstly, the model should be extended to practical systems with larger multi-dimensional geometries and turbulent flow conditions. A good place to begin would be to compare closed-chamber explosions at laboratory scale to the free-flame simulations presented in this thesis. This comparison would be useful from a practical perspective as suggested above, but also to validate the model under more industry relevant conditions.

The second direction is to use the current model to explore more fundamental aspects of dust and hybrid mixture flames. As discussed previously, more work is required in the areas of reaction mechanisms, gas diffusion and the impact on dust flames, isolated particle combustion, and radiation. The current model provides a novel framework which has been verified for laminar flame propagation, from which each of these features can be explored individually and in combination moving forward.

References

[1] Justice K.P. Richard. *The Westray Story – A Predictable Path to Disaster*. Report of the Westray Mine Public Inquiry (Province of Nova Scotia, Canada), 1997.

[2] P.R. Amyotte and A.M. Oehmen. Application of a loss causation model to the Westray mine explosion. *Process Safety and Environmental Protection*, 80:55–59, 2002.

[3] P.L. Carter. The Halifax explosion a century later: Lessons for our time. *The American Journal of Surgery*, 2018. doi: 10.1016/j.amjsurg.2017.12.010 (in press).

[4] Hon. D. Downe. *Westray: A Plan of Action*. Government's Response to the Report of the Westray Mine Public Inquiry (Province of Nova Scotia, Canada), 1997.

[5] NFPA. *Report of Important Dust Explosions*. National Fire Protection Agency, Quincy, MA, 1957.

[6] R.K. Eckhoff. *Dust Explosions in the Process Industries*. Gulf Professional Publishing, Amsterdam, 3rd edition, 2003.

[7] U.S Chemical Safety and Hazard Investigation Board. *Investigation Report: Combustible Dust Hazard Study*. Report No. 2006-H-1, 2006.

[8] M. Nifuku, T. Matsuda, and H. Enomoto. Recent development of standardization of testing methods for dust explosion in Japan. *Journal of Loss Prevention in the Process Industries*, 13:243–251, 2000.

[9] M.S. Mannan and S.P. Waldram. Learning lessons from incidents: A paradigm shift is overdue. *Process Safety and Environmental Protection*, 92:760–765, 2014.

[10] X.Q. Yan and J.L. Yu. Dust explosion incidents in China. *Process Safety Progress*, 31:187–189, 2012.

[11] T. Abbasi and S.A. Abbasi. Dust explosions: Cases, causes, consequences, and control. *Journal of Hazardous Materials*, 140:7–44, 2007.

[12] Z. Yuan, N. Khakzad, F. Khan, and P. Amyotte. Dust explosions: A threat to the process industries. *Process Safety and Environmental Protection*, 98:57–71, 2015.

[13] Y.P. Zheng, C.G. Feng, G.X. Jing, X.M. Qian, X.J. Li, Z.Y. Liu, and P. Huang. A statistical analysis of coal mine accidents caused by coal dust explosions in China. *Journal of Loss Prevention in the Process Industries*, 22:528–532, 2009.

[14] W. Bartknecht. *Dust Explosions: Course, Prevention, Protection.* Springer-Verlag, New York, NY, 1981.

[15] P.R. Amyotte, K.J. Mintz, M.J. Pegg, and Y.H. Sun. The ignitability of coal dust-air and methane-coal dust-air mixtures. *Fuel*, 72:671–679, 1993.

[16] M. Abuswer, P. Amyotte, F. Khan, and S. Imtiaz. Retrospective risk analysis and controls for Semabla grain storage hybrid mixture explosion. *Process Safety and Environmental Protection*, 100:49–64, 2016.

[17] Md. N. Hossain, P. Amyotte, M. Abuswer, A. Dastidar, F. Khan, R. Eckhoff, and Y. Chunmiao. Influence of liquid and vapourized solvents on explosibility of pharmaceutical excipient dusts. *Process Safety Progress*, 33:374–379, 2014.

[18] A. Denkevits. Explosibility of hydrogen–graphite dust hybrid mixtures. *Journal of Loss Prevention in the Process Industries*, 20:698–707, 2007.

[19] R. Pilão, E. Ramalho, and C. Pinho. Explosibility of cork dust in methane/air mixtures. *Journal of Loss Prevention in the Process Industries*, 19:17–23, 2006.

[20] M.S. Worsfold, P.R. Amyotte, F.I. Khan, A.G. Dastidar, and R.K. Eckhoff. Review of the explosibility of nontraditional dusts. *Industrial & Engineering Chemistry Research*, 51:7651–7655, 2012.

[21] P. Amyotte, F. Khan, S. Boilard, I. Iarossi, C. Cloney, A. Dastidar, R. Eckhoff, L. Marmo, and R. Ripley. Explosibility of nontraditional dusts: Experimental and modeling challenges. In *Proceedings of HAZARDS XXII, IChemE Symposium Series No. 158*, pages 83–90, 2012.

[22] A.G. Dastidar, B. Nalda-Reyes, and C.J. Dahn. Evaluation of dust and hybrid mixture explosion potential in process plants. *Process Safety Progress*, 24:294–298, 2005.

[23] NFPA 69. *Standard on Explosion Prevention Systems.* National Fire Protection Agency, Quincy, MA, 2014.

[24] NFPA 654. *Standard for the Prevention of Fire and Dust Explosions from the Manufacturing, Processing, and Handling of Combustible Particulate Solids.* National Fire Protection Agency, Quincy, MA, 2017.

[25] ASTM E1515-07. *Standard Test Method for Minimum Explosible Concentration of Combustible Dusts.* ASTM International, West Conshohocken, PA, 2010.

[26] NFPA 68. *Standard on Explosion Protection by Deflagration Venting.* National Fire Protection Agency, Quincy, MA, 2013.

[27] ASTM E1226-10. *Standard Test Method for Explosibility of Dust Clouds*. ASTM International, West Conshohocken, PA, 2010.

[28] G. Pellmont. Minimum ignition energy of combustible dusts and explosion behavior of hybrid mixtures. In *Proceedings of the 3rd International Symposium on Loss Prevention and Saftey Promotion in the Process Industries*, pages 851–862, Basel, Switzerland, 1980.

[29] A. Garcia-Agreda, A. Di Benedetto, P. Russo, E. Salzano, and R. Sanchirico. Dust/gas mixtures explosion regimes. *Powder Technology*, 205:81–86, 2011.

[30] R. Sanchirico, A. Di Benedetto, A. Garcia-Agreda, and P. Russo. Study of the severity of hybrid mixture explosions and comparison to pure dust-air and vapour-air explosions. *Journal of Loss Prevention in the Process Industries*, 24:648–655, 2011.

[31] P. Field. *Dust Explosions*. Elsevier Science Publishing, Amsterdam, 1989.

[32] J. Jiang, Y. Liu, and S.M. Mannan. A correlation of the lower flammability limit for hybrid mixtures. *Journal of Loss Prevention in the Process Industries*, 32:120–126, 2014.

[33] J. Jiang, Y. Liu, C.V. Mashuga, and S.M. Mannan. Validation of a new formula for predicting the lower flammability limit of hybrid mixtures. *Journal of Loss Prevention in the Process Industries*, 35:52–58, 2015.

[34] R.K. Eckhoff. Current status and expected future trends in dust explosion research. *Journal of Loss Prevention in the Process Industries*, 18:225–237, 2005.

[35] R.A. Ogle. *Dust Explosion Dynamics*. Elsevier Inc., Cambridge, MA, 2017.

[36] C.T. Cloney, R.C. Ripley, M.J. Pegg, and P.R. Amyotte. Laminar burning velocity and structure of coal dust flames using a unity Lewis number CFD model. *Combustion and Flame*, 190:87–102, 2018.

[37] D. Bradley, M. Lawes, H.Y. Park, and N. Usta. Modeling of laminar pulverized coal flames with speciated devolatilization and comparisons with experiments. *Combustion and Flame*, 144:190–204, 2006.

[38] H.Y. Park and Y.H. Park. Laminar burning velocities of atmospheric coal air mixtures. *KEPCO Journal on Electric Power and Energy*, 2:89–96, 2016.

[39] T. Skjold, B.J. Arntzen, O.R. Hansen, O.J. Taraldset, I.E. Storvik, and R.K. Eckhoff. Simulating dust explosions with the first version of DESC. *Process Saftey and Environmental Protection*, 83:151–160, 2005.

[40] T. Skjold. Review of the DESC project. *Journal of Loss Prevention in the Process Industries*, 20:291–302, 2007.

[41] T. Skjold, Ø. Larsen, and O.R. Hansen. Possibilities, limitations, and the way ahead for dust explosion modeling. In *Proceedings of HAZARDS XIX, IChemE Symposium Series No. 151*, 2006.

[42] P. Amyotte. *An Introduction to Dust Explosions*. Elsevier Inc., Oxford, UK, 2013.

[43] C.T. Cloney, P.R. Amyotte, F.I. Khan, and R.C. Ripley. Development of an organizational framework for studying dust explosion phenomena. *Journal of Loss Prevention in the Process Industries*, 30:228–235, 2014.

[44] P. Cardillo. Some historical accidental explosions. *Journal of Loss Prevention in the Process Industries*, 14:69–76, 2001.

[45] Mine Safety and Health Administration. *Fatal Underground Mine Explosion: Upper Big Branch Mine-South, Performance Coal Company. Montcoal, Raleigh County, West Virginia.* MSHA Report ID No. 46-08436, 2011.

[46] S.K. Kundu, J. Zanganeh, D. Eschebach, and B. Moghtaderi. Explosion severity of methane-coal dust hybrid mixtures in a ducted spherical vessel. *Powder Technology*, 323:95–102, 2018.

[47] H.K. Versteeg and W. Malalasekera. *An Introduction to Computational Fluid Dynamics: The Finite Volume Method*. Pearson Education Limited, Harlow, UK, 2nd edition, 2007.

[48] Ch. Proust, J. Daubech, and E. Leprette. Differentiated routes for the simulation of the consequences of explosions. *Journal of Loss Prevention in the Process Industries*, 22:288–294, 2009.

[49] L. Qiao and J. Xu. Detailed numerical simulation of flame propagation in coal-dust clouds. *Combustion Theory and Modelling*, 16:747–773, 2012.

[50] T. Skjold. Simulating vented maize starch explosions in a 236 m^3 silo. In *Proceedings of the Eleventh International Fire Safety Science Symposium*, pages 1469–1480, 2014.

[51] D. Castellanos, T. Skjold, K. van Wingerden, R.K. Eckhoff, and S.M. Mannan. Validation of the DESC code in simulating the effect of vent ducts on dust explosions. *Industrial & Engineering Chemistry Research*, 52:6057–6067, 2013.

[52] T. Skjold, B.J. Arntzen, O.R. Hansen, I.E. Storvik, and R.K. Eckhoff. Simulation of dust explosions in complex geometries with experimental input from standardized tests. *Journal of Loss Prevention in the Process Industries*, 19:210–217, 2006.

[53] K. van Wingerden, B.J. Arntzen, and P. Kosinski. Modelling of dust explosions. *VDI-Berichte*, 1601:411–421, 2001.

[54] B.J. Arntzen, H.C. Salvesen, H.F. Nordhaug, I.E. Storvik, and O.R. Hansen. CFD modeling of oil mist and dust explosion experiments. In *Proceedings of the Fourth International Seminar on Fire and Explosion Hazards*, pages 601–608, 2003.

[55] T. Skjold, D. Castellanos, K.L. Olsen, and R.K. Eckhoff. Experimental and numerical investigation of constant volume dust and gas explosions in a 3.6-m flame acceleration tube. *Journal of Loss Prevention in the Process Industries*, 30:164–176, 2014.

[56] M. Ghaffari, T. Skjold, K. van Wingerden, H. Hisken, R.K. Eckhoff, and A.C. Hoffman. A model validation framework for the dust explosion simulator FLACS-DustEx: Challenges, limitations and possibilities. In *Proceedings of the 11th International Symposium on Hazards, Prevention, and Mitigation of Industrial Explosions*, pages 223–238, 2016.

[57] R. Redlinger. Numerical simulation of hybrid dust/gas explosion experiments in the standard 20-l sphere. *Fusion Engineering and Design*, 100:419–424, 2015.

[58] D. Bradley, M. Lawes, M.J. Scott, and N. Usta. The structure of Coal-Air-CH_4 laminar flames in a low-pressure burner: CARS measurements and modeling studies. *Combustion and Flame*, 124:82–105, 2001.

[59] D. Bradley, G. Dixon-Lewis, and S. El-Din Habik. Lean flammability limits and laminar burning velocities of CH_4-air-graphite mixtures and fine coal dusts. *Combustion and Flame*, 77:41–50, 1989.

[60] D. Bradley, Z. Chen, S. El-Sherif, S. El-Din Habik, G. John, and G. Dixon-Lewis. Structure of laminar premixed carbon-methane-air flames and ultrafine coal combustion. *Combustion and Flame*, 96:80–96, 1994.

[61] R.W. Houim and E.S. Oran. Numerical simulation of dilute and dense layered coal-dust explosions. *Proceedings of the Combustion Institute*, 35:2083–2090, 2015.

[62] R.W. Houim and E.S. Oran. Structure and flame speed of dilute and dense layered coal-dust explosions. *Journal of Loss Prevention in the Process Industries*, 36:214–222, 2015.

[63] C.J. Greenshields. OpenFOAM user guide, version 4.0. http://foam.sourceforge.net/docs/Guides-a4/OpenFOAMUserGuide-A4.pdf, 2016. Accessed: 2017-06-30.

[64] R.J. Kee, M.E. Coltrin, and P. Glarborg. *Chemically Reacting Flow: Theory & Practice*. John Wiley & Sons, Inc., Hoboken, NJ, 2003.

[65] C.T. Cloney, R.C. Ripley, M.J. Pegg, and P.R. Amyotte. Evaluating regime diagrams for closed volume hybrid explosions. *Journal of Loss Prevention in the Process Industries*, 49:912–918, 2017.

[66] C.T. Cloney, R.C. Ripley, P.R. Amyotte, and F.I. Khan. Quantifying the effect of strong ignition sources on particle preconditioning and distribution in the 20-L chamber. *Journal of Loss Prevention in the Process Industries*, 26:1574–1582, 2013.

[67] C.T. Cloney, P.R. Amyotte, and R.C. Ripley. Ignition energy dependence of low-Kst steel dust in the 20-L explosion chamber. In *Proceedings of the 10th International Symposium on Hazards, Prevention, and Mitigation of Industrial Explosions*, pages 1511–1523, 2014.

[68] C.T. Cloney, R.C. Ripley, M.J. Pegg, and P.R. Amyotte. Ignition delay and flame radius for single particle combustion in high-temperature flammable gas/air mixtures. In *Proceedings of the 25th International Colloquium on the Dynamics of Explosions and Reactive Systems*, 2015.

[69] Yi. Liu, J. Sun, and D. Chen. Flame propagation in hybrid mixture of coal dust and methane. *Journal of Loss Prevention in the Process Industries*, 20:691–697, 2007.

[70] A. Di Benedetto, A. Garcia-Agreda, O. Dufaud, I. Khalili, R. Sanchirico, N. Cuervo, L. Perrin, and P. Russo. Flame propagation of dust and gas-air mixtures in a tube. In *Proceedings of the 7th Mediterranean Combustion Symposium*, 2011.

[71] Y. Li, H. Xu, and X. Wang. Experimental study on the influence of initial pressure of explosion of methane-coal dust mixtures. *Procedia Engineering*, 62:980–984, 2013.

[72] D. Torrado, N. Cuervo, S. Pacault, P. Glaude, and O. Dufaud. Influence of carbon black nanoparticles on the front flame velocity of methane/air explosions. *Journal of Loss Prevention in the Process Industries*, 49:919–928, 2017.

[73] C. Dong, M. Bi, and Y. Zhou. Effects of obstacles and deposited coal dust on characteristics of premixed methane-air explosions in a long closed pipe. *Safety Science*, 50:1786–1791, 2012.

[74] Q. Liu, Y. Hu, C. Bai, and M. Chen. Methane/coal dust/air explosions and their suppression by solid particle suppressing agents in a large–scale experimental tube. *Journal of Loss Prevention in the Process Industries*, 26:310–316, 2013.

[75] M.J. Ajrash, J. Zanganeh, and B. Moghtaderi. Methane-coal dust hybrid fuel explosion properties in a large cylindrical explosion chamber. *Journal of Loss Prevention in the Process Industries*, 40:317–328, 2016.

[76] J.B. Howard and R.H. Essenhigh. Mechanism of solid-particle combustion with simultaneous gas-phase volatiles combustion. In *Proceedings of the Eleventh Symposium (International) on Combustion*, pages 399–408, 1967.

[77] M.D. Horton, F.P. Goodson, and L.D. Smoot. Characteristics of flat, laminar coal-dust flames. *Combustion and Flame*, 28:187–195, 1977.

[78] L.D. Smoot and M.D. Horton. Propagation of laminar pulverized coal-air flames. *Progress in Energy and Combustion Science*, 3:235–258, 1977.

[79] J.L. Krazinski, R.O. Buckius, and H. Krier. Coal dust flames: A review and development of a model for flame propagation. *Progress in Energy and Combustion Science*, 5:31–71, 1979.

[80] Y. Xie, V. Raghavan, and A.S. Rangwala. Study of interaction of entrained coal dust particles in lean methane–air premixed flames. *Combustion and Flame*, 159:2449–2456, 2012.

[81] S.R. Rockwell and A.S. Rangwala. Influence of coal dust on premixed turbulent methane-air flames. *Combustion and Flame*, 160:635–640, 2013.

[82] M. Lee, S. Ranganathan, and A.S. Rangwala. Influence of the reactant temperature on particle entrained laminar methane–air premixed flames. *Proceedings of the Combustion Institute*, 35:729–736, 2015.

[83] M. Soo, P. Julien, S. Goroshin, J.M. Bergthorson, and D.L. Frost. Stabilized flames in hybrid aluminum–methane–air mixtures. *Proceedings of the Combustion Institute*, 34:2213–2220, 2013.

[84] S. Goroshin, I. Fomenko, and J.H.S. Lee. Burning velocities in fuel-rich aluminum dust clouds. In *Proceedings of the Twenty-Sixth Symposium (International) on Combustion*, pages 1961–1967, 1996.

[85] S. Goroshin, J. Mamen, A. Higgins, T. Bazyn, N. Glumac, and H. Krier. Emission spectroscopy of flame fronts in aluminum suspensions. *Proceedings of the Combustion Institute*, 31:2011–2019, 2007.

[86] P. Julien, S. Whiteley, S. Goroshin, M.J. Soo, D.L. Frost, and J.M. Bergthorson. Flame structure and particle–combustion regimes in premixed methane-iron-air suspensions. *Proceedings of the Combustion Institute*, 35:2431–2438, 2015.

[87] M.J. Ajrash, J. Zanganeh, and B. Moghtaderi. Effects of ignition energy on fire and explosion characteristics of dilute hybrid fuel in ventilation air methane. *Journal of Loss Prevention in the Process Industries*, 40:207–216, 2016.

[88] A. Denkevits and B. Hoess. Hybrid H_2/Al dust explosions in Siwek sphere. *Journal of Loss Prevention in the Process Industries*, 36:509–521, 2015.

[89] P. Kosinski, R. Nyheim, V. Asokan, and T. Skjold. Explosions of carbon black and propane hybrid mixtures. *Journal of Loss Prevention in the Process Industries*, 26:45–51, 2013.

[90] Y.F. Khalil. Experimental investigation of the complex deflagration phenomena of hybrid mixtures of activated carbon dust/hydrogen/air. *Journal of Loss Prevention in the Process Industries*, 26:1027–1038, 2013.

[91] Q. Li, B. Lin, H. Dai, and S. Zhao. Explosion characteristics of H_2/CH_4/air and CH_4/coal dust/air mixtures. *Powder Technology*, 229:222–228, 2012.

[92] A. Di Benedetto, A. Garcia-Agreda, P. Russo, and R. Sanchirico. Combined effect of ignition energy and initial turbulence on the explosion behavior of lean gas/dust-air mixtures. *Industrial & Engineering Chemistry Research*, 51:7663–7670, 2012.

[93] P.R. Amyotte, M. Lindsay, R. Domaratzki, N. Marchand, A. Di Benedetto, and P. Russo. Prevention and mitigation of polyethylene and hydrocarbon/polyethylene explosions. In *Proceedings of the 43rd Loss Prevention Symposium*, pages 597–612, 2009.

[94] A. Denkevits. Hydrogen/dust explosion hazard in ITER: Effect of nitrogen dilution on explosion behavior of hydrogen/tungsten dust/air mixtures. *Fusion Engineering and Design*, 85:1059–1063, 2010.

[95] O. Dufaud, L. Perrin, S. Traoré, S. Chazelet, and D. Thomas. Explosion of vapour/dust hybrid mixtures: A particular class. *Powder Technology*, 190:269–273, 2009.

[96] O. Dufaud, L. Perrin, and M. Traoré. Dust/vapour explosions: Hybrid behaviours? *Journal of Loss Prevention in the Process Industries*, 21:481–484, 2008.

[97] A. Garcia-Agreda. *Study of Hybrid Mixture Explosions*. PhD thesis, Università degli Studi di Napoli Federico II, Naples, Italy, 2010.

[98] P. Russo, A. Di Benedetto, and R. Sanchirico. Theoretical evaluation of the explosion regimes of hybrid mixtures. *Chemical Engineering Transactions*, 26:51–56, 2012.

[99] P. Julien, J. Vickery, S. Goroshin, J.M. Bergthorson, and D.L. Frost. Intrinsic instabilities of dust flames. In *Proceedings of the 11th International Symposium on Hazards, Prevention, and Mitigation of Industrial Explosions*, pages 338–348, 2016.

[100] O.-S. Han, M. Yashima, T. Matsuda, H. Matsui, A. Miyake, and T. Ogawa. A study of flame propagation mechanisms in lycopodium dust clouds based on dust particles' behavior. *Journal of Loss Prevention in the Process Industries*, 14:153–160, 2001.

[101] W. Gao, J. Yu, T. Mogi, X. Zhang, J. Sun, and R. Dobashi. Effects of particle thermal characteristics on flame microstructures during dust explosions of three long–chain monobasic alcohols in a half-closed chamber. *Journal of Loss Prevention in the Process Industries*, 32:127–134, 2014.

[102] H.H. Chiu, H.Y. Kin, and E.J. Croke. Internal group combustion of liquid droplets. In *Proceedings of the Nineteenth Symposium (International) on Combustion*, pages 971–980, 1982.

[103] M. Nakamura, F. Akamatsu, R. Kurose, and M. Katsuki. Combustion mechanism of liquid fuel spray in a gaseous flame. *Physics of Fluids*, 17:123301, 2005.

[104] L.A. Lovachev, V.S. Babkin, V.A. Bunev, A.V. V'Yun, V.N. Krivulin, and A.N. Baratov. Flammability limits: An invited review. *Combustion and Flame*, 20:259–289, 1973.

[105] L.A. Lovachev. Flammability limits – A review. *Combustion Science and Technology*, 20:209–224, 1979.

[106] L.G. Britton. Two hundred years of flammable limits. *Process Safety Progress*, 21:1–11, 2002.

[107] H.F. Coward and G.W. Jones. Limits of flammability of gases and vapors. *U.S. Bureau of Mines*, Bulletin 503, Washington, DC, 1952.

[108] M. Hertzberg, K.L. Cashdollar, and I.A. Zlochower. Flammability limit measurements for dust and gases: Ignition energy requirements and pressure dependence. In *Proceedings of the Twenty-First Symposium (International) on Combustion*, pages 303–313, 1986.

[109] K.L. Cashdollar, I.A. Zlochower, G.M. Green, R.A. Thomas, and M. Hertzberg. Flammability of methane, propane, and hydrogen gases. *Journal of Loss Prevention in the Process Industries*, 13:327–340, 2000.

[110] J.E. Going, K. Chatrathi, and K.L. Cashdollar. Flammability limit measurements for dusts in 20-L and 1-m^3 vessels. *Journal of Loss Prevention in the Process Industries*, 13:209–219, 2000.

[111] K. Chatrathi. Dust and hybrid explosibility in a 1 m^3 spherical chamber. *Process Saftey Progress*, 13:183–189, 1994.

[112] C.V. Mashuga and D.A. Crowl. Derivation of Le Chatelier's mixing rule for flammable limits. *Process Saftey Progress*, 19:112–117, 2000.

[113] H.F. Coward and G.W. Jones. Limits of inflammability of gases and vapors. *U.S. Bureau of Mines*, Bulletin 279, Washington, DC, 1931.

[114] C.V. Mashuga and D.A. Crowl. Flammability zone prediction using calculated adiabatic flame temperatures. *Process Safety Progress*, 18:127–134, 1999.

[115] N. Chawla, P.R. Amyotte, and M.J. Pegg. A comparison of experimental methods to determine the minimum explosive concentration of dusts. *Fuel*, 75:654–658, 1996.

[116] J. Yuan, W. Huang, B. Du, N. Kuai, Z. Li, and J. Tan. An extensive discussion on experimental test of dust minimum explosible concentration. *Procedia Engineering*, 43:343–347, 2012.

[117] K.L. Cashdollar. Coal dust explosibility. *Journal of Loss Prevention in the Process Industries*, 9:65–76, 1996.

[118] O. Kalejaiye, P.R Amyotte, M.J Pegg, and Cashdollar K.L. Effectivemenss of dust dispersion in the 20-l Siwek chamber. *Journal of Loss Prevention in the Process Industries*, 23:46–59, 2010.

[119] C. Engler. Beiträge zur Kenntniss der Staubexplosionen. *Chemische Industrie*, pages 171–173, 1885.

[120] G.V.R. Landman. Ignition behaviour of hybrid mixtures of coal dust, methane, and air. *The Journal of the South African Institute of Mining and Metallurgy*, 95:45–50, 1995.

[121] I. Khalili, O. Dufaud, M. Poupeau, N. Cuervo-Rodriguez, and L. Perrin. Ignition sensitivity of gas-vapor/dust hybrid mixtures. *Powder Technology*, 217:199–206, 2012.

[122] E.K. Addai, D. Gabel, and U. Krause. Lower explosion limit of hybrid mixtures of burnable gas and dust. *Journal of Loss Prevention in the Process Industries*, 36:497–504, 2015.

[123] R.W. Prugh. The relationship between flash point and LFL with application to hybrid mixtures. *Process Saftey Progress*, 27:156–163, 2008.

[124] M. Nifuku, H. Tsujita, K. Fujino, K. Takaichi, C. Barre, E. Paya, M. Hatori, S. Fujiwara, S. Horiguchi, and I. Sochet. Ignitability assessment of shredder dusts of refrigerator and the prevention of the dust explosion. *Journal of Loss Prevention in the Process Industries*, 19:181–186, 2006.

[125] P. Julien, J. Vickery, S. Whiteley, A. Wright, S. Goroshin, J.M. Bergthorson, and D.L. Frost. Effect of scale on freely propagating flames in aluminum dust clouds. *Journal of Loss Prevention in the Process Industries*, 36:230–236, 2015.

[126] Ch. Proust, M.R. Ben, M. Guessasma, K. Saleh, and J. Fortin. Thermal radiation in dust flame propagation. *Journal of Loss Prevention in the Process Industries*, 49:896–904, 2017.

[127] J. Droujko, P. Julien, M. Soo, S. Goroshin, J.M. Bergthorson, D.L. Frost, and N. Glumac. The role of radiative preheating on flame propagation in aluminum dust clouds. In *Proceedings of the 11th International Symposium on Hazards, Prevention, and Mitigation of Industrial Explosions*, pages 435–448, 2016.

[128] D.G. Goodwin, H.K. Moffat, and R.L. Speth. Cantera: An object-oriented software toolkit for chemical kinetics, thermodynamics, and transport processes. http://www.cantera.org, 2017. Version 2.3.0, Accessed: 2017-03-06.

[129] K.K. Kuo and R. Acharya. *Fundamentals of Turbulent and Multiphase Combustion*. John Wiley & Sons, Inc., Hoboken, NJ, 2012.

[130] K. Kuo. *Principles of Combustion*. John Wiley & Sons, Inc., Hoboken, NJ, 2005.

[131] G.G. Stokes. On the theories of internal friction of fluids in motion. *Transactions of Cambridge Philosophical Society*, 8:287–305, 1845.

[132] C.R. Wilke. A viscosity equation for gas mixtures. *The Journal of Chemical Physics*, 18:517, 1950.

[133] B.E. Poling, J.M. Prausnitz, and J.P. O'Connell. *The Properties of Gases and Liquids*. McGraw-Hill Companies Inc., New York, NY, 5th edition, 2001.

[134] J.O. Hirschfelder, C.F. Curtiss, and R.B. Bird. *Molecular Theory of Gases and Liquids*. John Wiley, New York, NY, 1954.

[135] W. Sutherland. The viscosity of gases and molecular force. *Philosophical Magazine Series 5*, 36:507–531, 1893.

[136] G. Dixon-Lewis. A Fortran computer code package for the evaluation of gas-phase multicomponent transport properties. *Proceedings of the Royal Society*, A 304:111–135, 1968.

[137] S. Marthur, P.K. Tondon, and S.C. Saxena. Thermal conductivity of binary, ternary and quaternary mixtures of rare gases. *Molecular Physics*, 12:569–579, 1967.

[138] CERFACS. Cantera Users Guide - Methane/Air Combustion. http://www.cerfacs.fr/cantera/mecha-nisms/meth.php/, 2017. Accessed: 2017-03-06.

[139] B. Franzelli, E. Riber, L.Y.M. Gicquel, and T. Poinsot. Large eddy simulation of combustion instabilities in a lean partially premixed swirled flame. *Combustion and Flame*, 159:621–637, 2012.

[140] A. Kazakov and M. Frenklach. Reduced reaction sets based on GRI-Mech 1.2. http://combustion.berkeley.edu/drm/, 1994. Accessed: 2017-03-06.

[141] G.P. Smith, D.M. Golden, M. Frenklach, N.W. Moriarty, B. Eiteneer, M. Goldenberg, C.T. Bowman, R.K. Hanson, S. Song, W.C. Gardiner, V.V. Lissianski, and Z. Qin. GRI-Mech 3.0. http://combustion.berkeley.edu/gri-mech/, 1999. Accessed: 2017-03-06.

[142] M. Frenklach, H. Wang, C.-L. Yu, M. Goldenberg, C.T. Bowman, R.K. Hanson, D.F. Davidson, E.J. Chang, G.P. Smith, D.M. Golden, W.C. Gardiner, and V. Lissianski. GRI-Mech 1.2. http://combustion.berkeley.edu/gri-mech/, 1995. Accessed: 2017-03-06.

[143] M. Frenklach, H. Wang, M. Goldenberg, G.P. Smith, D.M. Golden, C.T. Bowman, R.K. Hanson, W.C. Gardiner, and V. Lissianski. GRI-Mech – An optimized detailed chemical reaction mechanism for methane combustion. Research Institute Topical Report, 1995. Report No. GRI-95/0058.

[144] D.R. Stull and H. Prophet. *JANAF Thermochemical Tables*. National Standard Reference Data Series 37, USA, 2nd edition, 1971.

[145] G.M. Faeth. Evaporation and combustion of sprays. *Progress in Energy and Combustion Science*, 9:1–76, 1983.

[146] A. Putnam. Integratable form of droplet drag coefficient. *ARS Journal*, 31:1467–1468, 1961.

[147] C.K. Law. Recent advances in droplet vaporization and combustion. *Progress in Energy and Combustion Science*, 8:171–201, 1982.

[148] W.E. Ranz and W.R. Marshall. Evaporation from drops. *Chemical Engineering Progress*, 48:141–146, 1952.

[149] C.E. Brennen. *Fundamentals of Multiphase Flows*. Cambridge University Press, Pasadena, CA, 2005.

[150] G. Dixon-Lewis, D. Bradley, and S. El-Din Habik. Burning of coal and organic dusts in air. *Archivum Combustionis*, 7:85–98, 1987.

[151] D.M. Christ. *The Effect of Char Kinetics on the Combustion of Pulverized Coal under Oxyfuel Conditions*. PhD thesis, RWTH Aachen University, Germany, 2013.

[152] M.A. Field. Rate of combustion of size-graded fractions of char from a low-rank coal between 1200°K and 2000°K. *Combustion and Flame*, 13:237–252, 1969.

[153] R.R. Upadhyay and O.A. Ezekoye. Treatment of size-dependent aerosol transport processes using quadrature based moment methods. *Journal of Aerosol Science*, 37:779–819, 2006.

[154] M.A. van der Hoef, M. van Sint Annaland, N.G Deen, and J.A.M Kuipers. Numerical simulation of dense gas-solid fluidized beds: A multiscale modeling strategy. *Annual Review of Fluid Mechanics*, 40:47–70, 2008.

[155] D. Migdal and V.D. Agosta. A source flow model for continuum gas–particle flow. *Journal of Applied Mechanics*, 34:860–865, 1967.

[156] S.V. Patanker. *Numerical Heat Transfer and Fluid Flow*. Hemisphere Publishing Corporation, United States, 1980.

[157] C. Hirsch. *Numerical Computation of Internal and External Flows*. John Wiley & Sons, New York, NY, 1991.

[158] R.I. Issa. Solution of the implicitly discretized fluid flow equations by operator-splitting. *Journal of Computational Physics*, 62:40–65, 1986.

[159] H. Jasak. *Error analysis and estimation for the finite volume method with applications to fluid flows*. PhD thesis, Imperial College, London, 1996.

[160] G.B. Macpherson, N. Nordin, and H.G. Weller. Particle tracking in unstructured, arbitrary polyhedral meshes for use in CFD and molecular dynamics. *Communications in Numerical Methods in Engineering*, 25:263–273, 2009.

[161] E. Hairer and G. Wanner. *Solving Ordinary Differential Equations II: Stiff and Differential-Algebraic Problems*. Springer-Verlag, Berlin, 2nd edition, 1996.

[162] S.R. Turns. *An Introduction to Combustion: Concepts and Applications*. McGraw-Hill Companies Inc., New York, NY, 3rd edition, 2012.

[163] E. Hu, X. Li, X. Meng, Y. Chen, Y. Cheng, Y. Xie, and Z. Huang. Laminar flame speeds and ignition delay times of methane-air mixtures at elevated temperatures and pressures. *Fuel*, 158:1–10, 2015.

[164] X.J. Gu, M.Z. Haq, M. Lawes, and R. Woolley. Laminar burning velocity and Markstein lengths of methane-air mixtures. *Combustion and Flame*, 121:41–58, 2000.

[165] G. Rozenchan, D.L. Zhu, C.K. Law, and S.D. Tse. Outward propagation, burning velocities, and chemical effects of methane flames up to 60 atm. *Proceedings of the Combustion Institute*, 29:1461–1470, 2002.

[166] O. Park, P.S. Veloo, N. Liu, and F.N. Egolfopoulos. Combustion characteristics of alternative gaseous fuels. *Proceedings of the Combustion Institute*, 33:887–894, 2011.

[167] H.M. Heravi, A. Azarinfar, S.I. Kwon, P.J. Bowen, and N. Syred. Determination of laminar flame thickness and burning velocity of methane-air mixture. In *Proceedings of the Third European Combustion Meeting*, 2007.

[168] H. Xiao, R.W. Houim, and E.S. Oran. Formation and evolution of distorted tulip flames. *Combustion and Flame*, 162:4048–4101, 2015.

[169] S.I. Kwon, M. Arai, and H. Hiroyasu. Effects of cylinder temperature and pressure on ignition delay in direct injection diesel engine. *Bulletin of Marine Engineering Society of Japan*, 18:1, 1990.

[170] Y. Lafay, B. Renou, G. Cabot, and M. Boukhalfa. Experimental and numerical investigation of the effect of H_2 enrichment on laminar methane–air flame thickness. *Combustion and Flame*, 153:540–561, 2008.

[171] G.E. Andrews and D. Bradley. The burning velocity of methane–air mixtures. *Combustion and Flame*, 19:275–288, 1972.

[172] J. Göttgens, F. Mauss, and N. Peters. Analytic approximations of burning velocities and flame thicknesses of lean hydrogen, methane, ethylene, ethane, acetylene, and propane flames. *Proceedings of the Twenty-Fourth Symposium (International) on Combustion*, pages 129–135, 1992.

[173] C.J. Sun, C.J. Sung, L. He, and C.K. Law. Dynamics of weakly stretched flames: Quantitative description and extraction of global flame parameters. *Combustion and Flame*, 118:108–128, 1999.

[174] C.K. Law and C.J. Sung. Structure, aerodynamics, and geometry of premixed flamelets. *Progress in Energy and Combustion Science*, 26:459–505, 2000.

[175] D. Castellanos, V.H. Carreto-Vazquez, C.V. Mashuga, R. Trottier, A.F. Mejia, and S.M. Mannan. The effect of particle size polydispersity on the explosibility characteristics of aluminum dust. *Powder Technology*, 254:331–337, 2014.

[176] A.L. Berlad, H. Ross, L. Facca, and Y. Tangirala. Particle cloud flames in acoustic fields. *Combustion and Flame*, 82:448–450, 1990.

[177] F.D. Tang, S. Goroshin, A. Higgins, and J. Lee. Flame propagation and quenching in iron dust clouds. *Proceedings of the Combustion Institute*, 32:1905–1912, 2009.

[178] K. Seshadri, A.L. Berlad, and V. Tangirala. The structure of premixed particle-cloud flames. *Combustion and Flame*, 89:333–342, 1992.

[179] P.R. Amyotte, M. Lindsay, R. Domaratzki, N. Marchand, A. Di Benedetto, and P. Russo. Prevention and mitigation of dust and hybrid mixture explosions. *Process Safety Progress*, 29:17–21, 2002.

[180] A. Di Benedetto. The thermal/thermodynamic theory of flammability: The adiabatic flammability limits. *Chemical Engineering Science*, 99:265–273, 2013.

[181] J. Du, H. Ma, Z. Qu, and L. Wang. Prediction of methane's flammability using chemical equilibrium. *Process Safety Progress*, 34:31–35, 2015.

[182] A.G. Dastidar and P.R. Amyotte. Using calculated adiabatic flame temperatures to determine dust explosion inerting requirements. *Process Safety and Environmental Protection*, 82:142–155, 2004.

[183] G.V.R. Landman. *Ignition and initiation of coal mine explosions*. PhD thesis, University of Witwatersrand, Johannesburg, South Africa, 1992.

Appendix A

Equivalence Ratio Calculation

The equivalence ratio is used in combustion applications to indicate whether the fuel–oxidiser mixture is rich, lean, or stoichiometric [162]. The equivalence ratio is defined as the fuel-to-air ratio of the mixture, divided by the fuel-to-air ratio at stoichiometric conditions:

$$\Phi = \frac{(F/A)}{(F/A)_{\mathrm{St}}} \tag{A.1}$$

where (F/A) is the fuel-to-air ratio of the mixture on a mass basis and $(F/A)_{\mathrm{St}}$ is the stoichiometric fuel-to-air ratio. If Φ has a value of unity, the amount of oxidiser available can completely consume the fuel. The mixture is fuel-lean when $\Phi < 1$ and fuel-rich when $\Phi > 1$.

In this work, five equivalence ratios can be defined based on methane combustion, coal dust combustion considering only the volatile component, coal dust combustion considering both volatile and carbon components, hybrid mixtures considering only methane and the coal dust volatile component, and hybrid mixtures considering methane and coal dust volatile and carbon components. Each of these equivalence ratios are derived in the following sections.

Methane Gas

The gas equivalence ratio is defined as the fuel-to-air ratio of methane gas divided by the stoichiometric fuel-to-air ratio of methane:

$$\Phi_{\mathrm{g}} = \frac{(F/A)^{\mathrm{v}}_{\mathrm{g}}}{(F/A)^{\mathrm{v}}_{\mathrm{St}}} \tag{A.2}$$

where Φ_{g} is the methane gas equivalence ratio, $(F/A)^{\mathrm{v}}_{\mathrm{g}}$ is the fuel-to-air ratio of methane in the mixture, and $(F/A)^{\mathrm{v}}_{\mathrm{St}}$ is the stoichiometric fuel-to-air ratio of methane.

The fuel-to-air ratio of methane in the mixture can be defined in terms of the mass

fractions of methane and air. In a gas mixture containing only these two components:

$$(F/A)^{\mathrm{v}}_{\mathrm{g}} = \frac{Y_{\mathrm{CH_4}}}{Y_{\mathrm{air}}} = \frac{Y_{\mathrm{CH_4}}}{1 - Y_{\mathrm{CH_4}}} \tag{A.3}$$

where $Y_{\mathrm{CH_4}}$ is the mass fraction of methane and Y_{air} is the mass fraction of air.

The stoichiometric fuel-to-air ratio is determined by writing the balanced chemical equation for methane and computing the mass of fuel and air needed for stoichiometric combustion. This calculation is presented in Table A.1 for methane gas where carbon dioxide and water are assumed to be the final reaction products. In the calculation c_k, M_k, and m_k are individual specie molar mass, molecular weight, and mass, and c and m are the summation of molar mass and mass. The variables X_k and Y_k are the individual specie mole fraction and mass fraction, respectively. In Table A.1, the oxidiser is assumed to be air, and the number of mols of nitrogen, $c_{\mathrm{N_2}}$, is calculated from $c_{\mathrm{N_2}} = 3.762 c_{\mathrm{O_2}}$.

Table A.1: Balanced stoichiometry for methane gas in air used to calculate specie mass fractions for the stoichiometric fuel-to-air ratio.

		$\mathbf{CH_4}$	$\mathbf{O_2}$	$\mathbf{N_2}$	$\rightarrow$	$\mathbf{CO_2}$	$\mathbf{H_2O}$	$\mathbf{N_2}$
c_k	(mol)	1.000	2.000	7.524		1.000	2.000	7.524
M_k	(g/mol)	16.043	31.999	28.013		44.010	18.015	28.013
m_k	(g)	16.043	63.998	210.767		44.010	36.031	210.767
c	(mol)			10.523				10.523
m	(g)			290.808				290.808
X_k		0.095	0.190	0.715		0.095	0.190	0.715
Y_k		0.055	0.220	0.725		0.151	0.124	0.724

From the calculation presented in Table A.1, the mass fraction of methane for stoichiometric combustion is calculated as $Y_{\mathrm{CH_4}} = 0.055$. From this, the stoichiometric fuel-to-air ratio is determined:

$$(F/A)^{\mathrm{v}}_{\mathrm{St}} = \frac{0.055}{1 - 0.055} = 0.0582 \tag{A.4}$$

This allows the equivalence ratio to be specified based on the mass fraction of methane in the fuel-air mixture:

$$\Phi_{\mathrm{g}} = \frac{Y_k}{(1 - Y_k)\, 0.0582} \tag{A.5}$$

Since dust-air mixtures are often specified in terms of mass concentration, it is insightful to specify methane-air mixtures in terms of mass concentration. Methane mass fraction can be calculated from equivalence ratio by rearranging Equation A.5:

$$Y_{\mathrm{CH_4}} = \frac{0.0582\Phi_{\mathrm{g}}}{1 + 0.0582\Phi_{\mathrm{g}}} \tag{A.6}$$

The mass concentration of methane can be determined from the product of the methane mass fraction and overall gas density:

$$\rho_{\mathrm{CH_4}} = \rho Y_{\mathrm{CH_4}} \tag{A.7}$$

where $\rho_{\mathrm{CH_4}}$ is the component mass concentration of methane gas and ρ is the gas density of the mixture. The gas density can be calculated from the ideal gas law, again assuming that methane and air are the only components of the mixture:

$$\rho = \frac{P}{(\mathcal{R}/M_{\mathrm{mix}})\,T} \tag{A.8}$$

$$M_{\mathrm{mix}} = \frac{1}{\sum_{k=1}^{N_k} Y_k/M_k} = \frac{1}{\frac{Y_{\mathrm{CH_4}}}{M_{\mathrm{CH_4}}} + \frac{\left(1-Y_{\mathrm{CH_4}}\right)}{M_{\mathrm{air}}}} \tag{A.9}$$

where P is pressure, $\mathcal{R}$ is the universal gas constant, M_{mix} is the molecuilar weight of the gas mixture, and T is temperature. Letting $P = 101\,325\,\mathrm{Pa}$, $T = 300\,\mathrm{K}$, $M_{\mathrm{CH_4}} = 16.043\,\mathrm{g/mol}$, $M_{\mathrm{air}} = 28.85\,\mathrm{g/mol}$ and $\Phi_{\mathrm{g}} = 1$, gas density is calculated as $1.123\,\mathrm{kg/m^3}$. From Equation A.7 the stoichiometric mass concentration of methane is calculated as $62\,\mathrm{g/m^3}$.

Coal Dust (Volatile Component)

The coal dust equivalence ratio considering only the volatile component of the fuel is calculated as the fuel-to-air ratio of volatiles from the coal, divided by the stoichiometric fuel-to-air ratio:

$$\Phi_{\mathrm{p}}^{\mathrm{v}} = \frac{(F/A)_{\mathrm{p}}^{\mathrm{v}}}{(F/A)_{\mathrm{St}}^{\mathrm{v}}} \tag{A.10}$$

where the fuel-to-air ratio of coal is equal to the mass concentration of volatiles divided by the mass concentration of air:

$$(F/A)^{\mathrm{v}}_{\mathrm{p}} = \frac{\psi_{\mathrm{v}}\sigma_{\mathrm{p}}}{\rho_{\mathrm{air}}} \tag{A.11}$$

where σ_{p} is the total dust concentration, ψ_{v} is the mass fraction of volatiles in the coal and ρ_{air} is the density of air. Using the ideal gas law, the density of air at $P = 101\,325\,\mathrm{Pa}$ and $T = 300\,\mathrm{K}$ is calculated as $1.172\,\mathrm{kg/m^3}$.

In the current work, the mass fraction of volatiles in the dust is 40 % ($\psi_{\mathrm{v}} = 0.4$). The volatiles are assumed to contain only methane gas and therefore the stoichiometric fuel-to-air ratio is given by the value calculated in Equation A.4. Substituting these values into Equation A.10 gives the following for coal dust equivalence ratio considering only the volatile component of the dust:

$$\Phi^{\mathrm{v}}_{\mathrm{p}} = \frac{\psi_{\mathrm{v}}\sigma_{\mathrm{p}}}{0.0582 \cdot \rho_{\mathrm{air}}} = \frac{0.4 \cdot \sigma_{\mathrm{p}}}{0.0582 \cdot 1.172\mathrm{kg/m^3}} = 5.864\sigma_{\mathrm{p}} \tag{A.12}$$

where the dust concentration, σ_{p} must be specified in $\mathrm{kg/m^3}$. Letting $\Phi^{\mathrm{v}}_{\mathrm{p}} = 1$, the stoichiometric concentration of coal dust considering only the volatile component is calculated as $170\,\mathrm{g/m^3}$.

Coal Dust (Volatile and Carbon Components)

The coal dust equivalence ratio considering both the volatile and carbon components of the fuel, is calculated as the total fuel-to-air ratio from the dust divided by the total stoichiometric fuel-to-air ratio:

$$\Phi^{\mathrm{t}}_{\mathrm{p}} = \frac{(F/A)^{\mathrm{t}}_{\mathrm{p}}}{(F/A)^{\mathrm{t}}_{\mathrm{St}}} \tag{A.13}$$

In this work, the ash and moisture content of the coal is assumed negligible and the dust is assumed to contain only volatiles and carbon ($\sigma_{\mathrm{p}} = \sigma^{\mathrm{v}}_{\mathrm{p}} + \sigma^{\mathrm{s}}_{\mathrm{p}}$). The total fuel-to-air ratio is then defined based on the overall dust concentration:

$$(F/A)^{\mathrm{t}}_{\mathrm{p}} = \frac{\sigma_{\mathrm{p}}}{\rho_{\mathrm{air}}} \tag{A.14}$$

In order to determine the balanced chemical equation for methane and carbon reaction, the molar ratio between the two is required. The molar ratio can be specified based on the mass ratio:

$$\frac{c_{\mathrm{p}}^{\mathrm{s}}}{c_{\mathrm{p}}^{\mathrm{v}}} = \frac{M_{\mathrm{CH_4}}}{M_{\mathrm{C}}} \left(\frac{\sigma_{\mathrm{p}}^{\mathrm{s}}}{\sigma_{\mathrm{p}}^{\mathrm{v}}} \right) \tag{A.15}$$

where the mass ratio can be specified from the volatile mass fraction:

$$\frac{\sigma_{\mathrm{p}}^{\mathrm{s}}}{\sigma_{\mathrm{p}}^{\mathrm{v}}} = \frac{1 - \psi_{\mathrm{v}}}{\psi_{\mathrm{v}}} \tag{A.16}$$

Combining Equation A.15 with Equation A.16 allows the molar ratio between methane volatiles and carbon to be calculated:

$$\frac{c_{\mathrm{p}}^{\mathrm{s}}}{c_{\mathrm{p}}^{\mathrm{v}}} = \frac{16.043\mathrm{g/mol}}{12.011\mathrm{g/mol}} \left(\frac{1 - 0.4}{0.4} \right) = 2.004 \tag{A.17}$$

The balanced stoichiometric equation for coal dust containing 40 % methane volatiles and 60 % carbon is given in Table A.2. The molar ratio between carbon and methane is used to specify the reactant fuels and the gas is assumed to contain only air initially.

Table A.2: Balanced stoichiometry for coal dust in air including volatile methane and carbon components.

		$\mathbf{CH_4}$	$\mathbf{C}$	$\mathbf{O_2}$	$\mathbf{N_2}$	$\rightarrow$	$\mathbf{CO_2}$	$\mathbf{H_2O}$	$\mathbf{N_2}$
c_k	(mol)	1.000	2.004	4.004	15.061		3.004	2.000	15.061
M_k	(g/mol)	16.043	12.011	31.999	28.013		44.010	18.015	28.013
m_k	(g)	16.043	24.064	128.110	421.913		132.188	36.031	421.913
c	(mol)				22.068				20.065
m	(g)				590.130				590.130
X_k		0.045	0.091	0.181	0.682		0.150	0.100	0.750
Y_k		0.027	0.041	0.217	0.715		0.224	0.061	0.715

The stoichiometric fuel-to-air ratio is the total mass of fuel in the mixture divided by the mass of air. From Table A.2, the stoichiometric fuel-to-air ratio for coal dust considering both volatile and carbon components is calculated as:

$$(F/A)_{\mathrm{St}}^{\mathrm{t}} = \frac{m_{\mathrm{CH_4}} + m_{\mathrm{C}}}{m_{\mathrm{air}}} = \frac{16.043 + 24.064}{550.023} = 0.073 \tag{A.18}$$

Substituting Equation A.14 and Equation A.18 into Equation A.13 gives the following for coal dust equivalence ratio considering both the volatile and carbon components of the dust:

$$\Phi_{\mathrm{p}}^{\mathrm{t}} = \frac{\sigma_{\mathrm{p}}}{0.073 \cdot 1.172\mathrm{kg/m^3}} = 11.69\sigma_{\mathrm{p}} \tag{A.19}$$

again where the dust concentration, σ_{p}, is specified in kg/m^3. Letting $\Phi_{\mathrm{p}}^{\mathrm{t}} = 1$, the stoichiometric concentration of coal dust considering both the volatile and carbon components is calculated as 85 g/m^3.

Hybrid Mixture (Volatile Component)

The hybrid mixture equivalence ratio considering only the volatile component of the coal is calculated as the overall fuel-to-air ratio from the gas and dust volatiles, divided by the stoichiometric fuel-to-air ratio:

$$\Phi_{\mathrm{h}}^{\mathrm{v}} = \frac{(F/A)_{\mathrm{h}}^{\mathrm{v}}}{(F/A)_{\mathrm{St}}^{\mathrm{v}}} \tag{A.20}$$

where the fuel-to-air ratio includes components from the dust volatiles and methane gas. Combining Equation A.3 and Equation A.11 gives the following definition for fuel-to-air ratio:

$$(F/A)_{\mathrm{h}}^{\mathrm{v}} = \frac{\psi_{\mathrm{v}}\sigma_{\mathrm{p}} + Y_{\mathrm{CH_4}}\rho}{\rho_{\mathrm{air}}} \tag{A.21}$$

Allowing the gas to initially contain only methane and air ($\rho_{\mathrm{air}} = (1 - Y_{\mathrm{CH_4}})\,\rho$) the fuel-to-air ratio can be rewritten as follows:

$$(F/A)_{\mathrm{h}}^{\mathrm{v}} = \frac{\psi_{\mathrm{v}}\sigma_{\mathrm{p}} + Y_{\mathrm{CH_4}}\rho}{(1 - Y_{\mathrm{CH_4}})\,\rho} = \frac{\psi_{\mathrm{v}}\sigma_{\mathrm{p}}}{(1 - Y_{\mathrm{CH_4}})\,\rho} + \frac{Y_{\mathrm{CH_4}}}{1 - Y_{\mathrm{CH_4}}} \tag{A.22}$$

Lastly, substituting $(F/A)_{\mathrm{St}}^{\mathrm{v}}$ and Equation A.22 into Equation A.20 gives the following for hybrid mixture equivalence ratio considering the methane gas and coal dust volatiles:

$$\Phi_{\mathrm{h}}^{\mathrm{v}} = \frac{\psi_{\mathrm{v}}\sigma_{\mathrm{p}}}{0.0582 \cdot (1 - Y_{\mathrm{CH_4}})\,\rho} + \Phi_{\mathrm{g}} \tag{A.23}$$

When the mass fraction of methane is small, ρ_{air} is approximately equal to ρ, and the volatile component hybrid mixture equivalence ratio can be approximated by addition of the dust and gas equivalence ratios individually:

$$\Phi_{\mathrm{h}}^{\mathrm{v}} \approx \Phi_{\mathrm{p}}^{\mathrm{v}} + \Phi_{\mathrm{g}} \tag{A.24}$$

Hybrid Mixture (Volatile and Carbon Components)

The hybrid mixture equivalence ratio considering methane gas, coal dust volatiles, and carbon reaction, is calculated as the total fuel-to-air ratio divided by the stoichiometric fuel-to-air ratio from all three components:

$$\Phi_{\mathrm{h}}^{\mathrm{t}} = \frac{(F/A)_{\mathrm{h}}^{\mathrm{t}}}{(F/A)_{\mathrm{St}}^{\mathrm{t}'}} \tag{A.25}$$

where $(F/A)_{\mathrm{h}}^{\mathrm{t}}$ is the hybrid fuel-to-air ratio of the mixture and $(F/A)_{\mathrm{St}}^{\mathrm{t}'}$ is the total stoichiometric fuel-to-air ratio considering combustion of methane, volatiles, and carbon.

In a similar manner as $(F/A)_{\mathrm{h}}^{\mathrm{v}}$, the total hybrid fuel-to-air ratio of the mixture can be determined by combining Equation A.3 and Equation A.14:

$$(F/A)_{\mathrm{h}}^{\mathrm{t}} = \frac{\sigma_{\mathrm{p}}}{(1 - Y_{\mathrm{CH_4}})\,\rho} + \frac{Y_{\mathrm{CH_4}}}{1 - Y_{\mathrm{CH_4}}} \tag{A.26}$$

In order to determine the balanced chemical equation for methane and carbon reaction, the molar ratio is again required. The molar ratio can be specified based on the mass ratio of the available carbon and methane.

$$\frac{c_{\mathrm{p}}^{\mathrm{s}}}{c_{\mathrm{p}}^{\mathrm{v}}} = \frac{M_{\mathrm{CH_4}}}{M_{\mathrm{C}}} \left(\frac{\sigma_{\mathrm{p}}^{\mathrm{s}}}{\sigma_{\mathrm{p}}^{\mathrm{v}} + Y_{\mathrm{CH_4}}\rho} \right) \tag{A.27}$$

In this case, the molar ratio is not a fixed value and depends on the amount of methane gas in the hybrid mixture. In the limited case where $Y_{\mathrm{CH_4}}\rho \ll \sigma_{\mathrm{p}}^{\mathrm{v}}$, the total hybrid equivalence ratio can be estimated from the equivalence ratio of the methane and total equivalence ratio of the dust:

$$\Phi_{\mathrm{h}}^{\mathrm{t}} \approx \Phi_{\mathrm{p}}^{\mathrm{t}} + \Phi_{\mathrm{g}} \tag{A.28}$$

With the stoichiometric methane concentration occurring at $Y_{\mathrm{CH_4}}\rho = 62\,\mathrm{g/m^3}$, this approximation is only valid for high dust concentrations or very low methane gas concentrations. Otherwise, $(F/A)_{\mathrm{St}}^{\mathrm{t}'}$ must be calculated from the combustion stoichiometry using Equation A.27.

Since the molar ratio of carbon and methane is variable depending on the concentration of gas in the hybrid mixture, a single balanced stoichiometry equation cannot

be developed. Instead the stoichiometric fuel-to-air ratio must be determined based on the mass concentration of each component in the reactants:

$$(F/A)^{\mathrm{t}'}_{\mathrm{St}} = \frac{c_{\mathrm{CH_4}} M_{\mathrm{CH_4}} + c_{\mathrm{C}} M_{\mathrm{C}}}{c_{\mathrm{O_2}} \left(M_{\mathrm{O_2}} + 3.762 M_{\mathrm{N_2}}\right)} \tag{A.29}$$

Letting $c_{\mathrm{CH_4}} = 1$ and $c_{\mathrm{C}} = c^{\mathrm{s}}_{\mathrm{p}}/c^{\mathrm{v}}_{\mathrm{p}}$, $c_{\mathrm{O_2}}$ is calculated as $c^{\mathrm{s}}_{\mathrm{p}}/c^{\mathrm{v}}_{\mathrm{p}} + 2$, from stoichiometry. Substituting these values into Equation A.29 gives the final relation for stoichiometric fuel-to-air ratio:

$$(F/A)^{\mathrm{t}'}_{\mathrm{St}} = \frac{M_{\mathrm{CH_4}} + \frac{c^{\mathrm{s}}_{\mathrm{p}}}{c^{\mathrm{v}}_{\mathrm{p}}} M_{\mathrm{C}}}{\left(2 + \frac{c^{\mathrm{s}}_{\mathrm{p}}}{c^{\mathrm{v}}_{\mathrm{p}}}\right) \left(M_{\mathrm{O_2}} + 3.762 M_{\mathrm{N_2}}\right)} \tag{A.30}$$

Lastly, substituting Equation A.26 and Equation A.30 into Equation A.25 gives the hybrid mixture equivalence ratio considering coal dust volatile and carbon components:

$$\Phi^{\mathrm{t}}_{\mathrm{h}} = \frac{\left(\sigma_{\mathrm{p}} + Y_{\mathrm{CH_4}} \rho\right) \left(2 + \frac{c^{\mathrm{s}}_{\mathrm{p}}}{c^{\mathrm{v}}_{\mathrm{p}}}\right) \left(M_{\mathrm{O_2}} + 3.726 M_{\mathrm{N_2}}\right)}{\left(1 - Y_{\mathrm{CH_4}}\right) \rho \left(M_{\mathrm{CH_4}} + \frac{c^{\mathrm{s}}_{\mathrm{p}}}{c^{\mathrm{v}}_{\mathrm{p}}} M_{\mathrm{C}}\right)} \tag{A.31}$$

where $c^{\mathrm{s}}_{\mathrm{p}}/c^{\mathrm{v}}_{\mathrm{p}}$ is calculated from Equation A.27, and σ_{p} and ρ are specified in the same units.